DEVELOPMENT OF CATALYTIC PROCESS FOR BIOGAS UPGRADING: STUDY OF STRUCTURE AND OXYGEN MOBILITY ON Ni AND Pt NANOPARTICLES ENCAPSULATED CATALYSTS

André Luiz Alvarenga Marinho

Tese de Doutorado apresentada ao Programa de Pós-graduação em Engenharia Química, COPPE, da Universidade Federal do Rio de Janeiro, como parte dos requisitos necessários à obtenção do título de Doutor em Engenharia Química.

Orientador(es): Fábio Souza Toniolo
Fábio Bellot Noronha
Nicolas Bion

Rio de Janeiro

Outubro de 2020

DEVELOPMENT OF CATALYTIC PROCESS FOR BIOGAS UPGRADING: STUDY OF STRUCTURE AND OXYGEN MOBILITY ON Ni AND Pt NANOPARTICLES ENCAPSULATED CATALYSTS

André Luiz Alvarenga Marinho

TESE SUBMETIDA AO CORPO DOCENTE DO INSTITUTO ALBERTO LUIZ COIMBRA DE PÓS-GRADUAÇÃO E PESQUISA DE ENGENHARIA DA UNIVERSIDADE FEDERAL DO RIO DE JANEIRO COMO PARTE DOS REQUISITOS NECESSÁRIOS PARA A OBTENÇÃO DO GRAU DE DOUTOR EM CIÊNCIAS EM ENGENHARIA QUÍMICA.

Orientadores: Fábio Souza Toniolo
Fábio Bellot Noronha
Nicolas Bion

Aprovada por: Prof. Fábio Souza Toniolo
Dr. Fábio Bellot Noronha
Dr. Nicolas Bion
Profª. Carla Eponina Hori
Profª. Florence Epron
Prof. Patrick da Costa
Prof. Argimiro Resende Secchi

RIO DE JANEIRO, RJ - BRASIL
OUTUBRO DE 2020

Marinho, André Luiz Alvarenga

Development of Catalytic Process for Biogas Upgrading: Study of Structure and Oxygen Mobility on Ni And Pt Nanoparticles Encapsulated Catalysts / André Luiz Alvarenga Marinho – Rio de Janeiro: UFRJ/COPPE, 2020.

XVI, 132 p. 200: il.; 29,7 cm.

Orientadores: Fábio Souza Toniolo

Fábio Bellot Noronha

Nicolas Bion

Tese (doutorado) – UFRJ/ COPPE/ Programa de Engenharia Química, 2029.

Referências Bibliográficas: p. 161-186.

1. Reforma seca do metano. 2. Níquel. 3. Core-shell. 4. Coque. 5. Desativação catalítica I. Toniolo, Fábio Souza e*t al*. II. Universidade Federal do Rio de Janeiro, COPPE, Programa de Engenharia Química. III. Título.

"Soyes moins curieux des gens et plus curieux des idées" – Marie Curie

ACKNOWLEDGEMENTS

This thesis is a result of a lot of effort with important contributions of many colleges. Firstly, I would like to thank my advisors Fábio Souza Toniolo, Fábio Bellot Noronha and Nicolas Bion for their valuable guidance and patience throughout these 4 years. I thank Fábio Bellot and Fábio Toniolo for their dedication and their valuable help in the experimental work, discussion of results and great ideas. I am grateful to Dr. Nicolas Bion to received me in his group at the University of Poitiers and has mentoring me for one year in addition to the fruitful collaboration.

I want to thank the National Institute of Technology for allowed me to conduct my research and the LACAT-INT technical team for the characterization analyzes and help in laboratory. To NUCAT team (students, researchers, technicians and teachers), thank you very much for the good work environment and quality of research. To all my friends at NUCAT and LACAT that contribute for this research and funny moments.

I would like to thanks CAPES, COFECUB and CNPq for the financial support during this research.

Finally, I want to especially thanks my dear family for all support throughout my life. To my mother Eliane and my father José who invested in me and are responsible for who I am and for what I conquered. My sister Letícia for the fellowship and friendship. Especial thanks to my beloved wife Elienai for the attention, love and help.

Resumo da Tese apresentada à COPPE/UFRJ como parte dos requisitos necessários para a obtenção do grau de Doutor em Ciências (D.Sc.)

DESENVOLVIMENTO DE PROCESSO CATALÍTICO PARA APROVEITAMENTO DO BIOGÁS: ESTUDO DA ESTRUTURA E MOBILIDADE DE OXIGÊNIO DE CATALISADORES COM NANOPARTÍCULAS Ni E Pt ENCAPSULADAS

André Luiz Alvarenga Marinho

Outubro/2020

Orientadores: Fábio Souza Toniolo
Fábio Bellot Noronha
Nicolas Bion

Programa: Engenharia Química

Este trabalho avalia o efeito do encapsulamento Ni e Pt no processo de reforma seca do metano renovável a partir do biogás. Os resultados mostraram que Ni incorporado no CeO_2 melhorou a resistência à sinterização ao longo da redução a altas temperaturas e levou a uma maior interação metal-suporte em comparação com o catalisador impregnado. A dopagem do CeO_2 com Zr aumentou a mobilidade de oxigênio no suporte. A dopagem da CeO_2 com Gd e Sm não apresentou o mesmo efeito, ocorrendo diminuição da redutibilidade do CeO_2. Catalisadores de Ni dispersos nos mesoporos da alumina apresentaram pequenas partículas metálicas de Ni quando sintetizados junto ao suporte. A impregnação pós-síntese leva a formação de grandes partículas de Ni, favorecendo a formação de carbono sobre o catalisador. A adição de CeO_2 conferiu capacidade de armazenamento de oxigênio ao suporte. O trabalho com catalisadores de Pt mostrou que a estrutura embebida favorece a mobilidade de oxigênio no catalisador. Os catalisadores $Ni@CeZrO_2$ e $10Ni\text{-}CeO_2\text{-}Al_2O_3$ apresentaram alta resistência ao coque na condição de reforma seca do metano.

Abstract of Thesis presented to COPPE/UFRJ as a partial fulfillment of the requirements for the degree of Doctor of Science (D.Sc.)

DEVELOPMENT OF CATALYTIC PROCESS FOR BIOGAS UPGRADING: STUDY OF STRUCTURE AND OXYGEN MOBILITY ON Ni AND Pt NANOPARTICLES ENCAPSULATED CATALYSTS

André Luiz Alvarenga Marinho

October/2020

Advisors: Fábio Souza Toniolo
Fábio Bellot Noronha
Nicolas Bion

Department: Chemical Engineering

This work evaluates the effect of Ni and Pt encapsulation in the dry reforming of renewable methane from biogas. Results showed that Ni embedded in ceria improved the resistance to sintering along the reduction at high temperature and led to a higher metal-support interaction compared to impregnated catalyst. Doping ceria with Zr increased the oxygen mobility as revealed by oxygen isotopic exchange experiments. The doping with Gd and Sm did not present the same effect, occurring the decrease in ceria reducibility. Ni-based mesoporous mixed CeO_2-Al_2O_3 oxide catalysts presented small metallic Ni particles when it is synthetized with the support. The impregnation post-synthesis leads to the formation of large Ni particles favoring the carbon formation over the 10Ni/CeAl catalyst. The addition of CeO_2 increased the oxygen storage capacity of the support. The work with Pt-based catalysts showed the positive effect of embedded structure to enhance the oxygen mobility in the catalyst. The Ni@$CeZrO_2$ and 10Ni-CeO_2-Al_2O_3 catalysts presented high resistance to coke under dry reforming of methane condition.

SUMMARY

LIST OF FIGURES

LIST OF TABLES

CHAPTER 1

Introduction

The world has been observed a high demand by energy in the last decades, mainly because economic development of the countries. Actually, the fossil fuels, such as petroleum, natural gas and coal, play as energy source due the existence of well-established technologies to obtain energy from these sources (ABDULLAH; ABD GHANI; VO, 2017).

However, the use of fossil fuels has increasingly gained resistance due to the release of greenhouse gases to atmosphere that contribute to global warming (LUNSFORD, 2000). Moreover, the biggest reserves of petroleum are sited at Middle East and the region has historical instabilities which affect the oil market. Therefore, the diversification of the energy matrix is necessary, mainly in the insertion of renewable energy sources.

Biomass has attracted more attention, mainly in Brazil, as a renewable source of energy. As a large country with high agricultural activities, the residues generated by this industry have been increasingly studied for its use for energy generation. The biogas generated from anaerobic decomposition of biomass is composed mainly by CH_4 and CO_2 that cannot be released directly into the environment since it has two of the gases with the greatest global warming potential. However, this biogas can be seen with great energy potential, as a renewable source of CH_4 and raw material for products of higher added value, such as synthesis gas.

Reforming reactions are the most industrially process for syngas production, where methane can react with water (steam reforming), carbon dioxide (dry reforming) or oxygen (oxidative reforming), with steam reforming being the most conventional method for hydrogen production from hydrocarbons (PALMA et al., 2016). The dry reforming is efficient for biogas upgrading because the high concentration of CO_2 in biogas composition, producing synthesis gas and reducing the emission of greenhouse gases (YANG et al., 2014). The catalysts with the best performance for dry reforming of methane are those supported by noble metal, such as Pt, Pd and Rh, and non-noble metal, such as Ni (ROSTRUP-NIELSEN; HANSEN, 1993). However, the extreme operating conditions leads to the catalyst deactivation by coke formation or metallic particle sintering.

The challenge is to develop a Ni-based and Pt-based catalyst that is resistant to coke deactivation. One approach to minimize coke formation is to decrease the metallic particle size through modifications in catalyst structure. Recently, the development of catalysts with core-shell and mesoporous structures have been successful to prevent

sintering process (FANG et al., 2015; LI et al., 2016). Core-shell catalysts have a metal core covered by an oxide layer, with unique characteristics compared to traditional supported catalysts. Among the inorganic layers used to confine the metal, CeO_2 and doped-CeO_2 are interesting due to their oxygen mobility, promoting carbon removal mechanism (CARGNELLO et al., 2010). Whereas, mesoporous materials with high surface area and well-defined pores also present high resistance to sintering, resulting in a homogeneous catalyst with high Ni dispersion into mesopores and strong metal-support interaction (GROSSO et al., 2004).

Therefore, the subject of this work is to evaluate the performance and resistant to coke formation during the dry reforming of methane over two different encapsulating structures: (i) Ni@CeO_2 and Pt@CeO_2 catalysts with core-shell structure prepared by a facile sol-gel synthesis method; (ii) Ni nanoparticles into CeO_2-Al_2O_3 mesoporous supports prepared by Evaporation Induced Self-Assembly (EISA) method. This work will bring fundamental conclusions about the effect of structure, active phase, oxygen mobility, dopant addition and operating conditions to prevent catalyst deactivation by metal sintering and/or carbon formation. The thesis was developed under a co-tutelle agreement between the Federal University of Rio de Janeiro in Brazil and the University of Poitiers in France. In Brazil, core-shell catalyst preparation was performed, as well as basic characterizations and catalytic tests. During the internship at the University of Poitiers, *in-situ* measurements were performed to study the reaction mechanism, transmission electron microscopy analyses and isotopic exchange measurements in order to observe oxygen mobility in the materials and the carbon removal mechanism.

The thesis is divided in a brief Literature Review, the Methodology employed, Results and Discussion divided in four chapters: (i) Effect of embedded structure and oxygen mobility in Ni/CeO_2, Ni@CeO_2 and Ni@$CeZrO_2$; (ii) Effect of metal dopant in Ni@$CeMO_2$ catalysts (M = Zr, Gd and Sm); (iii) Effect of Ni encapsulating into CeO_2-Al_2O_3 mesoporous support by EISA method; (iv) Effect of oxygen mobility in Pt/CeO_2, Pt@CeO_2 and Pt@$CeZrO_2$. Finally, it is presented the General Conclusions about this thesis and Suggestions for future works.

CHAPTER 2

Literature Review

2.1 Renewable Energy

The demand of energy has observed a long increase during the last decades due to the development of the human society (OLIVEIRA; TRINDADE, 2018). According with IEA (International Energy Agency), the energy demand grew 2.3 % at 2018, the fastest pace in the decade. This increase is driven by the robust global economy and the main source of energy is natural gas (45 % of energy consumption). Fossil fuels demands in general observed an increase around 70 % (IEA, 2019).

The concept of non-renewable source is limited and not geography distributed homogeneously (OLIVEIRA; TRINDADE, 2018). The biggest reserves of petroleum are sited at Middle East and the region has historical instabilities which affect the oil market. Furthermore, the use of oil, natural gas and coal contributes significantly to global warming due the emission of greenhouse gases. Therefore, the problems cited have prompted the movement to diversification of the energy matrix by the countries. Around 90 % of primary energy is derived from these non-renewable sources, however the participation of renewable sources, mainly solar and wind, grow up in the last years. The projection of Energy Information Administration (EIA) to 2050 is the growth of all primary energy sources. However, the renewable sources become the leading source of primary energy in the world driven by policy and economic drivers together with a decline for petroleum and other liquid fuels in the energy matrix (EIA, 2019).

2.2 Biogas: Biomass-derived energy source

Even the emission of methane contributes with only 10 % of global greenhouse gas emission, in the last few years an increase in methane emissions has been observed and the potential of this gas to contribute for global warming is higher compared to the main greenhouse gas, i.e. CO_2, about 25 greater than CO_2 (IPCC, 2007). Therefore, new strategies to reduce methane emissions must be adopted by the countries.

The renewable energy according to Intergovernmental Panel on Climate Change (IPCC) have the potential to slow down the effects of global warming (IPCC, 2012). Among the alternatives of renewable energy, biomass have an important participation in the countries with high agricultural activities, for example Brazil. The Brazilian matrix energy shows the participation of renewable energy, around 40 %, mainly for hydroelectric generation and sugarcane biomass.

The biogas generated from anaerobic digestion of biomass can be an alternative way to minimize the waste of biomass industry. Besides the biomass industry, other biogas sources can be considered such as landfills, animal manure or forestry residues (PÉREZ-CHÁVEZ; MAYER; ALBERTÓ, 2019). Its composition is basically CH_4, CO_2 and N_2, with the presence of some trace species such as H_2S, H_2, NH_3 and H_2O. Table 2.1 presents the composition of some biogas sources compared to natural gas. The biogas generated at Anaerobic Digester (AD) are like that generated at landfills with a slightly increase at CH_4 content. In comparison to natural gas, biogas have a high content of CO_2 which is responsible for decreasing the biogas heating value (YANG et al., 2014). Since biogas presents in its composition basically CH_4 and CO_2, this gas is one big source of greenhouse gases and must be upgraded in order to prevent its emission in the environment.

Table 2.1. Biogas composition from different sources in comparison to natural gas (YANG et al., 2014).

Compound	AD Biogas	Landfill Biogas	Natural Gas
CH_4 (%)	53-70	30-65	81-89
CO_2 (%)	30-50	25-47	0.67-1
N_2 (%)	2-6	<1-17	0.28-14
O_2 (%)	0-5	<1-3	0
H_2 (%)	---	0-3	---
H_2S (ppm)	0-2000	30-500	0-2.9
NH_3 (ppm)	<100	0-5	---
Siloxanes (µg/g-gas)	<0.08-0.5	<0.3-36	---

In order to purify this biogas and obtain biomethane some techniques are used to upgrade the biogas. The technologies used at industrial scale include adsorption, absorption, membrane separation and cryogenic. These techniques are used to separate CO_2 from biogas; however, pre-upgrade stages are required to remove H_2S, H_2O and siloxanes (ULLAH KHAN et al., 2017), since these components cause seriously damages to the equipment.

Despite the direct utilization of biogas to generate energy, an alternative way to produce chemicals with high value-added products by Gas-To-Liquids process (GTL) applying the biogas driven special attention in the last years. The GTL process consists in the conversion of natural gas to liquid fuels by chemical reactions replacing the fuel derived from petroleum-based fuels (WANG; ECONOMIDES, 2009). Therefore, the gradual substitution of natural gas by biogas in the GTL process is an interesting route to obtain liquid fuels environmentally friendly.

The reforming process are the main routes to produce syngas at large scale in the world. There are three reforming process, e.g. dry reforming of methane (DRM) (Eq. 2.1), steam reforming of methane (SRM) (Eq. 2.2) or partial oxidative reforming of methane (POM) (Eq. 2.3) or a combination of these reactions and the H_2/CO molar ratio obtained for syngas can be manipulated by the reforming process applied (IZQUIERDO et al., 2013). Actually, the steam reforming of methane is the reaction employed industrially to obtain synthesis gas with high purity of H_2 (BOYANO et al., 2012).

$$CH_4 + CO_2 \rightleftharpoons 2\ CO + 2\ H_2 \qquad \Delta H_{25\ °C} = 247\ kJ/mol \qquad (2.1)$$

$$CH_4 + H_2O \rightleftharpoons 3\ H_2 + CO \qquad \Delta H_{25\ °C} = 206\ kJ/mol \qquad (2.2)$$

$$2\ CH_4 + O_2 \rightleftharpoons 2\ CO + 4\ H_2 \qquad \Delta H_{25\ °C} = -38\ kJ/mol \qquad (2.3)$$

2.3 Dry reforming of methane

The Table 2.2 presents an overview about the process and it is important to highlight the efficiency of dry reforming in the biogas reforming due the presence of CH_4 and CO_2 at its composition, eliminating the step of CO_2 removal from biogas pretreatment. However, the main disadvantage to perform this catalytic process is the carbon formation over the catalyst, which can cause blockage of the reformer and loss of activity.

The DRM reaction is an endothermic reaction that only occurs with high conversions above 700 °C. At high temperature, some side reactions are favored in the reactor, such as CH_4 decomposition (Eq. 2.4), reverse Boudouard reaction (Eq. 2.5) and reverse water-gas shift reaction (RWGS) (Eq. 2.6) (PAKHARE; SPIVEY, 2014). The main challenge for DRM reaction is the parallel occurrence of CH_4 decomposition and Boudouard reaction, responsible to the formation of solid carbon over the catalyst. The presence of carbon in the reactor must be avoided to prevent catalyst deactivation by

coke formation and it is necessary the development of catalysts and adjustment of operating parameters in order to disfavor the reactions responsible to carbon formation.

Table 2.2. Advantages and disadvantages of different reforming process to produce syngas (YANG et al., 2014).

Methods	Advantages	Disadvantages
Dry reforming	Can use both CH_4 and CO_2 in biogas; high conversion efficiency.	Carbon formation; moderate selectivity; side reaction consumes hydrogen; high operating temperature and energy demand; catalyst can be expensive.
Steam reforming	Produces high-purity hydrogen fuel; low carbon formation; widely used for hydrogen production.	Needs to remove H_2S and add oxidizing agents; high operating temperature and energy demand; catalyst can be expensive.
Partial oxidative reforming	High energy efficiency; relatively low operating temperature; can be combined with other reforming methods.	May completely oxidize methane to CO_2 and H_2O; limited industrial application.

$$CH_4 \rightleftarrows C(s) + 2\ H_2 \qquad \Delta H_{25\ ^\circ C} = 75\ kJ/mol \qquad (2.4)$$

$$C_{(s)} + CO_2 \rightleftarrows 2\ CO \qquad \Delta H_{25\ ^\circ C} = 171\ kJ/mol \qquad (2.5)$$

$$CO_2 + H_2 \rightleftarrows CO + H_2O \qquad \Delta H_{25\ ^\circ C} = 41{,}2\ kJ/mol \qquad (2.6)$$

A brief analysis about the thermodynamic and the favoring of each reaction in function of temperature can be taken analyzing the Gibbs free energy equations (WANG; LU, 1996). Assuming $\Delta G° = 0$, the DRM reaction can proceed above 640 °C. The CH_4 decomposition and reverse Boudouard reaction occur above 557 °C and 700 °C, respectively. Therefore, in this range of temperature, the carbon formed during reaction proceed from CH_4 decomposition and Boudouard reaction. In order to favor the

reverse Boudouard reaction and take high conversion of CH_4 and CO_2 in the DRM reaction, the reaction may occur at high temperature, normally above 800 °C.

The Figure 2.1 shows the thermodynamic equilibrium in the range of 0 – 1000 °C of each component based on the calculation of minimum ΔG° in two different scenarios: the first one where the carbon formation is suppressed in the reactor (A); and the second one where the carbon formation occurs in the reactor (B) (PAKHARE; SPIVEY, 2014). In the first scenario, the H_2/CO molar ratio after 300 °C vary between 0.8 and 1.0 due the occurrence of RWGS reaction, producing water and consuming H_2. However, when the formation of solid carbon is allowed the amount of CO decrease due the Boudouard reaction, increasing H_2/CO molar ratio to values higher than 1.0. The calculations also show that the carbon formation is thermodynamic favorable below 900 °C and the use of catalyst that do not accelerates the reactions responsible for that are extremely necessary for DRM reaction.

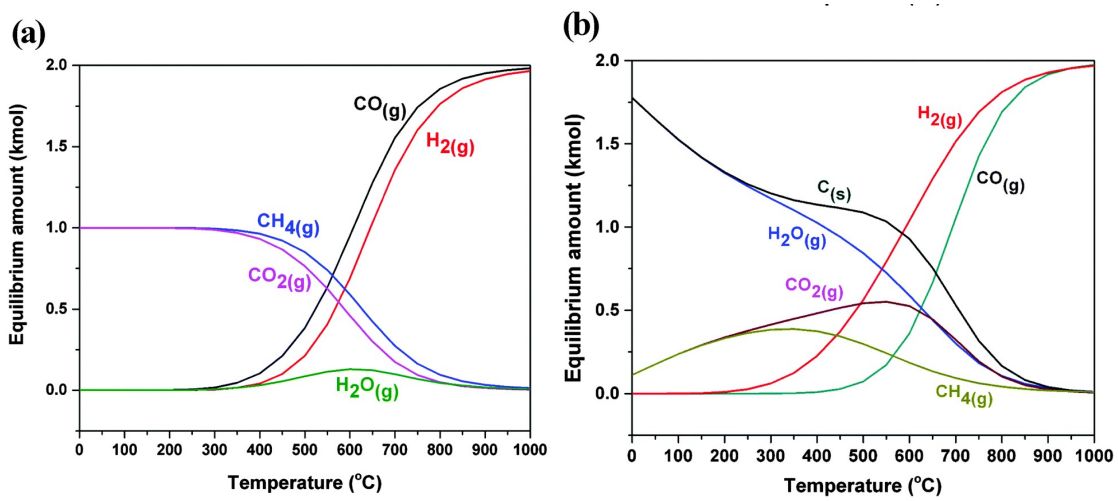

Figure 2.1. Thermodynamic equilibrium at two different scenarios: (A) carbon-free reactor; (B) presence of carbon in the reactor (PAKHARE; SPIVEY, 2014).

2.3.1 Operating Parameters

The adjustment of operating parameters is important to obtain the maximum yield, selectivity for specific product and to avoid the occurrence of side reactions responsible to carbon formation. (BRADFORD; VANNICE, 1999; SERRANO-LOTINA; DAZA, 2014). Considering the scenario without carbon (Fig. 2.1), the conversion of CH_4 and CO_2 increases with the increase of temperature, such as the H_2/CO molar ratio. The increase in conversions are justified by the endothermicity of the DRM reaction. The conversion of CO_2 is higher than CH_4 conversion, such as the

H_2/CO always lower than 1.0. This an effect of the occurrence of RWGS reaction, consuming H_2 and CO_2 to produce CO and H_2O. At high temperature, the RWGS reaction is favored but the conversion of reagents is closer again due the increase in CH_4 conversion due the reaction of CH_4 with H_2O produced and the CH_4 decomposition (SERRANO-LOTINA; DAZA, 2014)

The authors also investigated the effect of CO_2/CH_4 in the feed gas. At CH_4/CO_2 molar ratio higher than 1.0, RWGS reaction is disfavored, which decreases the amount of H_2O and increase the H_2/CO molar ratio. It is observed a decrease in CH_4 conversion and an increase in CO_2 conversion, which is the limiting reagent at this condition. They observed carbon deposits in the post-reaction sample, indicating the participation of CH_4 decomposition reaction. The increase of CO_2 in the feed gas causes an increase in CH_4 conversion and a decrease in CO_2 conversion, evidencing the excess of CO_2 in the reaction and CH_4 acting as limiting reagent. It is observed also the increase of H_2O in the composition of outlet gas with the decrease in H_2/CO molar ratio, suggesting the favoring of RWGS reaction.

Table 2.3 presents some literature works about the influence of operating conditions in terms of catalytic activity, H_2/CO molar ratio and coke formation. Then, the adjustment of reaction parameters plays a key role to avoid carbon formation during the catalytic process. A second approach is the design of catalysts extremely resistant to coke formation even at reaction conditions favored to coke formation, like which is proposed the dry reforming of biogas. The study of reaction mechanism and carbon formation mechanism are very important to understand the catalytic parameters responsible to design a catalyst free of carbon with high activity for DRM reaction.

2.3.2 Reaction mechanism

The DRM reaction mechanism involves the CH_4 dehydrogenation as the first steps, leading to the formation of carbon species adsorbed over the metal particle. Some authors also concluded that CH_4 activation is the rate-determining step (BRADFORD; VANNICE, 1999; HU; RUCKENSTEIN, 2004; WEI; IGLESIA, 2004a). However, these species may be oxidized quickly to avoid the formation of unreactive coke and catalyst deactivation. Therefore, the study of carbon formation mechanism is extremely important to understand the approaches to design a coke-resistant catalyst for DRM reaction.

Table 2.3. Literature works discussing the effect of reaction conditions in the DRM reaction.

Reference	Catalyst	Reaction Condition	Subject	Conclusions
(DAN; MIHET; LAZAR, 2020)	Ni/Al_2O_3	T = 600, 650 and 700 °C, P = 1 atm $CH_4:CO_2:H_2O$ = 1:0.48:1.2-6.1	Adjustment of reaction parameters in order to maximize the H_2 purity in the produced syngas from biogas	The addition of water caused an increase of CH_4 conversion with an increase at H_2/CO molar ratio in syngas. The condition with highest H_2 yield was $CH_4:CO_2:H_2O$ = 1:0.48:6.1 at 600 °C.
(SORIA et al., 2011)	Ru/ZrO_2-La_2O_3	T = 400, 450 and 500 °C, P = 1 atm $CH_4:CO_2:H_2O$ = 10:10:0-5, He balance	Effect of water content to improve the CH_4 conversion and catalyst stability	The presence of water decreased the catalyst deactivation from 15 % to 5%, varying the amount of water from 0 to 5%. The temperature affected positively the CH_4 and CO_2 conversion and the amount of water improved CH_4 conversion and H_2/CO. However, a decrease at CO_2 conversion is observed due the favoring of water-gas shift reaction.
(KHAJENOORI; REZAEI; MESHKANI, 2015)	Ni/CeO_2-MgO	T = 700 °C, P = 1 atm CH_4/CO_2 = 0.2 – 2.0	Effect of CH_4/CO_2 molar ratio in the catalyst activity	The excess of CH_4 or CO_2 in the stream leads to a decrease in the conversion of reagent in excess

(YASYERLI et al., 2011)	Ru@Ni-MSM-41	T = 600 °C, P = 1 atm CO_2:CH_4:Ar = 1:1:1, 1:0.5:1.5, 1:0.66:1.33 It was also tested CO_2/CH_4 ratio less than one, but not reported the exact condition.	The effect of CO_2/CH_4 molar ratio in the coke formation and H_2/CO	The tests with CO_2/CH_4 less than one presented high carbon formation with quickly deactivation by reactor blockage. The increase in CO_2 amount led to an increase at CH_4 conversion and decreases the H_2 yield, due the preference for RWGS reaction.
(YANG et al., 2018)	$La_{0.9}Sr_{0.1}NiO_3$	T = 650 °C, P = 1 bar CO_2:CH_4:H_2O = 1:1:0, 1:1:0.5	Study about coke formation and H_2 yield in Bi reforming of methane	At DRM condition, it was observed high carbon formation with low H_2/CO molar ratio (<1.0). The addition of water suppressed completely the carbon formation and an increase at H_2/CO molar ratio to 1.27 was observed. The addition of water improved the rate of carbon gasification, leading to a control at syngas ratio.

Such as CH_4, CO_2 activation is also structure sensitive and it is promoted at defect sites or corner atoms (BRADFORD; VANNICE, 1999). CO_2 activation can occur on the metallic particle or on the support, it depends on the properties of the metal and support. Bi-functional mechanism allows the activation over the support, while the activation over the metal is called Mono-functional mechanism (DAS et al., 2018; FERREIRA-APARICIO et al., 1999). When the support does not have the ability to promote the CO_2 dissociation, for example SiO_2, the activation will occur over the metal and the mechanism is called Mono-functional mechanism. In the Bi-Functional mechanism, the activation of CO_2 will occur on supports with basic properties and/or oxygen vacancies. Therefore, the support acts to disperse the metallic phase and dissociates CO_2.

O'Connor et al. (1998) performed *in-situ* DRIFTS to determine the reaction mechanism of DRM reaction at 600 °C with Pt/ZrO_2 catalyst (Figure 2.2). After exposition to CH_4/Ar for 1 min, it is possible to observe the band at 2040 cm^{-1}, ascribed to CO linearly adsorbed on Pt metallic. They concluded that CO is formed from the oxidation of carbon derived from CH_4 activation, generating oxygen vacancies in the material. Afterwards, CO_2/Ar was injected in the chamber and the spectrum after 1 min indicates the presence of CO linearly adsorbed at 2040 cm^{-1}. After 10 min, this band is no more observed and another band at 1435 cm^{-1} appears, ascribed to carbonates species. These observations show the process of CO_2 activation over ZrO_2. The oxygen vacancies generated during carbon oxidation in the CH_4 activation are replenished by CO_2. The process of storage and release oxygen to oxidize the carbon is called carbon removal mechanism. After all oxygen vacancies are occupied again, CO_2 adsorbs on basic sites in form of carbonates species.

Returning to CH_4 atmosphere, the CO band is identified over again, due the oxidation of carbon from lattice oxygen. Besides, the intensity of carbonates band decreased, indicating the participation of carbonates in the process of oxygen storage. In absence of CO_2 as supplier of O, carbonates play this role, supplying the oxygen vacancies generated. Even after 10 min it is possible to observe CO band and carbonates band, which show the continuous process of storage and release oxygen on the surface of ZrO_2. A schematic of DRM reaction over supports with oxygen vacancies can be observed in the Fig. 2.3.

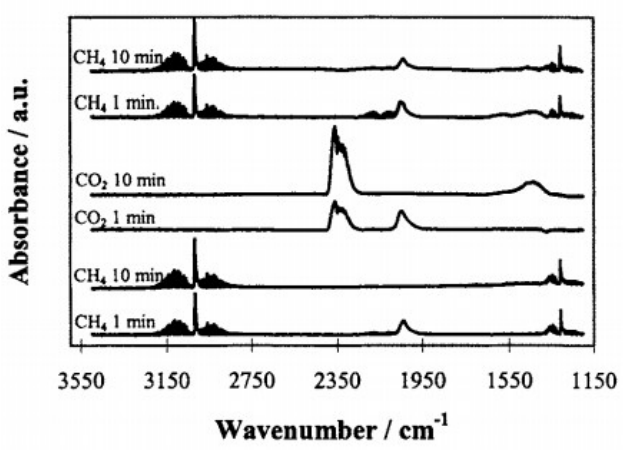

Figure 2.2. DRIFTS spectra after exposure to CH_4 and CO_2 over the Pt/ZrO_2 catalyst (O'CONNOR; MEUNIER; ROSS, 1998).

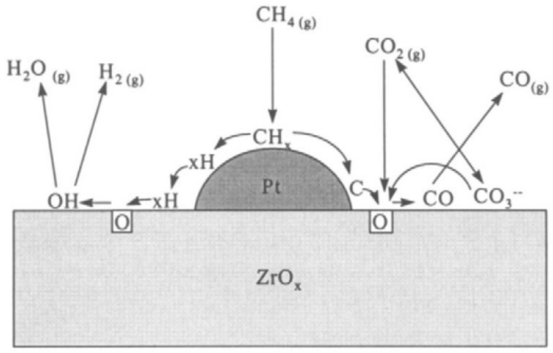

Figure 2.3. Reaction mechanism of DRM reaction over Pt/ZrO_2 catalyst (O'CONNOR; MEUNIER; ROSS, 1998).

2.3.3 Catalyst deactivation

➢ *Carbon formation mechanism*

The main source of carbon in DRM reaction is the CH_4 decomposition that occur over the metallic particle. Carbon also can be produced from the equilibrium amount in the Boudouard reaction (FORZATTI; LIETTI, 1999). In general, there are three different coke based on their morphology and structure (BARTHOLOMEW, 1982; OCHOA et al., 2020):

- Encapsulating coke: It is formed from the adsorbed species which polymerize over the metallic particle, resulting in a coke film. The formation temperature is low (< 500 °C) and its formation is not favored at reforming reaction condition.

- Filamentous coke: This coke is formed at temperatures above 450 °C and it has filament-like morphology, in form of carbon nanotubes or carbon nanofibers. It is the most common type of coke identified in the literature for DRM reaction.
- Pyrolytic coke: This type of coke is formed by hydrocarbon cracking at high temperature (> 600 °C) and its formation is observed at severe deactivation stages. This coke encapsulates the metal particle, resulting in the catalyst deactivation. However, it is not common for reforming reactions, where normally the catalyst regenerates before reaching this state.

The carbon formation mechanism for DRM reaction was deeply studied in the literature. The mechanism of filamentous coke involves: (i) adsorption of atomic carbon from CH_4 decomposition; (ii) diffusion of carbon through the metal particle; (iii) nucleation and (iv) growing in form of filaments. This condition separates the metal particle from support, but the metallic surface is still available for reactants on the top, which will not result in a decrease of activity. However, the excess of carbon filaments can cause loss of activity due blockage of reactor, if the carbon filaments are fractured or an encapsulating effect by the meeting with another carbon filament.

It is reported in the literature the low solubility of carbon through noble metals (PAKHARE; SPIVEY, 2014). Rostrup-Nielsen and Trimm (1977) studied the carbon formation over Ni-based catalyst and they concluded that the diffusion of carbon species from surface to interface metal-support occurs through the metal particle and it is driven by a concentration gradient. An important parameter to determine the rate of carbon formation is the metallic particle size. The particle size affects directly the equilibrium constant of CH_4 decomposition and Boudouard reaction, as demonstrated by Rostrup-Nielsen (1972). Nowadays, it is well accepted that smaller Ni particle size affected negatively the nucleation of carbon in the interface metal-support (HELVEG; SEHESTED; ROSTRUP-NIELSEN, 2011).

- *Metal sintering*

Sintering is a thermally process where the metal particle growth and the metallic surface decreases. Therefore, less sites for reaction will be available on the metal surface (ROSTRUP-NIELSEN; PEDERSEN; SEHESTED, 2007). Temperature is the most common factor to influence the metal sintering. When the temperature is above the Tamman temperature, the metal shows some mobility over the support and the sintering occurs. Noble metals have higher Tamman temperature, but Ni presents low value,

leading to an inevitable sintering at DRM condition (Pt = 741 °C, Pd = 641 °C, Ni = 590 °C) (OCHOA et al., 2020). The sintering process can follow two different paths: (Figure 2.4 -A) Oswald ripening, where adatoms migrate to larger particles or (Figure 2.4-B) migration of small particles to larger particles until thermodynamic equilibrium .

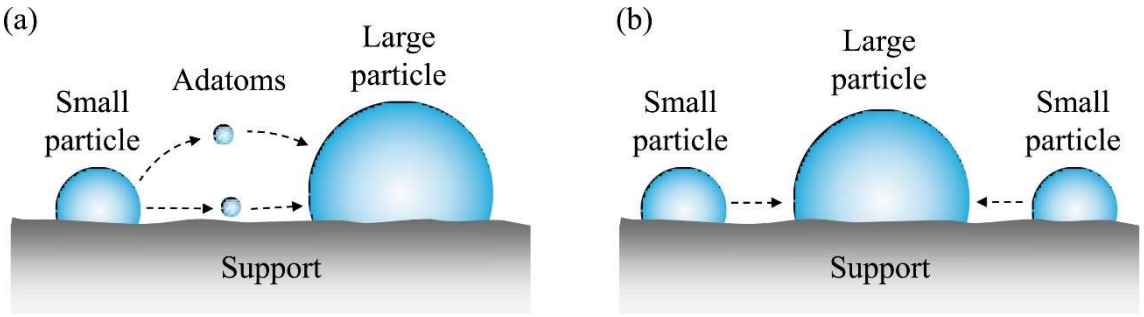

Figure 2.4. Metal sintering mechanisms (a) Ostwald ripening and (b) particle migration and coalescence (OCHOA et al., 2020).

As DRM is a structure sensitive reaction, metal sintering affects the activity per exposed active site, which is called as turnover frequency (TOF), resulting in a decrease of catalytic activity. Furthermore, as discussed previously, large metallic particles favor CH_4 decomposition, responsible to coke formation. Then, the metal sintering must be avoided in the catalysts for application at DRM in order to maintain the catalytic activity and minimize the carbon formation.

The study about catalyst deactivation allow us to determine two approaches in the research to target this problem: (i) development of catalysts with small metallic particles, avoiding sintering process at high temperature; (ii) development of supports with high oxygen mobility to perform the carbon removal mechanism. The parameters listed on Table 2.4 play key role to design a high activity and coke-resistant catalyst for DRM reaction. The next topic will focus in the discussion of these catalysts already presented in the literature.

Table 2.4. Parameters to design a high activity and coke-resistant catalyst for DRM reaction (JANG et al., 2019).

Parameter	Subject
Strong interaction metal-support	Avoid sintering
High Dispersion and small metal particle size	Avoid CH_4 decomposition rate
Strong Basicity	CO_2 adsorption
High Oxygen storage capacity	Carbon gasification
High Reducibility	Catalyst activity
High Porosity and surface area	Adsorption of reactants

2.4 Catalysts for DRM reaction

The DRM reaction was extensively studied with a high variety of supported metallic catalysts. As discussed previously, the carbon formation is the main challenge to scale-up this technology to industrial scale and it propels the research of DRM reaction in the last years. Catalysts with noble metals, such as Pd, Pt, Rh and others, present high activity and coke resistant due the low dissolution of carbon in their lattices (NAKAMURA et al., 1994). Based on the reaction mechanism study, the metal nature affects directly the kinetic of reaction. Studying different metal supported catalysts, Rostrup-Nielsem and Hansen (1993) observed the following activity order: Ru > Rh, Ni > Ir > Pt > Pd at 773 and 923 K. Although, the carbon formation followed the order: Ni > Pd >>> Ir > Pt, with Ru and Rh forming negligible carbon deposits. Ferreira-Aparicio et al. (1998) performed an extensively study of metals from group VIII supported on Al_2O_3 and SiO_2. Based on TOF results, they established the following order of activity: Rh> Ni > Ir > Ru~Pt > Co for Al_2O_3 supported catalysts and Ni > Ru > Rh~Ir > Co~Pt for SiO_2 supported catalysts. The selectivity for hydrogen did not change with the active phase and it is not influenced by the nature of metal. Another works from literature analyzing the different active phases are listed on Table 2.5.

Noble metals are limited in the environment and it stimulates the research of non-noble metals to perform the reaction with similar activity. The research has shown the efficiency of Ni to maintain activity similar to noble metals with low cost, however this metal is prone to coking. Among the noble metals, Pt has low activity compared to Ni, but it is more resistant to coke formation. Therefore, this work will focus from now in the discussion of Ni and Pt as active phase for DRM reaction.

Table 2.5. Literature works discussing the effect of active phase in the DRM reaction.

Reference	Catalyst	Reaction Condition	Subject	Conclusions
(SOLYMOSI; KUTSÁN; ERDÖHELYI, 1991)	M/Al_2O_3 M = Pt, Pd, Rh, Ir, Ru	T = 550 °C, CH_4:CO_2 = 1:1	Establishment of CH_4 conversion in function of metal nature.	The rate of reaction followed the order: Rh>Pt>Pd>Ru>Ir. They also calculated the amount of carbon in the following order: Ru>Rh~Pt>Ir>Pd.
(MARK; MAIER, 1996)	M/Al_2O_3 M = Pt, Pd, Rh, Ir, Ru	T = 700 °C, CH_4:CO_2 = 1:1	Analyze the effect of nature metal in DRM reaction	Rh, Ir and Ru based catalysts were stable for long time, but Pd and Pt based catalysts presented deactivation. They associated the deactivation of Pd/Al_2O_3 with coke formation. In terms of TOF, the activity follows as: Rh>Ru>Ir>>Pd~Pt.
(ZHANG et al., 1996)	Rh/support Support = YSZ, Al_2O_3, TiO_2, SiO_2, La_2O_3, MgO	T = 650, 700 °C CH_4:CO_2 = 1:1	Effect of Rh particle size and the origins of deactivation in function of support.	The activity of Rh-based catalysts is affected by particle size, decreasing with increasing the average crystallite size. The deactivation of the catalysts is associated to three factors: carbon deposition (Al_2O_3), metal sintering (Al_2O_3, SiO_2, TiO_2) and poisoning by species originating from support (TiO_2, YSZ, MgO). The occurrence of one or a combination of these factors is correlated to the nature of support and Rh particle size.

(VERYKIOS, 2003)	Rh/Al_2O_3	T = 650 °C, P = 1 atm CH_4: CO_2: = 1:1	Mechanistic study over Rh/Al_2O_3 catalyst.	The mechanistic study with isotopes carried out by the authors concluded that carbon species are originated from CO_2 dissociation. Rh has the capacity to dissociate CO_2 molecule and the activation of both reactants occurs only over the metallic sites. At higher temperatures (>650 °C), the carbon deposits decreased due the occurrence of carbon gasification and reverse Boudouard reaction.
(WEI; IGLESIA, 2004b)	Ir/ZrO_2	T = 600 °C, P = 1 atm CH_4:CO_2 = 1:1	Isotopic study to determine the kinetic of DRM reaction over Ir-based catalysts	The authors observed that the limiting step is the CH_4 activation over Ir clusters. The C-H bond activation is irreversible ad the activation of CO_2 is quasi-equilibrated and reversible. They also observed the WGS reaction in thermodynamic equilibrium at reforming conditions.
(ARAUJO et al., 2008)	$LaNi_{1-x}Ru_xO_3$ X = 0, 0.1, 0.2 and 1.0	T = 750 °C, P = 1 atm CH_4:CO_2 = 1:1	The effect of Ni replacement by Ru in perovskite-based catalysts.	The substitution of Ni by Ru in the perovskite structure increased the resistance to coke formation, with $LaNi_{0.8}Ru_{0.2}O_3$ the most resistance among the perovskite substituted catalysts. The strength of Ru-O-La and Ni-O-La bonds increased in bimetallic catalysts, due a synergy between the metals.

As discussed before, the strategy to avoid carbon formation is the equilibrium between CH_4 decomposition rate and carbon gasification rate. It is possible to target this equilibrium applying supports with high oxygen mobility, which promotes carbon gasification before the formation of stable carbon deposits. CeO_2 or CeO_2-doped materials appear as excellent candidate for support application at DRM reaction. A second approach is the development of alternative catalyst synthesis methods against the traditional ones, where the metal is protected against sintering. The synthesis of new structures, such as mesoporous materials and core-shell catalysts, can avoid metal sintering at reforming conditions. For that reason, the combination of these two approaches is a strategy to design a coke-resistant catalyst for DRM reaction.

2.4.1 Supports for DRM reaction

The support must offer metal dispersion in addition with thermal stability, avoiding metal sintering at reforming conditions. The strong interaction metal-support is important to prevent the sintering process. Furthermore, the support provides sites for CO_2 adsorption and dissociation, promoting the carbon removal mechanism during reaction. (PAPADOPOULOU; MATRALIS; VERYKIOS, 2012).

Alumina (Al_2O_3) is the most common support studied in the literature for DRM reaction due to the low cost and high specific surface area (PAPADOPOULOU; MATRALIS; VERYKIOS, 2012). However, the stability of Ni/Al_2O_3 catalyst depends on structure, composition, synthesis methods to improve the resistance to catalyst deactivation due the formation of $NiAl_2O_4$ spinel phase (Becerra et al.; 2001) This spinel phase is formed during calcination process by the reaction between NiO and Al_2O_3 and it is hardly reduced, normally above 800 °C.

Zhou et al. (2015) studied Ni/Al_2O_3 catalysts calcined at 350, 700 and 900 °C for DRM reaction. The XRD data of calcined samples shows the presence of NiO characteristic lines for the sample Ni/Al_2O_3 (350). The sample Ni/Al_2O_3 (700) is a transition state between NiO and $NiAl_2O_4$, with the presence of both phases in the XRD pattern. Finally, the sample Ni/Al_2O_3 (900) only presented the characteristic lines of $NiAl_2O_4$ spinel phase. Then, the temperature where the reaction between NiO and $NiAl_2O_4$ is in accordance with the temperature found by Sahli et al. (2006). After reduction at 800 °C, the characteristic line of Ni metallic phase appeared, indicating the reduction of NiO or part of $NiAl_2O_4$. The three samples presented similar Ni crystallite size (around 10 nm), however the amount of carbon formation was extremely affected

by calcination temperature. With the increase on calcination temperature, the Ni reduced from $NiAl_2O_4$ phase has stronger interaction with support, decreasing the coke amount. The authors also suggested that when Ni migrates from $NiAl_2O_4$ phase, some defects in the structure are created, promoting oxygen mobility in the material and increasing the rate of carbon gasification.

Although many researches are focused on Al_2O_3 as support for DRM reaction, the catalysts do not present high stability and coke formation is still observed. Then, it is necessary to study different supports mainly with basic properties and oxygen mobility to promote the carbon removal mechanism. Damyanova et al. (2012) studied Ni supported on different oxides in order to prevent carbon formation in the DRM reaction. They evaluated the Al_2O_3, SiO_2-Al_2O_3, ZrO_2-Al_2O_3 and $MgAl_2O_4$ supports. The Ni/$MgAl_2O_4$ presented the highest activity with the smallest Ni particle size determined by microscopy (5.1 nm). This high dispersion is a clear effect of high metal-support interaction on this sample. The second consequence of this high Ni dispersion is the absence of carbon on the post-reaction sample, observed by thermogravimetric analysis. Therefore, the strong metal-support interaction and the high number of active Ni sites contribute to the high stability of Ni/$MgAl_2O_4$ catalyst for DRM reaction.

Ballarini et al. (2005) evaluated the influence of basicity doping over Pt/Al_2O_3 catalyst with Na and K for DRM application. Without the dopants, Pt/Al_2O_3 presented poor activity and stability, associated to the high carbon formation. Besides, they observed Pt sintering when the catalyst was submitted to high temperature. When Na or K is added, the Pt/Na-Al_2O_3 and Pt/K-Al_2O_3 catalysts have high stability and activity during 5800 min in the DRM reaction, consequence of higher Pt dispersion obtained for these catalysts. They also did not observe carbon formation. The basic character increased the CO_2 adsorption rate, promoting at same time the carbon removal mechanism in the catalyst. Table 2.6 presents some works from the literature with different supports utilized for DRM reaction.

Table 2.6. Literature works discussing the effect of support in the DRM reaction.

Reference	Catalyst	Reaction Condition	Subject	Conclusions
(BITTER et al., 1996)	Pt/γ-Al_2O_3 Pt/TiO_2 Pt/ZrO_2	T = 600 °C, CH_4:CO_2:N_2:Ar = 25:25:5:45	Effect of support in the resistance to coke formation	The deactivation observed for the three catalysts were associated only to carbon formation, since the metallic surface area returned to initial values after carbon burn off. The carbon amount followed the order: Al_2O_3>TiO_2>ZrO_2 and they associated to the inability of Al_2O_3 to partially reduce at DRM condition, as observed for TiO_2 or ZrO_2.
(THERDTHIANWONG; SIANGCHIN; THERDTHIANWONG, 2008)	Ni/xZrO_2-Al_2O_3 x = 5, 10 and 15 wt%	T = 700 °C, P = 1 atm CH_4:CO_2 = 1:1.25	Effect of ZrO_2 addition to Al_2O_3 support in order to prevent coke formation	The addition of ZrO_2 decreased at least 50 % of carbon formation in comparison to Ni/Al_2O_3 catalyst. They concluded that 5-10 wt% ZrO_2 is the ideal amount, where above it there is a decrease of the specific surface. ZrO_2 promotes dissociation of CO_2 forming oxygen intermediates close to Ni nanoparticles, where carbon deposits are gasified.
(LIU et al., 2016)	NiMgAl La-NiMgAl	T = 550 °C CH_4:CO_2:Ar = 1:1:8	Effect of La addition in the hydrotalcite structure to enhance the resistance for coke formation	The presence of La promotes the formation of $La_2O_2CO_3$ intermediate species, able to gasify the carbon deposits over Ni nanoparticle. They also observed an increase at medium basic sites, enhancing the CO_2 adsorption rate compared to the undoped NiMgAl catalyst.

➢ *Ceria and doped-ceria based supports*

The works presented until now in this section were focused on non-reducible supports. However, the continuous availability of oxygen lattice on the surface to promote carbon removal mechanism efforts the research of oxides that can change their oxidation state depending on the environment with high oxygen storage capacity (OSC). The main example of this group of oxides is ceria (CeO_2). Ceria has the ability to release or store oxygen depending on the environment, following a Mars-Van Krevelen mechanism (PAPADOPOULOU; MATRALIS; VERYKIOS, 2012). Under DRM conditions, ceria releases mobile oxygen species from its surface to oxidize carbon deposits presented over metallic particles, changing its oxidation from Ce^{4+} to Ce^{3+} and creating oxygen vacancies by charge compensation in the metal-support interface. CO_2 activation occurs preferentially on those oxygen vacancies, storing oxygen into ceria lattice (Figure 2.5). Laosiripojana and Assabumrungrat (2005a) demonstrated in their work that Ni/CeO_2 catalyst was much more resistant to coke formation than Ni/Al_2O_3 due the increase on support OSC.

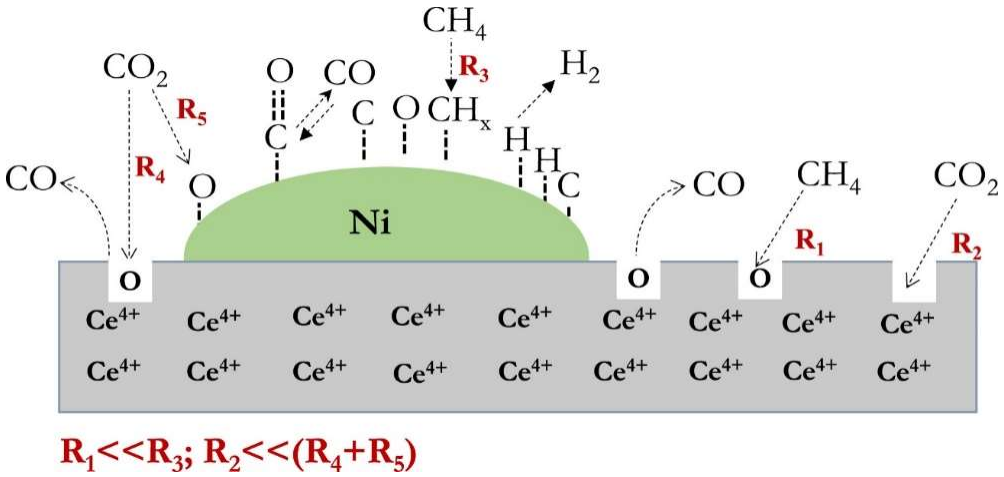

Figure 2.5. Role of oxygen vacancies on DRM reaction mechanism (ABDULRASHEED et al., 2019; MAKRI et al., 2016).

In addition to participation on carbon removal mechanism, CeO_2 also enhances the dispersion and stabilization of small metallic particles. Strong metal-support interaction improves thermal resistance at high temperature, avoiding the metal sintering process. Therefore, in the DRM conditions the metal particle remains small preventing the coke formation.

The maximization of OSC can be reached by the addition of dopants into ceria lattice forming solid solutions. The oxygen vacancy can be generated by charge compensation or structural defects, but it depends from oxidation state of foreign cation and ionic radius. The addition of low-valence elements, such as Gd, Sm, La or other trivalent elements, causes the formation of oxygen vacancy by charge compensation, as observed in the Eq. 2.19 with Kroger-Vink notation (LI et al., 2019). These cations have higher ionic radius compared to Ce^{4+}, but literature reports that ceria structure is only slightly affected when these cations are inserted. Some works showed the low variation at ceria lattice parameter by doping with Gd, Sm, Y, Pr (AUGUSTO et al., 2014; BORCHERT et al., 2005; DA SILVA et al., 2017; LUISETTO et al., 2019; WANG et al., 2001). In the trivalent rare-earth doped ceria, Gd and Sm appear as promising dopants in order to enhance conductivity and ionic conductivity (KARACA; ALTINÇEKIÇ and FARUK ÖKSÜZÖMER, 2010).

$$2\ M_2O_3 + 3\ Ce_{Ce}^{\times} + O_O^{\times} = 4\ M_{Ce}' + 2V_O + 3\ CeO_2 \qquad (2.7)$$

Fonseca et al. (2019) studied the influence of Gd-doping CeO_2 over $Pt/Ce_xGd_{1-x}O_2/Al_2O_3$ catalyst for DRM reaction. The Pt/Al_2O_3 catalyst rapidly deactivates and exhibits the highest amount of carbon detected by TPO (0.45 $mgC.g_{cat}^{-1}.h^{-1}$). The carbon deposits cover Pt sites, decreasing CH_4 conversion with time. When Pt is impregnated over $Ce_xGd_{1-x}O_2/Al_2O_3$, the oxygen mobility ascribed to solid solution promotes carbon removal mechanism, decreasing the rate of carbon formation and maintaining stable CH_4 conversion. The decrease of Ce/Gd molar ratio from 4:1 to 1:1 leads to slightly decrease on Ce^{3+} molar fraction calculated from in-situ XANES during reduction. It was also observed a decrease on ceria reducibility when the amount of $Ce_{0.8}Gd_{0.2}O_2$ solid solution increased from 24wt% to 36wt%, due the loss of surface area. Sadykov et al. (2005) also observed a maximum of oxygen mobility using Ce/Gd molar ratio 4:1.

Luisetto et al. (2019) synthesized Ni/CeO_2 catalysts doped with Sm, La and Zr by citric acid method for DRM reaction. The doping with Sm and La did not prevent Ce and Ni sintering, as observed on CeO_2 and Ni crystallite size after reduction at 800 °C (Table 2.7). However, the doping with Zr increased thermal stability of the material, decreasing the observed sintering process. The Table 2.7 also shows the Ce reducibility by TPR, where the doping with Zr increased the amount of Ce^{3+} in the reduced sample.

The authors observed that the doping with Sm and La did not enhance ceria reducibility as observed by Zr-doped material.

Table 2.7. Crystallite size of CeO_2 and Ni reduced samples and ceria reducibility (Adapted from Luisetto et al., 2019)

Catalyst	Crystallite size (nm)		Ce^{3+} (%)
	CeO_2	Ni	
Ni/CeO_2	41.3	24.2	18.8
Ni/Zr-DC	13.3	9.2	33.5
Ni/Sm-DC	32.7	18.8	18.2
Ni/La-DC	30.7	20.6	18.8

As demonstrated above, Zr has distinct behavior when doped ceria compared to low valence elements in order to improve ceria reducibility. In the literature Zr is the most common element used for ceria doping in DRM reaction. The insertion of ZrO_2 into ceria structure causes structural defects, which increases the OSC value of the support. Madier et al. (1999) observed a substantial increase in the OSC of $CeZrO_2$ due the participation of oxygen sublayers, while the OSC is limited to surface for pure CeO_2, indicating the participation of bulk oxygen when $CeZrO_2$ solid solution is formed. During the process of oxygen release, the reduction of Ce^{4+} to Ce^{3+} is limited by the stress energy arising from the volume expansion. However, the introduction of Zr^{4+}, that has a smaller ionic radius compared to Ce^{4+}, compensates this stress energy due the formation of structure defects, increasing ceria reducibility. Then, the addition of Zr leads to higher mobility of oxygen from bulk phase to surface (LI et al., 2019; VLAIC et al., 1997).

CeO_2 thermal stability is a critical point to maintain the promotional effects of ceria in the catalysts. Pijolat et al. (1995) observed that the insertion of smaller dopants than Ce^{4+} stabilized CeO_2 against sintering due the formation of defects in the structure. Besides the improvement of OSC, substitution with Zr also increases CeO_2 thermal stability. Hori et al. (1998b) observed high thermal stability for $Ce_{0.75}Zr_{0.25}O_2$ solid solution aged at 1000 °C prepared by hydroxides precipitation. BET surface are increased from 2 to 14 m^2/g and the amount of surface O rises from 11 to 61 μmol/g compared to pure CeO_2. The $Ce0_{.75}Zr_{0.25}O_2$ solid solution presented the highest OSC, 3-

5 times higher than pure CeO_2. The same improvement on surface area and OSC are reported by other authors (ARIBI et al., 2018; KAMBOLIS et al., 2010; MATTOS et al., 2002; YENTEKAKIS et al., 2019).

Faria et al. (2014) studied the influence of Ce/Zr molar ratio over $Ni/CeZrO_2/Al_2O_3$ catalyst for DRM reaction. The authors synthesized catalysts with Ce/Zr molar ratio 0.5, 0.75 and 1.0. XRD patterns shown the formation of $CeZrO_2$ solid solution by the decrease on ceria lattice parameter. The insertion of Zr into ceria lattice enhanced OSC and thermal stability. The catalysts were tested in the DRM reaction at 800 °C and CH_4/CO_2 = 1.0 and the catalysts were stable during 24 h TOS, but the amount of coke is different. The authors associate the high resistance to carbon formation observed on the $Ni/Ce_{0.5}Zr_{0.5}O_2/Al$ catalyst to the higher oxygen mobility. Other authors also observed good results for Ce-Zr based materials in DRM reaction (DAMYANOVA et al., 2009; RADLIK et al., 2015; WOLFBEISSER et al., 2016; XU; SONG; CHOU, 2012).

Table 2.8 shows more works from literature for the application of ceria or doped-ceria in reforming reactions. The high temperature required for DRM reaction is a critical issue to avoid metal sintering in traditional supported catalysts even with the application of support with high surface area or high metal-support interaction. Therefore, in the last years a novel approach has been investigated in order to encapsulate metal nanoparticles into oxides or well-defined structures, isolating these nanoparticles. The next section will discuss the effect of encapsulated catalysts in DRM reaction and the catalytic advantages brought by these new structures.

Table 2.8. Literature works related to influence of dopants and Ce addition in reforming reactions.

Reference	Catalyst	Reaction Condition	Subject	Conclusions
(WOLFBEISSER et al., 2016)	Ni/ZrO_2 Ni/CeO_2 $Ni/CeZrO_2$_CTAB $Ni/CeZrO_2$_CP	T = 600 °C, CH_4:CO_2:Ar = 10:10:80	Effect of $CeZrO_2$ solid solution by two different synthesis procedures.	The formation of $CeZrO_2$ improves thermal stability and carbon resistance in comparison to pure ZrO_2 or CeO_2. The $Ni/CeZrO_2$_CP presented the highest carbon resistance with high conversion, while the $Ni/CeZrO_2$_CTAB was not active for DRM reaction due the coverage of Ni particles by ceria-zirconia layer.
(NORONHA et al., 2001)	Pt/Al_2O_3 $Pt/Ce_xZr_{1-x}O_2$	T = 800 °C, CH_4:CO_2 = 2:1	Effect of Ce/Zr molar ratio in order to improve resistance to catalyst deactivation	Pt/Al_2O_3 catalyst rapidly deactivates presenting high carbon formation. The authors associated the deactivation by coke deposition over Pt particles. The optimum composition to less amount of carbon was $Pt/Ce_{0.75}Zr_{0.25}O_2$ catalyst, providing labile oxygen to carbon removal mechanism.

(GURAV et al., 2017)	12Ni/GDC_CP (Co-Precipitation) 12Ni/GDC_CIT (Citrate method) 12Ni/GDC_IMP (Impregnation)	T = 800 °C CH_4:CO_2:N_2 = 1:1:1	Different synthesis procedures to understand its effect on Ni particle size	The co-precipitation method generates the catalyst with high surface area and small Ni particle size after reduction at 800 °C. After reaction, sintering occurs for all the catalysts, but in low intensity for 12Ni/GDC_CP, explaining the lower carbon formation in comparison to citrate and impregnated methods.
(LAOSIRIPOJANA; SUTTHISRIPOK; ASSABUMRUNGRAT, 2005b)	Ni/Al_2O_3 $Ni/8wt\%CeO_2/Al_2O_3$	T = 900 °C, P = 1 atm CH_4: CO_2: = 1:0.3	Influence of Ce as promoter on Ni/Al_2O_3 catalyst	The addition of Ce decreases formation of carbon monolayers from 4.26 to 0.85. The reaction on ceria surface occurs simultaneously to reaction on Ni surface, reducing the amount of carbon deposits generated from CH_4 dehydrogenation. XPS data after exposure to CH_4/CO_2 mixture detected the formation of Ce^{3+}, indicating the reduction of Ce^{4+} to Ce^{3+} by oxygen release to carbon oxidation.

(WANG et al., 2001)	Ni/xYDC x = 0, 5, 10, 20, 40 mol%	T = 450 °C, P = 1 atm CH_4:CO_2:Ar = 1:1:2	Structural and redox properties investigation of Y-doped ceria	The authors observed by EPR and XPS that the addition of Y inhibits ceria reducibility, increasing the amount of coke detected by TPH after reaction. Yttrium doping also affected Ni-CeO_2 interaction and the Ni dispersion becomes poorer with increase of yttrium loading.
(DUARTE et al., 2011)	Ni/Sm_2O_3-CeO_2/Al_2O_3	Partial oxidation of methane T = 800 °C, P = 1 atm CH_4:O_2:N_2 = 2:1:0.9	Effect of Sm_2O_3 addition to Pt/CeO_2/Al_2O_3 catalyst	The doping with Sm promoted better dispersion of Pt over the support due to the enhancement of metal-support interaction. The authors observed that the optimum interaction between Pt and surface oxygen vacancies occurs with 3 wt% of Sm_2O_3, where presented the lowest carbon formation.

2.4.2 Encapsulated Catalysts: Core@shell and mesoporous structures

Confined/Embedded metal or metal oxides into a structure provide different catalytic characteristics to the material in comparison to a traditional impregnated catalyst. The confined environment leads to a better thermal stability against metal sintering, in which the coating stabilizes the active metal in the catalyst due the creation of physic barrier between different metal particles (ABDULRASHEED et al., 2019). In terms of morphology, the encapsulated catalysts can be defined into by four groups: (1) core@shell; (2) core@tube; (3) mesoporous structures and (4) lamellar structures (Figure 2.6) (TIAN et al., 2015). This work will focus in the application of core@shell and mesoporous structures in DRM reaction.

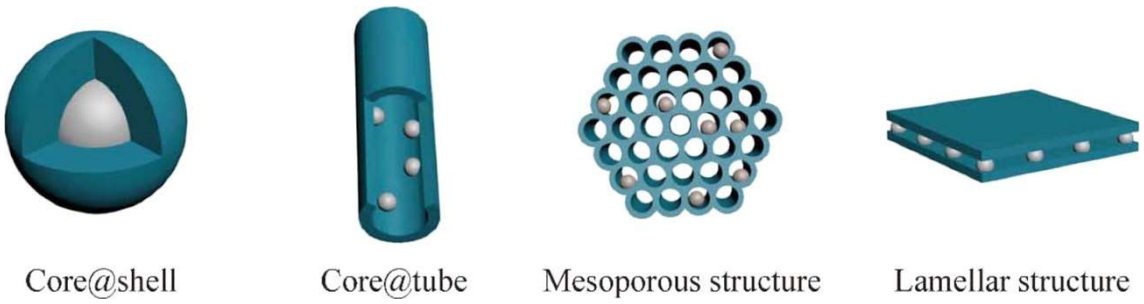

Figure 2.6. Different morphologies of encapsulated catalysts (LI; GONG, 2014; TIAN et al., 2015).

- *Core@shell catalysts*

Core@shell structure is composed by a core (active metal) surrounded by a chemically different matrix (shell). The main advantage in comparison to traditional supported catalysts is the highest resistance to metal sintering, where the shell provides a physical protection, avoiding deactivation by agglomeration of active phase. In the specific case of DRM reaction, the resistance of sintering also decreases the carbon formation rate. Furthermore, the increase of interfacial area strengthened metal-support interaction leading to enhancement of catalytic performance (Figure 2.7) (MELCHIONNA; TROVARELLI; FORNASIERO, 2020).

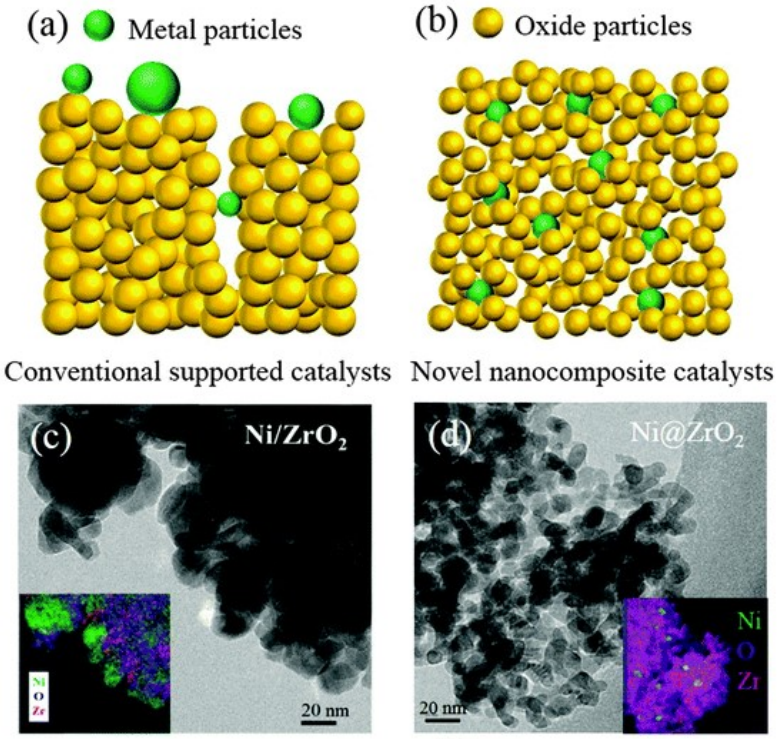

Figure 2.7. Morphology and Ni position on (a) and (c) traditional supported Ni/ZrO_2; (b) and (d) core@shell structure $Ni@ZrO_2$ (LI et al., 2013; LI and GONG, 2014).

Despite the advantages of core@shell structure against traditional supported catalysts, this new structure still has many challenges in the research field in order to expand its application for a large range of reactions. Some problems can be listed as: (1) Efficiency of synthesis methods are not well established for application with different materials than the reported ones; (2) the control of core size and shell thickness are difficulty; (3) core@shell yield is low; (4) effect of blockage by shell, decreasing catalytic activity (ARORA; PRASAD, 2016). Meanwhile, the researches about core@shell catalyst focus mainly in the development of a synthesis procedure that can produce a very active catalyst with high yield.

Huang et al. (2017) studied the $Ni@Al_2O_3$ catalyst prepared by inverse microemulsion method for DRM reaction in comparison to Ni/Al_2O_3 prepared by traditional impregnation. The impregnation of Ni caused blockage of pores, decreasing surface area and the reduction at 800 °C generates large Ni crystallites (14.8 nm). The core@shell structure avoided Ni sintering (9.5 nm) by physical confinement. The Ni/Al_2O_3 catalyst rapidly deactivated, because of the Ni sintering during the reaction as observed by XRD from post-reaction sample. Ni crystallites grew from 14.8 to 21.2 nm. On the other hand, $Ni@Al_2O_3$ catalyst maintained similar conversion during all time

and Ni sintering was not detected by XRD over post-reaction sample. Post-reaction samples analysis detected carbon formation for both catalysts, but higher amount over Ni/Al_2O_3.

Many authors reported $Ni@SiO_2$ core@shell catalysts for DRM reaction (GUNDUZ MERIC; ARBAG; DEGIRMENCI, 2017; ZHANG; LI, 2015). Wang et al. (2016) successfully synthesized $Ni@SiO_2$ core@shell catalysts by microemulsion method for DRM reaction. The supported catalysts presented large Ni crystallites after reduction, 30.8 nm and 26.9 nm to $5Ni/SiO_2$ and $15Ni/SiO_2$, respectively, whereas Ni sintering was avoided on core@shell catalysts ($Ni@SiO_2$_30min – 5.4 nm and $Ni@SiO_2$_2h – 5.6 nm). The carbon analysis indicates the highest carbon formation over supported catalysts, because of the presence of large Ni particles favoring CH_4 decomposition. SiO_2 presented good results for DRM application but carbon formation is still observed, and Ni sintering was not totally avoided.

The use of CeO_2 in core@shel configuration in order to promote carbon gasification led researchers to design core@shell catalysts. The difficulty to design CeO_2 shell is related to the low availability of surface functionalized Ce precursors, control of Ce precursors hydrolysis and the assembling of hydrolyzed small Ce particles upon the core surface (LI; WANG; KAWI, 2019). Cargnello et al. (2010) developed one of the first publications using CeO_2 as shell on $Pd@CeO_2$ core@shell catalyst by microemulsion method. The method consists on the metal reduction into solution by $NaBH_4$; protection with passive agent against re-oxidation and enrichment of Pd surface with carboxylic groups; self-assembly of Ce precursor; hydrolysis of Ce precursor. Similar procedure was used by Saw et al. (2015) in the synthesis of $NiCu@CeO_2$ catalyst. In other works hydrazine is used as reducing agent of Ni precursors to obtain Ni metallic nanoparticles in solution (ELURI; PAUL, 2012; NIK ROSELINA; AZIZAN; LOCKMAN, 2012). To conclude, the methods described in the literature request many steps in laboratory, which will generate a low yield at the end of synthesis procedure. Furthermore, the utilization of reducing agents and ultra-centrifugation enhances the complexity of the method. Then, there is a lack in the literature to design simple routes for CeO_2 shell production.

Das et al. (2018) synthesized $Ni\text{-}SiO_2@CeO_2$ core@shell catalysts for application in biogas reforming (CH_4/CO_2 = 1.5). The authors observed by *in-situ* DRIFTS that on $Ni\text{-}SiO_2$ catalyst, the reaction followed a mono-functional mechanism while the application of CeO_2 layer changed the reaction mechanism to bi-functional

pathway, where the activation of CO_2 occurred in the oxygen vacancies presented on CeO_2 layer (Figure 2.8). Therefore, Ni-SiO_2@CeO_2 joined the two main factors to avoid carbon formation: small Ni particles by confinement effect and redox properties from CeO_2. The authors in accordance with other works (SAW et al., 2015) also observed higher amount of oxygen vacancies in core@shell structure when compared to traditional supported catalysts, consequence of higher metal-support interaction.

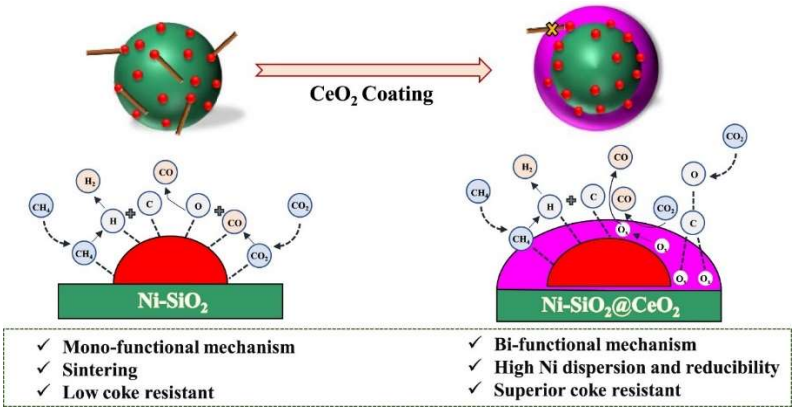

Figure 2.8. (a) Mono-functional pathway on Ni-SiO_2 and (b) Bi-functional pathway on Ni-SiO_2@CeO_2 (ABDULRASHEED et al., 2019; Adapted from Das et al. (2018)).

Ni@CeO_2 catalyst was prepared by hydrothermal method with urea and tested for DRM reaction by Tang et al. (2017). The microscopy images showed that Ni nanoparticles are encapsulated by CeO_2 shell and CeO_2 thickness can be controlled by varying synthesis time. The increase on time synthesis increased the CeO_2 thickness, surface area and metal-support interactions, as observed by the enhancement of oxygen lattice species by XPS. Ni@CeO_2 catalyst prepared with a synthesis time of 18 h was tested for DRM reaction and compared to Ni@SiO_2 catalyst. CeO_2 shell could promote carbon removal mechanism, decrease the amount of carbon deposited over the catalyst after 24 h, as observed by TGA, but carbon remains present in the Ni@CeO_2 catalyst. Even if the hydrothermal method is a simple synthesis method, the microscopy images showed large Ni particles encapsulated into CeO_2 in the selected time synthesis, justifying the presence of carbon on Ni@CeO_2 catalyst.

Wang et al. (2017) have developed a facile modified sol-gel method with citric acid to obtain Cu@CeO_2 core@shell catalyst for application at hydrogenation of methyl acetate at low temperature. Microscopy images showed the high dispersion of Cu nanoparticles embedded into CeO_2 matrix. The chemical similarity between Cu and Ni

permits to adapt the synthesis for $Ni@CeO_2$ catalyst and the challenge here is the behavior of the catalyst at high temperature required for DRM reaction. Sol-gel synthesis is a polymerization process widely used to prepare metal oxides nanoparticles due the high potential to control textural and surface properties with homogeneous distribution. The process consists in few steps such as hydrolysis, condensation and drying, resulting in the solid product (RAO; MUKHERJEE; REDDY, 2017).

- *Mesoporous catalysts*

Mesoporous supports have been investigated for application at DRM reaction due to its textural properties. High surface area and high pore volume with uniform distribution contribute to higher activity (USMAN; WAN DAUD; ABBAS, 2015; XU et al., 2012). Moreover, the metal confinement inside pores leads to a confinement effect, improving thermal stability against metal sintering. Some works (SUN et al., 2010; ZHANG et al., 2006) showed the stabilization of Ni nanoparticles loaded within mesoporous supports.

Literature reports the application of many mesoporous supports for DRM reaction, such as MCM-22 (AMIN et al., 2016), SBA-15 (KAYDOUH et al., 2015), MCM-41 (YASYERLI et al., 2011), ZSM-5 (SARKAR et al., 2012) and others. As discussed previously, Ni-based catalysts supported on Al_2O_3 are interesting for DRM application. Ordered mesoporous Al_2O_3 has been used as support for DRM reaction due to high interaction between Ni and Al_2O_3 in the form of $NiAl_2O_4$, avoiding Ni sintering at high temperature, high surface area, controllable pore size and high thermal stability. However, traditional impregnation normally leads to blockage of pores, decreasing the surface area of final material. Then, the use of one-pot synthesis procedure in order to obtain mesoporous structure and high Ni accessibility after reduction is important to obtain high activity and coke-free catalyst for DRM reaction.

Evaporation-Induced Self-Assembly (EISA) method has been applied to synthesize mesoporous metal oxides with high surface area and well-defined pore distribution. EISA approach to prepare Ni/Al_2O_3 catalysts consists in direct addition of Ni precursor to the synthesis medium of alumina matrix, containing Al precursor, organic structuring agent and organic solvent. After evaporation, the mesoporous structure with mixed oxides Ni^{2+}/Al^{3+} are formed, that is calcined at high temperature to liberates porosity and to form $NiAl_2O_4$ spinel phase. Finally, after reduction Ni^0

nanoparticles are formed and well dispersed into Al_2O_3 mesoporous (KARAM et al., 2019).

Fang et al. (2015) compared Ni/Al_2O_3 catalysts prepared by EISA method and Ni classical impregnation over commercial γ-Al_2O_3 to application on DRM reaction. BET surface area strongly decreased when Ni was impregnated on γ-Al_2O_3 due to the blockage of pores, while EISA method could generate a high surface area catalyst. Consequently, Ni crystallite size is smaller for EISA produced catalyst. Ni/Al_2O_3-IMP deactivated increasing TOS, while Ni/Al_2O_3-EISA was stable during 75 h TOS. The authors associated the formation of ordered mesoporous structure and higher Ni dispersion to be the reasons for high stability and coke resistance of the Ni/Al_2O_3 prepared by EISA method.

Similar results were obtained by other authors for DRM reaction over Ni/Al_2O_3 catalyst by EISA method (XIANG et al., 2016; XU et al., 2012). However, the formation of carbon is not totally avoided due the low availability of mobile oxygen, in the form of hydroxyls groups, in Al_2O_3 surface (FERREIRA-APARICIO et al., 2000). Then, the high resistance to Ni sintering was not enough to inhibit carbon formation and the enhancement of redox properties in the support are necessary. Some authors observed an increase in the catalysts stability and coke resistance when rare-earth elements are added together with Ni into mesoporous structures (KAYDOUH et al., 2015; OMOREGBE et al., 2016; PU et al., 2018; ZHANG et al., 2013b).

The addition of Ce into Ni/Al_2O_3 mesoporous catalyst prepared by EISA for DRM reaction was studied by Wang et al. (2014). The authors observed that at Ce/Al = 4 the mesoporous structure became partially disordered, decreasing strongly the BET surface area from 242 m^2/g (R=2) to 64 m^2/g (R=4), where R = Ce/Al. All the EISA samples presented the formation of $NiAl_2O_4$ spinel phase and the increase on Ce content promoted oxygen mobility in the material at lower temperature.

The catalysts were tested in the DRM reaction (Figure 2.9) and a progressive decrease of activity was observed for Ni/Al and Ni/CeAl-IMP (R=1) prepared by impregnation. XRD analysis of post-reaction samples showed Ni sintering during reaction for Ni/CeAl-IMP (R=1) and Ni/CeAl (R=2) catalysts, leading to a decrease of Ni active sites. The Ni sintering observed for impregnated is caused by the formation of segregated NiO, which leads to Ni nanoparticles with weak interaction with support. The Ni growth observed for Ni/CeAl (R = 2) is due to the collapse of mesoporous structure during reaction, as observed by XRD at low angle. Therefore, Ni/Al and

Ni/CeAl (R=1) maintained the mesoporous structure and Ni sintering was avoided. However, Ni/Al presented high deactivation with TOS and the authors associated this deactivation to high presence of carbon deposits, as observed by TGA. The catalyst without Ce did not promote carbon removal mechanism during reaction, leading to high carbon formation. The Ni/CeAl (R = 1) presented the best activity among the catalysts tested without Ni sintering and good redox behavior. However, the authors still detected formation of carbon species on spent catalyst.

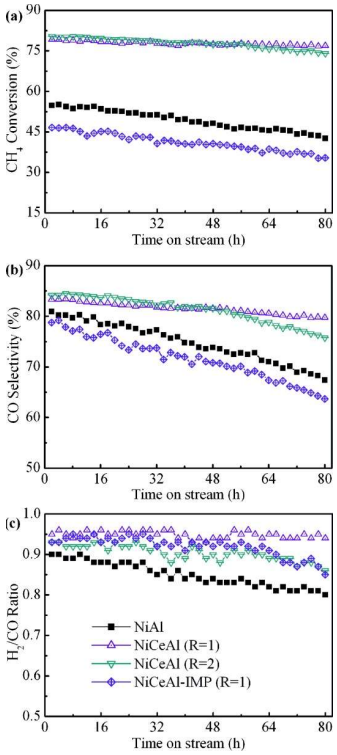

Figure 2.9. CH_4 conversion, CO selectivity and H_2/CO molar ratio as a function of TOS for Ni/Al and Ni/CeAl (R) catalysts on DRM reaction. T = 700 °C, CH_4/CO_2 = 1 and GHSV = 36000 mL($h.g_{cat}$) (WANG et al., 2014).

Recently, Fonseca et al. (2019) have synthesized also by EISA method CeAl mesoporous materials with different $n_{Ce}/(n_{Ce} + n_{Al})$ from 2 to 20 % with high redox properties. In their work, authors observed that the incorporation of Ce in Al precursor solution for EISA synthesis leads to the formation of small CeO_2 nanoclusters highly dispersed around Al_2O_3 mesoporous up to limited composition ($n_{Ce}/(n_{Ce} + n_{Al})$ up to 10 %). Above this amount of Ce, bigger CeO_2 crystallites are observed by XRD. Oxygen isotopic exchange experiment at 550 °C showed the promotional effect of Ce addition in order to enhance oxygen mobility in the material. Ce10Al presented similar

number of exchanged oxygens compared to commercial CeO_2 and higher values were obtained for Ce15Al and Ce20Al (Figure 2.10). Due the good oxygen mobility and small CeO_2 nanoparticles, Ce10Al appears as promising alternative to application as Ni-support with excellent redox abilities in DRM reaction. Table 2.9 shows more works related to confinement effect as an approach to improve Ni particle stability at high temperature and design a resistant catalyst against coke formation.

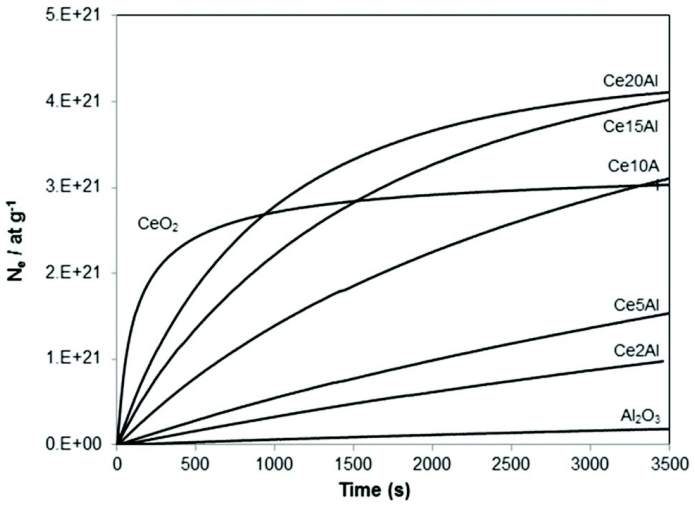

Figure 2.10. Oxygen isotopic exchange at 550 °C for all samples (FONSECA et al., 2019).

Table 2.9. Literature works related to confinement effect as an approach to increase coke resistance.

Reference	Catalyst	Reaction Condition	Subject	Conclusions
(LIM et al., 2016)	Ni@yolk-ZrO_2	Steam Reforming of Methane T = 750 °C, P = 1 atm $H_2O:CH_4$ = 2.5:1	Effect of Brij L4 surfactant in the thermal stability of the catalysts	The amount of Brij L4 affected mainly the pore size distribution in ZrO_2 shell. Without the addition of surfactant, the catalyst was not active for reaction, limiting the permeation of gases to Ni core. Over addition of Brij L4 leads to the formation of weak ZrO_2 shell, collapsing the structure after 24 TOS. The authors observed a optimum Brij L4:Ni proportion = 2.4 to synthesize stable and high activity catalyst for SRM.
(DOU et al., 2019)	SiO_2@Ni@ZrO_2	T = 700 °C, P = 1 atm $CH_4:CO_2:N_2$ = 1:1:1	Addition of ZrO_2 shell over Ni deposited on SiO_2 spheres	ZrO_2 coating was responsible to improve thermal stability on the catalyst. Without ZrO_2 shell, large Ni particles around 33 nm were formed over SiO_2 surface, leading to high carbon formation. The porous ZrO_2 shell avoided Ni sintering, generating small Ni particles around 6 nm. Then, the addition of ZrO_2 shell improved catalytic activity and coke resistance on the catalysts for DRM reaction.

(XIANG et al., 2020)	Ni-$Ce_{0.8}Gd_{0.2}O_{2-\delta}$/KIT-6	T = 700 °C, P = 1 atm CH_4:CO_2 = 1:1	Effect of Ni-$Ce_{0.8}Gd_{0.2}O_{2-\delta}$ addition over KIT-6 at different mass ratio	The deposition of Ni-$Ce_{0.8}Gd_{0.2}O_{2-\delta}$ over mesoporous KIT-6 with high surface area improved Ni dispersion via confinement effect. Furthermore, the authors observed enhancement of oxygen vacancies compared to unsupported catalyst. After reaction, Ni-$Ce_{0.8}Gd_{0.2}O_{2-\delta}$ without KIT-6 deactivates with time due Ni sintering, leading to high carbon formation. In contrast, Ni-$Ce_{0.8}Gd_{0.2}O_{2-\delta}$/KIT-6 presented better stability during 80 h TOS, with optimum value ascribe to mass ratio 1.8 where the formation of carbon detected by TGA was lower.
(ZHANG et al., 2013b)	NiCe/SBA-16 Ni/CeO_2 Ni/SBA-16	T = 700 °C, P = 1 atm CH_4: CO_2:He = 5:5:5	Effect of Ce addition to Ni/SBA-16 catalyst for DRM reaction.	Ce-doped Ni/SBA-16 improved Ni dispersion in comparison to Ni/CeO_2 and Ni/SBA-16 because of the strong interaction between Ni and Ce and the confinement effect caused by mesoporous of SBA-16. Furthermore, the addition of Ce avoided collapse of SBA-16 framework during reaction, improving the catalyst stability and resistance to coke formation.

This chapter presented the challenges to upgrade biogas to syngas by DRM reaction. The theory and publications in DRM reaction demonstrate the difficulties and challenges to design a high active and coke resistant catalyst for the reaction. Core@shell and mesoporous structures with redox properties appear as alternatives to obtain well-dispersed catalysts. Therefore, this work will evaluate the synthesis, characterization, activity and deactivation of Ni@CeO_2 and Pt@CeO_2 catalysts for DRM at different variables: (1) Ni-based core@shell structure against classical impregnation and the effect of Zr as dopant into ceria; (2) Effect of trivalent dopants (Gd^{3+} and Sm^{3+}) in comparison to Zr^{4+} in Ni@CeO_2 catalyst; and the effect of Ce/Zr molar ratio; (3) Pt-based core@shell structure against classical impregnation and the effect of Zr as dopant into ceria. The Al_2O_3 mesoporous structure as support for DRM reaction will be also evaluated: (4) Effect of Ni loading and Ce addition to prepare Ni/CeAl catalyst by EISA method and the comparison with classical impregnation method.

CHAPTER 3

Experimental

3.1 Catalyst Synthesis

3.1.1 $Ni@CeO_2$ and $Pt@CeO_2$ catalysts series

Catalysts were prepared following the method previously described in the literature (WANG et al., 2017). A solution of cerium nitrate (1.7 $mol.L^{-1}$, 25 mL, Aldrich) was prepared, followed by the addition of an appropriate amount of nickel nitrate (Aldrich) or hexachloroplatinic acid (Aldrich) to obtain 10 wt% of Ni and 1 wt% Pt, respectively. In another becker, a solution of citric acid (6.7 $mol.L^{-1}$, 25 mL, Aldrich) was prepared, using a citric acid/metals molar ratio equal to 1.0. Both solutions were mixed and stirred for 2 h at room temperature. Then, the solution was heated at 70 °C under vacuum to remove water. The remaining material was dried at 100 °C overnight. The calcination occurred in 2 steps: 2 h at 300 °C and 4 h at 400 °C, using a heating rate of 1 °C/min. These catalysts were denominated as $Ni@CeO_2$ and $Pt@CeO_2$.

Figure 3.1. Experimental setup for catalyst synthesis.

For comparison, a Ni/CeO_2 and Pt/CeO_2 catalysts were prepared by incipient wetness impregnation of CeO_2 support with an aqueous solution of nickel nitrate or hexachloroplatinic acid. In this case, CeO_2 was synthesized by the method previously described but without the addition of nickel or platinum precursor. The drying and calcination process followed the same procedure described above.

The ceria-doped materials were prepared using the same sol-gel method with the addition of zirconyl nitrate, samarium nitrate or gadolinium nitrate to metals solution. Zirconia-doped ceria catalysts were synthesized with 3 different Ce/Zr molar ratio (4.0, 1.0 and 0.25) while the catalysts doped with Sm and Gd contained a Ce/dopant ratio of

4.0. The drying and calcination process followed the same procedure described above. The catalysts were denoted as follow: Ni@CeSmO$_2$, Ni@CeGdO$_2$, Ni@CeZrO$_2$(4), Ni@CeZrO$_2$ (1); Ni@CeZrO$_2$ (0.25).

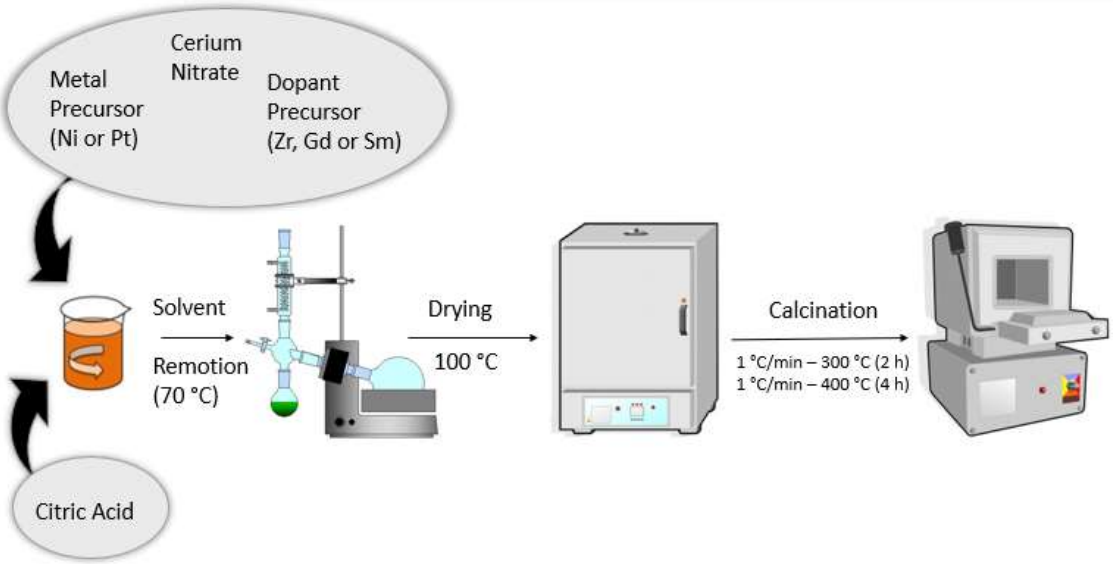

Figure 3.2. Schematic of core-shell catalysts synthesis.

3.1.2 Ni-CeAl mesoporous catalysts series

The mesoporous catalysts were prepared using the EISA method described in the literature (YUAN et al., 2008). 5 g of the surfactant Pluronic 123 (Aldrich) was dissolved in 100 mL of ethanol (Fluka) in a beaker and maintained under stirring for 1 hour. After that, 6 mL of HNO$_3$ (90 wt%, Sigma-Aldrich) were added to the solution, followed by the addition of aluminum isopropoxide (Aldrich), cerium acetate (Aldrich) and nickel acetate (Aldrich). The solution was maintained under stirring for 5 hours. The evaporation of the solvent was carried out in an oven at 60 °C for 5 days and the samples were calcined in a muffle furnace at 800 °C for 4 hours with a ramp of 1 °C/min. The concentration of metals in solution was fixed at 0.5 mol/L and a Ce/(Ce + Al) molar ratio equal to 0.1 was used as well as two Ni loadings (5 and 10 wt%). The series of samples was denoted as follows: CeAl, 10Ni-Al, 10Ni-CeAl and 5Ni-CeAl.

For comparison, the catalyst denoted as 10Ni/CeAl was prepared by incipient-wetness impregnation of the support CeAl prepared above. In this case, the Ni precursor was nickel nitrate (Aldrich) and the impregnation process occurred in ethanol solution.

The next chapters will be focused in the discussion of these catalysts by different groups. Therefore, for better understanding, the Table 3.1 presents the catalysts divided

by groups and the corresponding chapter where the discussion will occur. Sometimes for comparison the same catalyst will be analyzed in different groups.

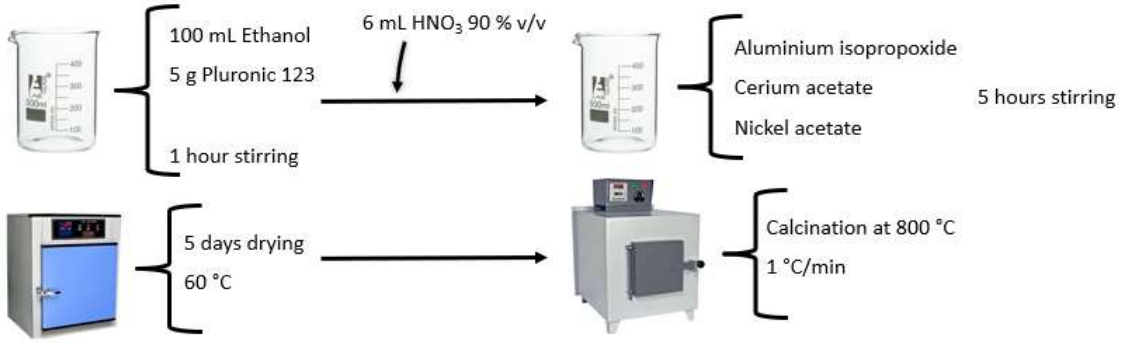

Figure 3.3. Schematic representation of Ni-based mesoporous catalysts prepared by EISA method.

Table 3.1. Distribution of catalyst at different groups.

Group	Chapter	Catalysts
1	4	Ni/CeO_2; Ni@CeO_2; Ni@$CeZrO_2$ (4)
2	5	Ni@CeO_2; Ni@$CeGdO_2$; Ni@$CeSmO_2$; Ni@$CeZrO_2$(4); Ni@$CeZrO_2$ (1); Ni@$CeZrO_2$ (0.25)
3	6	5Ni-CeAl; 10Ni-CeAl; 10Ni/CeAl; 10Ni-Al
4	7	Pt/CeO_2; Pt@CeO_2; Pt@$CeZrO_2$

3.2 Catalyst Characterization

3.2.1 X-ray fluorescence (XRF)

The chemical composition of the Ni@CeO_2 catalysts series was determined by an X-ray fluorescence spectrometer RIGAKU RIX-3100.

3.2.2 Inductively Coupled Plasma Optical Emission Spectrometry (ICP-OES)

The chemical composition of the Pt@CeO_2 and Ni-CeAl series was determined by ICP-OES with a PerkinElmer Optima 2000 DV instrument. The samples were totally mineralized using a mixture of HNO_3 and HCl.

3.2.3 N_2 physisorption

The BET surface area of the samples was measured by N_2 adsorption using a Micromeritics Tristar 3000 apparatus at – 196 °C. The samples (100 mg) were degassed at 300 °C under vacuum before the analysis.

3.2.4 Transmission electron microscopy (TEM)

TEM analyses of reduced and used catalysts were made in a JEOL 2100 UHR apparatus, with 0.19 and 0.14 nm punctual and linear resolution, respectively, equipped with a LaB_6 filament. Energy dispersive X-ray (EDX) analysis was also performed to determine the local chemical composition. The range used to collect the X-rays emitted from the sample upon electron impact was 0 – 20 keV. Before the analysis, the samples were reduced at 800 °C for 1h, the same temperature used for the reaction.

3.2.5 X-ray diffraction (XRD)

In-situ X-ray diffraction of group 1 was performed at the XPD-10 B beamline at the Brazilian Synchroton Light Laboratory (LNLS). The samples were reduced under a 5 % H_2/He mixture at a heating rate of 10 °C/min, from 25 to 800 °C, remaining at the final reduction temperature for 1 h. The XRD patterns were obtained at 2θ range from 23° to 56° and the wavelength used was 1.55002 Å.

In-situ X-ray diffraction was performed in a Bruker D8 Advance X-ray powder diffractometer operated at 40 kV and 40 mA, using CoK_α radiation (λ = 1.790307 Å), equipped with a Position Sensitive Detector, VANTEC-1, kβ filter (Ni), used in scanning mode, for the catalysts groups 2 and 4. The 2θ range analyzed was 10 to 80°, step of 0.05°, step time equal to 2 s. The flow of reduction was composed of 10 % H_2/He and the XRD patterns were collected at different temperatures ((room temperature, 200 °C, 600 °C, 800 °C and room temperature after reduction)).

The XRD pattern of group 4 was obtained using a Miniflex Rigaku equipment, with Cukα radiation (λ = 1.54184 Å). The 2θ range varied from 20 to 70°, step of 0.05° and 2 s per step. It was performed also at Miniflex Rigaku equipment the XRD analysis of reduced and passivated samples from groups 2 and 4. The passivation occurred at -70 °C with a mixture of 5 % O_2/N_2 for 1 hour and more 1 hour at room temperature (FARIA et al., 2014).

The average crystallite size of NiO, metallic Ni and CeO_2 was calculated using the Scherrer equation (Eq. 3.1). The CeO_2 lattice parameter (Eq. 3.2) was determined by

the Bragg's Law (Eq. 3.3), assuming an orthorhombic structure and the *(111)* CeO_2 plane. K is the shape factor (0.9 is the typical value), θ is the Bragg angle, λ is the X-ray wavelength and β is the line broadening at half the maximum intensity.

$$d = \frac{K\lambda}{\beta \cos\theta} \quad (3.1)$$

$$a = \sqrt{d_{hkl}\,(h^2 + k^2 + l^2)} \quad (3.2)$$

$$d_{hkl} = \frac{\lambda}{2\,\mathrm{sen}\,(\theta)} \quad (3.3)$$

3.2.6 In-situ X-ray absorption near edge structure (XANES)

XANES analysis was performed at the DXAS beamline at LNLS to obtain information about the reduction degree of Ni during the reduction procedure for group 1. The samples were diluted with boron nitride, used as inert, and pressed to obtain a pellet. The pellet was placed in a tubular reactor and reduced under a 5 % H_2/He mixture up to 750 °C, keeping this temperature for 30 min. The treatment of XANES data was carried out using PrestoPronto software (FIGUEROA; PRESTIPINO, 2016). The fraction of metallic Ni phase was calculated as a function of reduction temperature by linear combination using NiO and Ni^0 foil XANES spectra as references.

3.2.7 Raman spectroscopy

The RAMAN spectra were recorded at room temperature using a Horiba LabRam HR-UV800/Jobin-Yvon spectrometer. The 532 nm wavelength was used to observe the carbon structure.

3.2.8 $^{18}O_2/^{16}O_2$ isotopic exchange

The experiments were carried out in a closed recycling system connected to a Pfeiffer Vacuum quadrupole mass spectrometer in one side and a vacuum pumper in the other side. Firstly, the sample (c.a. 20 mg) was pre-treated under $^{16}O_2$ flow (50 mL/min, 500 °C, 1 h) and evacuated for 1 h. After the pre-treatment, the sample was cooled down to reaction temperature.

For the Isothermal Oxygen Isotopic Exchange (IOIE), the reactions occurred at 350 °C, 400 °C and 450 °C (group 1) and 400 °C, 450 °C and 500 °C (group 4). It was inserted into the reactor 55 mbar of pure $^{18}O_2$ (≥ 99 at.%, ISOTEC) and each isotopomer concentration was analyzed by monitoring the following m/z signals: 32 ($^{16}O_2$), 34 ($^{18}O^{16}O$), 36 ($^{18}O_2$).

The behavior of the oxygen exchange was studied as a function of the temperature (Temperature-Programmed Oxygen Isotopic Exchange – TPOIE). For this experiment, pure $^{18}O_2$ (55 mbar) was injected in the reactor at 200 °C and the sample was heated up to 500 °C (2 °C/min).

The following equations were used to calculate the atomic fraction of $^{18}O_2$ in the gas phase at the time t (α_g^t) (Eq. 3.4), initial rate of exchange (R_e) (Eq. 3.5), the number of oxygen exchanged (N_e) (Eq. 3.6), where P_x^t is the partial pressure of each isotopomer at the time t (x = 32, 34 and 36); Ng is the total number of oxygen atoms in the gas phase; w is the weight of catalyst; α_g^0 is the initial atomic fraction of $^{18}O_2$ in the gas phase.

$$\propto_g^t = \frac{1/2 P_{34}^t + P_{36}^t}{P_{32}^t + P_{34}^t + P_{36}^t} \quad (3.4)$$

$$R_e = -N_g \frac{d\propto_g^t}{dt} \frac{1}{w} \quad (3.5)$$

$$N_e = \left(\propto_g^0 - \propto_g^t\right) N_g \frac{1}{w} \quad (3.6)$$

3.2.9 Temperature-Programmed Reduction (TPR)

Experiments of temperature-programmed reduction (TPR) were performed in a setup equipped with thermal conductivity detector. The Table 3.2 described the conditions of each group for TPR experiment.

Table 3.2. TPR conditions for each group.

Group	Weight (mg)	H_2/He (%)	Pre-treatment
2	300	10	400 °C with O_2
3	400	10	200 °C with He
4	150	1	400 °C with O_2

3.2.10 Oxygen Storage Complete Capacity (OSCC)

The measurements of Oxygen Storage Complete Capacity (OSCC) were carried out in an atmospheric quartz fixed-bed reactor placed in a furnace connected to a Porapak column and a TCD detector. The method described elsewhere (DUPREZ et al., 2001) consists in a pretreatment of 20 mg of catalyst under He (30 mL/min) from room temperature to 500 °C, with a ramp of 2 °C/min. At this temperature, the sample is completely oxidized by 10 O_2 pulses. After that, 10 pulses of CO are injected up to the maximum reduction of the sample and a series of O_2 pulses to reoxidize the oxide solid. The consumption of CO and O_2 as well as the production of CO_2 are determined from the area of corresponding peaks obtained with the TCD detector. The OSCC values are calculated from the CO_2 production instead of CO uptake, due to the possibility to form carbonate species during the CO pulses. The OSCC is expressed in µmol $CO_2.g^{-1}$. The same procedure was made twice and a mean value of OSCC was retained.

3.2.11 Diffuse Reflectance Infrared Spectroscopy (DRIFTS)

In order to characterize the adsorbed species on the catalysts during the reaction of dry reforming of methane, the technique of Diffuse Reflectance Infrared Spectroscopy (DRIFTS) was performed *operando*. The experiments were carried out in a Bruker Tensor II equipped with a MCT detector and a DRIFTS Harrick environment chamber. The experiments consisted in: (i) reduction up to at 750 °C for 1 h, with 10 °C/min heating rate, under 10 % H_2/N_2 mixture (50 mL/min); (ii) purge of the chamber with N_2 (50 mL/min) at the same temperature for 30 min and collection of the background after the purge; (iii) flow of CH_4/N_2 mixture (30 mL/min CH_4 + 70 mL/min N_2) through the sample for 10 min; (iv) flow of CO_2/N_2 mixture (30 mL/min CO_2 + 70 mL/min N_2) through the sample for 10 min; (v) flow of CH_4/N_2 mixture (30 mL/min CH_4 + 70 mL/min N_2) through the sample for 10 min; (vi) flow of $CH_4/CO_2/N_2$ mixture (30 mL/min CH_4 + 30 mL/min CO_2 + 70 mL/min N_2) through the sample for 10 min. The spectrum was registered in the range of 1200-4000 cm^{-1} by collecting 30 scans with a resolution of 4 cm^{-1}.

3.2.12 Thermogravimetric analysis (TG)

In order to quantify the amount of coke formed on the catalyst, thermogravimetric analyses of the post-reaction samples were carried out in a TA Instruments equipment (SDT Q600). Approximately 10 mg of the spent catalyst was

heated under synthetic air flow (100 mL/min) from room temperature to 1000 °C at a heating rate of 20 °C/min and the weight change was measured.

3.2.13 Scanning electron microscopy (SEM)

SEM analyses of the spent catalysts were carried out using a field emission scanning electron microscope (FE-SEM) Quanta FEG 450 FEI operating with an accelerating voltage of 20 kV.

3.3 Catalytic Tests

3.3.1 Dry Reforming of methane

Groups 1, 2 and 4 were tested at National Institute of Technology. The DRM was performed in a fixed-bed reactor at atmospheric pressure. Before the reaction, the catalysts were reduced under pure H_2 (30 mL/min) at 800 °C for 1 h and purged under N_2 at the same temperature for 30 min. A reactant mixture with CH_4:CO_2 under flow rate of 100 mL/min was used for the DRM at 800 ºC. The CH_4/CO_2 molar ratio tested was 1.0 and 1.5

The samples were diluted with SiC (SiC mass/catalyst mass ratio = 1.5) to better distribution of temperature. The reaction products were analyzed by gas chromatography (Agilent 6890) equipped with a thermal conductivity detector and Carboxen 1010 column (Supelco). The W/F parameter were: 0.2 $g_{cat}\ L^{-1}min^{-1}$ (Group 1); 0.2 – 1.4 $g_{cat}\ L^{-1}min^{-1}$ (Group 2); 0.4 $g_{cat}\ L^{-1}min^{-1}$ (Group 4)

The group 3 was tested at University of Poitiers. The DRM tests were carried out in a quartz fix-bed reactor at atmospheric pressure. The catalyst was mixed with SiC to ensure a better thermal control in the reactor (SiC/catalyst = 1.5). In order to compare the reaction under similar conversion, the mass of catalyst introduced in the reactor was 20 (W/F = 0.2 $g_{cat}\ L^{-1}min^{-1}$) and 30 mg (0.3 $g_{cat}\ L^{-1}min^{-1}$) for 10 wt%Ni and 5 wt%Ni, respectively. The pressure of the reactor was monitored online by a pressure sensor (Keller PR21S, 0-5 bar) to verify the absence of pressure drop. The sample was reduced *in situ* with pure H_2 (30 mL/min) from room temperature up to 800 °C for 1 hour, with a ramp of 10 °C/min. After the reduction, the reactor was purged with N_2 (30 mL/min). The outlet gas is analyzed online in 2 analysis zone: the zone 1 consists in a Varian GC equipped with 3 columns (13X Molecular Sieve, Porapak Q and 5A Molecular Sieve) to separate all the gases, and FID and TCD detectors, using He as carrier gas. In this zone

CH_4, CO_2 and CO are analyzed. The zone 2 concerns the hydrogen analysis in a Varian GC equipped with 5A Molecular Sieve column, using argon as carrier gas, and a TCD detector.

The calculations for the quantification of CH_4 conversion (X_{CH4}), CO_2 conversion (X_{CO2}) and H_2/CO molar ratio are described in Eq. 3.7, Eq. 3.8 and Eq. 3.9, respectively.

$$X_{CH_4} = \frac{(n_{CH_4})_{feed} - (n_{CH_4})_{exit}}{(n_{CH_4})_{feed}} \ 100 \tag{3.7}$$

$$X_{CO_2} = \frac{(n_{CO_2})_{feed} - (n_{CO_2})_{exit}}{(n_{CO_2})_{feed}} \ 100 \tag{3.8}$$

$$\frac{H_2}{CO} = \frac{n_{H_2}}{n_{CO}} \tag{3.9}$$

The group 2 was also evaluated in order to obtain the TOF parameter for each catalyst. Additionally, it was performed catalytic tests at 600 °C to obtain low CH_4 conversion, with CH_4/CO_2 = 1.0. At this condition, it is possible to consider the reactor as a differential reactor, where the rate of CH_4 conversion (r_a) can be calculated as follow, where F_{ao} is the molar flow; X_a is the CH_4 conversion; m_{cat} is the mass of catalyst utilized in the catalytic test.:

$$r_a = F_{ao} \frac{X_a}{m_{cat}} \tag{3.10}$$

The TOF parameter can be calculated by the Equation 3.11, as the number of CH_4 mols converted per mols of active sites. The number of active sites is defined as the amount of Ni mols multiplied by its dispersion. For Ni-based catalysts, the dispersion is defined as the inverse of crystallite size calculated by Scherrer Equation (D = 1/d) (RUCKENSTEIN and HU, 1997).

$$TOF = \frac{r_a}{\text{Number of active sites}} \tag{3.11}$$

CHAPTER 4

Embedded Ni nanoparticles in $CeZrO_2$ as stable catalyst for dry reforming of methane

Published by Elsevier

Applied Catalysis B: Environmental 268 (2020) 118387

4.1 Motivation

The development of catalysts resistant to deactivation by carbon deposition has been the focus of several studies. Ni-based catalysts have high activity and low cost, but metal sintering may occur during the DRM and thus favor the production of coke on its surface, leading to catalyst deactivation (ROSTRUP-NIELSEN, 1972). Recently, the literature reported a series of catalysts in which the metal phase is embedded into an oxide, improving the catalyst stability by avoiding the metal sintering (BONIFACIO et al., 2015; CARGNELLO et al., 2010; MAJEWSKI; WOOD, 2014; PU et al., 2018). The development of metallic Ni particles embedded into oxides with high OSC could combine two advantages: to limit the metal sintering and prevent or remove carbon deposition.

In this work, we aim to prepare Ni-embedded CeO_2 catalysts using a one-step synthesis method and test them for DRM reaction. The use of ZrO_2 as dopant was also evaluated. A Ni/CeO_2 catalyst prepared by traditional impregnation method was also tested for comparison. Important structure properties were investigated by Transmission Electron Microscopy, Raman Spectroscopy, in-situ X-ray Diffraction and in-situ X-ray Absorption. The mobility of oxygen in the material was characterized by Oxygen Isotopic Exchange. The carbon formation was analyzed by Thermogravimetric analysis, Raman Spectroscopy, Scanning and Transmission Electron Microscopy.

4.2 Results and discussion

4.2.1 Catalyst characterization

Table 4.1 shows the Ni content, Ce/Zr molar ratio and the textural properties of the catalysts. The Ni loading is close to the nominal value (10 wt%) for all samples, as well as the Ce/Zr molar ratio of the $Ni@CeZrO_2$ catalyst (i.e., Ce/Zr = 4). The surface area and pore volume for Ni/CeO_2 and $Ni@CeO_2$ catalysts were similar but decreased when zirconia was added to ceria. After the reduction process at 800 °C under H_2, the BET surface area dropped to less than 10 m^2/g to Ni/CeO_2 and $Ni@CeO_2$ catalysts. This reduction in the BET surface area can be correlated to sintering of CeO_2 at high temperature (AY; ÜNER, 2015; LI; VAN VEEN, 2018). The decrease in BET surface area of $Ni@CeZrO_2$ sample was lower than that for the other samples. According to the literature (HORI et al., 1998), the addition of Zr into the ceria structure with the

formation of a solid solution improves the thermal stability of the ceria support, inhibiting or minimizing sintering and surface area lost at high temperatures.

Table 4.1. Ni loading, Ce/Zr molar ratio and textural properties of the samples.

Catalyst	Ni loading (%)	Ce/Zr	BET surface area (m^2/g)*	Pore Volume (cm^3/g)	Pore Size (Å)
Ni/CeO_2	10.1	---	52 (<10)	0.12	65.8
$Ni@CeO_2$	9.7	---	61 (<10)	0.16	58.0
$Ni@CeZrO_2$	9.5	4.0	36 (20)	0.09	70.0

* The values in parentheses corresponds to the samples reduced at 800 °C for 1h.

The TEM images of the reduced Ni/CeO_2, $Ni@CeO_2$ and $Ni@CeZrO_2$ catalysts are shown in Figs. 4.1 to 4.3. The image of Ni/CeO_2 catalyst shows large Ni particle segregated on the surface of the sample, with average particle size around 30 nm. The local chemical analysis showed only the presence of Ni due the large size and CeO_2 could not be detected in the area of analysis (white circle). For $Ni@CeO_2$ and $Ni@CeZrO_2$ catalysts, the TEM images reveals the presence of small Ni nanoparticles embedded in the ceria matrix formed during reduction. Segregated Ni particles could not be observed on the TEM images of $Ni@CeO_2$ and $Ni@CeZrO_2$ catalysts. Ni-embedded catalysts presented smaller metal particle size than Ni/CeO_2. For $Ni@CeO_2$ and $Ni@CeZrO_2$, the Ni particles sizes were around 13 and 6 nm, respectively. It was possible to detect the CeO_2 signal by EDX in the selected area (white circle) due the small Ni particle size and it seems that the nanoparticles embedded in the ceria matrix are protected.

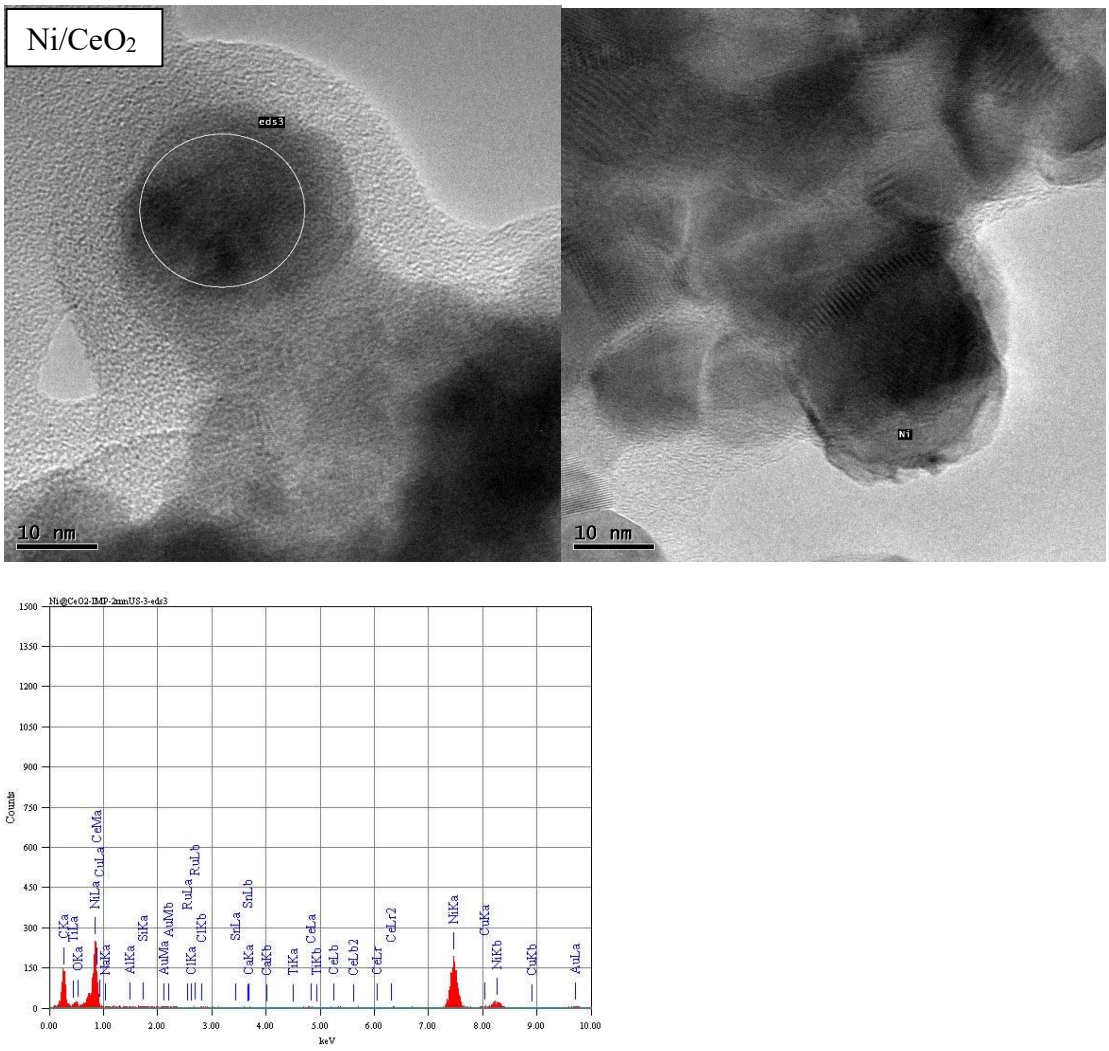

Figure 4.1. TEM images and EDX of selected areas of Ni/CeO_2 catalyst after reduction at 800 °C.

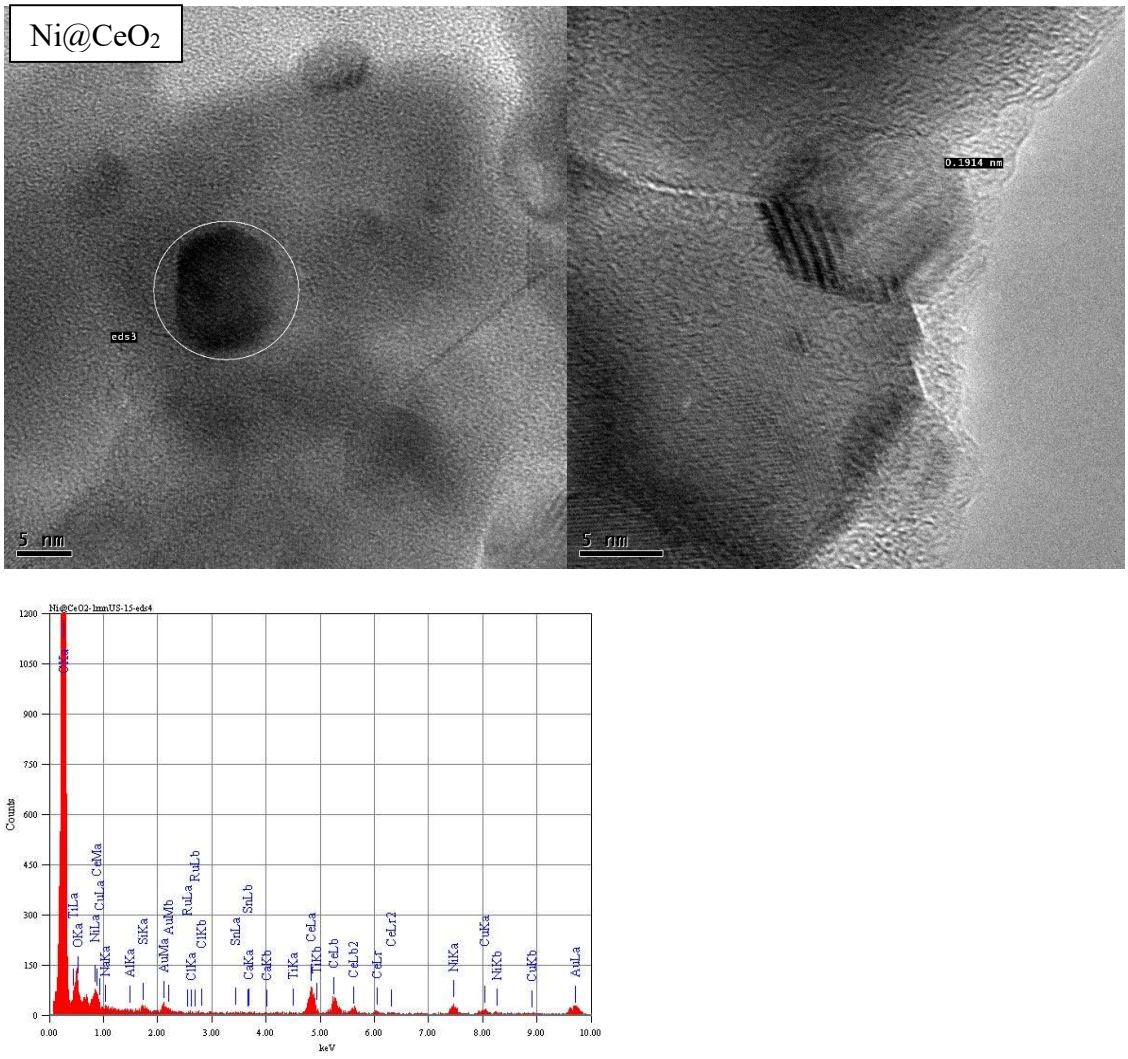

Figure 4.2. TEM images and EDX of selected areas of Ni@CeO_2 catalyst after reduction at 800 °C.

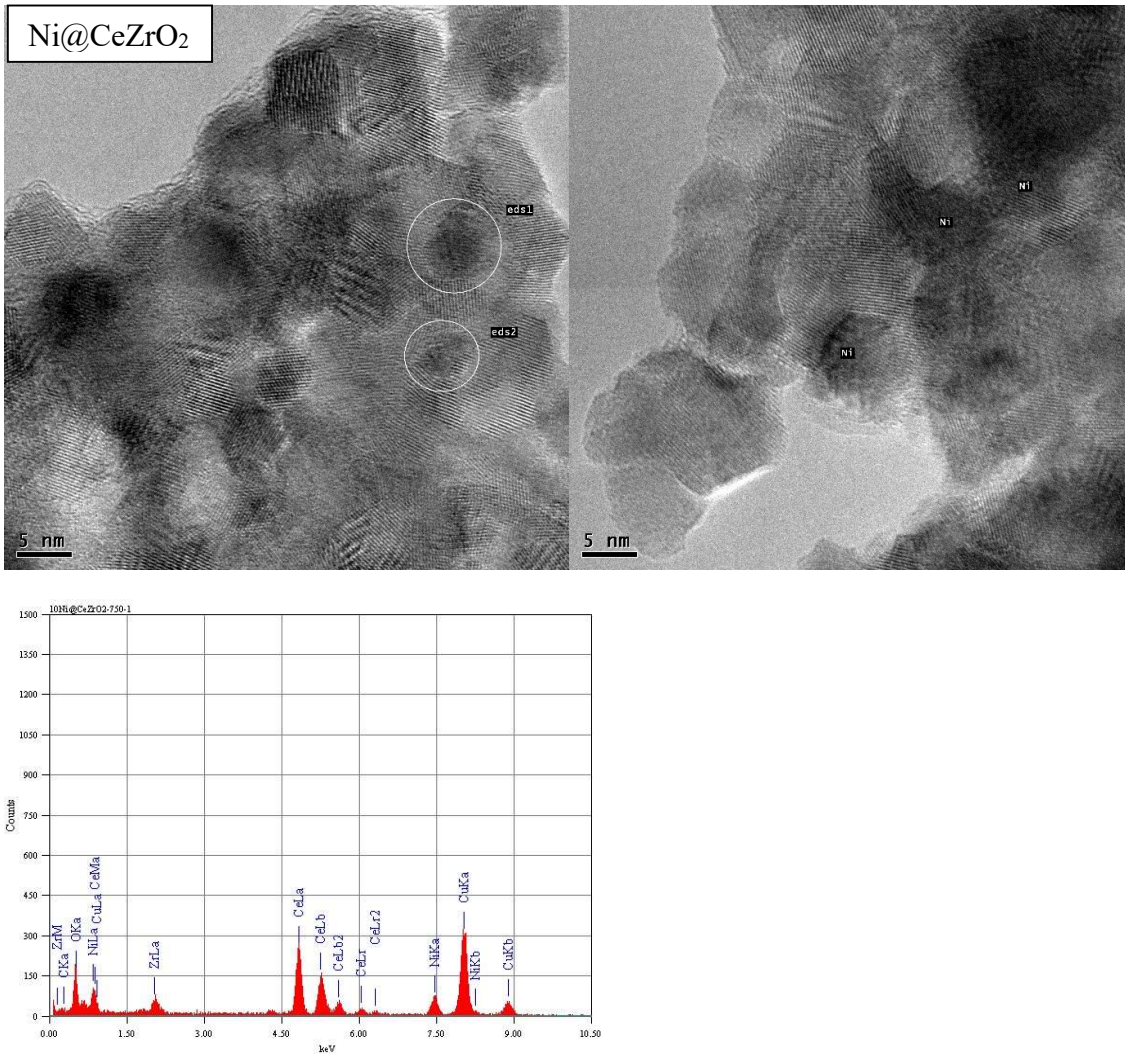

Figure 4.3. TEM images and EDX of selected areas of Ni@CeZrO$_2$ catalyst after reduction at 800 °C.

The Raman spectra of the calcined samples are shown in Fig. 4.4. The spectrum of CeO$_2$ support is also presented for comparison. The support exhibits only one intense band at 462 cm^{-1} assigned to the symmetrical stretching mode between the eight oxygen atoms bound to the cerium atom in the triple degenerate F_{2g} mode. The impregnation of ceria with Ni does not affect the spectrum of Ni/CeO$_2$, but Ni@CeO$_2$ and Ni@CeZrO$_2$ samples show a ceria structure completely different from the impregnated one. Besides the intense band around 462 cm^{-1}, the spectra display bands at 224, 544 and 632 cm^{-1}, corresponding to second-order transverse acoustic mode (2TA) and defect-induced mode. These samples exhibited two different defects in the structure, which were reported in the literature as defect space including O^{2-} vacancy (544 cm^{-1}) and defect space without O^{2-} vacancy (632 cm^{-1}) (NAKAJIMA; YOSHIHARA; ISHIGAME,

1994; TANIGUCHI et al., 2009). The NiO also presents bands in the region of 570 cm^{-1} corresponding to TO and LO vibration modes (MIRONOVA-ULMANE et al., 2007). However, this band is not detected, or it has a very weak intensity in the spectrum of Ni/CeO_2 sample. Therefore, the bands observed at 544 cm^{-1} and 632 cm^{-1} in the spectra of $Ni@CeO_2$ and $Ni@CeZrO_2$ samples might be attributed to oxygen vacancies. Therefore, the one-step synthesis of the catalyst with Ni embedded in the ceria structure can promote the formation of defect in the ceria, creating oxygen vacancies in its structure.

The Raman spectra did not detect the formation of a $Ni\text{-}CeO_2$ solid solution, as described by Barrio et al (BARRIO et al., 2010). The formation of $Ni\text{-}CeO_2$ solid solution significantly shifted the frequency for the first-order F_{2g} peak to lower values, around 445 cm^{-1}. Then, the absence of the shift of this band for the $Ni@CeO_2$ catalyst shows that the Ni is embedded in CeO_2 structure instead of in a solid solution.

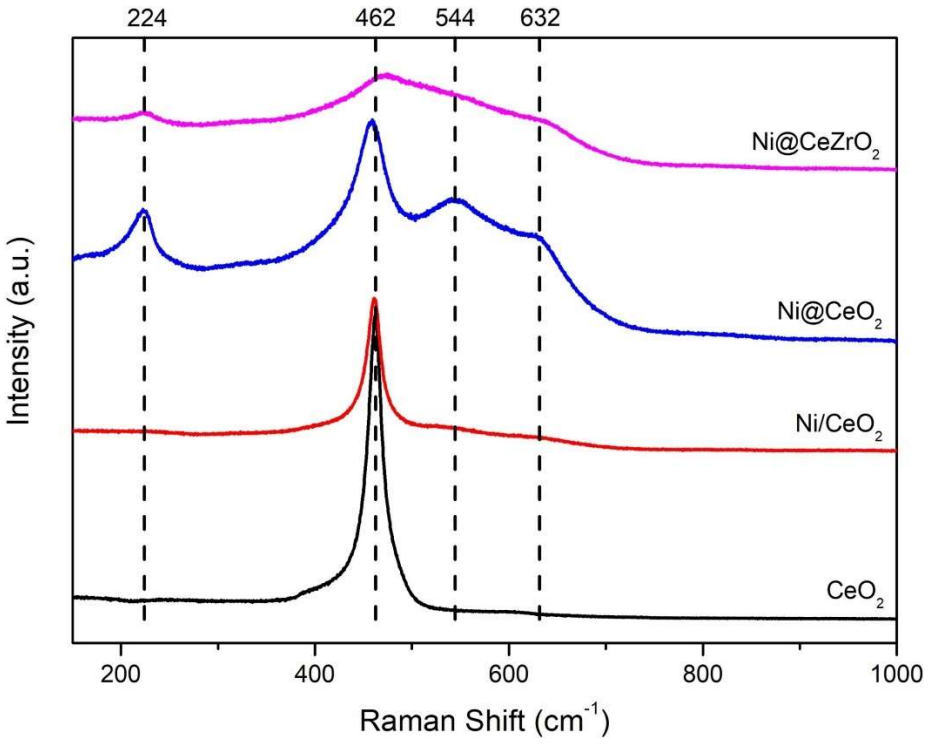

Figure 4.4. Raman spectra for the calcined samples and a CeO_2 reference.

XANES experiments at the Ni K-edge were performed to study the reduction of nickel oxide for all samples (Figs. 4.5, 4.6 and 4.7). The XANES spectrum of the calcined Ni/CeO_2 sample shows the white line at 8352 eV characteristic of NiO. Increasing the reduction temperature under 5 % H_2/He mixture led to a continuous

decrease in the intensity of this peak. At 450 °C, the spectrum is characteristic of metallic Ni, indicating that nickel oxide was completely reduced to Ni^0. The same trend was observed for $Ni@CeO_2$ and $Ni@CeZrO_2$ catalysts as shown in Figs. 4.6 and 4.7.

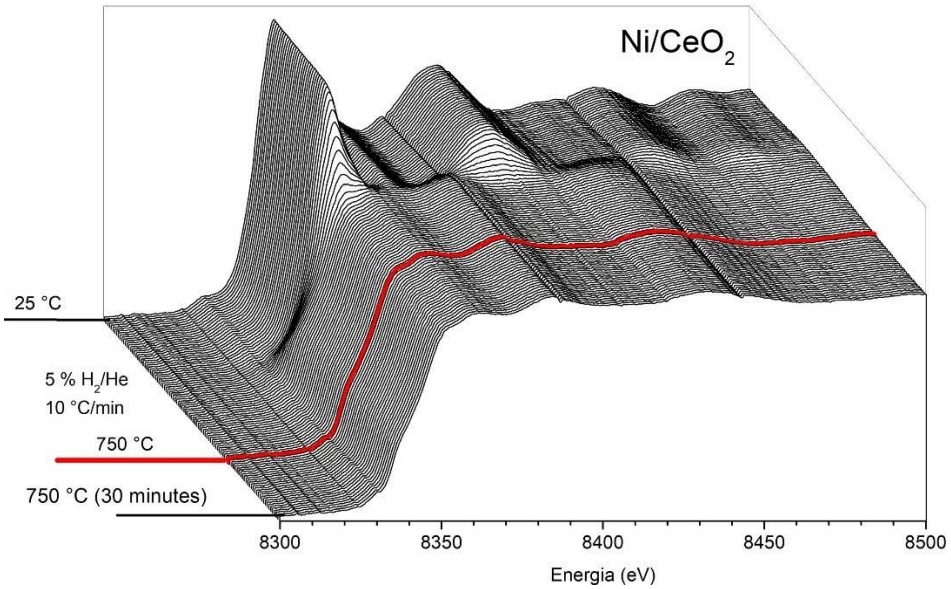

Figure 4.5. XANES spectra obtained during the reduction of Ni/CeO_2 catalyst.

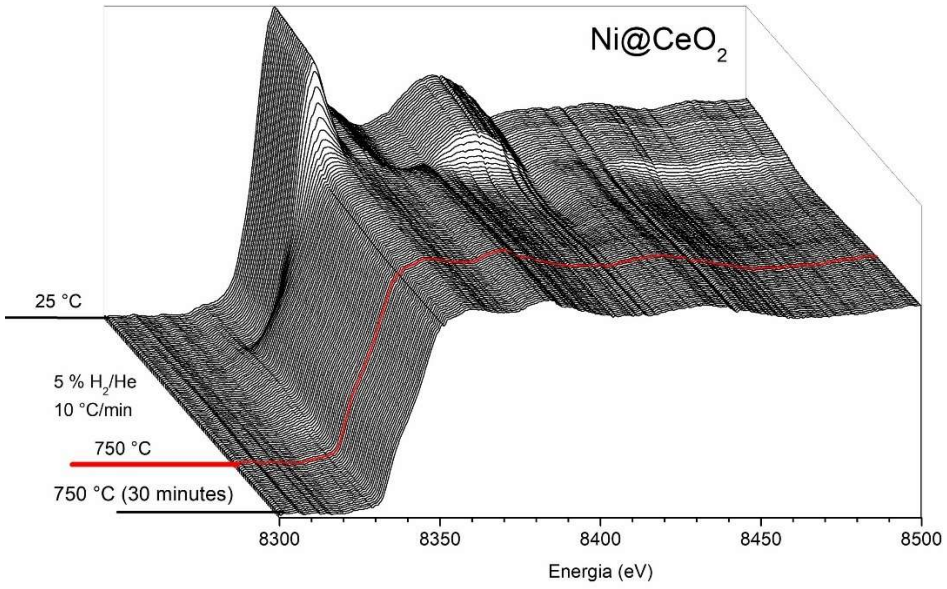

Figure 4.6. XANES spectra obtained during the reduction of $Ni@CeO_2$ catalyst.

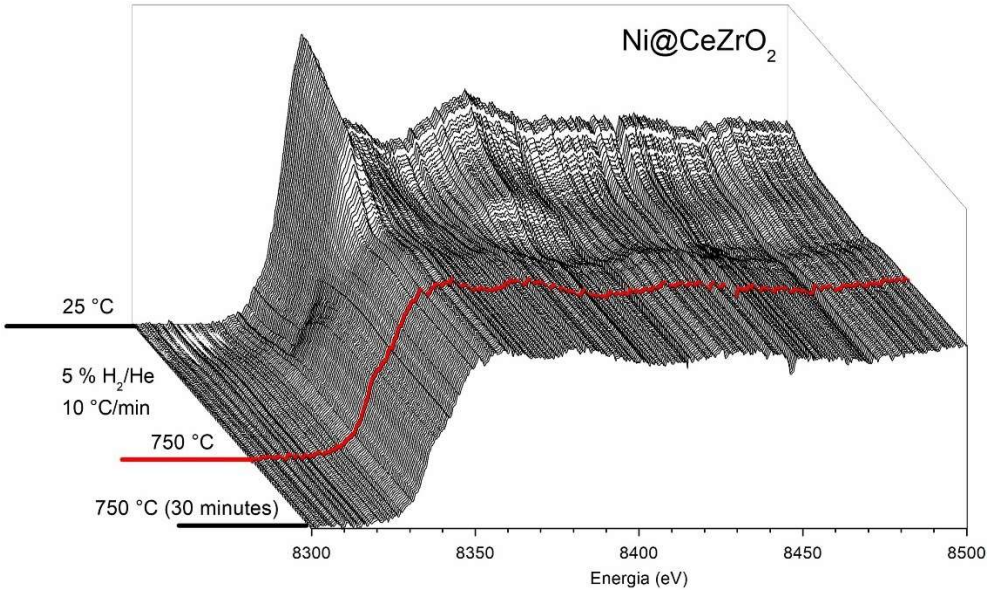

Figure 4.7. XANES spectra obtained during the reduction of Ni@$CeZrO_2$ catalyst.

However, the temperature range for the reduction of Ni oxide was different for the catalysts prepared by impregnation and sol-gel methods. Fig. 4.8 shows the evolution of the metallic Ni species during reduction calculated by the linear combination of Ni K-edge XANES spectra of references. The reduction of Ni/CeO_2 and Ni@CeO_2 samples starts at 290 and 277 °C, respectively, but at 190 °C for Ni@$CeZrO_2$ catalyst. The total reduction of nickel oxide on Ni/CeO_2 sample is achieved at 450 °C, while the complete reduction of the Ni@CeO_2 and Ni@$CeZrO_2$ samples occurs at higher temperatures (700 and 530 °C, respectively). The shift of reduction temperature to higher values is likely due to a higher metal-support interaction. Therefore, these results suggest that nickel oxide particles embedded in the CeO_2 or $CeZrO_2$ matrix have stronger interaction with the support than nickel oxide particles impregnated on CeO_2. Stronger interaction demands higher temperature of reduction to remove oxygen from the oxide structure.

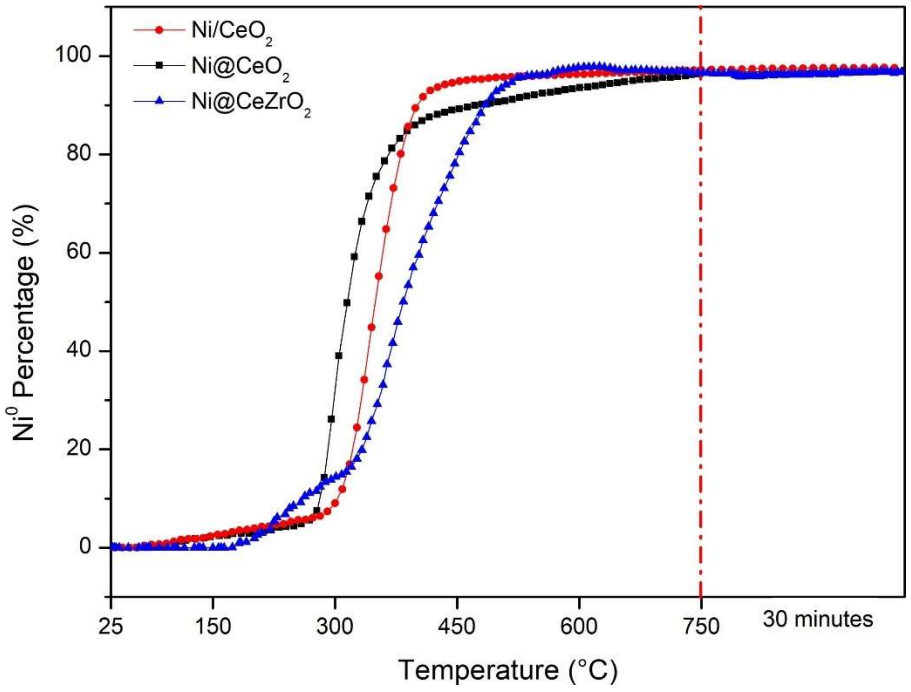

Figure 4.8. Fraction of Ni^0 calculated by the linear combination of Ni K-edge XANES spectra of references during the reduction for all catalysts.

Fig. 4.9 shows the diffractograms of the calcined samples. Ni/CeO_2 and $Ni@CeO_2$ samples exhibit the characteristic lines of CeO_2 with fluorite structure (PDF 34-0394) at $2\theta = 28.7°$, 33.2° and 47.7°. The typical lines of NiO phase (PDF 47-1049) ($2\theta = 37.3°$ and 43.3°) are only detected for Ni/CeO_2 sample. The absence of diffraction lines ascribed to NiO phase in the diffractogram of $Ni@CeO_2$ sample can be attributed to the presence of very small NiO crystallites in this catalyst, indicating that sintering did not occur during the calcination. For $Ni@CeZrO_2$ sample, the lines characteristic of NiO phase are not detected either whereas the lines corresponding to CeO_2 are shifted to higher 2θ positions. The partial substitution of Ce^{4+} by Zr^{4+} ions in the ceria structure shifted the CeO_2 lines to higher Bragg angles that corresponds to a decrease in the lattice parameter (Table 5.2) due to the difference between the ionic radii of the cations Ce^{4+} (0.97 Å) and Zr^{4+} (0.84 Å) (BONK et al., 2015). According to the literature, this shift indicates the formation of a CeO_2-ZrO_2 solid solution for the $Ni@CeZrO_2$ catalyst (FARIA et al., 2014; KOZLOV et al., 2002). Ni/CeO_2 catalyst exhibited a ceria lattice parameter higher than that one reported in the literature (5,4112 Å), while it further decreased for $Ni@CeO_2$ with Ni embedded in CeO_2. The CeO_2 crystallite size of the Ni/CeO_2 sample is 13.4 nm, while a significant decrease is observed for $Ni@CeO_2$ and $Ni@CeZrO_2$ catalysts (4.4 and 4.1 nm, respectively) (Table 4.2). Wang et al. (2017)

synthesized a Cu@CeO_2 catalyst using the same method and they observed the same effect on ceria crystallite size during calcination.

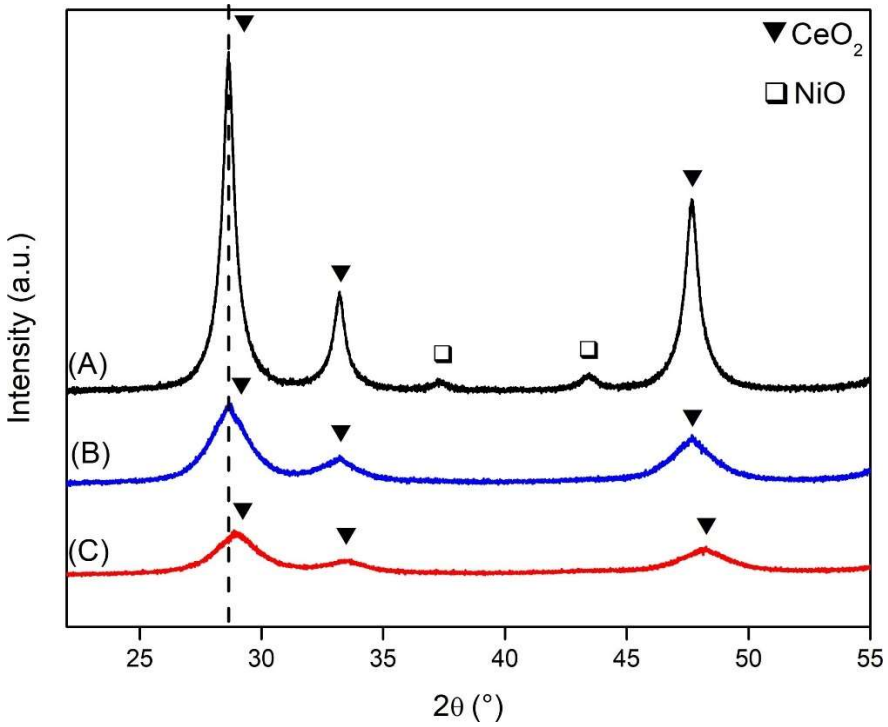

Figure 4.9. X-ray diffraction patterns of calcined samples: (A) Ni/CeO_2; (B) Ni@CeO_2; and (C) Ni@$CeZrO_2$.

Table 4.2. Lattice parameter of CeO_2 and CeO_2 and NiO crystallite size calculated by Scherrer equation.

Sample	**Lattice parameter of CeO_2 (Å)**	**Crystallite size (nm)**	
		CeO_2 *(111)*	**NiO (200)**
Ni/CeO_2	5.4261	13.4	11.9
Ni@CeO_2	5.4189	4.4	---
Ni@$CeZrO_2$	5.3615	4.1	---

X-ray diffraction patterns obtained during reduction under 5 % H_2/He mixture from room temperature to 800 °C for Ni/CeO_2, Ni@CeO_2 and Ni@$CeZrO_2$ samples are shown in Figs. 4.10-A, 4.11-A and 4.12-A. The evolution of the mean crystallite size of NiO, Ni^0 and CeO_2 during reduction procedure is presented in Figs. 4.10-B, 4.11-B and 4.12-B.

For Ni/CeO_2 catalyst (Fig. 4.10-A), the diffractograms show the decrease in the intensities of the lines corresponding to NiO at 2θ = 37.3° and 43.3° during reduction. Above 300 °C, the typical lines of NiO disappear and a new line is observed at 2θ = 44.5°, corresponding to metallic Ni phase (PDF 4-850). Further heating up to 800 °C and isothermal period of 1h at this temperature led to an increase in the intensities of the characteristic lines of Ni^0 and CeO_2. These results suggest a sintering of CeO_2 and Ni^0 crystallites during the reduction, as shown in Fig. 8b. The crystallite size of CeO_2 increased from 12 nm (580 °C) to 65 nm (800 °C for 1h), whereas the Ni^0 crystallite size grew from 5 nm (300 °C) to 33 nm (800 °C for 1h).

For Ni@CeO_2 and Ni@$CeZrO_2$ catalysts, only the typical lines of CeO_2 are observed below 500 °C. Above this temperature, the appearance of the lines corresponding to metallic Ni is noticed at 525 °C and 600 °C on the diffractograms of Ni@CeO_2 and Ni@$CeZrO_2$ catalysts, respectively. These results reveal that the reduction of nickel oxide is more difficult for the samples prepared by the sol-gel method, which is likely due to the strong interaction between nickel oxide and CeO_2. These results agree with the TEM images and *in-situ* XANES experiments, which showed that the embedded Ni particles in the ceria matrix are more hardly reduced than the segregated particles characteristic of the impregnated catalyst. The strong interaction between Ni and CeO_2 has been reported as an approach to improve the dispersion and avoid the metal sintering at high temperature (ZHENG et al., 2008). Kathiraser et al. (2017) studied the influence of Ce addition to Ni/SiO_2 catalysts for the oxidative reforming of biogas. They observed the increase in NiO reduction temperature with the presence of small amount of Ce (0.5 wt%) in the catalyst. This result was attributed to a higher interaction Ni-CeO_2 than Ni-SiO_2 as well as to a smaller NiO crystallite size as revealed by EXAFS. The TPR peaks of Ni@SiO_2 core-shell structure were shifted to higher temperatures in comparison to Ni/SiO_2 indicating that nickel oxide was hardly reduced in the core-shell structure (WANG; XU; SHI, 2016). This result was associated with a stronger metal-support interaction.

For Ni@CeO_2, the CeO_2 crystallite size increased during the reduction from 5 nm (325 °C) to 68 nm (800 °C for 1h), revealing a strong sintering at high temperature even for this sample prepared by the sol-gel method (Fig. 5.11-B). A significant growth of the Ni^0 crystallite size was also observed, increasing from 5 nm (630 °C) to 19 nm (800 °C for 1h). In the case of Ni@$CeZrO_2$ catalyst, the CeO_2 crystallite size only slightly varied from 5 to 8 nm after reduction at 800 °C for 1h. The same trend was observed for the Ni^0 crystallite size that increased from 5 to 10 nm at the end of the reduction (Fig. 4.12-B**)**.

The values of BET surface area of the samples before and after reduction (Table 4.1) showed that the addition of Zr into ceria structure significantly improved the thermal stability of the Ni@$CeZrO_2$ catalyst. The effect of type of dopant on the thermal stability and redox properties of ceria has been studied in the literature (DA SILVA et al., 2017; KAŠPAR; FORNASIERO; GRAZIANI, 1999, p. 2; SILVA et al., 2005). A higher thermal stability of $CeZrO_2$ in comparison to CeO_2 was attributed to the formation of a CeZr solid solution (HORI et al., 1998). The samples aged at 1000 °C under reduction condition showed CeO_2 crystallite size equal to 73 and 39, for Pt/CeO_2 and Pt/$Ce_{0.75}Zr_{0.25}O_2$, respectively. In our work, the higher thermal stability of the ceria structure is likely due to the formation of the $CeZrO_2$ solid solution as revealed by XRD.

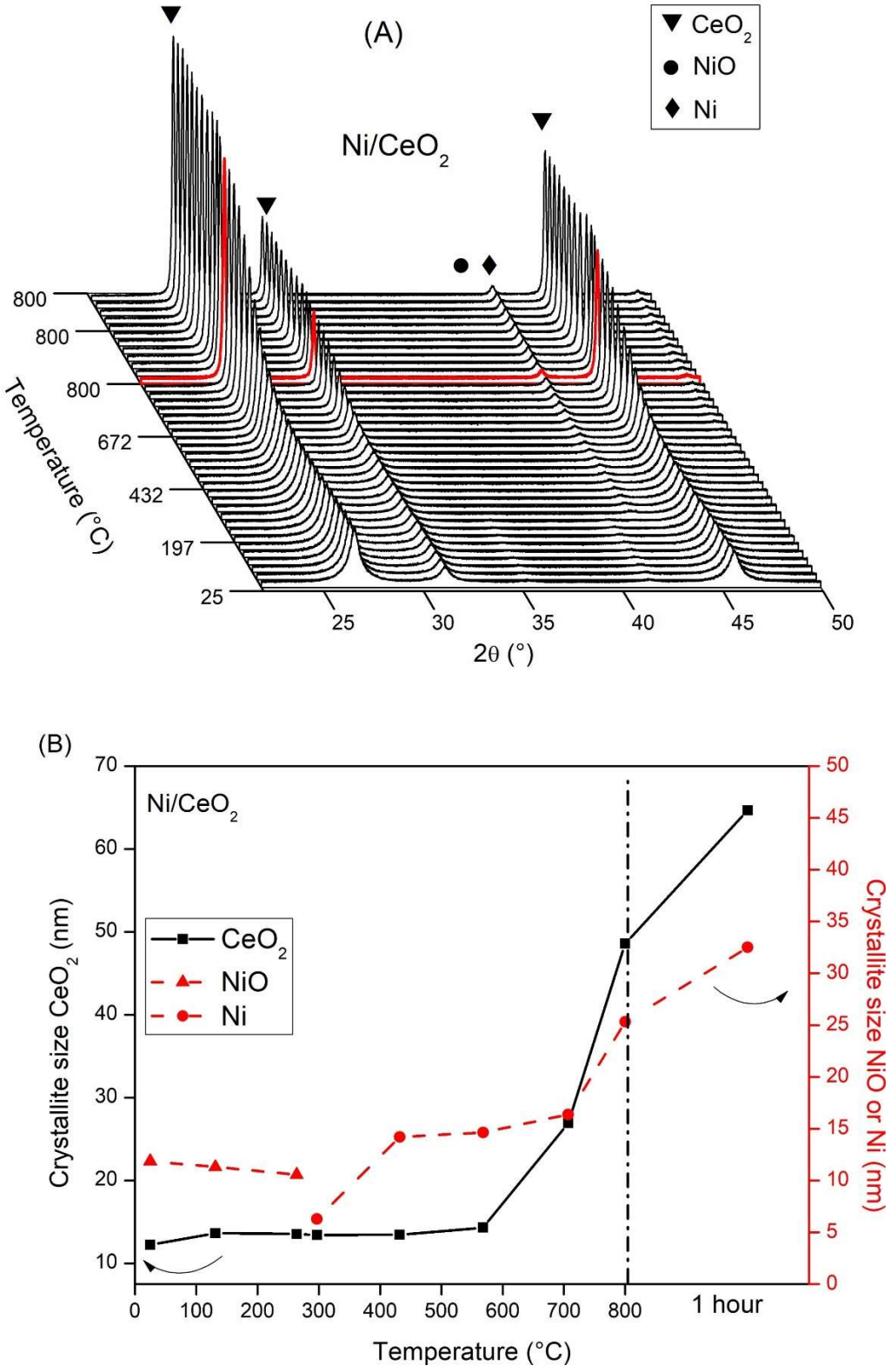

Figure 4.10. (A) X-ray diffraction patterns obtained during reduction from room temperature to 800 °C for Ni/CeO_2; (B) Crystallite size of NiO, Ni^0 and CeO_2 during the reduction process.

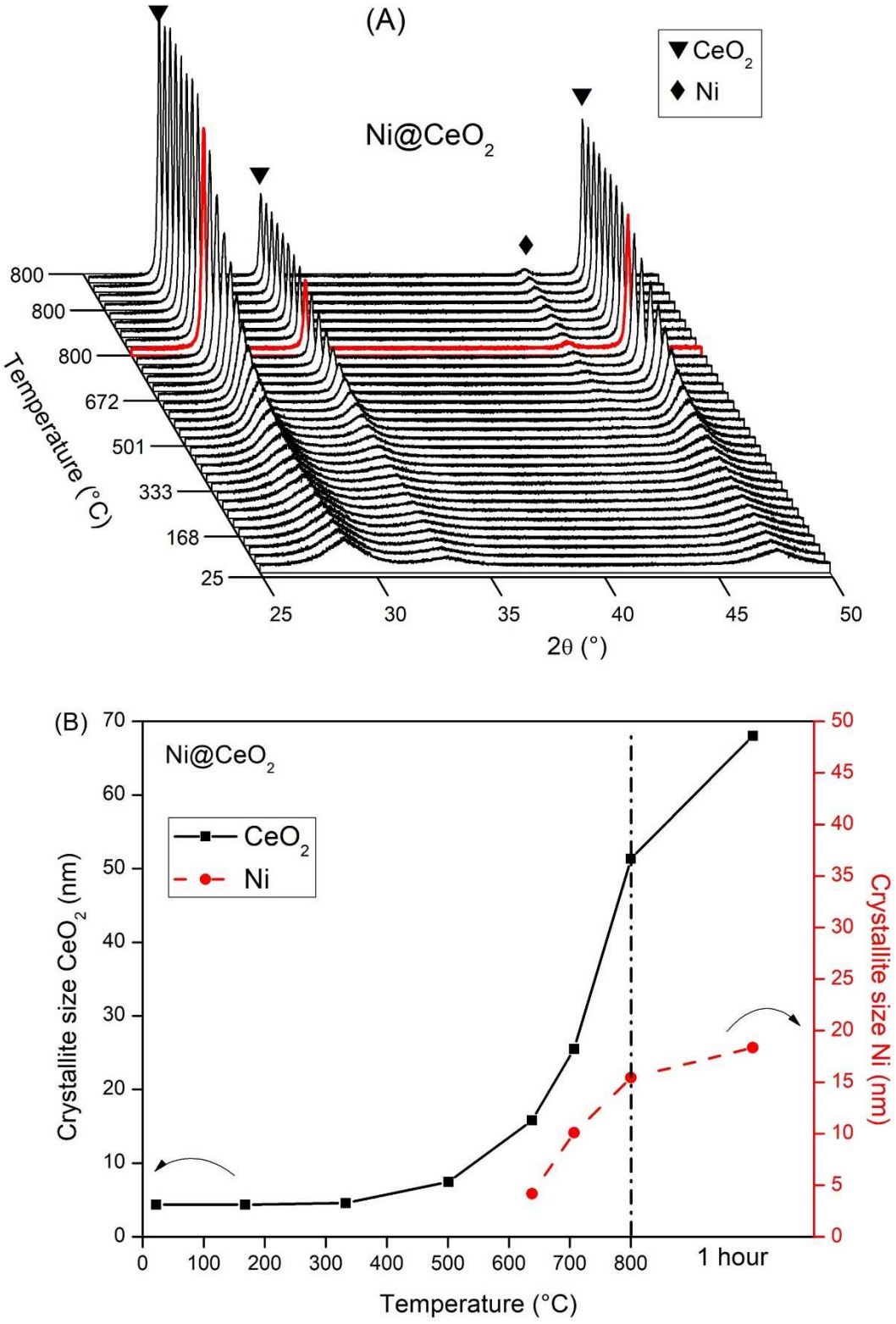

Figure 4.11. (A) X-ray diffraction patterns obtained during reduction from room temperature to 800 °C for Ni@CeO_2; (B) Crystallite size of Ni^0 and CeO_2 during the reduction process.

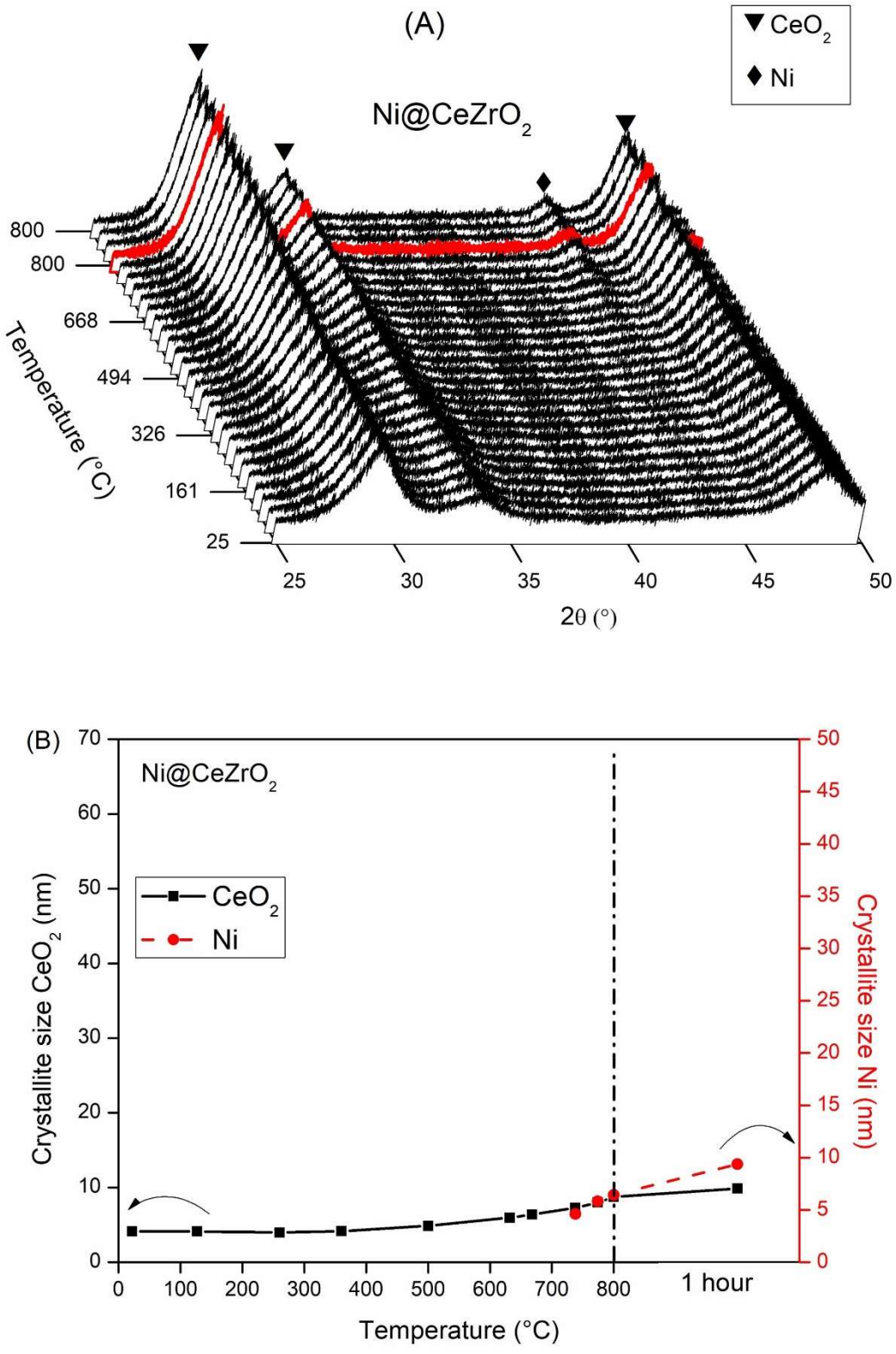

Figure 4.12. (A) X-ray diffraction patterns obtained during reduction from room temperature to 800 °C for Ni@$CeZrO_2$; (B) Crystallite size of Ni^0 and CeO_2 during the reduction process.

The increase in the reduction temperature led to a shift of the ceria lines to lower angles. The variation of CeO_2 lattice parameter during reduction of the samples is shown in Fig. 4.13 (solid line). Increasing the reduction temperature increased the lattice parameter. The increase in the lattice parameter could be due to the thermal expansion as well as the change in the oxidation state of ceria from Ce^{4+} to Ce^{3+}. In order to evaluate the effect of thermal expansion on the ceria lattice parameter during the reduction of all catalysts, an experiment was carried out with a physical mixture containing NiO and CeO_2 (Sigma-Aldrich) under air. The linear increase in the lattice parameter of NiO-CeO_2 up to 700 °C (see dotted line in Fig. 4.13) is attributed to the thermal expansion of the samples. However, the curves obtained for Ni/CeO_2, Ni@CeO_2 and Ni@$CeZrO_2$ catalysts deviates from this linear increase of the lattice parameter above 200 °C, indicating that the reduction of ceria began. Furthermore, a sharp increase in the lattice parameter was observed for Ni/CeO_2 and Ni@CeO_2 catalysts around 700 °C. The ceria reduction at low temperature region is generally attributed to the reduction of surface ceria, whereas the reduction at high temperature corresponds to the ceria bulk reduction (PERRICHON et al., 1994). The non-linear increase of the lattice parameter with the reduction temperature is likely due to the conversion of Ce^{4+} to Ce^{3+} (BARRIO et al., 2010). Ce^{3+} ions have a higher ionic radius (1.034 Å) as compared to the Ce^{4+} ions (0.97 Å). Then, the formation of Ce^{3+} ions in ceria structure causes a change in the Ce-O bond length, which produces a lattice expansion and create oxygen vacancies (PIUMETTI et al., 2016). The higher variation of lattice parameter for Ni@$CeZrO_2$ suggests the formation of a higher number of oxygen vacancies on this catalyst during reduction.

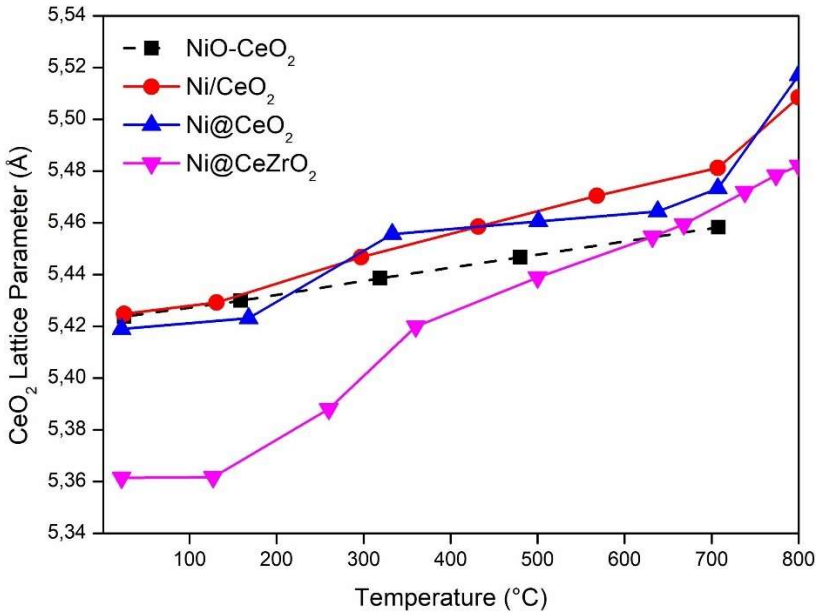

Figure 4.13. The variation of CeO_2 lattice parameter as a function of reduction temperature for all catalysts; (---) NiO-CeO_2 physical mixture, (___) Samples.

The TPOIE experiments (Fig. 4.14) were performed to investigate the oxygen exchange capacity of the support as a function of temperature. The CeO_2 support only starts to exchange oxygen at 380 °C, reaching the value of 39 x 10^{20} at.g^{-1}. The oxygen exchange begins at around 280 °C for Ni/CeO_2 catalyst and it occurs until Ne = 35 x 10^{20} at.g^{-1} at 500 °C. For the embedded Ni@CeO_2 catalyst, the exchange started at lower temperature compared to the impregnated one (250 °C). At 500 °C, the number of exchanged oxygen atoms is 39 x 10^{20} at.g^{-1}. In comparison to Ni/CeO_2 and Ni@CeO_2 catalysts, the oxygen exchange begin at higher temperature for Ni@$CeZrO_2$ (300 °C) and the number of O atoms exchanged at 500 °C was 42 x 10^{20} at.g^{-1}. Da Silva et al. (2017) have reported similar results for CeO_2 and CeNb supports. The catalysts showed similar isotopic distribution during the experiment (Fig. 4.15), indicating the occurrence of simple and multiple heteroexchange mechanisms (MADIER et al., 1999).

The presence of metal decreases the energy required to start the exchange process compared with the CeO_2 support, because the exchange will occur mainly through the metal particle (MARTIN; DUPREZ, 1996). The doping of CeO_2 by Zr increases the temperature in which the exchange start. This delay can be associated with a decrease in the surface oxygen concentration due to the lower specific surface area of $CeZrO_2$ compared to CeO_2. On the contrary there is a fast increase in the number of atoms exchanged for Ni@$CeZrO_2$. The structural defects caused by Zr doping on ceria

promote the oxygen mobility from bulk phase to surface, increasing the number of O atoms exchanged during the experiment. Therefore, the Ni@$CeZrO_2$ catalyst exhibited the highest number of oxygen exchanged compared with Ni/CeO_2 and Ni@CeO_2.

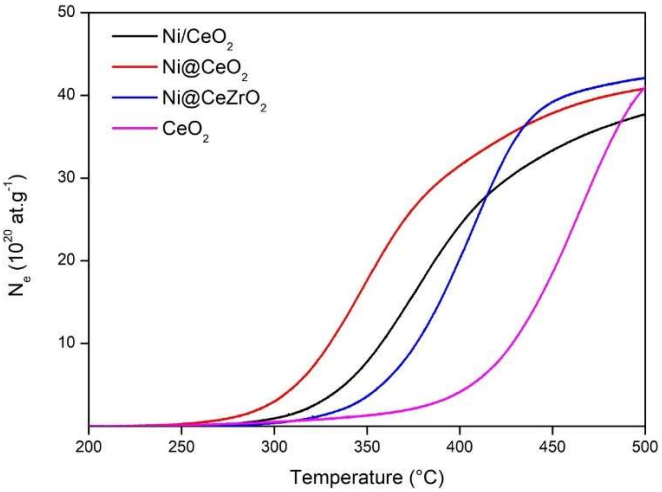

Figure 4.14. Evolution of the number of exchanged oxygen atoms during TPOIE over Ni/CeO_2, Ni@CeO_2, Ni@$CeZrO_2$ and CeO_2.

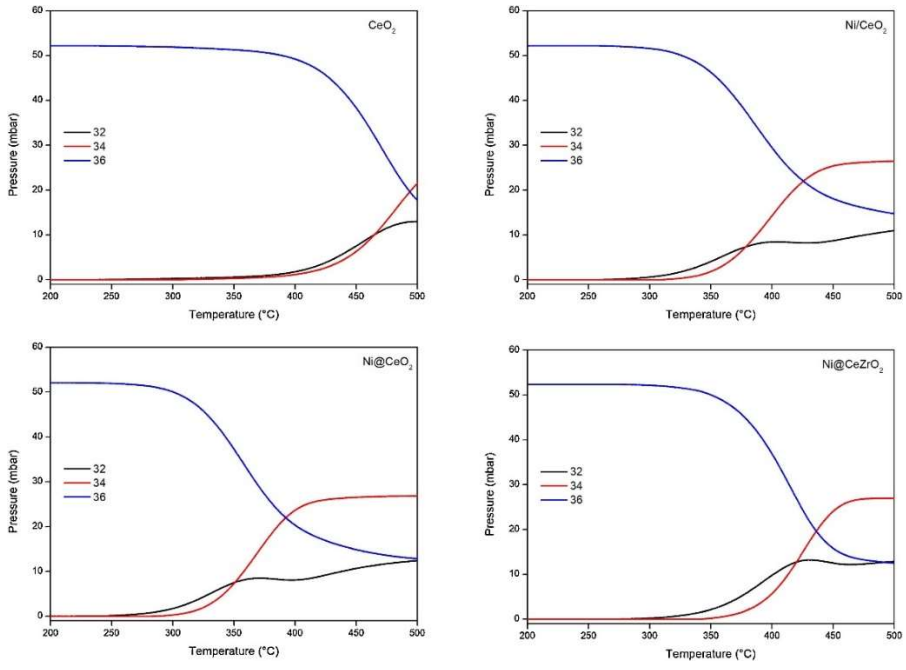

Figure 4.15. Isotopic distribution during the TPOIE for Ni/CeO_2, Ni@CeO_2, Ni@$CeZrO_2$ and CeO_2.

The experiments of isotopic oxygen exchange were carried out at 350, 400 and 450 °C. Figs. 4.16 and 4.17 illustrate the evolution of the number of exchanged atoms (N_e) and the isotopic distribution which occurs during the experiment at 400 °C. The experiments carried out at 350 and 450 °C are reported in the Appendix A. Table 4.3 reports the initial rate of exchange calculated from IOIE for the 3 temperatures. The exchange for CeO_2 is very low compared with the samples containing Ni, because the metal promotes the spillover of oxygen to ceria surface, as observed also in the TPOIE experiment. Comparing the Ni/CeO_2 and $Ni@CeO_2$ catalysts, the presence of Ni nanoparticles embedded on ceria structure does not affect significantly the number of O atoms exchanged at the gas/solid equilibrium, but it increases significantly the initial rate of exchange, showing the positive influence of the close contact between Ni nanoparticles and ceria support (Table 4.3). The lower initial exchange rate and the higher N_e after 20 min reaction that are observed for $Ni@CeZrO_2$ catalyst confirms the results obtained in TPOIE experiment: a lower surface exchange activity compared to ceria-based samples but a higher bulk diffusion.

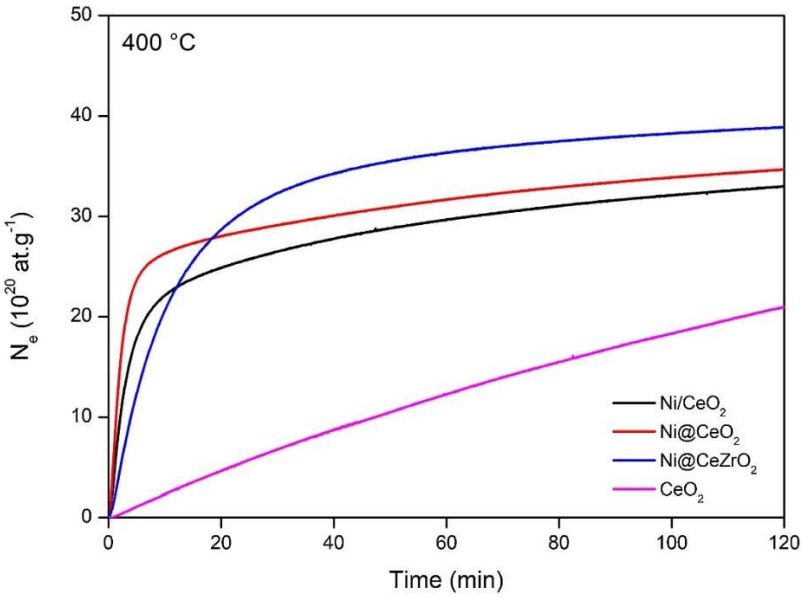

Figure 4.16. Evolution of the number of exchanged oxygen atoms during IOIE at 400 °C over CeO_2, Ni/CeO_2, $Ni@CeO_2$ and $Ni@CeZrO_2$.

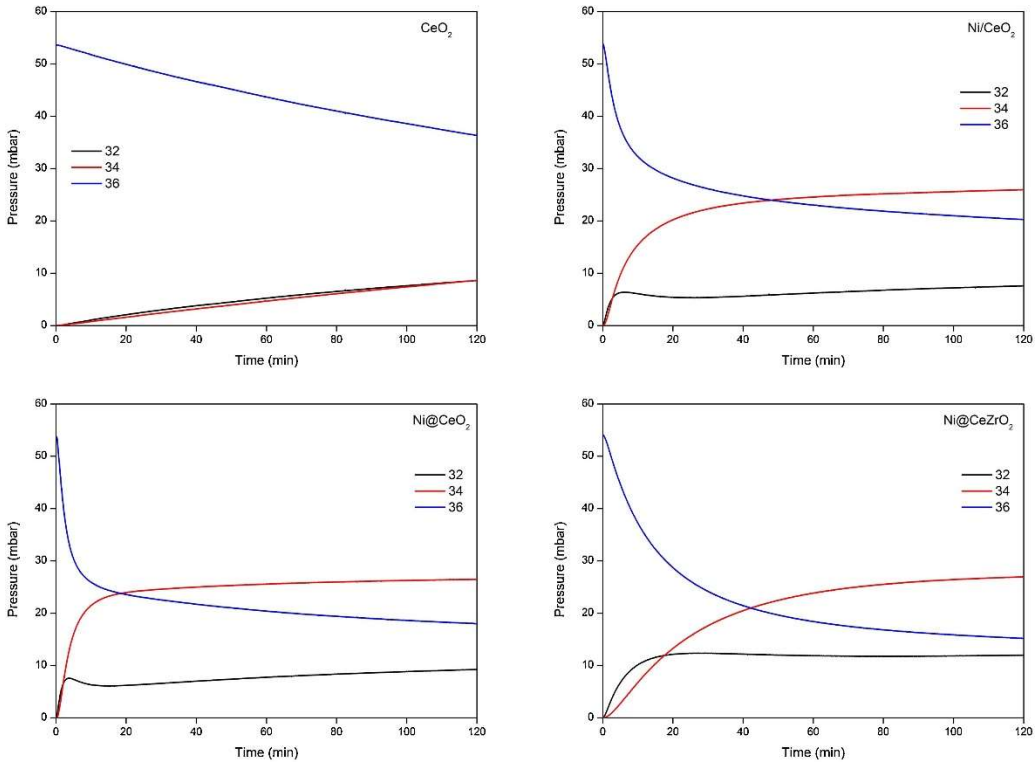

Figure 4.17. Isotopic distribution during the IOIE at 400 °C.

Table 4.3. Initial rate of exchange calculated from IOIE at 350, 400 and 450 °C.

Catalyst	Initial Rate of exchange (10^{17} at.g^{-1}.s^{-1})		
	350 °C	**400 °C**	**450 °C**
Ni/CeO₂	8.5	48.5	123.0
Ni@CeO₂	55.8	150.0	310.0
Ni@CeZrO₂	5.2	20.5	62.3

Indeed, the Ni@CeZrO$_2$ catalyst showed the highest number of N_e and the percentage of O atoms exchanged (Table 4.4). Furthermore, this catalyst exhibits a different behavior in the beginning of exchange at each temperature, with more formation of $^{32}O_2$ than $^{34}O_2$. On the opposite, Ni/CeO$_2$ and Ni@CeO$_2$ catalysts had a simultaneous formation of $^{32}O_2$ and $^{34}O_2$. Then, the Ni@CeZrO$_2$ catalyst favors the multiple exchange in comparison to the simple exchange at the beginning. Multiple heteroexchange occurs when two oxygen atoms are exchanged at the same time. Madier

et al. (1999) observed the same behavior for $Ce_{0.76}Zr_{0.32}O_2$ samples, which was attributed to a higher concentration of superoxides species (O_2^-) at the surface of the samples after oxidizing pre-treatment. Rossignol et al. (1999) also correlated the presence of these species to the higher oxygen storage capacity when the Zr^{4+} is inserted in the ceria structure.

Table 4.4. Number of O atoms exchanged during the isothermal oxygen isotopic exchange at 400 °C.

Catalyst	N_e (10^{20} at.g^{-1})	N_O (10^{20} at.g^{-1})*	O atoms exchanged (%)
CeO_2	21.1	70	30.1
Ni/CeO_2	33.1	71.3 (10.4)	46.4
Ni@CeO_2	34.7	71.3 (10.0)	48.7
Ni@$CeZrO_2$	39.0	71.3 (9.7)	54.7

* In parentheses is the total number of oxygens derived from the NiO species.

4.2.2 DRM reaction

The evolution of CH_4 an CO_2 conversions and H_2/CO molar ratio in function of time on stream (TOS) at 800 ºC are presented in Fig. 4.18. The initial CH_4 and CO_2 conversions were approximately the same for all catalysts and they remained quite constant during 24 h of TOS. The reaction produces H_2 and CO with a H_2/CO molar ratio around 0.8. The CO_2 conversion was higher than the CH_4 conversion due to the occurrence of RWGS, leading to the production of CO and H_2O and consequently, the H_2/CO ratio was lower than 1.0.

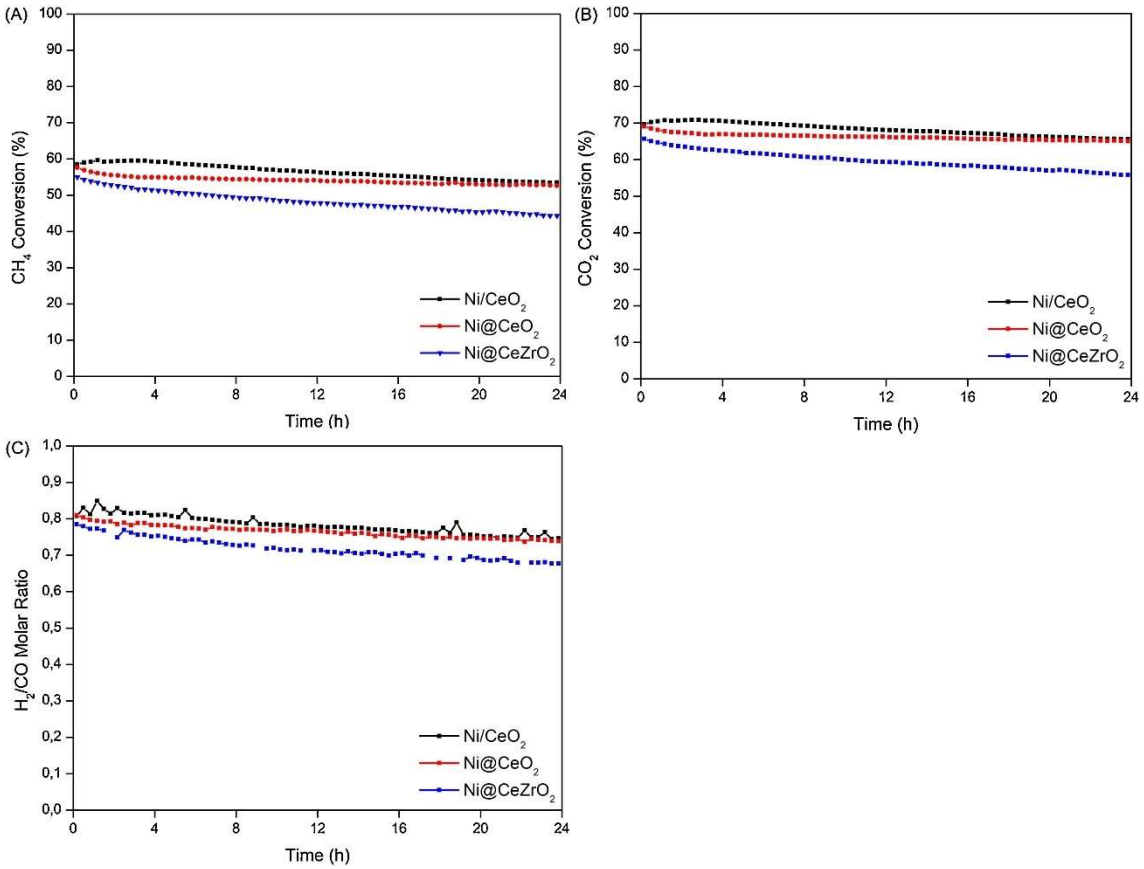

Figure 4.18. CH_4 and CO_2 conversion and H_2/CO molar ratio in function of TOS for DRM reaction at 800 °C and CH_4/CO_2 = 1.0.

4.2.3 Characterization of used catalysts after DRM reaction

The main challenge on the design of a catalyst for the DRM reaction is the deactivation caused by carbon deposition. In order to investigate the formation of carbon during DRM reaction, the spent catalysts were characterized by SEM, TEM, Raman and TGA analysis. SEM images of the catalysts after DRM at 800 °C for 24 h of TOS are displayed in Fig. 4.19. SEM image revealed the presence of carbon filaments on Ni/CeO_2 and $Ni@CeO_2$, mainly on the catalyst prepared by impregnation. On the other hand, carbon filaments were hardly detected on $Ni@CeZrO_2$ catalyst.

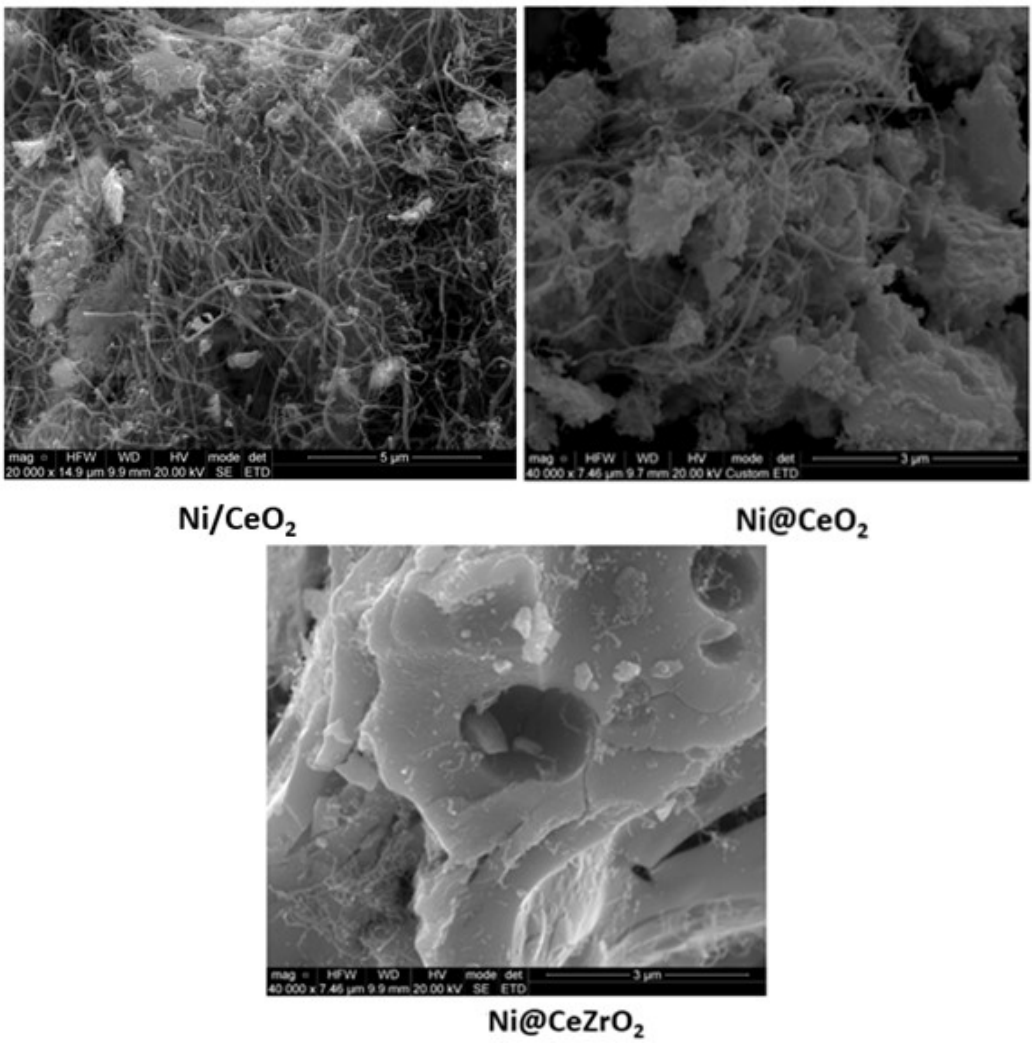

Figure 4.19. SEM images of spent catalysts after DRM at 800 °C for 24 h of TOS.

The TEM images of used catalysts shown in Fig. 4.20 can provide information about metal sintering as well as the formation of carbon filaments during the reaction. Ni/CeO_2 catalyst presented Ni nanoparticles without any interaction with CeO_2 matrix. Some Ni nanoparticles are located inside the carbon filaments, which avoid their sintering. There are also large nanoparticles outside the carbon nanotubes with particle size around 40 nm. For $Ni@CeO_2$ catalysts, TEM images reveal the presence of Ni nanoparticles into CeO_2 bulk but sintering is observed (Ni particle size around 20 nm). This higher interaction inhibits the detachment of Ni particles from CeO_2 and the growth of carbon filament. The TEM images of $Ni@CeZrO_2$ show Ni nanoparticles embedded into ceria matrix with very small particle size (around 8 nm) after 24 h of TOS. Furthermore, carbon filaments are not observed, which demonstrate that inhibiting Ni sintering suppress the formation of carbon filaments.

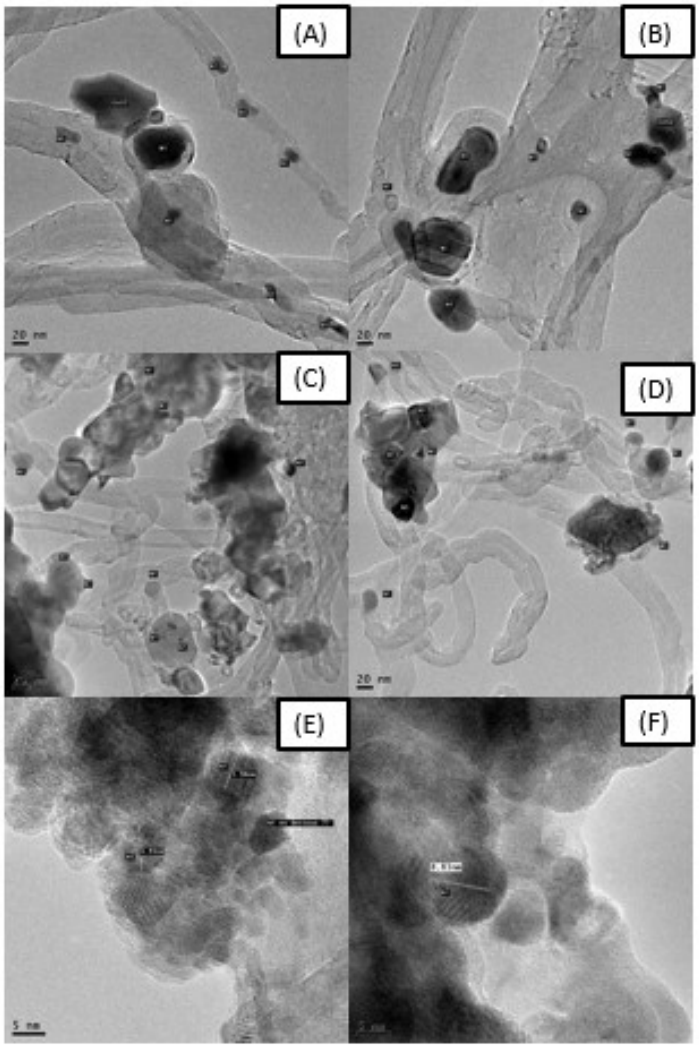

Figure 4.20. TEM images of spent catalysts after DRM at 800 °C for 24 h of TOS; (A) and (B) Ni/CeO_2; (C) and (D) $Ni@CeO_2$; (E) and (F) $Ni@CeZrO_2$.

The Raman spectra of used catalysts exhibit two bands in the range of 1200 to 1800 cm^{-1}, which are indicative of carbon formation (Fig. 4.21). The G-band at 1581 cm^{-1} is indicative of ordered carbon, whereas the band at 1350 cm^{-1} (D-band) has been related to disordered carbon structures (ALVAREZ et al., 2002). The D-band in the range of 1285-1300 cm^{-1} is ascribed to single-walled carbon nanotubes (SWCNT), while the position around 1330 cm^{-1} is related to multi-walled carbon nanotubes (MWCNT) or crystalline graphite-like forms (BELIN; EPRON, 2005; RABELO-NETO et al., 2018). The position of the D-band in 1350 cm^{-1} and the SEM images suggest the presence of MWCNT. Furthermore, the intensity of these bands was higher for Ni/CeO_2, indicating that the highest carbon deposition took place on this catalyst. These

bands are barely detected on the spectrum of Ni@$CeZrO_2$, which suggests the presence of very low amount of carbon deposits on this catalyst, in agreement with the SEM image.

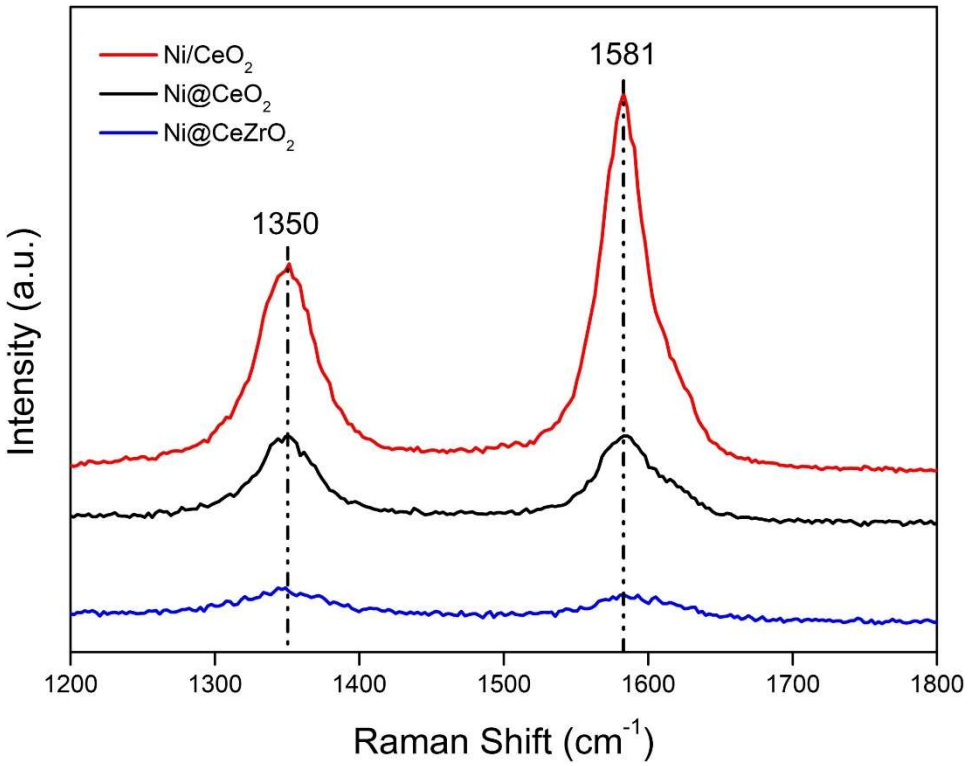

Figure 4.21. Raman spectra of post-reaction catalysts.

The derivative of weight during the TGA analysis is shown in Fig. 4.22. The DTG profile of Ni/CeO_2 sample exhibited an intense peak at 614 °C, whereas a broad peak at 518 °C is observed in the DTG profile of Ni@CeO_2 catalyst. No peak was detected on the DTG profile of Ni@$CeZrO_2$, indicating that carbon was not deposited on this catalyst. Table 4.5 reports the rate of carbon formation for each catalyst during DRM reaction at 800 °C. Ni/CeO_2 catalyst exhibited the highest amount of carbon deposits but the carbon formation rate was significantly reduced for the catalysts containing Ni nanoparticles embedded in ceria structure. Ni@$CeZrO_2$ catalyst did not show evidences of carbon formation after DRM reaction.

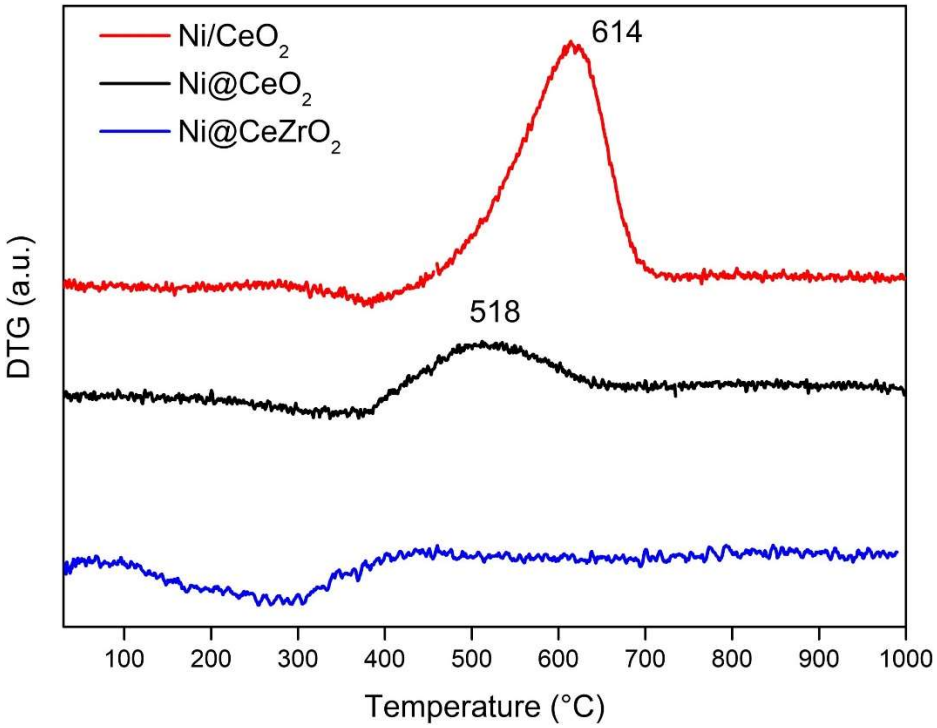

Figure 4.22. DTG of the post-reaction samples.

Table 4.5. Carbon formation rate during DRM reaction at 800 °C over Ni/CeO_2, $Ni@CeO_2$ and $Ni@CeZrO_2$ catalysts.

Catalyst	Carbon formation rate ($mgC.g_{cat}^{-1}.h^{-1}$)
Ni/CeO_2	9.7
$Ni@CeO_2$	1.6
$Ni@CeZrO_2$	0.0

4.2.4 The effect of Ni embedded in CeO_2 on catalyst deactivation for DRM

The mechanism of carbon formation over Ni-based catalysts during DRM has been extensively discussed in the literature (BRADFORD; VANNICE, 1999; FERREIRA-APARICIO et al., 2000; WEI; IGLESIA, 2004a) and involves the dissociation of methane on the surface of nickel particles, producing hydrogen and carbon (C_α). In the presence of a support with redox properties such as ceria and ceria-zirconia mixed oxides, this highly reactive carbon species (C_α) may reacts with oxygen from the support producing CO (MARINHO et al., 2016; NORONHA et al., 2001;

RABELO-NETO et al., 2018). The unbalance between the rate of methane decomposition and the reaction rate of carbon with oxygen from the support will lead to the accumulation of a less active carbon (C_β) that may also migrate into the nickel particle producing carbon filaments. Furthermore, the oxygen vacancies in the catalysts acts like active sites for CO_2 dissociative adsorption, which increase the amount of oxygen species on its surface. Therefore, the support plays an important role on the DRM reaction, keeping the metal surface free of carbon deposits. Yan et al. (2019) recently demonstrated the importance of reactive oxygen species in close contact with Ni nanoparticles to oxidize the C_α before its polymerization for Ni/CeO_2-SiO_2 catalysts. The conversion of C_α species to CO by the reactive oxygen species could enhance the catalytic properties and stability of the catalyst Ni/CeO_2-SiO_2. The same result was reported by (MARINHO et al., 2016) for the steam reforming of ethanol over $LaNiO_3/CeSiO_2$ precursor catalyst. The strong metal-support interaction favored the transfer of oxygen from the support to metal through the metal-support interface. Roh et al. (2008) successfully synthetized Ni catalyst supported on CeO_2-ZrO_2 solid solution. They could observe the enhancement on catalyst stability for $Ni/Ce_{0.8}Zr_{0.2}O_2$, which was due to the higher oxygen storage capacity and Ni dispersion.

Moreover, the rate of carbon formation is strongly affected by the Ni crystallite size (ROSTRUP-NIELSEN, 1972). The initiation step of carbon formation is more difficult over smaller particles. Then, carbon formation is minimized or inhibited on catalysts with small Ni particle sizes. Wang et al. (2016) showed that the confinement of Ni nanoparticles inside SiO_2 spheres on $Ni@SiO_2$ inhibited metal sintering during dry reforming of methane, minimizing carbon formation. Pu et al. (2018) evaluated the influence of Ce on $Ni@Al_2O_3$ core-shell catalysts to improve the coke resistance for steam reforming of acetic acid. The $Ni@Al_2O_3$ core-shell structure could avoid metal sintering (Ni crystallite size < 5 nm) but carbon formation was observed yet. However, the addition of Ce suppressed carbon deposition, which was attributed to the oxygen mobility of the material. The combination of small Ni size with oxygen mobility was fundamental to design a catalyst resistant to carbon formation.

In our work, the slight decrease in CH_4 and CO_2 conversions is likely due to the growth of Ni particle size as revealed by TEM. Furthermore, the inclusion of Ni nanoparticles into the $CeZrO_2$ structure for $Ni@CeZrO_2$ catalyst reduced metal sintering, as revealed by in situ XRD and TEM, due to the thermal stability of $CeZrO_2$ support during the reduction pre-treatment. In addition, this catalyst exhibited the

highest number of O atoms exchanged during the isothermal oxygen isotopic exchange at 400 °C as well as the highest amount of oxygen vacancies formed as shown by XRD and Raman spectroscopy. Therefore, the control of Ni particle size and the high oxygen mobility of Ni@$CeZrO_2$ catalyst inhibited carbon deposition and favored the mechanism of carbon removal, promoting catalyst stability.

4.3 Conclusions

The one step preparation of Ni@CeO_2 and Ni@$CeZrO_2$ catalysts led to Ni nanoparticles embedded in the oxide, which had a positive effect on the stabilization of the Ni particle size during the reduction at high temperature (800 °C). It also generates more oxygen vacancies and increases the interaction with $CeZrO_2$ and CeO_2 in comparison with an impregnated catalyst Ni/CeO_2. Furthermore, doping of ceria with Zr could maintain the ceria structure throughout the thermal treatment and increase the mobility of oxygen in the material, compared to ceria alone, favoring the carbon removal mechanism during the reaction. Thus, the protection of the metal particle against sintering as well as the oxidation of carbon species by the support for the catalyst Ni@$CeZrO_2$ resulted in the suppression of carbon deposition during the DRM in our work.

CHAPTER 5

Effect of dopant on $Ni@CeMO_2$ embedded catalysts (M= Gd, Sm and Zr) to produce syngas by dry reforming of biogas

5.1 Motivation

The addition of dopants promotes the oxygen mobility in ceria-based materials (DA SILVA et al., 2017; FU; CHEN; HUANG, 2010; LUISETTO et al., 2019; MOGENSEN; SAMMES; TOMPSETT, 2000; NAKAJIMA; YOSHIHARA; ISHIGAME, 1994). The most common dopant found in the literature is zirconium, where the substitution of Ce^{4+} by Zr^{4+} generates oxygen vacancies due to the distortion of ceria lattice (FARIA et al., 2014; KAMBOLIS et al., 2010; ZHANG et al., 2020). Zirconium also promotes thermal stability of ceria, avoiding the sintering at high temperature (HORI et al., 1998). The last chapter showed the positive effect to doping Ce with Zr (ratio Ce/Zr = 4), increasing the resistance against sintering and carbon formation at DRM conditions. However, there is a gap in the literature about the application of other metal dopants for the dry reforming of methane (DRM) reaction and the effect of Ce/Zr molar ratio. The doping of ceria with rare-earths elements with lower valency, like Gd^{3+} and Sm^{3+}, also induces the formation of oxygen vacancies by charge compensation (MOGENSEN; SAMMES; TOMPSETT, 2000). Moreover, the use of Gd and Sm-doped ceria materials have been discussed in the literature as promising material for fuel cell application, then their study under reforming conditions is interesting. Therefore, the aim of this chapter is to investigate different metal dopants (Gd^{3+} and Sm^{3+}) and Ce/Zr molar ratio and compare them with Zr-doped ceria as support for Ni embedded catalyst. Important structure properties were investigated by *in-situ* X-ray diffraction, temperature-programmed reduction and N_2 physisorption. The carbon formation was analyzed by thermogravimetric analysis and scanning electron microscopy. This chapter will focus firstly in the presentation of results and the discussion will occur in the last section of the chapter.

5.2 Results and discussion

5.2.1 Catalyst characterization

The chemical composition and BET surface area of the samples after reduction at 800 °C under pure H_2 are reported in Table 5.1. The Ni content and Ce/dopant molar ratio are close to the nominal value (i.e. 10 wt.% of Ni and Ce/dopant molar ratio = 0.25, 1.0, and 4.0). All catalysts exhibited very low surface area due to the low thermal stability of ceria at this high reduction temperature (MONTINI et al., 2016), as observed for the Ni@CeO_2 catalyst. The addition of Gd or Sm did not change the thermal stability of the material, with BET surface area lower than 10 m^2/g. Some works also did not report changes in the BET surface area after Ce-doping with Gd (DA SILVA et al., 2017; SATO et al., 2009). The addition of Zr slightly improved the thermal stability of the catalyst, regardless of Zr loading, decreasing the degree of loss of surface area at high temperature. Several works in the literature (HORI et al., 1998; MONTE; KAŠPAR, 2004; RODRIGUEZ et al., 2003; TERRIBILE et al., 1998) showed the positive effect of Zr to enhance CeO_2 thermal stability by the formation of $CeZrO_2$ solid solution.

Table 5.1. Chemical composition and BET surface area after reduction of the catalysts at 800 °C.

Catalyst	Ni (wt%)	CeO_2 (wt%)	Dopant (wt%)	Ce/Dopant molar ratio	BET surface area of reduced samples (m^2/g)
Ni@CeO_2	9.7	87.2	---	---	<10
Ni@$CeGdO_2$	9.8	72.1	15.1	4.2	<10
Ni@$CeSmO_2$	9.7	72.4	17.9	4.1	<10
Ni@$CeZrO_2$(4.0)	9.5	74.4	13.4	4.0	21
Ni@$CeZrO_2$ (1)	11.1	47.8	38.0	0.9	11
Ni@$CeZrO_2$ (0.25)	10.7	21.4	65.0	0.24	16

Fig. 5.1 shows the diffractograms of the fresh samples at room temperature. The XRD patterns were converted to CuKα for better understanding and the peak at 44.5° is ascribed to Khantal owned from the XRD equipment. The Ni@CeO_2 catalyst exhibited XRD pattern with the characteristic lines of CeO_2 with fluorite-like structure (JCPDS 34-0394) at 2θ = 28.6°, 33.1°, 47.5° and 56.4°. These lines are marked with the dashed lines for better understanding about the shifts observed with the addition of different dopants. The insertion of dopants shifts the main CeO_2 line to lower or higher 2θ value (Fig. 5.1 – B) (Ni@$CeGdO_2$ = 28.368°, Ni@$CeSmO_2$ = 28.333°, Ni@$CeZrO_2$ (4) = 28.788° and Ni@$CeZrO_2$ (1) = 29.298°), as a consequence of expansion or contraction of the ceria lattice, respectively. The ceria lattice for the calcined samples were: Ni@CeO_2 (5.4237 Å); Ni@$CeGdO_2$ (5.4460 Å); Ni@$CeSmO_2$ (5.4565 Å); Ni@$CeZrO_2$ (4.0) (5.3681 Å); Ni@$CeZrO_2$ (1.0) (5.2822 Å). The Ni@$CeZrO_2$ (0.25) catalyst presented very small $CeZrO_2$ crystallite size, resulting in a large peak centered at 31.6°. Because of that, the peak is not very well defined to determine the ceria lattice. The partial substitution of Ce^{4+} (0.97 Å) by atoms with larger atomic radii such as Gd^{3+} (1.16 Å) or Sm^{3+} (1.08 Å) causes an expansion in the ceria lattice (DEGUCHI et al., 2005; SINGH; ACHARYA; BHOGA, 2007). The Zr addition leads to a contraction of the ceria lattice since its atomic radii (0.84 Å) is smaller than that for Ce^{4+} (0.97 Å).

The decrease of Ce/Zr molar ratio from 4 to 1 further contracted the ceria lattice, indicating that more Zr is inserted into ceria structure. The excess of Zr (Ce/Zr = 0.25) results in the formation of very small $CeZrO_2$ crystallites with tetragonal structure (JCPDS 50-1089), as observed previously in the literature (TELES et al., 2019). In our work, the XRD of fresh samples reveal that Gd, Sm and Zr partially substituted Ce^{4+} into structure, leading to the formation of $CeGdO_2$, $CeSmO_2$ and $CeZrO_2$ solid solutions (DURGASRI; VINODKUMAR; REDDY, 2014; FARIA et al., 2014; KARACA; ALTINÇEKIÇ; FARUK ÖKSÜZÖMER, 2010).

The lines characteristic of NiO were not detect in the diffractograms of the calcined samples, indicating the presence of highly dispersed particles. The same result was observed for the Ni-based catalysts described in Chapter 4.

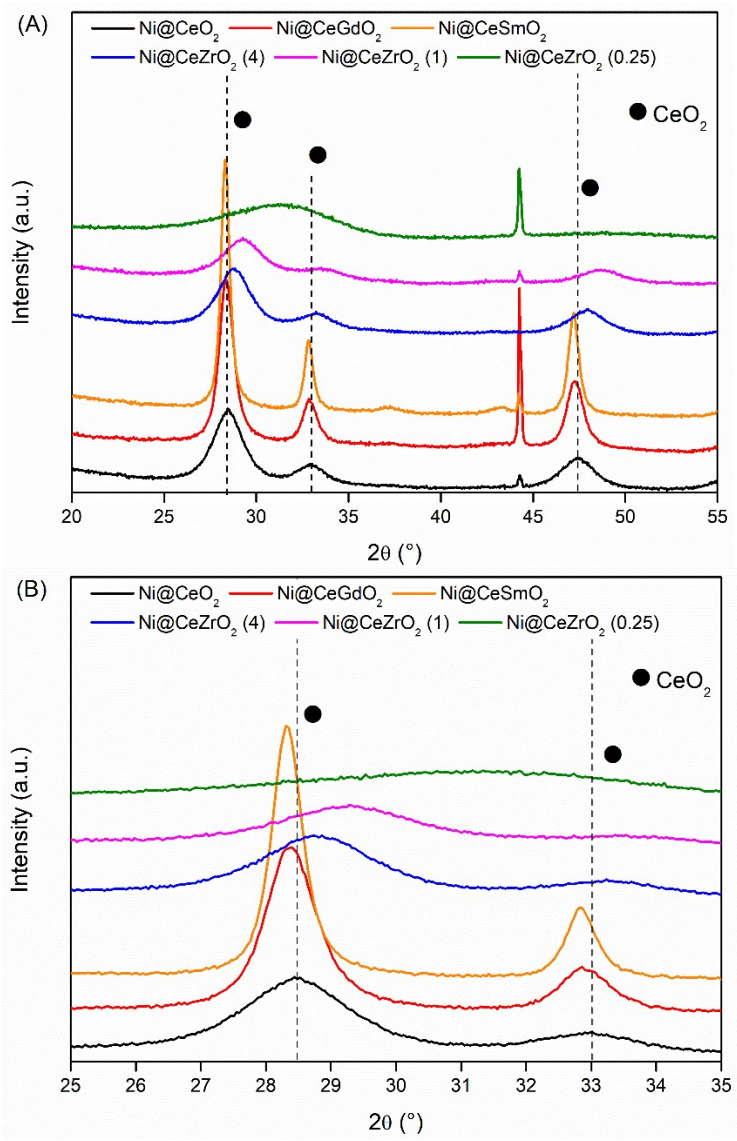

Figure 5.1. XRD patterns of fresh samples at room temperature: (A) 2θ = 20 - 55°; (B) 2θ = 25-35°.

In-situ XRD during reduction are presented in Figs. 5.2 and 5.3. For Ni@CeO_2, Ni@$CeGdO_2$ and Ni@$CeSmO_2$, the position of the ceria lines remained unchanged during reduction up to 500 °C. Further heating to 800 °C, diffraction lines slightly shifted to lower 2θ angles, indicating the expansion of ceria lattice. The shift of characteristic lines of ceria to lower 2θ angles during reduction of all samples is due to both phenomena: (i) thermal expansion of the unit cell; (ii) reduction of Ce^{4+} to Ce^{3+}, which has larger ionic radii (1.14 Å) (BONK et al., 2015). Therefore, the shift on the ceria lines observed during the reduction process is a result of the balance between these two effects.

On the other hand, for the Ni@$CeZrO_2$ (4) and Ni@$CeZrO_2$ (1) catalysts, a shift in the ceria lines is observed when the samples are reduced at 500 °C, and this

displacement increases when the samples are heated up to 800 °C. The formation of $CeZrO_2$ solid solution favors ceria reduction at lower temperature compared to Ce-doped with Gd or Sm. The Ni@$CeZrO_2$ (0.25) only presented crystalline phase at 800 °C ascribed to $CeZrO_2$ solid solution with tetragonal structure. Madier et al. (1999) also observed the formation of tetragonal ZrO_2 phase by XRD analysis of $CeZrO_2$ material calcined at 900 °C with Ce/Zr = 0.18.

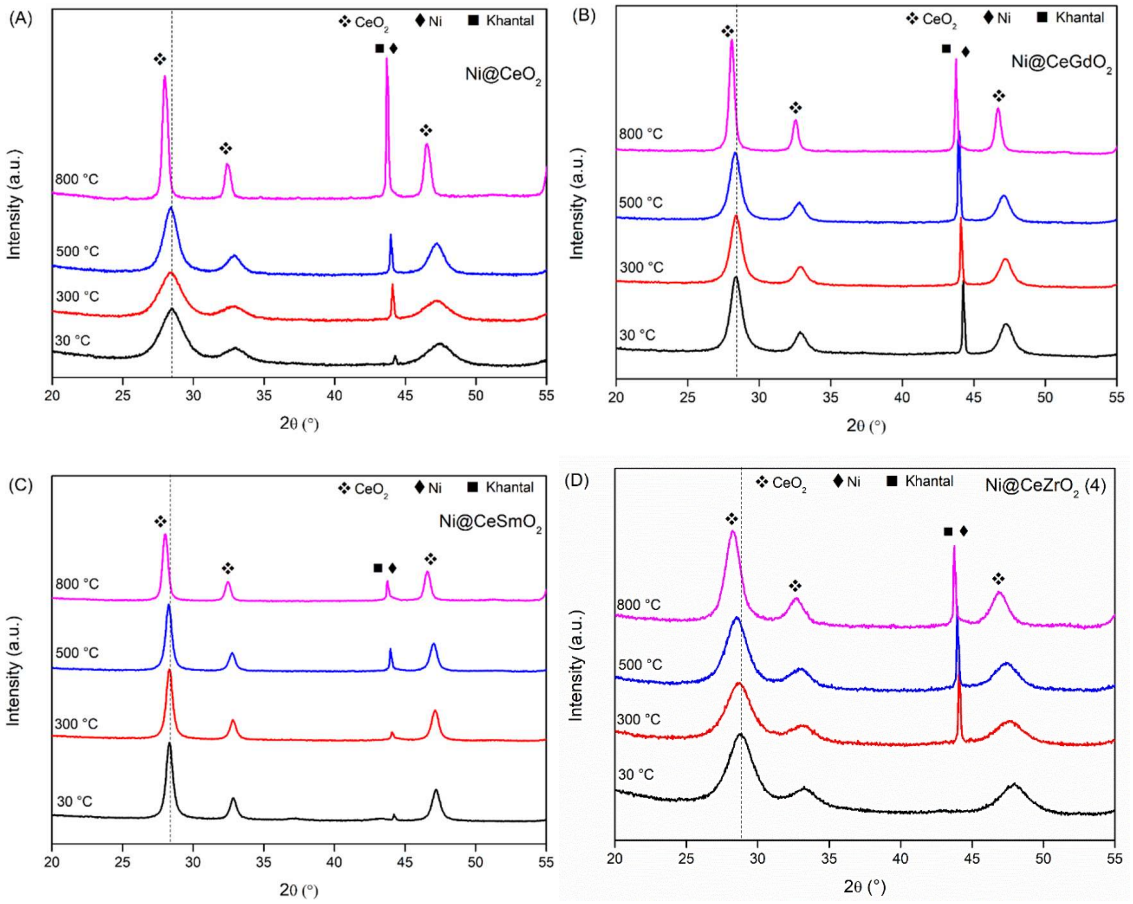

Figure 5.2. Effect of metal dopant by i*n-situ* XRD obtained during reduction process for the (A) Ni@CeO_2, (B) Ni@$CeGdO_2$, (C) Ni@$CeSmO_2$ and (D) Ni@$CeZrO_2$ (4) catalysts.

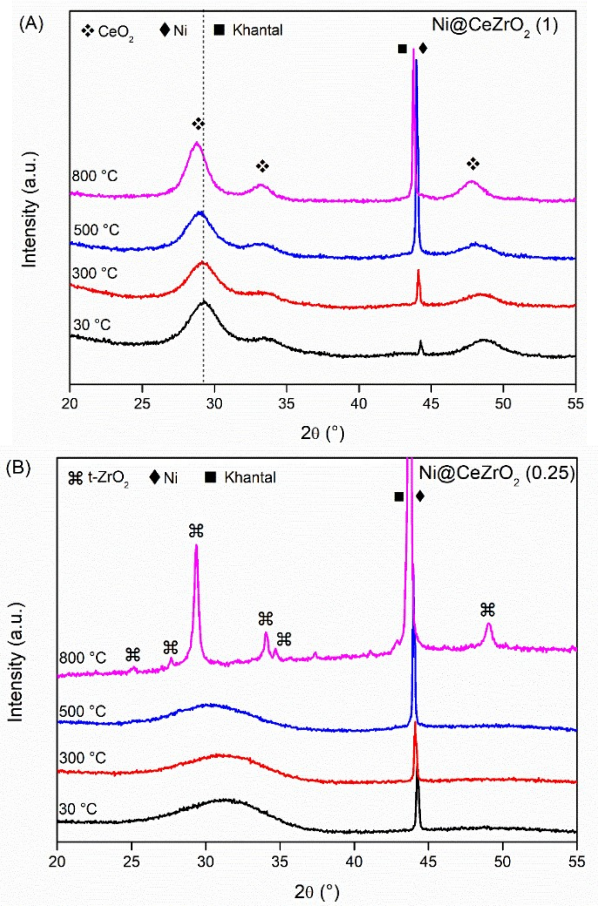

Figure 5.3. Effect of Ce/Zr molar ratio in the $CeZrO_2$ solid solution structure by *in-situ* XRD obtained during reduction process for the (A) Ni@$CeZrO_2$ (1), (B) Ni@$CeZrO_2$ (0.25) catalysts.

Previous *in-situ* XRD experiments during reduction of a NiO-CeO_2 physical mixture up to 800 °C revealed that the thermal expansion of CeO_2 only increased ceria lattice parameter of 0.04 Å and an expansion higher than that this value can be associated to the formation of Ce^{3+} by ceria reduction.

Increasing the temperature up to 800 °C, it is observed a slight increase in the ceria lattice parameter for Ni@CeO_2, Ni@$CeGdO_2$ and Ni@$CeSmO_2$ catalysts (Fig. 5.4-A). However, the increase is much more important when the $CeZrO_2$ solid solution was formed. The ceria lattice expansion follows the order: Ni@$CeGdO_2$ (0.0556 Å) < Ni@$CeSmO_2$ (0.0656 Å) < Ni@CeO_2 (0.0924 Å) ~ Ni@$CeZrO_2$ (1) (0.0976 Å) < Ni@$CeZrO_2$ (4) (0.1011 Å).

Therefore, the values of ceria lattice expansion higher than 0.04 Å indicate the formation of Ce^{3+} by ceria reduction for all catalysts, but at different degree as a function of the metal dopant.

The XRD data suggests that the doping with Gd and Sm inhibits ceria reduction since the shift observed for these catalysts is lower than that for Ni@CeO_2 catalyst. Furthermore, the undoped Ni@CeO_2 and Ce-doped with Gd and Sm did not prevent CeO_2 sintering (Fig. 5.3-B). The Ni@$CeSmO_2$ catalyst sintered during calcination, presenting the larger CeO_2 crystallite size among the fresh samples with slight increase during reduction. The Ni@CeO_2 and Ni@$CeGdO_2$ catalysts sintered at high temperature during reduction pretreatment. These results are in accordance with the results obtained by N_2 physisorption, where the CeO_2 sintering is responsible to the loss of surface area. On the other hand, the doping with Zr in the ratio 4 and 1 enhances ceria reduction, which is responsible to generate oxygen vacancies in the material during reduction process. Moreover, high thermal stability was observed for these catalysts, generating the catalysts with smallest CeO_2 crystallite sizes after reduction at 800 °C. Many authors (HORI et al., 1998; MATTOS et al., 2002; TELES et al., 2019) have showed the high resistance to CeO_2 sintering as a consequence of $CeZrO_2$ solid solution formation, what is not observed for Gd-doped ceria materials (DA SILVA et al., 2017).

The main characteristic line of metallic Ni is overlapped by Khantal line at 44.5° and the *(200)* plane of Ni^0 has low intensity and it is barely detected. Therefore, the Ni crystallite size was calculated by XRD after *ex-situ* reduction of the catalysts at 800 °C and passivation. The results are reported in Table 5.2. The Ni crystallite size was approximately the same for Ni@CeO_2, Ni@$CeGdO_2$, and Ni@$CeSmO_2$ (between 9.5 to 11.0 nm) while it was smaller for Zr-doped materials (between 2.0 to 5.4 nm). The high resistance to CeO_2 sintering observed for Ce-doped with Zr catalysts avoid Ni sintering, as it is observed for Ni@CeO_2, Ni@$CeGdO_2$ and Ni@$CeSmO_2$.

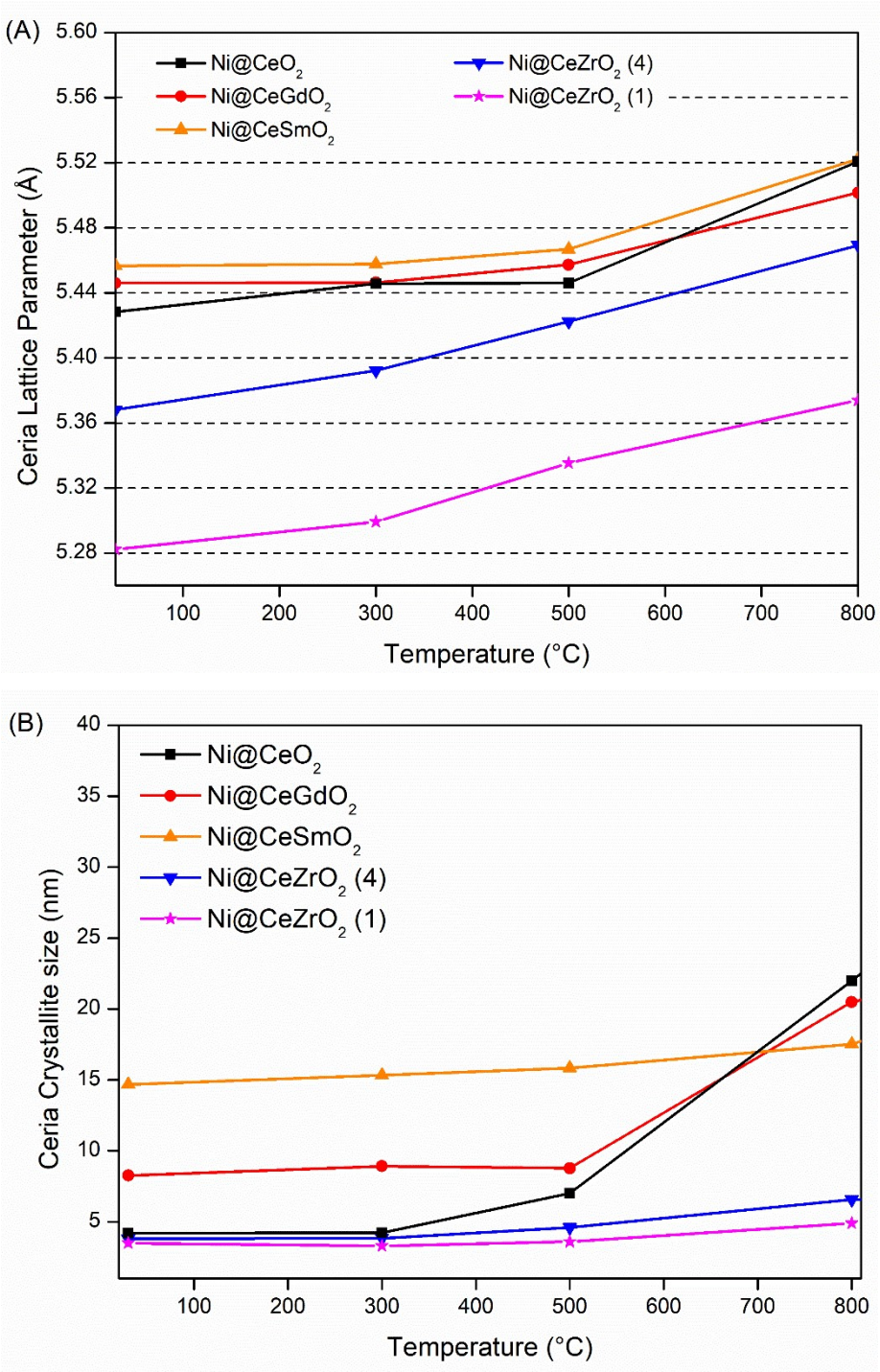

Figure 5.4. Variation of (A) ceria lattice parameter and (B) ceria crystallite size during reduction process.

Table 5.2. Ni crystallite size from the reduced and passivated samples.

Catalyst	Ni Crystallite size (nm)
Ni@CeO_2	10.7
Ni@$CeGdO_2$	11.0
Ni@$CeSmO_2$	9.5
Ni@$CeZrO_2$ (4)	5.4
Ni@$CeZrO_2$ (1)	3.0
Ni@$CeZrO_2$ (0.25)	2.0

TPR analysis were performed to study the reducibility of each catalyst and the profiles are shown in Fig. 5.5. For catalysts here studied, one can note that Ni@CeO_2 catalyst presented peaks at low temperature (below 600 °C) and another one centered at 880 °C. The Ni@$CeGdO_2$ and Ni@$CeSmO_2$ catalysts exhibited only one reduction region between 300-500 °C. The formation of $CeZrO_2$ solid solution changed the TPR profile, as observed previously in the *in-situ* XRD. The peak at 880 °C is no longer observed for the catalysts doped with Zr. This change in the TPR profile is in accordance with the shift of CeO_2 lines to lower temperature observed for the *in-situ* XRD.

According to the literature, CeO_2 oxide presents a first peak of reduction at 400 °C and another one above 800 °C ascribed to surface ceria and bulk ceria reduction, respectively (LAFAYE; BARBIER; DUPREZ, 2015; YAO, 1984). Bulk NiO oxide presents the reduction peak around 300 °C (LE et al., 2017; LI; CHEN, 1995). H_2 uptake shown in Table 5.3 indicates that all NiO is reduced to Ni metallic and 20 wt% of CeO_2 was reduced to Ce_2O_3. The Ni@$CeGdO_2$ catalyst exhibited the lowest ceria reduction degree (7 wt%), followed by Ni@$CeSmO_2$ catalyst (13wt%), indicating the poor oxygen mobility in these materials. *In-situ* XRD showed that these catalysts presented the lowest shift in CeO_2 lines, which suggested the low ceria reducibility, in accordance with this TPR result. The low ceria reducibility also was observed by Hennings and Reimert, (2007) based on TPR experiments. Da Silva et al. (2017) observed by oxygen isotopic exchange the poor oxygen mobility for Ni/$CeGdO_2$ catalyst compared to Ni/CeO_2. Therefore, the doping with Gd and Sm did not enhance the ceria reducibility in the material.

In terms of H_2 uptake, the presence of Zr strongly increased the Ce^{4+}/Ce^{3+} reduction degree from 20 % ($Ni@CeO_2$) to 35 % ($Ni@CeZrO_2$ (4)), with a slight increment a maximum on Ce/Zr = 1.0 (53 %), decreasing in Ce/Zr = 0.25 (39 %). The higher reducibility for Zr-doped catalysts is due to the formation of $CeZrO_2$ solid solution which has higher oxygen mobility (KAMBOLIS et al., 2010). The $CeZrO_2$ solid solution is described in the literature as a highly reducible material and it has been extensively used as catalyst support for DRM reaction (BEDRANE; DESCORME; DUPREZ, 2002; KUHN et al., 2013; YENTEKAKIS et al., 2019). Chen et al. (2008) studied the $Ni/Ce_{0.75}Zr5_{0.25}O_2$ catalyst for DRM reaction and they also observed high H_2 consumption for $CeZrO_2$ materials compared to pure CeO_2. The doping with Zr promoted the mobility of oxygen from bulk to surface, enhancing the ceria reducibility.

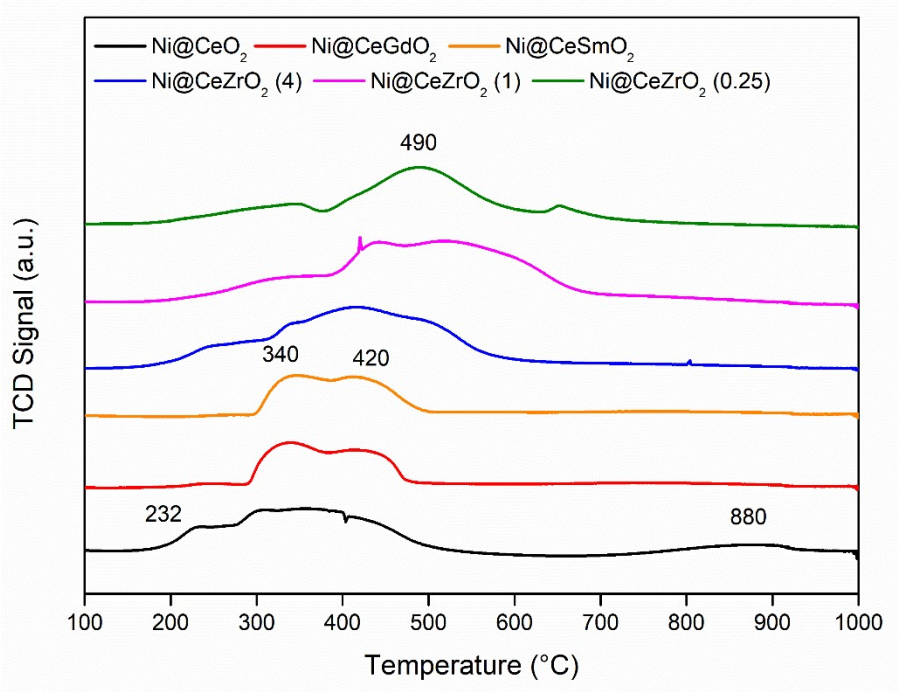

Figure 5.5. TPR profiles for the catalysts.

Table 5.3. H_2 uptake and CeO_2 reduction degree calculated by TPR.

Catalyst	H_2 uptake (µmol/g)		Theorical H_2 consumption for total reduction (µmol/g)		Ce^{4+}/Ce^{3+} Reduction (%)
	Low temperature	High temperature	Ni^{2+}/Ni^0	Ce^{4+}/Ce^{3+}	
Ni@CeO_2	2022.7	643.3	1652.7	5066.4	20
Ni@$CeGdO_2$	1963.0	-----	1669.7	4190.1	7
Ni@$CeSmO_2$	2199.7	-----	1652.7	4207.5	13
Ni@$CeZrO_2$ (4)	3131.4	-----	1618.5	4322.7	35
Ni@$CeZrO_2$ (1)	3410.3	-----	1891.2	2876.8	53
Ni@$CeZrO_2$ (0.25)	2264.4	-----	1823.0	1132.9	39

5.2.2 DRM reaction

Table 5.4 lists the initial Turnover Frequency (TOF) values of the catalysts at 600 °C calculated from catalytic test at low CH_4 conversion. The measured catalysts presented TOF values between 0.7 and 3.7, although the Ce-doped catalyst presented a slightly higher value, but the variation is too low to consider any difference in terms of activity. TOF values are in accordance with those observed by Wei and Iglesia (2004a) for Ni/MgO (4.0 s^{-1} – Ni crystallite size = 6.7 nm). The TOF parameter for Ni@$CeZrO_2$ (1.0) and Ni@$CeZrO_2$ (0.25) were not calculated due to the initial deactivation of the catalysts and, therefore, is not possible to obtain the exact number of active sites.

Table 5.4. TOF from the catalysts.

Catalyst	Catalyst Weight (mg)	CH_4 conversion (%)	TOF (s^{-1})
Ni@CeO_2	13.9	25	3.6
Ni@$CeGdO_2$	3.5	5	3.6
Ni@$CeSmO_2$	3.3	6	3.7
Ni@$CeZrO_2$(4)	6.3	15	2.7

The stability test was carried out to evaluate the resistance of the catalysts to form carbon deposits during the DRM. CH_4 and CO_2 conversions and H_2/CO molar ratio as a function of time on stream (TOS) are shown in Figs. 5.6 and 5.7, respectively. Ni@CeO_2, Ni@$CeGdO_2$, Ni@$CeSmO_2$ and Ni@$CeZrO_2$ (4.0) catalysts were stable for 24 hours of TOS. The decrease in Ce/Zr molar ratio was followed by a decrease in the initial CH_4 and CO_2 conversion, as observed before in the catalytic tests at low conversion. Because of that, it was necessary to increase W/F in order to obtain similar initial CH_4 and CO_2 conversion, which allows to compare the catalysts in terms of carbon formation. Ni@$CeZrO_2$ (1.0) catalyst slightly deactivated, while Ni@$CeZrO_2$ (0.25) catalyst exhibited a strong deactivation at the beginning of reaction. This drop in the conversion can be associated with the initial metal oxidation by the CO_2, as observed by other authors (FARIA et al., 2014; TAKANABE et al., 2005). The presence of available sites for CO_2 adsorption on the support disfavors its adsorption over metallic particle, preventing the oxidation of metal. After 4h on stream, the conversion of reactants increases followed by the increase in the amount of H_2 in the outlet gas, indicating that the H_2 produced in the beginning reduced again the Ni nanoparticles oxidized by CO_2.

The CO_2 conversion was higher than CH_4 conversion for all tests. Moreover, the H_2/CO molar ratio obtained was lower than 1.0. These results suggest the occurrence of RWGS reaction, which is thermodynamically favored at the reforming conditions. The same result was reported by other authors (AL-FATESH, 2017; DA FONSECA et al., 2019; FARIA et al., 2014). The Gd and Sm-doped catalysts presented higher initial H_2/CO molar ratio, followed by Ni@CeO_2 and Ni@$CeZrO_2$.

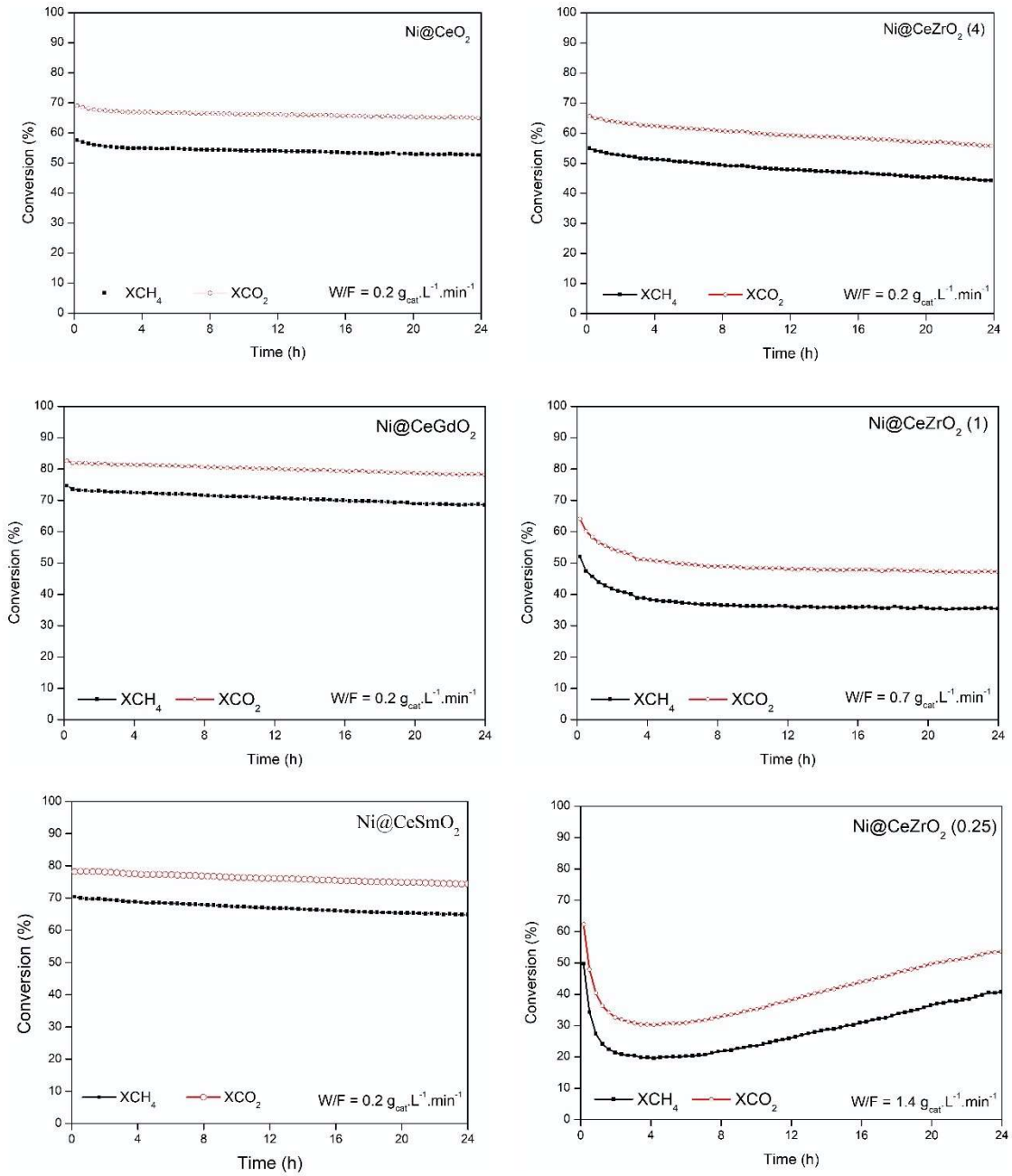

Figure 5.6. Conversion of CH_4 and CO_2 during DRM at 800 °C and CH_4/CO_2 molar ratio of 1.0.

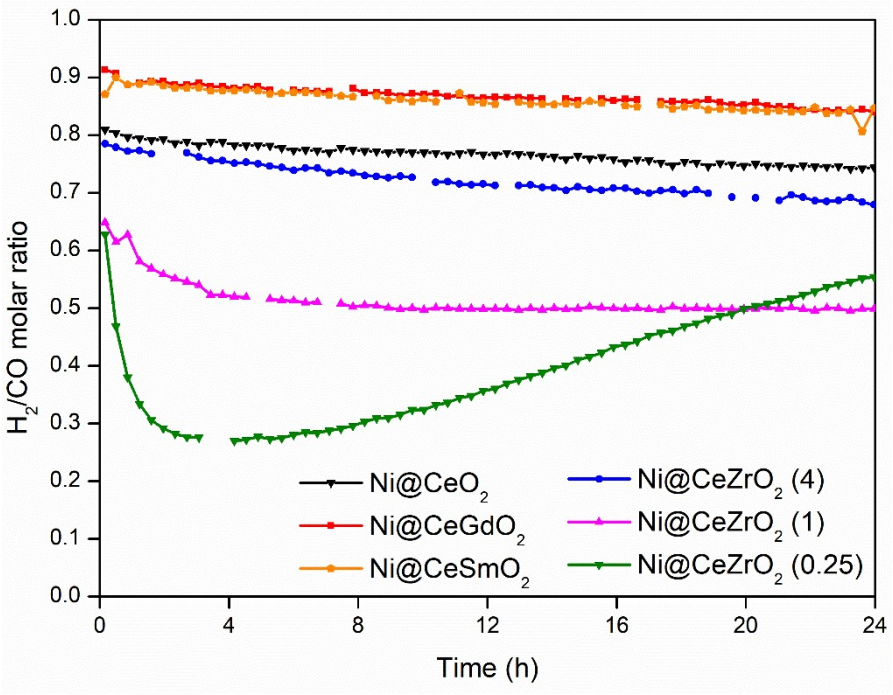

Figure 5.7. H_2/CO molar ratio obtained in the DRM at 800 °C and CH_4/CO_2 molar ratio of 1.0.

5.2.3 Carbon characterization

After the stability test, the post-reaction catalysts were analyzed by TGA and SEM to investigate the occurrence of carbon deposits. SEM images (Fig. 5.8) of Ni@CeO_2, Ni@$CeGdO_2$ and Ni@$CeSmO_2$ post-reactions samples show the presence of many carbon filaments. The presence of carbon filaments is barely observed on Ni@$CeZrO_2$ (4), Ni@$CeZrO_2$ (1) and Ni@$CeZrO_2$ (0.25) catalysts in the SEM images, suggesting that carbon formation was suppressed for these samples.

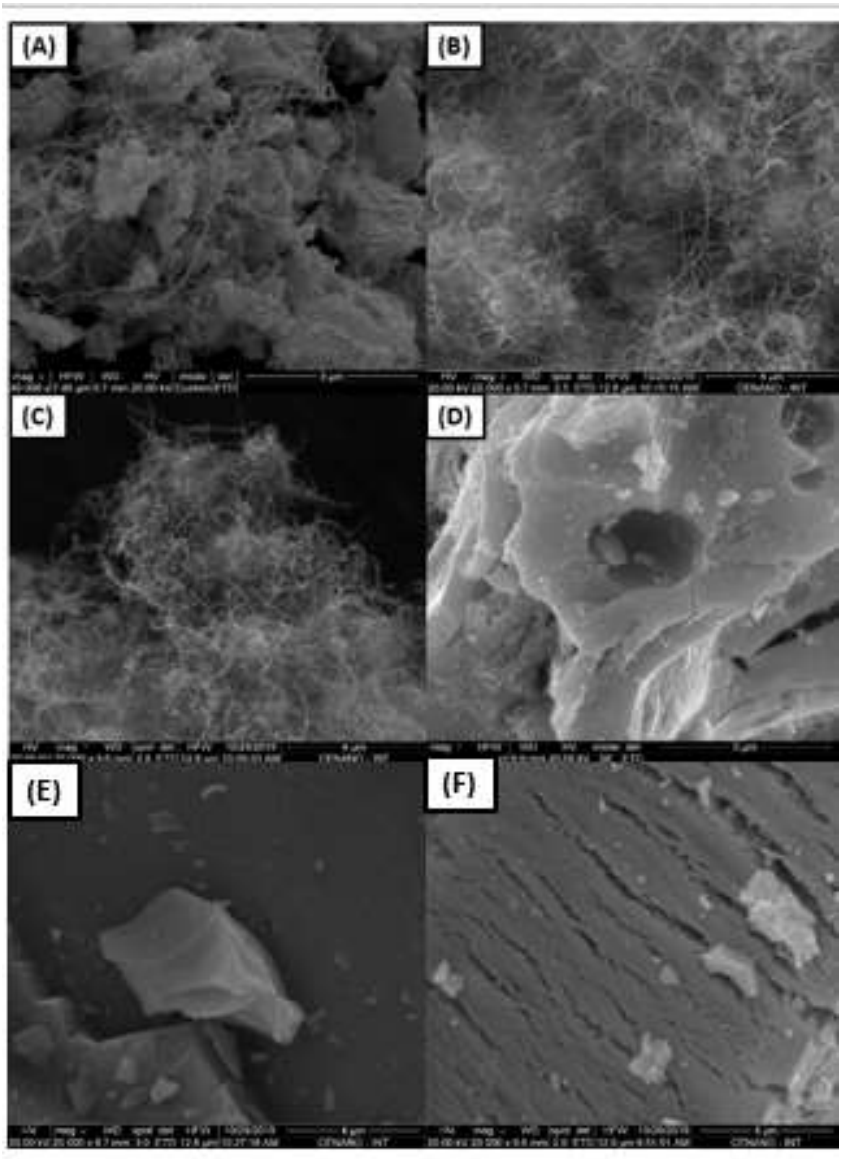

Figure 5.8. SEM images of post-reaction samples: (A) Ni@CeO_2, (B) Ni@$CeGdO_2$, (C) Ni@$CeSmO_2$, (D) Ni@$CeZrO_2$ (4), (E) Ni@$CeZrO_2$ (1) and (F) Ni@$CeZrO_2$ (0.25).

Fig. 5.9 displays DTG profiles of each post-reaction sample. The Ni@$CeGdO_2$ and Ni@$CeSmO_2$ exhibited a peak with high intensity at around 604 °C. Ni@CeO_2 showed a small peak at 503 °C and the Zr-doped catalysts did not present any peak in the profile. According to the literature (NATESAKHAWAT et al., 2005; SÁNCHEZ-SÁNCHEZ; NAVARRO; FIERRO, 2007), the peak around 503 °C is ascribed to amorphous carbon and the peak at 604 °C is due to carbon filaments with single or multiple walls. Then, the DTG peaks are in accordance with SEM suggesting high carbon formation following the order: Ni@$CeGdO_2$ > Ni@$CeSmO_2$ > Ni@CeO_2 > Ni@$CeZrO_2$ (4) ~ Ni@$CeZrO_2$ (1) ~ Ni@$CeZrO_2$ (0.25). Table 5.5 presents the rate of

carbon formation during the DRM for 24 h of TOS, with Ni@CeGdO$_2$ exhibiting the highest carbon formation and Zr-doped catalysts without carbon formation. High carbon formation also was reported in other works with Ce and Sm-doped materials for DRM reaction (BONURA; CANNILLA; FRUSTERI, 2012; HARSHINI et al., 2014).

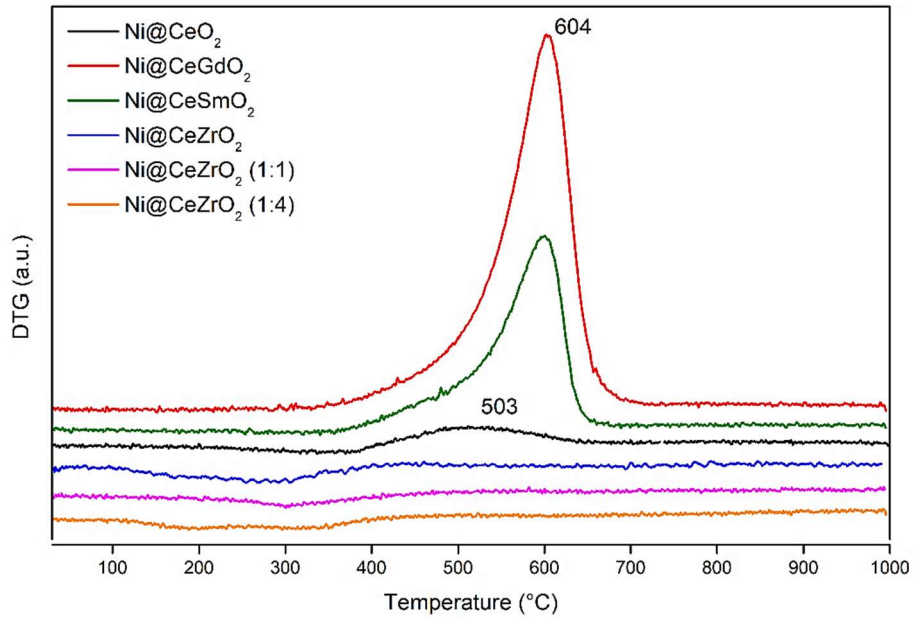

Figure 5.9. DTG profiles of the post-reaction samples.

Table 5.5. Rate of carbon formation obtained by TGA.

Catalyst	Rate of carbon formation (mgC.g_{cat}^{-1}.h^{-1})
Ni@CeO$_2$	1.6
Ni@CeGdO$_2$	21.9
Ni@CeSmO$_2$	9.8
Ni@CeZrO$_2$ (4)	0.0
Ni@CeZrO$_2$ (1)	0.0
Ni@CeZrO$_2$ (0.25)	0.0

5.2.4 Effect of dopant type in catalytic stability

The DRM reaction mechanism is well described in the literature over Ni-based catalysts (AVETISOV et al., 2010; JIANG et al., 2017; LUSTEMBERG et al., 2016; RABELO-NETO et al., 2018; WEI; IGLESIA, 2004a). The activation of CH_4 occurs over Ni metallic particles, generating reactive carbon species (C_α) and hydrogen. These carbon species can diffuse through the Ni particle towards the interface with the support. If the support does not present an appropriated oxygen mobility, the C_α species polymerizes, leading to the formation of less active carbon deposits (C_β), increasing its graphitization degree and growing in the form of filaments (ROSTRUP-NIELSEN; TRIMM, 1977). These filaments are no more reactive and can only be oxidize at high temperature and oxidative atmosphere. The solubility of carbon through Ni metallic particle is determined by its size; the larger the particle, the higher the driven force which promotes the diffusion. Therefore, the strategy of embedding Ni into support by steric effect is a promising alternative to design coke-resistant catalysts (LI et al., 2016; TIAN et al., 2015). Sarkar et al. (2012) successfully synthesized Ni@SiO_2 catalyst by microemulsion method and they also observed high resistance to sintering by the protection of SiO_2 shell caging Ni particles. Ni particles were formed with an average size of 5 nm.

The catalysts studied in this work, even showing some CeO_2 sintering at high temperature treatment, still maintain small Ni particles, below 10 nm, evidencing a protective effect of Ni embedded particles. The doping with Zr enhanced CeO_2 thermal stability, which contributed to inhibit the growth of the Ni crystallite size after reduction in comparison to the other doped-ceria catalysts. In spite of the importance of controlling the Ni particle to improve catalyst stability, several authors have reported the formation of carbon on Ni-based core-shell catalysts with high resistance to Ni sintering (BAKTASH et al., 2015; HAN et al., 2019; HUANG et al., 2017; ZHANG; LI, 2015; ZHANG et al., 2019). The presence of carbon species may be attributed to the absence of reducible support in their catalysts.

The support plays a key role on the CO_2 activation and carbon removal mechanism. The support with high oxygen mobility promotes the oxidation of C_α species before their polymerization, forming CO and maintaining the metal surface free from carbon/coke. The release of oxygen towards metal generates an oxygen vacancy, in which CO_2 is preferentially adsorbed dissociative as CO and O species. The CO_2 dissociation replenishes the oxygen vacancies of the support, as indicated by Eqs. 5.1

and 5.2 for CeO_2 support. Then, the support should have high oxygen mobility to promote the removal of carbon formed during DRM conditions.

$$2\ CeO_2 + C \rightarrow Ce_2O_3 + CO \quad (5.1)$$

$$Ce_2O_3 + CO_2 \rightarrow 2\ CeO_2 + CO \quad (5.2)$$

Laosiripojana and Assabumrungrat (2005) associated the high resistance to carbon formation observed for Ni supported on high surface CeO_2 with the higher OSC of this material, compared to Ni/Al_2O_3. For DRM reaction, the reaction rate between the lattice oxygen from ceria with carbon deposits is improved and the carbon removal mechanism occurs successfully.

The Ce-promoted $Ni@Al_2O_3$ catalyst was studied in order to improve the resistance to coke formation for the steam reforming of acetic acid (PU et al., 2018). The suppression of coke formation is due to the mobile oxygen from ceria, decreasing the amount of carbon from 8.03 % (Ni@Al) to 0.61 % (Ni@Al30Ce). Ceria has demonstrated good results in order to improve the resistance to carbon formation at reforming reactions, especially DRM reaction (KATHIRASER et al., 2017; KHAJENOORI; REZAEI; MESHKANI, 2015; MARINHO et al., 2016; NATESAKHAWAT et al., 2005).

An important parameter to enhance the CO_2 dissociation and supply oxygen to the support is the creation of oxygen vacancies. Oxygen vacancies (V''_O) can be introduced by the ceria reduction process (Eq. 5.3) or the addition of dopants into ceria lattice (Eqs. 5.4-5.6), as observed with Kröger-Vink notation. The ceria reduction is a reaction at thermodynamic equilibrium, and it is favored at high temperature and low P_{O2} (MOGENSEN; SAMMES; TOMPSETT, 2000).

$$O_O + 2\ Ce_{Ce} \rightleftharpoons \tfrac{1}{2}\ O_{2\,(g)} + V''_O + 2\ Ce'_{Ce} \quad (5.3)$$

$$Gd_2O_3 \rightleftharpoons 2\ Gd'_{Ce} + V''_O + 3\ O_O \quad (5.4)$$

$$Sm_2O_3 \rightleftharpoons 2\ Sm'_{Ce} + V''_O + 3\ O_O \quad (5.5)$$

$$ZrO_2 \rightleftharpoons Zr'_{Ce} + V''_O + 2\ O_o \quad (5.6)$$

The addition of Gd, Sm and Zr creates oxygen vacancies in the material, but their nature is different. Gd^{3+} and Sm^{3+} are trivalent cations and the partial substitution of Ce^{4+} by them creates oxygen vacancies by charge compensation (MOGENSEN;

SAMMES; TOMPSETT, 2000). The structure is not much affected because Gd^{3+}, Sm^{3+} and Ce^{4+} have similar ionic radius. Different behavior occurs when Zr^{4+} is inserted, for which the charge is the same, but the ionic radii is lower compared to Ce^{4+}. Therefore, the partial substitution of Ce^{4+} by Zr^{4+} creates oxygen vacancies due to the structural relaxation in the ceria structure (KUHN et al., 2013; VLAIC et al., 1997). Zr has a preference for 6-fold coordination, in contrast to the 8-fold coordination observed in the fluorite structure (KUHN et al., 2013). The change in the structure directly affects the redox properties of ceria. As observed in the *in-situ* XRD and TPR experiments, the addition of Zr increased the amount of reducible ceria. The contraction in the lattice creates a driven force of oxygen bulk species to surface (KUHN et al., 2013; RODRIGUEZ et al., 2003), increasing the number of oxygen species available to be released, where in the Kröger-Vink notation is represented by O_O. Therefore, the equilibrium shifts towards the formation of more oxygen vacancies in the material, promoting the carbon removal mechanism in the DRM reaction. Oxygen Isotopic Exchange measurements showed the highest oxygen mobility for $Ni@CeZrO_2$ (4.0) due to the migration of oxygen bulk species to the surface (Chapter 4).

According to the literature, doping ceria with Gd and Sm did not change structurally the catalyst, since they have similar ionic radii that Ce^{4+}, limiting the diffusion of oxygen species from bulk phase to surface , i.e. decreasing the value of O_O. Da Silva et al. (2017) showed that $Ni/CeGdO_2$ catalyst has a low oxygen mobility by performing Oxygen Isotopic Exchange. Similar conclusion was observed by Sadykov et al. (2010). The oxygen mobility is required to increase total OSC in the material, which means that in the absence of oxygen mobility, less oxygen vacancies are needed to achieve the thermodynamic equilibrium of ceria reduction. The equilibrium rapidly is reached, and no more oxygen vacancies will be generated by ceria reduction, as observed by the poor ceria reducibility during TPR analysis and by other authors (PÉREZ-COLL et al., 2007; SHE et al., 2009). In our work, the doping with Gd and Sm created oxygen vacancies in the fresh samples by charge compensation, reaching quickly the thermodynamic equilibrium for oxygen vacancy generation. Therefore, the formation of oxygen vacancies by ceria reduction is not favored, resulting at low ceria reducibility, as observed by TPR for $Ni@CeGdO_2$ and the same behavior is expected for $Ni@CeSmO_2$ catalyst. The doping with Gd and Sm worsens the redox cycle and carbon removal mechanism during DRM reactions, leading to a high carbon formation on $Ni@CeGdO_2$ and $Ni@CeSmO_2$.

The formation of $CeZrO_2$ solid solution shifted the reduction of ceria bulk to lower temperature, as observed by TPR. Moreover, the increase of ceria reducibility creates high amount of oxygen vacancies during DRM reactions. Faria et al. (2014) studied the effect of Ce/Zr molar ratio on the performance of $Ni/CeZrO_2/Al_2O_3$ catalysts for the DRM reactions. The authors also observed a low activity of Ni/Al_2O_3 catalyst at the beginning of reaction, which was associated to Ni oxidation due to the absence of oxygen vacancies for CO_2 adsorption. Rabelo-Neto et al. (2018) also associated the initial deactivation observed for DRM reaction due to the low basicity of the support, which favored Ni oxidation by CO_2 as demonstrated by XPS. Wolfbeisser et al. (2016) also studied the $Ni/Ce_xZr_{1-x}O_2$ system in order to avoid carbon formation during DRM reaction. The stability against carbon filaments improved, decreasing the amount of carbon detected on the post-reaction samples. The authors associated this higher resistance to the ability of the support to release oxygen to the metal, promoting the carbon removal mechanism.

According to the literature, the CO_2 adsorption occurs over ceria basic sites, increasing the amount of oxygen species in the interface metal-support. In our work, the decrease on Ce/Zr molar ratio did not change the carbon resistance but the activity was strongly affected. Considering that the activity is correlated only to metal particle, it seems that decreasing the Ce loading and consequently the number of CO_2 adsorption sites on the support favored the process of Ni oxidation by CO_2, which led to the low initial conversion for $Ni@CeZrO_2$ (0.25). Finally, the results in this work show the importance of the oxygen mobility to promote the carbon removal mechanism over $Ni@Ce_xZr_{1-x}O_2$ catalysts applied in the hydrocarbon reforming reactions.

5.3 Conclusions

The sol-gel method employed to synthesize $Ni@CeO_2$, $Ni@CeGdO_2$, $Ni@CeSmO_2$, $Ni@CeZrO_2$ (4.0), $Ni@CeZrO_2$ (1.0) and $Ni@CeZrO_2$ (0.25) catalysts led to the formation of Ni nanoparticles embedded into ceria-doped oxide. The thermal stability of Zr avoided Ni metal sintering at high temperature (800 °C). The addition of dopants created oxygen vacancies in the material, however the ceria reducibility was different in the presence of each dopant. The lattice distortions caused by Zr insertion into ceria lattice enhanced the bulk oxygen diffusion towards surface, increasing ceria reducibility. The doping with Gd and Sm only created oxygen vacancies by charge

compensation, saturating the surface with oxygen vacancies and decreasing ceria reducibility in comparison to pure ceria and Zr-doped ceria. As consequence, high carbon formation was detected for Sm and Gd-doped catalysts. Ce/Zr molar ratio affected directly the catalyst activity due to the presence of less CO_2 adsorption sites over $CeZrO_2$ support, which favored initial Ni oxidation. Therefore, the combination of (i) small Ni crystallite size, (ii) high ceria reducibility and (iii) high CO_2 adsorption sites promoted the equilibrium between CH_4 decomposition and carbon gasification, resulting in the suppression of carbon deposits under DRM reaction and high activity for Ni@$CeZrO_2$ (4) catalyst.

CHAPTER 6

Highly active and stable Ni dispersed on mesoporous CeO_2-Al_2O_3 catalysts for production of syngas by dry reforming of methane

Published by Elsevier

Applied Catalysis B: Environmental 281 (2021) 119459

6.1 Motivation

Mesoporous materials with high surface area and well-defined pores have shown interesting results to disperse the metal into the structure. The use of a one-step method to synthetize Ni-based catalysts allows the homogeneous dispersion of Ni with strong metal-support interaction. Evaporation Induced Self-Assembly (EISA) method has been employed by some authors (GROSSO et al., 2004; KUEMMEL et al., 2005; MA et al., 2019; XU et al., 2014) to generate very well ordered mesoporous material. The oxygen vacancies in the material promote the dissociation of CO_2 into CO and O atoms on the surface (FARIA et al., 2014). The balance between the rate of carbon gasification and the rate of methane decomposition determines the stability of the catalyst (STAGG-WILLIAMS et al., 2000). CeO_2 presents high oxygen capacity (OSC), which is related to the Ce^{4+}/Ce^{3+} redox couple associated to the generation of oxygen vacancies.

The aim of this study is the preparation of Ni supported on mesoporous CeO_2-Al_2O_3 catalysts by one pot EISA method with high surface area and high Ni dispersion and accessibility for the production of syngas through DRM at high temperature. Two specific parameters have been deeply investigated: the influence of the confinement effect of the one step EISA method compared with the post-impregnation of the Ni; the role of the Ce introduction in the mixed oxide on the carbon gasification properties. N_2 physisorption was performed to study the surface area and porosity. The structure was analyzed by Transmission Electronic Microscopy (TEM) and X-ray diffraction (XRD). In-situ X-ray diffraction (XRD) and Temperature-Programmed Reduction (TPR) were used to follow the reducibility of $NiAl_2O_4$. The carbon formed was analyzed by Thermogravimetric analysis (TGA) and TEM. A brief study was finally carried out by *in-situ* DRIFTS to investigate the mechanism of carbon removal.

6.2 Results and Discussion

6.2.1 Catalyst characterization

Table 6.1 reports the chemical composition and textural properties of each sample. The Ni and Ce contents are close to the nominal values. Fig. 6.1-A shows the nitrogen adsorption-desorption curves of the samples after calcination. The isotherms are type IV according to the IUPAC classification, characteristic of a mesoporous material, with H1-type hysteresis corresponding to cylindrical pores. Some information on the organization of these pores is given in Fig. 6.1-B, with narrow distribution of

pores for all catalysts. The smallest pore size is obtained for 10Ni-Al sample (distribution between 4 and 6 nm) while the highest pore size and distribution are observed for 10Ni-CeAl (between 4 and 10 nm). The comparison between 10Ni-Al and 10Ni/CeAl catalysts show that the addition of Ce in the catalyst leads to higher pore size and wider pore distribution. On the contrary, despite of the narrow pore distribution of 10Ni/CeAl, its surface area and pore volume decreased in comparison to CeAl. These result show that the incipient-wetness impregnation of Ni probably causes the blockage of some pores.

The structure of the various samples was characterized by performing XRD and TEM analyses. The XRD at low angle (Appendix B) does not show any peak characteristic from hexagonal mesoporosity while N_2 physisorption isotherms suggested a rather narrow pore size distribution. Therefore, it seems that the porosity of the material is not well organized, as it can be confirmed by TEM of the calcined 10Ni-CeAl sample (Fig. 6.2).

Table 6.1. Chemical composition and textural properties of the catalysts.

Sample	Ni wt%	CeO_2 wt%	Ce/(Ce+Al)	S_{BET} ($m^2.g^{-1}$)	Pore Volume ($cm^3.g^{-1}$)	Mean Pore Diameter (nm)
CeAl	---	21.7	0.10	196	0.47	7.1
5Ni-CeAl	5.1	21.9	0.11	221	0.44	5.8
10Ni-CeAl	9.4	17.5	0.09	208	0.50	7.3
10Ni/CeAl	12.6	18.3	0.10	144	0.35	7.1
10Ni-Al	9.2	---	---	232	0.42	5.2

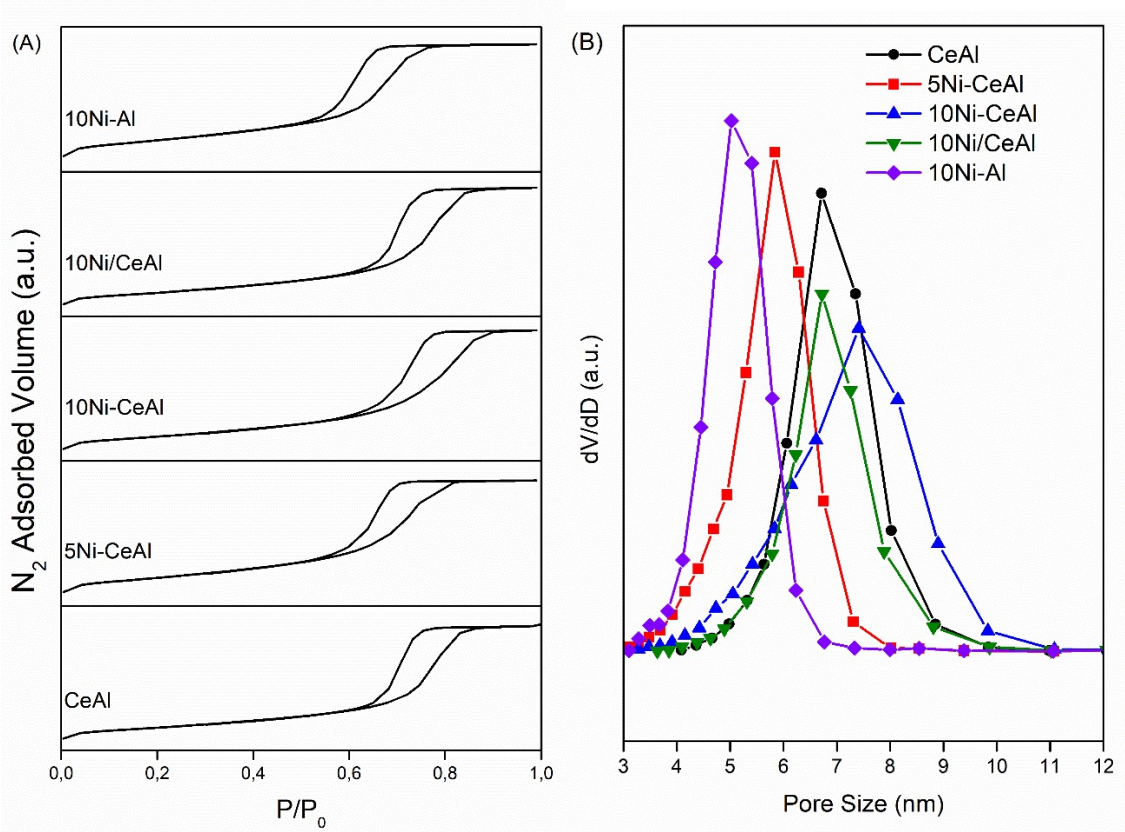

Figure 6.1. (A) N_2 adsorption-desorption curves and (B) distribution of pore size obtained by BJH desorption.

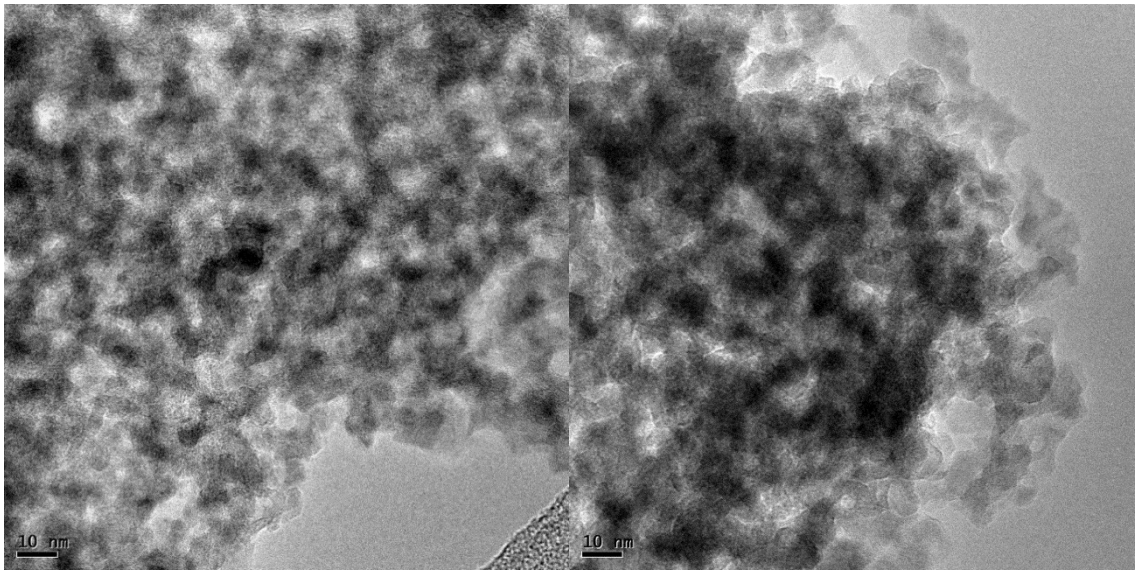

Figure 6.2. TEM images of the calcined 10Ni-CeAl catalyst.

Fig. 6.3 shows the XRD patterns of (A) Al_2O_3 and references (Ni/CeO_2 and $NiAl_2O_4$), (B) CeAl, 5Ni-CeAl, 10Ni-CeAl, 10Ni/CeAl and 10Ni-Al samples. Al_2O_3 exhibits peaks at 2θ = 38.0°, 44.0°, 53.7° and 80.1°, characteristic of γ phase (JCPDS 00-010-0425). $NiAl_2O_4$ phase (JCPDS 98-006-9509) presents an XRD pattern similar to Al_2O_3 with peaks at 2θ = 37.8°, 44.1°, 53.8° and 79.4°. The diffractograms of CeAl and 5Ni-CeAl samples do not show any peak, corresponding to an amorphous structure. Then, the addition of Ce or 5 wt% Ni into Al_2O_3 prevents its crystallization during calcination process. On the other hand, the diffractograms of the samples containing 10 wt% Ni show several peaks; 10Ni-CeAl (2θ = 43.2°, 53.2° and 78.6°); 10Ni/CeAl (2θ = 43.3°, 53.0° and 78.2°); and 10Ni-Al (2θ = 43.6°, 53.5° and 79.0°) Although the XRD patterns of $NiAl_2O_4$ and γ-Al_2O_3 are very similar, the position of most intense lines at high angle characteristic of $NiAl_2O_4$ phase is located at lower 2θ value in comparison to γ-Al_2O_3 . These results suggest the presence of a significant amount of $NiAl_2O_4$ phase for 10Ni-CeAl, 10Ni/CeAl and 10Ni-Al samples. No peaks due to CeO_2 phase were observed for all the catalysts prepared by EISA method or impregnation. This result suggests that ceria nanoparticles are highly dispersed as nanoclusters on the large alumina surface as observed in our previous work (FONSECA et al., 2019).

In order to investigate the reduction behavior of the samples, *in situ* XRD was performed during reduction with diluted hydrogen for 5Ni-CeAl, 10Ni-CeAl and 10Ni/CeAl samples (Fig. 6.4). All the XRD patterns show peaks at 2θ = 51.5° and 75.6° related to Kanthal owned to the equipment. For 5Ni-CeAl, the structure remains completely amorphous from 25 and 600 °C. A peak at 2θ = 62° characteristic of metallic Ni phase (ICSD 98-004-1508) appears at 800 °C. The Ni crystallite size after reduction at 800 °C was 5.4 nm.

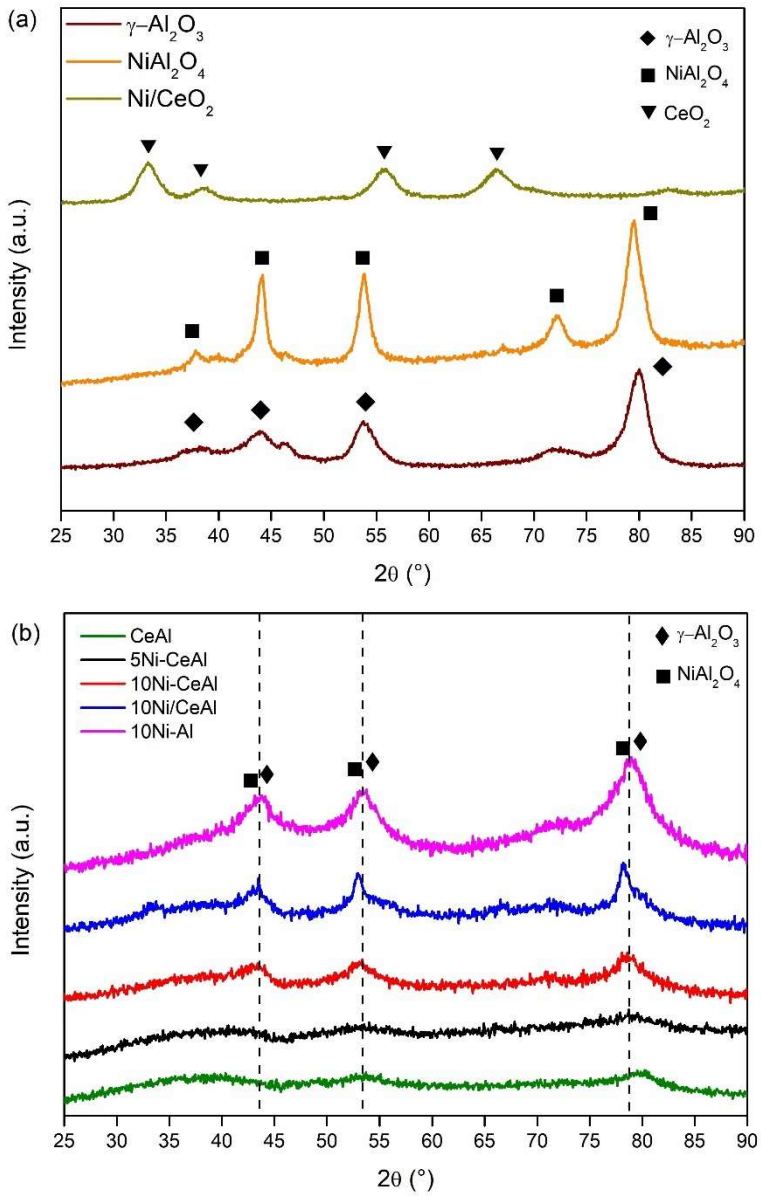

Figure 6.3. Diffractograms of (a) Al_2O_3 and references (Ni/CeO_2 and $NiAl_2O_4$), (b) CeAl, 5Ni-CeAl, 10Ni-CeAl, 10Ni/CeAl and 10Ni-Al calcined samples.

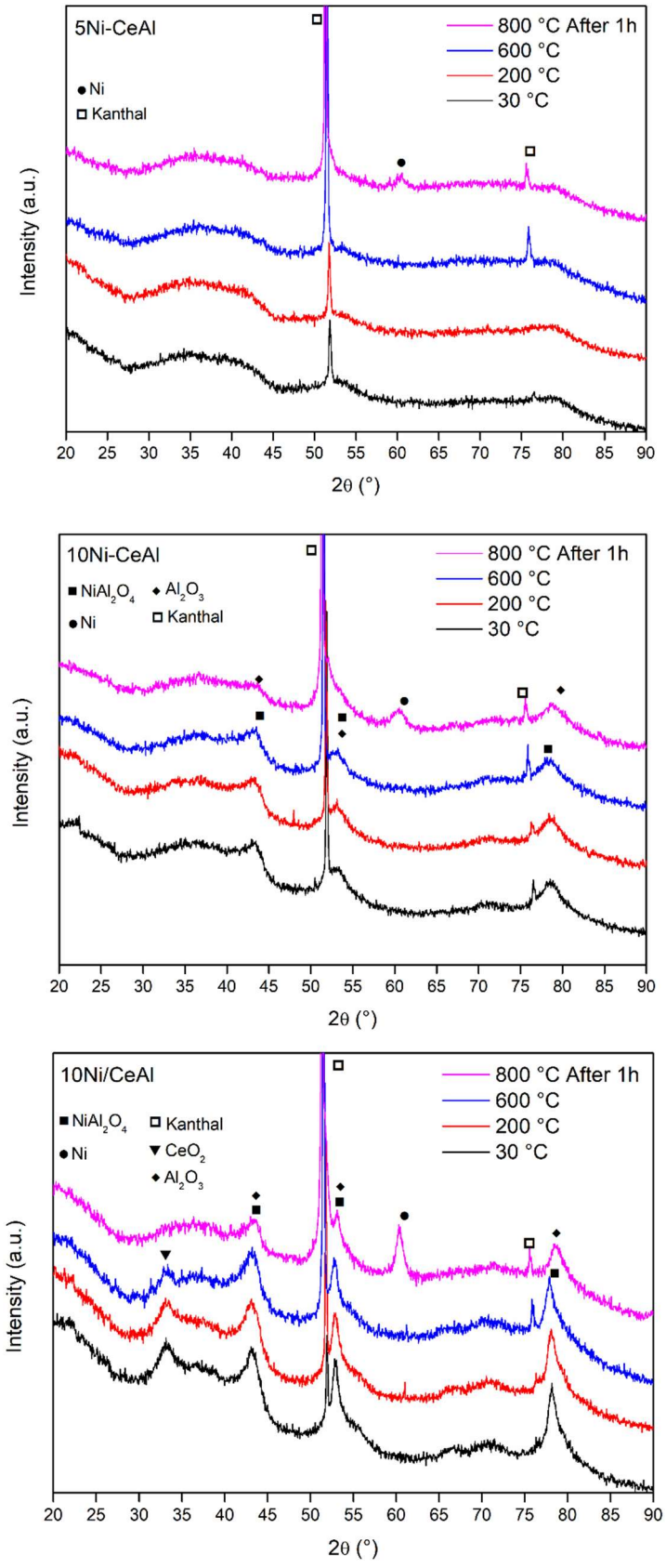

Figure 6.4. In situ X-ray diffraction patterns of 5Ni-CeAl, 10Ni-CeAl and 10Ni/CeAl during the reduction steps up to 800°C.

For 10Ni-CeAl and 10Ni/CeAl catalysts, the intensity of the characteristic lines of γ-Al_2O_3 and/or $NiAl_2O_4$ decreases and they are shifted to higher 2θ position, when the catalysts are heated under H_2 at 800 °C. Furthermore, it is also observed the appearance of the diffraction line attributed to metallic Ni at 2θ = 62°. These results suggest the reduction of $NiAl_2O_4$ phase, producing metallic Ni and Al_2O_3. The calculated Ni crystallite size for 10Ni-CeAl catalyst is 4.1 nm. The presence of $NiAl_2O_4$ spinel could prevent the sintering of Ni even after reduction at high temperature. The spinel structure is partially transformed into highly dispersed Ni^0 on Al_2O_3 during reduction. 10Ni/CeAl catalyst has larger Ni crystallite size (11.3 nm) compared to 10Ni-CeAl, which is a clear effect of the preparation method on the control of the growth of Ni crystallite size at high reduction temperature. However, regardless of the mode of introduction of Ni in the CeAl support prepared by EISA method, $NiAl_2O_4$ spinel structure is formed upon the calcination process at 800°C.

The spinel phase has been commonly used to control the Ni sintering during reduction at high temperature, providing a high metal dispersion on the catalyst (XU et al., 2001). Karam et al. (2019) synthetized unsupported $NiAl_2O_4$ by EISA method. After reduction at 800 °C, they observed the formation of Ni^0 nanoparticles dispersed over γ-Al_2O_3 with very low crystallite size in order of 7 nm.

The diffractogram of calcined 10Ni/CeAl sample also exhibited the main peak ascribed to CeO_2, at 2θ = 33.2 (Fig. 4), which is likely due to its segregation after Ni impregnation and calcination since the CeAl sample did not display this feature (Fig. 6.3-b). However, the intensity of this line starts to decrease when the sample is heated at 200 °C and it is no longer observed after reduction at 800 °C. According to the literature and previous results with Ni@CeO_2 catalysts, the reduction of ceria-based materials leads to the shift of the lines characteristic to CeO_2 to lower angles due to the conversion of Ce^{4+} to Ce^{3+} species but the intensities of these lines do not change (DA FONSECA et al., 2019). Therefore, what is causing the disappearance of the CeO_2 lines during reduction?

In order to investigate the ceria reduction behavior, Ni@CeO_2 catalyst reference sample was analyzed by *in-situ* XRD during reduction (Chapter 5 - Fig. 5.1-A). It is noticed a shift of the lines corresponding to CeO_2 to lower 2θ values, indicating an increase in the ceria lattice parameter due to the formation of Ce^{3+} species. In addition, the intensities of these peaks increase as a result of the growth of ceria crystallite size,

However, the lines corresponding to ceria phase are always observed during the reduction process instead of disappearing as it was observed for the 10Ni/CeAl catalyst.

We have previously prepared Ce_xAl samples with different Ce contents (6.0; 11.0; 20.8; 29.3 and 35.3 wt.% Ce) by EISA method (FONSECA et al., 2019). The diffractograms of the calcined samples did not show the lines corresponding to alumina and the lines typical of CeO_2 were only detected for the samples containing 29.3 and 35.3 wt.% Ce. For Ce_xAl containing 6.0; 11.0; 20.8 wt.% of Ce, the CeO_2 lines were only detected when the samples were heated under air at 1000 °C. This result indicates that Ce_xAl samples prepared by EISA method contain very small and well dispersed CeO_2 nanoclusters. The reduction of the sample with 29.3 wt.% Ce was followed by in situ XRD. No lines were detected on the diffractograms up to 800 °C but the lines characteristic of $CeAlO_3$ appeared only after heating at 1000 °C. TPR and *in situ* XANES experiments showed that Ce^{4+} is completely reduced to Ce^{3+} between 400 – 500ºC, while a commercial CeO_2 sample exhibited a much lower reduction degree (10%). Based on Isotopic Exchange and solid-state NMR experiments, it was proposed a reduction mechanism involving the reaction between the ceria nanoclusters and alumina with formation of perovskite-like $CeAlO_3$ (Eq. 6.1).

$$2\ CeO_2 + H_2 + Al_2O_3 \rightarrow 2\ CeAlO_3 + H_2O \quad (6.1)$$

Luisetto et al. (2015) also observed the disappearance of the lines characteristic of CeO_2 as well as the presence of the line attributed to $CeAlO_3$ after reduction at 1073 K of a NiCeAl sample prepared by the sol-gel method. This result was attributed to the reduction of CeO_2 to Ce_2O_3, which reacted with alumina to form the $CeAlO_3$ phase (Eqs. 6.2 and 6.3). For the sample prepared by the citric acid method, the diffractograms of the calcined and reduced NiCeAl sample did not exhibit the lines characteristic of CeO_2 or $CeAlO_3$ phases. This result was also observed in our work for 5Ni-CeAl and 10Ni-CeAl catalysts.

$$2\ CeO_2 + H_2 \rightarrow Ce_2O_3 + H_2O \quad (6.2)$$

$$Ce_2O_3 + Al_2O_3 \rightarrow 2\ CeAlO_3 \quad (6.3)$$

Chen et al. (2013) prepared 10 wt.%Ni/xCeO_2/Al_2O_3 catalysts containing different ceria content (x = 0, 5, 10, 15 wt.% CeO_2) by impregnation of γ- Al_2O_3 support with a solution of $Ce(NO_3)_3 \cdot 6H_2O$ followed by calcination at 450 °C for 2h. Then, the samples were impregnated with aqueous solution of $Ni(NO_3)_2 \cdot 6H_2O$ and calcined at 500 °C for 5h. *in situ* XRD showed the decrease in the intensity of the lines characteristic of CeO_2 and the appearance of the lines corresponding to metallic Ni when the samples were heated at 600 °C. Increasing the reduction temperature continuously decreased the CeO_2 lines, whereas the intensities of the metallic Ni lines increased. At 900 °C, the lines typical of CeO_2 completely disappeared and new lines corresponding to $CeAlO_3$ were detected, indicating that CeO_2 was reduced to $CeAlO_3$.

Shyu et al. (1988) proposed that small crystallite of CeO_2 can be transformed into $CeAlO_3$ at reduction temperatures higher than 600ºC, whereas the conversion of large CeO_2 particles to $CeAlO_3$ occurs above 800ºC. In our work, the decrease in the intensity of the line characteristic of CeO_2 on the diffractogram of 10Ni/CeAl catalyst during reduction suggests that Ce^{3+} species, once they are formed, diffuses into the alumina lattice, forming a $CeAlO_3$ phase that it is not crystalline and, then it is not detected by XRD. For the other catalysts, CeO_2 is highly dispersed over alumina and then, their lines are not detected on the diffractograms. However, the formation of $CeAlO_3$ is expected for all catalysts prepared by EISA method.

TEM images of reduced 10Ni-CeAl catalyst (Fig. 6.5) show high number of black spots corresponding to Ni metallic formed after reduction. The Ni particles are homogeneously distributed on the support, with particle sizes around 5 nm, in accordance with values obtained by XRD. The high dispersion of Ni results from the reduction of $NiAl_2O_4$, as observed from the XRD experiments, which prevents sintering at high temperature.

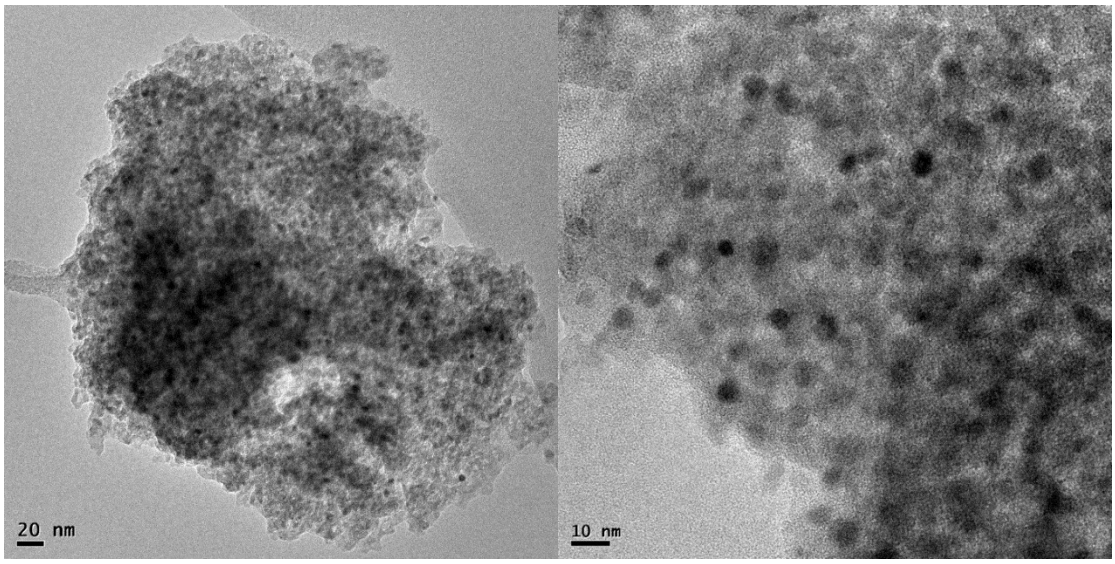

Figure 6.5. TEM images from the structure of the 10Ni-CeAl catalyst after reduction at 800 °C.

The reducibility of the samples was studied by TPR and the profiles are shown in Fig. 6.6. The sample CeAl presents a broad peak between 400 and 680 °C. According to the literature, Ce-based compounds normally present a first reduction peak at 400 °C, corresponding to the reduction of surface ceria to Ce_2O_3 while a second peak above 800 °C is attributed to the reduction of Ce^{4+} to Ce^{3+} in the bulk phase (LAFAYE; BARBIER; DUPREZ, 2015; YAO, 1984).

In our work, CeAl sample contains only ceria surface species. The 5Ni-CeAl and 10Ni-CeAl catalysts prepared by the one-pot method show two main reduction peaks; a broad one between 250 and 500 °C and an intense peak with a maximum at around 800°C. The 10Ni/CeAl sample, prepared in two steps, presents the same TPR profile, except that the second reduction peak is shifted to higher temperature, with a maximum at 860°C. For these 3 samples, the first reduction region could be attributed to the surface ceria reduction, as observed for the CeAl sample, or to the reduction of bulk NiO species (FARIA et al., 2014). However, 10Ni-Al does not present any peak in this temperature range, which suggests the absence of isolated NiO particles in the Ni-based catalysts whatever the mode of incorporation of Ni, in one step (Ni-CeAl) or in two steps (Ni/CeAl), or the composition of the support (CeAl or Al). Therefore, the broad peak between 250 and 500 °C can be mainly attributed to surface ceria reduction. The second peak around 800 °C observed for all Ni-based catalysts is ascribed in the literature to the reduction of $NiAl_2O_4$ spinel phase, where Ni is in strong interaction with the support (ZIELIŃSKI, 1982). Furthermore, some authors also attributed this

TPR peak to the reduction of Ce^{4+} to Ce^{3+} and the formation of $CeAlO_3$ perovskite phase above 827 °C in the TPR profile (LUISETTO et al., 2015). However, the support CeAl does not presented this peak at high temperature and we can assume that this peak can be correlated only to $NiAl_2O_4$ reduction. The same reduction peak was observed by Ma et al. (MA et al., 2019) in their study about Ni-Al_2O_3 catalysts prepared by EISA method and calcined at 700 °C, and it was attributed to the reduction of Ni in spinel structure of alumina. They also confirmed the absence of bulk NiO phase because of the absence of peak at lower temperature in the TPR profile, which was confirmed also by XRD.

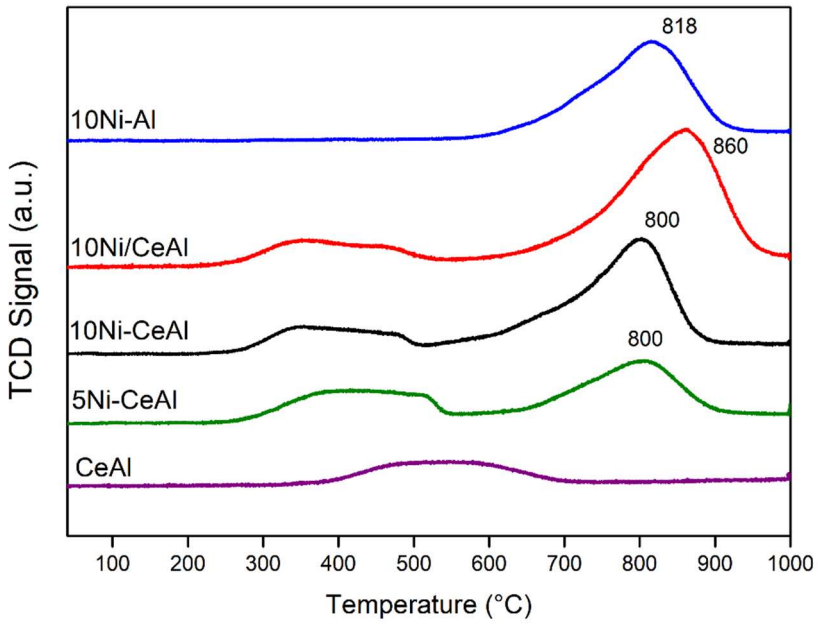

Figure 6.6. TPR profiles of the catalysts and the support CeAl.

It is reported in the literature (MOLINA; PONCELET, 1998) that the formation of $NiAl_2O_4$ in the Ni/Al_2O_3 catalysts may occur when the catalyst is calcined above 600 °C, by the reaction between the Ni precursor and the surface Al_2O_3 oxides. Scheffer et al. (1989) studied the effect of the calcination temperature of Ni/Al_2O_3 catalysts on the Ni phase. The increase of the calcination temperature from 400 °C to 900 °C shifts the main reduction peak from low temperature, centered at 450 °C, to higher temperature, above 750 °C. The higher calcination temperature favors the diffusion of Ni cations inside the support, making Ni oxide more hardly reducible. Morris et al. (2008) observed by using ^{27}Al MAS NMR the replacement of tetrahedrally coordinated Al by Ni, forming $NiAl_2O_4$ in the samples with 10 wt% of Ni, showing the

high solubility of Ni into the Al_2O_3 framework. They also did not observe the presence of NiO phase in their catalysts. Then, the TPR results of the present study suggest that the EISA method does not favor the formation of bulk NiO species on the support. In contrast the Ni would be incorporated in the Al_2O_3 framework.

Now, if one compares the TPR profiles of the Ni/CeAl and Ni-CeAl samples to the one of CeAl, it can be seen that the peak ascribed to ceria surface reduction shifts to lower temperature when Ni is present. This supposes that Ni^{2+} diffused to alumina framework could weaken the interaction between Ce and Al and then ceria can easily reduce in this range of temperature. In order to obtain the reduction degrees of Ce and Ni, the values of H_2 consumption and the theoretical values for each reduction are listed on the Table 6.2. The H_2 consumption of Ce and Ni was calculated assuming at first approximation the reduction of CeO_2 to Ce_2O_3 below 600 °C and $NiAl_2O_4$ to Ni^0 above 800 °C. The results obtained suggests that CeO_2 and $NiAl_2O_4$ are not completely reduced during the TPR, with a reduction degree around 50%. Our previous work (FONSECA et al., 2012) showed that CexAl materials calcined at low temperature (400 °C), containing $CeAlO_3$ pseudo phase displayed around 100 % of reduction of ceria below 500°C. Therefore, the calcination at high temperature strengthens the interaction between Ce and Al in the framework, decreasing its reducibility.

Table 6.2. H_2 consumption, theorical consumption and reduction degree for Ce and Ni from the catalysts.

Sample	H_2 consumption ($\mu mol.g^{-1}$)		Theoretical H_2 consumption ($\mu mol.g^{-1}$)		Reduction degree (%)	
	Below 600 °C	Above 800 °C	Ce	Ni	Ce	Ni
CeAl	370.0	---	630.4*	---	59	---
5Ni-CeAl	359.4	513.2	636.2*	861.3**	56	60
10Ni-CeAl	208.7	931.4	508.4*	1571.6**	41	59
10Ni/CeAl	243.3	1253.4	531.6*	2118.8**	46	59
10Ni-Al	---	837.8	---	1537.9**	---	54

* $2\ CeO_2 + H_2 \rightarrow Ce_2O_3 + H_2O$ ** $NiAl_2O_4 + H_2 \rightarrow Ni + Al_2O_3 + H_2O$

Results of the OSCC measurements, performed to obtain more information about the redox properties of the catalysts, are presented in the Table 6.3. CO can be oxidized by the O from the CeO_2 phase or NiO phase. The oxygen released from CeO_2 is of major importance for the DRM reaction because it can react with the carbon formed during CH_4 decomposition, avoiding the catalyst deactivation by carbon deposition. It should be mentioned that during the OSCC measurements the 10Ni-Al sample does not exhibit any CO_2 production. It is explained by the absence of NiO phase in this sample and the inability of $NiAl_2O_4$ phase to directly oxidize CO at this temperature. The same assumption will be adopted for the samples 5Ni-CeAl and 10Ni-CeAl, considering that all the O atoms are released from CeO_2 structure.

Table 6.3. OSCC at 500 °C for calcined CeAl, 5Ni-CeAl, 10Ni-CeAl and 10Ni/CeAl samples.

Catalyst	OSCC (μmol $CO_2.g^{-1}$)
CeAl	273
5Ni-CeAl	348
10Ni-CeAl	309
10Ni/CeAl	323
10Ni-Al	0

The presence of Ce in the structure increases the OSCC value due its reducibility, as observed for the all catalysts as well as for the CeAl support. Furthermore, the addition of Ni in the structure slightly increases the OSCC value. The insertion of Ni into alumina framework led to an increase in the oxygen mobility of oxygen species around Ce atoms, favoring the reduction of Ce^{4+} to Ce^{3+}. The higher mobility of oxygen in the Ni-based samples prepared by EISA method is in agreement with the shift to lower temperature in the Ce reduction observed during TPR, generating more oxygen vacancies (CAMPBELL; PEDEN, 2005). During the re-oxidation step it was not formed CO_2, which is an indication of the low basicity of these samples, characteristic of CeAl material, as shown in a previous study (FONSECA et al., 2019).

6.2.2 DRM reaction

The curves of the CH_4 and CO_2 conversions and H_2/CO molar ratio during the DRM reaction are presented in Fig. 6.7. 10Ni-Al and 5Ni-CeAl catalysts exhibited low initial CH_4 and CO_2 conversions that significantly increased during the first 2 h of TOS and then they levelled off. For 10Ni-CeAl and 10Ni/CeAl catalysts, the CH_4 and CO_2 conversions remained constant since the beginning of reaction. However, the test was interrupted after 24 h of TOS for 10Ni/CeAl catalyst due to the significant increase in the pressure drop on the reactor. The H_2/CO molar ratio after 72 h of TOS was between 0.70 – 0.85 for all catalysts. The H_2/CO molar ratio lower than 1.0 and the conversion of CO_2 higher than the conversion of CH_4 are due to the occurrence of RWGS reaction.

The induction period observed for the 10Ni-Al and 5Ni-CeAl catalysts, and to a lesser extent for 10Ni-CeAl, has been reported in the literature for some Ni-based catalysts with low basicity (TAKANABE et al., 2005). Faria et al. (2014) investigated the changes in Ni phase for Ni/Al_2O_3 catalyst by XRD. After exposition to a CO_2 stream, the diffractogram reveal the appearance of the lines characteristics of NiO phase and the lines attributed to Ni^0 phase are no longer detected. Rabelo-Neto et al. (2018) carried out *in situ* XPS under dry reforming conditions using $LaNiO_3$ precursor catalyst. They observed a decrease in the intensity of the peak characteristic of metallic Ni at 66.6 eV during the first 120 min of time of stream, which suggests the oxidation of metallic Ni particles. Then, the intensity of this peak increased, indicating that NiO is reduced by the H_2 produced in the DRM reaction. These results demonstrated that CO_2 can oxidize the surface of Ni particles when the catalysts are initially contacted with the feed, resulting in a loss of activity. But the partially oxidized Ni particles were reduced again by the syngas produced during the reaction, increasing the conversion of reactants. In our work, it is also possible to observe the low H_2/CO at the beginning of the reaction for these catalysts and its increase together with the enhancement in CH_4 conversion after few minutes of time on stream.

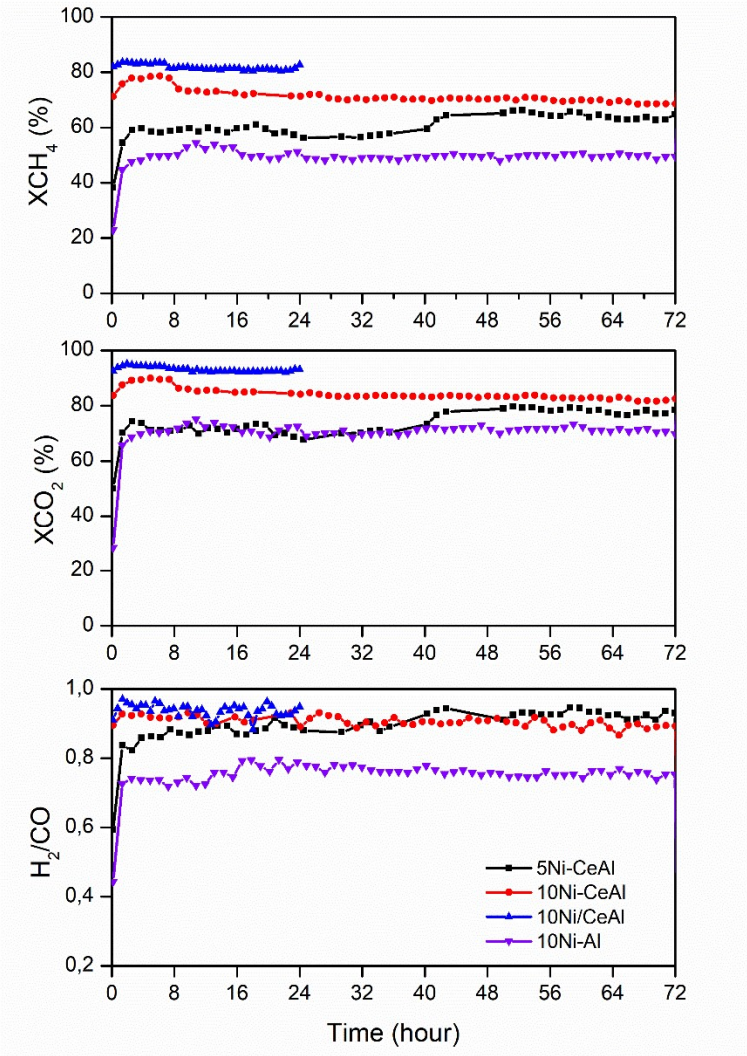

Figure 6.7. CH_4 conversion, CO_2 conversion and H_2/CO molar ratio during the dry reforming of methane performed for the catalysts.

6.2.3 Characterization of post-reaction catalysts

The main drawback on the development of catalysts for the dry reforming of methane is the deactivation by carbon formation. Therefore, it is very important to evaluate the carbon formed after the catalytic test. The mechanism of formation and growth of carbon filaments at the metal surface of Ni-based catalysts is well known (ROSTRUPNIELSEN, 1977). The source of this carbon is methane and its dehydrogenation on the surface of the metallic particle, which is the first step of the DRM mechanism. Carbon might be oxidized by O atoms produced by the CO_2 dissociation at the metal-support interface or it can migrate into the particle structure, leading to the growth of carbon filament. The analysis of the carbon deposited on the samples was made by thermogravimetric analysis after reaction and the corresponding

DTG curves are presented in Fig. 6.8. The 5Ni-CeAl and 10Ni-CeAl catalysts do not present any peak corresponding to the oxidation of carbon species. The 10Ni/CeAl sample displays two peaks centered at 490 and 616 °C while the 10Ni-Al sample has only one centered at 640 °C. According to literature (DE LIMA et al., 2010; SÁNCHEZ-SÁNCHEZ; NAVARRO; FIERRO, 2007), the peak at 490 °C ascribed to amorphous carbon structure and the peaks above 600 °C are correlated to filamentous carbon with single or multiple walls (SWNT and MWNT). The characterization by RAMAN spectroscopy of the spent catalyst confirms the formation of MWCNT with low degree of crystallinity with bands at 1350 and 1580 cm^{-1} assigned to D and G bands respectively (Appendix B) (RABELO-NETO et al., 2018). The rate of carbon formation for the catalysts during DRM at 800 °C for 72 h of TOS are listed on Table 6.4.

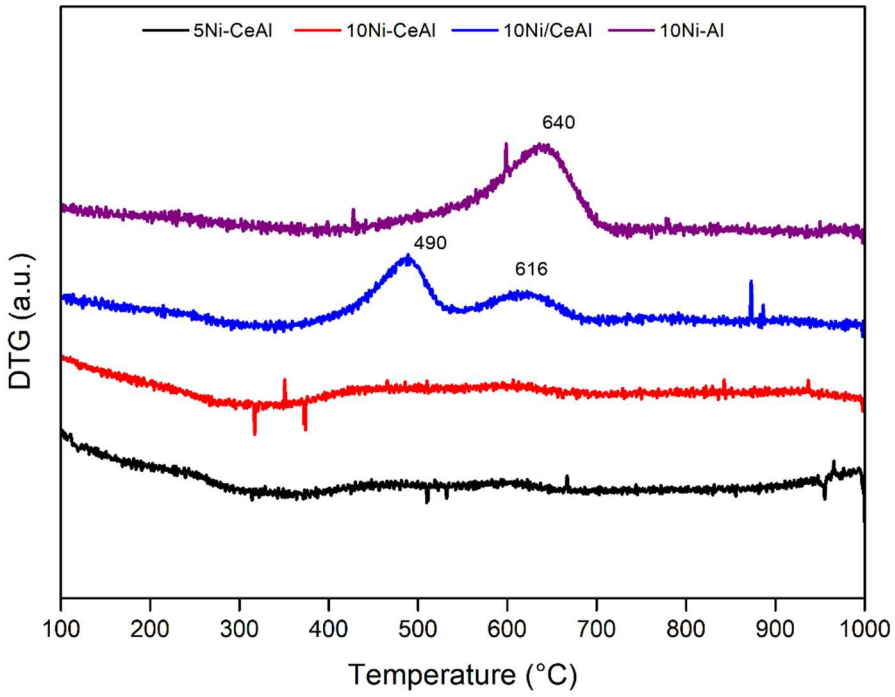

Figure 6.8. DTG curves obtained from the post-reaction samples analyzed by TGA

Table 6.4. Rate of carbon formation on all Ni-CeAl catalysts of this work and data from the literature after DRM.

Catalyst	Reaction Conditions	Rate of carbon deposition ($mg_C/g_{catal}/h$)	Reference
5Ni-CeAl	800 °C, CH_4:CO_2 = 1:1	0.0	This work
10Ni-CeAl	800 °C, CH_4:CO_2 = 1:1	0.0	This work
10Ni/CeAl	800 °C, CH_4:CO_2 = 1:1	2.0	This work
10Ni-Al	800 °C, CH_4:CO_2 = 1:1	0.8	This work
Ni/0Ce-AlO	800 °C, CH_4:CO_2 = 1:1	3.7	(CHEN et al., 2013b)
Ni/05CeAlO	800 °C, CH_4:CO_2 = 1:1	2.8	(CHEN et al., 2013b)
Ni/10CeAlO	800 °C, CH_4:CO_2 = 1:1	1.8	(CHEN et al., 2013b)
Ni/15CeAlO	800 °C, CH_4:CO_2 = 1:1	1.2	(CHEN et al., 2013b)
Ni/CeO_2	800 °C, CH_4:CO_2 = 1:1	9.7	(MARINHO et al., 2020)
Ni@CeO_2	800 °C, CH_4:CO_2 = 1:1	1.6	(MARINHO et al., 2020)
Ni@$CeZrO_2$	800 °C, CH_4:CO_2 = 1:1	0.0	(MARINHO et al., 2020)
$LaNiO_3$	800 °C, CH_4:CO_2 = 1:1	27.0	(RABELO-NETO et al., 2018)
$LaNiO_3$/$SiCeO_2$	800 °C, CH_4:CO_2 = 1:1	0.3	(RABELO-NETO et al., 2018)
NiCu/$Ce_{0.9}Gd_{0.1}O_2$	800 °C, CH_4:CO_2 = 1:1	12.2	(BONURA; CANNILLA; FRUSTERI, 2012)

Ni/CeO_2	800 °C, CH_4:CO_2 = 1:1	4.8	(LUISETTO et al., 2019)
Ni/CZ100	700 °C, CH_4:CO_2 = 1:1	0.4	(KAMBOLIS et al., 2010)
Ni/CZ75	700 °C, CH_4:CO_2 = 1:1	3.5	(KAMBOLIS et al., 2010)
Ni/CZ44	700 °C, CH_4:CO_2 = 1:1	1.7	(KAMBOLIS et al., 2010)
Ni/CZ28	700 °C, CH_4:CO_2 = 1:1	0.7	(KAMBOLIS et al., 2010)

Fig. 6.9 shows the TEM images of the post-reaction 10Ni-CeAl, 10Ni-Al and 10Ni/CeAl catalysts. No carbon filaments are observed on the TEM images of 10Ni-CeAl catalyst, in agreement with TG analysis. For this sample, the average Ni particle size is around 10 nm, which indicates a slight increase in comparison to the reduced sample (4-5 nm according to the XRD and TEM results). On the contrary, the images of 10Ni-Al and 10Ni/CeAl catalysts after DRM reaction reveals high carbon formation, with the presence of many carbon filaments. Due to the presence of Ni on the extremity of the carbon filaments (Fig. 7.9-D and 7.9-F), these catalysts remained quite active during the reaction until blockage of reactor. The Ni particle size is higher than the ones observed for the 10Ni-CeAl catalyst after three days on stream (around 20 nm for both catalysts).

6.2.4 Reaction mechanism for DRM

With the aim of better understand the mechanism of reaction, *in-situ* DRIFTS experiments were performed under alternatively flowing CH_4, CO_2, CH_4 and CH_4/CO_2. Fig. 6.10 displays the spectra collected for 10Ni-Al catalyst obtained after subtraction of the background spectrum. Under CH_4 atmosphere, the spectrum presents a very intense band at 3010 cm^{-1} assigned to gas-phase CH_4. After 10 min of TOS a band at 2060 cm^{-1} assigned to the stretching vibration mode of linear CO species adsorbed on metallic Ni (DAS et al., 2018; KITLA; SAFONOVA; FÖTTINGER, 2013; NÉMETH et al., 2015) appears, corresponding to the oxidation of C produced by the decomposition of CH_4 with the oxygen coming from the support. Bands with negative intensities are observed

in the 3600-3800 cm^{-1} region, corresponding to the hydroxyl groups of alumina (AMENOMIYA; MORIKAWA; PLEIZIER, 1977; FERREIRA-APARICIO et al., 2000). It means that there was a consumption of hydroxyl groups concomitant with the formation of CO adsorbed on the metal. Ferreira-Aparicio et al. (2000) studied the DRM mechanism over Ru/Al_2O_3 catalysts and they also observed the participation of OH groups from alumina on the oxidation of carbon formed during the CH_4 decomposition. The hydroxyl groups diffuse towards the metal particle promoting the oxidation of carbonaceous species and generating oxygen vacancies on the surface.

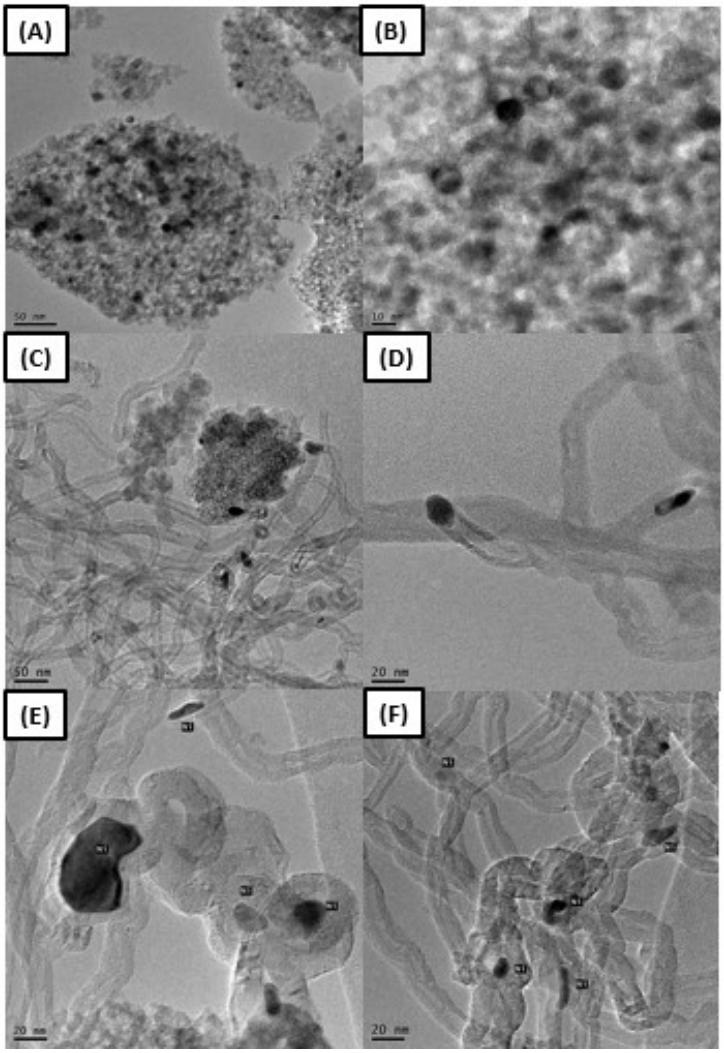

Figure 6.9. TEM images of the 10Ni-CeAl (A, B), 10Ni-Al (C,D) and 10Ni/CeAl (E, F) post-reaction catalysts.

Switching the gas to CO_2, there is the appearance of a very intense band at 2360 cm^{-1} due to gas-phase CO_2. Furthermore, the adsorbed CO is rapidly desorbed and gives gas-phase CO (double bands centered at 2143 cm^{-1}), which disappears during time on stream while bands at 1573 and 1517 cm^{-1}, assigned to asymmetric $\nu_{C=O}$ stretching mode of carbonate species (CO_3^{2-}) appears (FERREIRA-APARICIO et al., 2000). The 3600-3800 cm^{-1} region is complicated to analyze due the influence of some bands attributed to gas-phase CO_2, but there is no regeneration of OH group with time, indicating the difficulty of the support to store O from gas phase and to fill in the oxygen vacancies previously generated. Switching again to CH_4, there is CO formation only in gas phase and the bands in OH region, showing the consumption of carbonates species. The release of oxygen to the metal generates oxygen vacancies on the support, which is occupied by the oxygen from carbonate species. The carbonate species acts as O supply in the absence of CO_2. The participation of these species was also observed by (O'CONNOR; MEUNIER; ROSS, 1998). Finally, in the presence of the two gases, CH_4 and CO_2, it is possible to observe CH_4, CO_2 and CO in gas phase. It is important to note the absence of carbonate species and the negative bands in OH region under DRM conditions, indicating a surface with deficiency of lattice oxygen species. Then, there is a high consumption of oxygen by carbon gasification in this catalyst and the unbalance between this reaction and the methane decomposition explains the high carbon formation observed for this catalyst. The observed reactions are demonstrated in the equations 6.4 to 6.11.

$$CH_4\,(g) + 2\,* \rightleftharpoons CH_3* + H* \quad (6.4)$$

$$CH_3* + * \rightleftharpoons CH_2* + H* \quad (6.5)$$

$$CH_2* + * \rightleftharpoons CH* + H* \quad (6.6)$$

$$CH* + * \rightleftharpoons C* + H* \quad (6.7)$$

$$C* + OH* \rightleftharpoons CO* + V_O + H* \quad (6.8)$$

$$CO_{2\,(g)} + V_O + H* \rightleftharpoons CO* + OH \quad (6.9)$$

$$CO_{2\,(g)} + O^{2-} \rightleftharpoons 2\,CO_3^{2-} \quad (6.10)$$

$$CO_3^{2-} + V_O + H* \rightleftharpoons 2\,OH^- + CO* \quad (6.11)$$

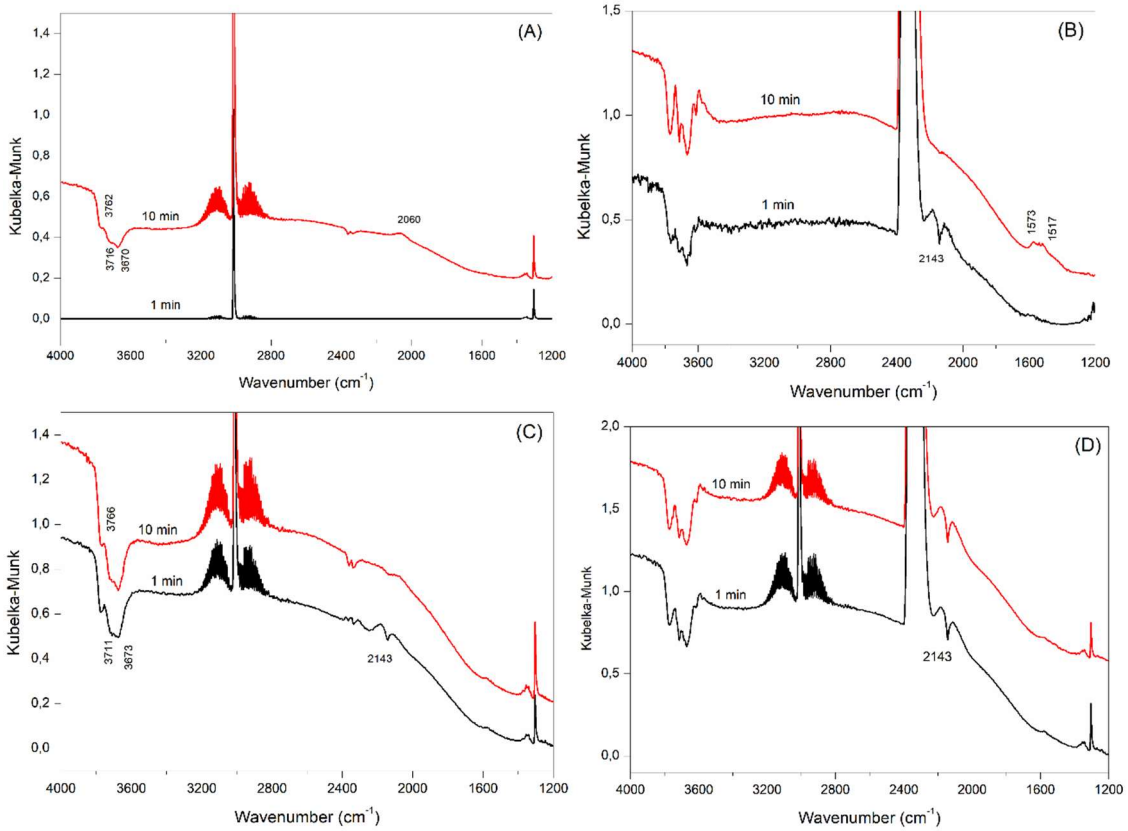

Figure 6.10. DRIFTS spectra for 10Ni-Al at 750 °C after; (A) flow of CH_4; (B) flow of CO_2; (C) flow of CH_4; (D) flow of equimolar CH_4/CO_2.

Fig. 6.11 shows the spectra of *in-situ* DRIFTS experiment for the 10Ni-CeAl catalyst, which enables the evaluation of the influence of Ce addition. The same adsorbed species observed on the spectra of 10Ni-Al in the presence of CH_4 are also detected for 10Ni-CeAl. However, in the presence of CO_2 the bands ascribed to hydroxyl groups with negative intensities at 3600-3800 cm^{-1} are no longer observed and the intensity of carbonate bands are higher compared to 10Ni-Al catalyst. Then, the presence of Ce increased the oxygen storage capacity in the material, as observed previously by OSCC. Under DRM condition (Fig. 6.11-D), the bands corresponding to carbonate species are still present, which was not the case for 10Ni-Al. This result indicates that 10Ni-CeAl catalyst has a higher amount of oxygen species on its surface, in the form of CO_3^{2-} and hydroxyl groups. These carbonate species donate oxygen and promotes the carbon removal mechanism. Therefore, the correct balance between methane decomposition and carbon gasification explains the absence of carbon deposits during the DRM over 10Ni-CeAl catalyst.

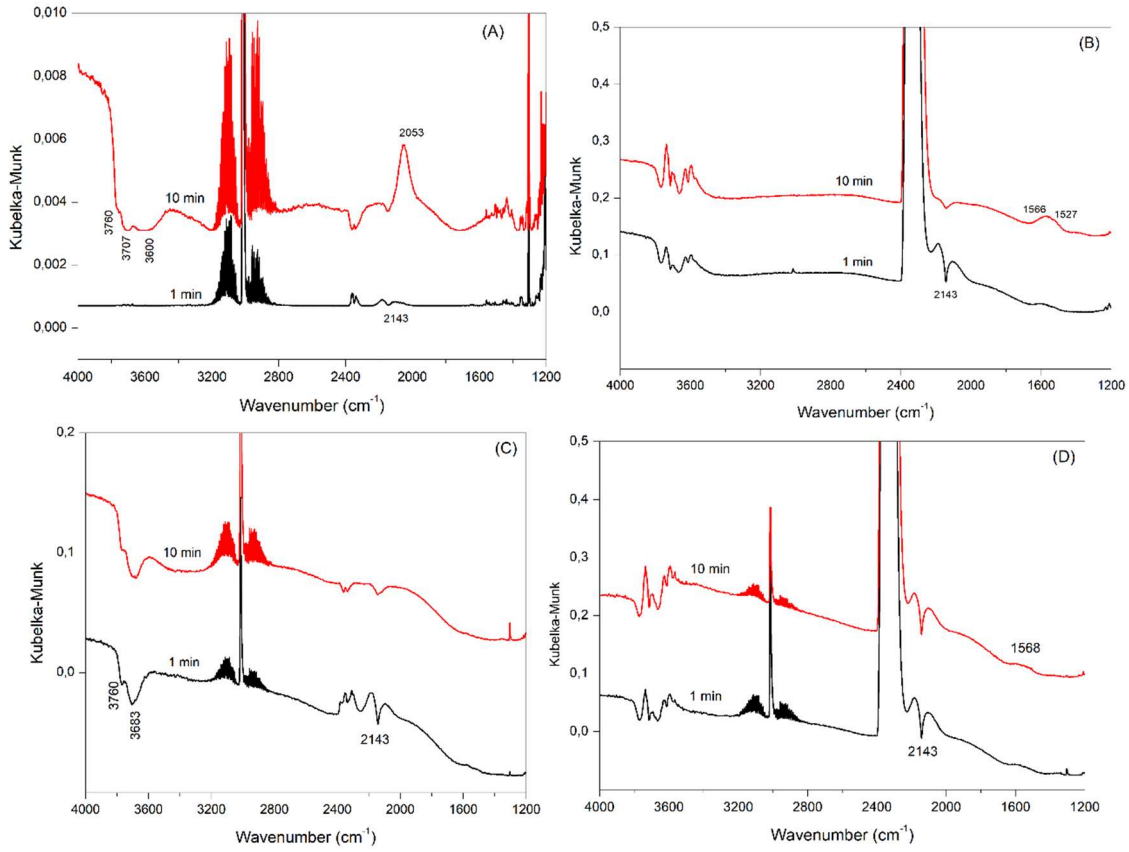

Figure 6.11. DRIFTS spectra for 10Ni-CeAl at 750 °C after; (A) flow of CH_4; (B) flow of CO_2; (C) flow of CH_4; (D) flow of equimolar CH_4/CO_2.

The DRIFTS spectra of the 10Ni/CeAl catalyst in the presence of CH_4 do not show the bands corresponding to adsorbed CO (Fig. 7.12-A). It has been reported that the CO heat of adsorption is lower on large Ni metal particles than on the small ones (SHAIKHUTDINOV et al., 2003). Consequently, the CO is more easily desorbed than for catalysts prepared by EISA method due its larger Ni crystallite size, as observed by XRD. Under DRM condition (Fig. 12-D), the catalyst exhibits a spectrum very similar to the one observed for 10Ni-Al, with no bands attributed to carbonate species. Then, less oxygen species is available on the surface to promote the carbon oxidation. Therefore, the unbalance between carbon gasification and carbon formation rates is responsible for the high formation of carbon over this catalyst during the catalytic test. The *in-situ* DRIFTS shows that the addition of Ni and Ce by EISA method improves the amount of oxygen species on the surface of the 10Ni-CeAl catalyst under DRM condition and avoids catalyst deactivation.

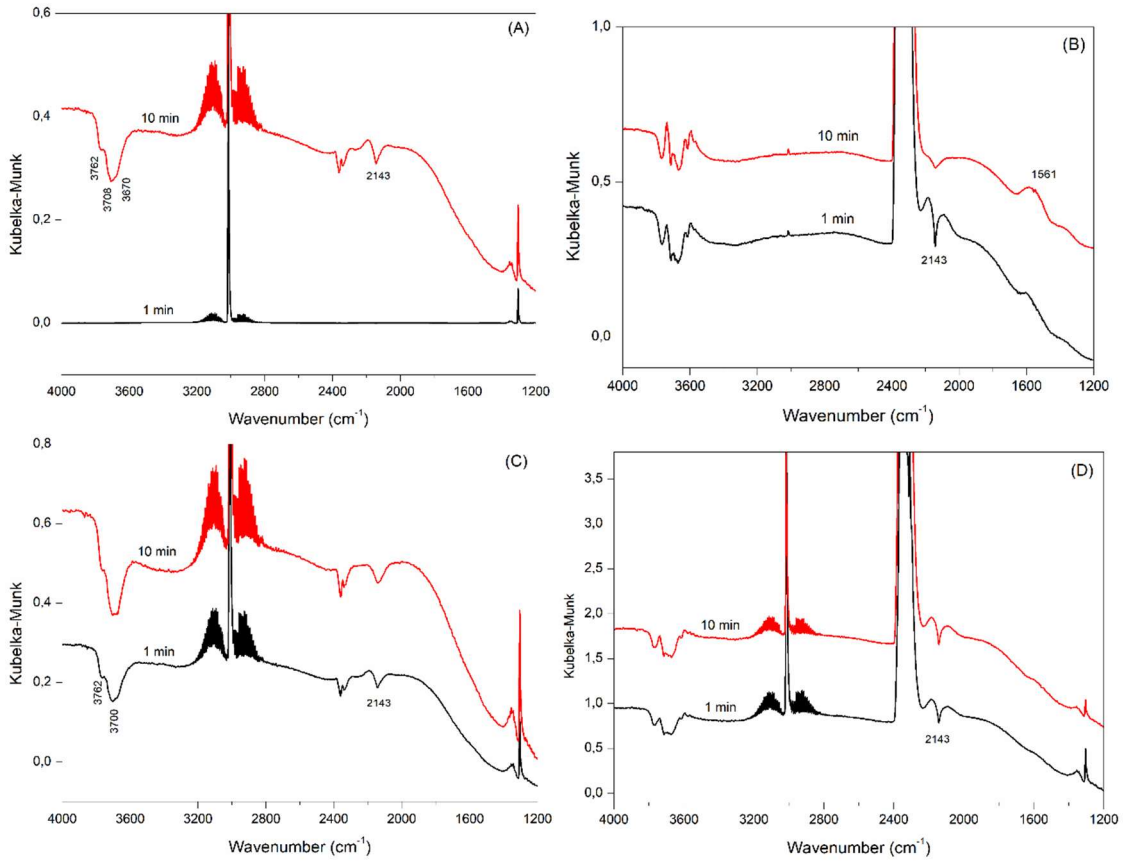

Figure 6.12. DRIFTS spectra for 10Ni/CeAl at 750 °C after; (A) flow of CH_4; (B) flow of CO_2; (C) flow of CH_4; (D) flow of equimolar CH_4/CO_2.

The mechanism observed in the *in-situ* DRIFTS experiments is in agreement with the bi-functional mechanism described in the literature by many authors for dry reforming of methane (BITTER; SESHAN; LERCHER, 1998; FERREIRA-APARICIO et al., 2000; O'CONNOR; MEUNIER; ROSS, 1998; WEI; IGLESIA, 2004a). The CH_4 adsorption occurs at the surface of metallic Ni particle, producing hydrogen atoms and reactive carbon species. The rate of this reaction is extremely affected by the Ni particle size and the formation of carbon species is favored on large Ni particles (KIM et al., 2000). The carbon can be oxidized by the oxygen atoms present at the metal-support interface, producing CO. The oxygen vacancy generated is replenished by the oxygen from the CO_2 dissociative adsorption, promoting the mechanism of carbon removal from the metallic surface. Furthermore, CO_2 also adsorbs on the basic sites of the support in the form of carbonate species, which also acts like source of oxygen for the regeneration of oxygen vacancies. However, if the support does not release enough oxygen to the metal particle, the carbon species polymerize to less active carbon,

leading to the grow of carbon filaments. Therefore, it is important to have a balance between the rate of methane decomposition on the metal and the rate of carbon gasification at the metal/support interface.

6.2.5 Effect of control of Ni particle size and oxygen mobility on catalyst stability

The control of Ni particle size plays an important role on the prevention of carbon deposition and catalyst stability during DRM reaction (KIM et al., 2000; PADI et al., 2020; ROSTRUPNIELSEN, 1977). Therefore, different catalyst preparation methods have been proposed in the literature to produce small and stable metal particles (HUANG et al., 2017; LIU, 2016; PADI et al., 2020; WANG et al., 2014). The encapsulated structures, for example core-shell and mesoporous catalysts, have been extensively studied to develop stable catalysts for DRM (BIAN; KAWI, 2018; DAS et al., 2018). In this case, the metal is confined into support structure which inhibits metal sintering and suppress carbon deposition. In the Chapter 4, we developed embedded-Ni catalyst in CeO_2 and $CeZrO_2$ supports which exhibited high resistance against Ni sintering, as well as an enhanced oxygen mobility due to the high interaction between Ni and the support, suppressing carbon formation.

The core-shell catalysts have been studied for DRM reaction, however its complexity and the use of high-value added reagents for synthesis methods, has stimulated the search for new synthesis procedures simpler to replicate. Xiang et al. (2016) have synthesized NiSiAl samples by EISA method and the catalyst was stable during 100 hours at 700 °C for the DRM reaction with low carbon formation, showing the absence of any sintering process.

In the present work, the Ni particle size effectively affected the carbon deposition rate. The EISA method allowed to synthetize very well dispersed Ni particles on the high surface area support (5Ni-CeAl and 10Ni-CeAl catalysts). The $NiAl_2O_4$ spinel phase precursor, as observed by XRD and TPR, produced small Ni crystallite size during reduction at 800 °C, regardless of the Ni loading, whereas larger particles were formed on the catalysts prepared by the incipient-wetness impregnation method. The smaller Ni crystallite size could control the rate of methane decomposition and avoid carbon formation. However, carbon deposition was still observed on the 10Ni-Al catalyst also prepared by EISA method, which indicates that the presence of ceria is fundamental for catalyst stability (LAOSIRIPOJANA; SUTTHISRIPOK; ASSABUMRUNGRAT, 2005). The addition of Ce increases oxygen storage capacity

and base properties of the support, leading to an enhanced carbon resistance (STROUD et al., 2018). In this work, the addition of Ce to prepare the CeAl mixed oxide by EISA method does not contribute to modify the acid-base properties of the support (Appendix B).

Liang et al. (2020) studied the Ni-CeO_2-Al_2O_3 catalyst prepared by EISA method for DRM reaction. The authors obtained very small Ni nanoparticles over Al_2O_3 cluster as the support matrix, obtaining different Ni crystallite sizes according to Ni:Ce:Al proportions. The 10Ni-5Al-1Ce catalyst presented the lowest Ni crystallite size before and after stability test, 5.2 and 12.2 nm, respectively, without catalytic deactivation during DRM reaction. The addition of Ce enhanced catalytic stability, due the better dispersion of Ni and the inhibition of the formation of encapsulated carbon species. The high interaction between Ni-O-Ce prevents further Ni sintering at DRM condition.

Luiseto et al. (2015) studied the influence of Ce addition on the performance of Ni/Al_2O_3 catalyst prepared by different synthesis methods for DRM reaction. The amount of carbon accumulated on the catalysts after DRM at 1073 K decreased from 1000 to 60 mg of carbon/g of catalyst when the Ni crystallite size decreased from 22.6 to 5.8 nm. The catalyst with the highest Ni dispersion exhibited also the highest amount of Ce^{3+} species determined by XPS. According to the authors, the combination of small Ni crystallite size and high amount of $CeAlO_3$ favored the lower carbon formation on the NiCeAl catalyst during DRM reaction. The formation of $CeAlO_3$ was also observed by (CHEIN; FUNG, 2019) with the addition of 5wt% of Ce in Ni/Al_2O_3 catalyst for DRM reaction. The authors associated the carbon suppression to the role of $CeAlO_3$ in the catalyst activity, promoting the redox pair Ce^{4+}- Ce^{3+} during carbon removal mechanism.

Chen et al. (2013) compared the performance of 10 wt.%Ni/xCeO_2/Al_2O_3 catalysts containing different ceria content (x = 0, 5, 10, 15 wt.% CeO_2) for the DRM at 800ºC. The rate of carbon deposition on the catalysts after 250 h of TOS varied from 3.68 mg of carbon/g of catalyst/h (Ni/Al_2O_3) to 1.16 mg of carbon/g of catalyst/h (Ni/15CeO_2/Al_2O_3). TEM images revealed that the Ni particle size was approximately the same for all catalysts reduced below 900 °C (at around 10 nm). Therefore, the authors ruled out the effect of Ni dispersion on the formation of carbon. The authors proposed that $CeAlO_3$ formed during reduction reacts with CO_2, producing CeO_2 and

CO (Eqs. 6.12 and 6.13). Then, CeO_2 carries out the oxidation of CH_x species formed on the metal surface, restoring and maintaining the redox cycle active.

$$2\ CeAlO_3 + CO_2 \rightarrow Al_2O_3 + 2CeO_2 + CO \quad (6.12)$$

$$Al_2O_3 + 2\ CeO_2 + CH_x \rightarrow CO + 2\ CeAlO_3 + x/2\ H_2 \quad (6.13)$$

Table 6.4 summarizes the rate of carbon deposition during DRM over different catalysts from the literature. It is clear that the Ni-based catalysts containing ceria prepared by EISA method of our work exhibits lower carbon formation rates than other catalysts from the literature. In the present study, the 10Ni-Al catalyst, which does not have any oxygen mobility in its structure, as shown by the OSCC experiments at 500 °C, is not able to prevent carbon deposition. DRIFTS experiments showed that, at high temperature, the hydroxyl groups can oxidize the carbon formed but the adsorption of CO_2 is not favored, decreasing the presence of oxygen species at the surface and consequently high carbon formation, as showed in TEM images. The presence of CeO_2 promotes oxygen mobility in the catalyst, which is responsible to oxidize the carbon formed on the Ni surface. Therefore, the Ni-based catalysts prepared by EISA method combine the two characteristics necessary for both high activity and resistance to deactivation by carbon formation. Because of the high resistance to coke formation, its application in other reforming process, such as steam reforming of methane, can be interesting in order to maximize the yield for H_2 production, with potential to application in pilot plant scale.

6.3 Conclusions

A series of Ni-based catalysts prepared by EISA method was tested in the dry reforming reaction. It was possible to produce materials with high surface area and well defined mesopores. The synthesis conditions favored the formation of $NiAl_2O_4$ spinel phase with very well dispersed Ni particles on the support, which inhibits the sintering process at high temperature. The presence of Ce interacting strongly with Al_2O_3 promotes the oxygen mobility in the material, responsible for the carbon removal mechanism, and enhances the activity of the catalyst. The combination of small Ni crystallite and oxygen mobility could suppress carbon formation due the control of the rates of both CH_4 decomposition and carbon gasification. These results indicate that the

EISA method is appropriate to produce Ni dispersed catalysts with high surface area and oxygen mobility for application in reforming reactions.

CHAPTER 7

Pt nanoparticles embedded in CeO_2 and $CeZrO_2$ catalysts for biogas upgrading. Investigation on carbon removal mechanism by oxygen isotopic exchange and DRIFTS

7.1 Motivation

Pt-based catalysts present high activity for the DRM (PAKHARE; SPIVEY, 2014; POMPEO et al., 2007), due to its capability to cleave the C-H bond at elevated temperature (ZHANG et al., 2013a; ZHOU et al., 2010). More recently the use of core-shell structures have been highlighted to increase the interaction metal-support (LI et al., 2016). The use of CeO_2 in a core-shell structure has been studied (CARGNELLO et al., 2010; WANG et al., 2013, 2016), but the methods to prepare this type of catalyst are quite complex as described before. In the Chapter 4 we have synthesized Ni@CeO_2 and Ni@$CeZrO_2$ catalysts based on a simple sol-gel method for application in the DRM reaction. To the best of our knowledge, a simple synthesis procedure to obtain Pt embedded in ceria bulk in a configuration similar to a core-shell catalyst was never reported in the literature reported for application in reforming reactions.

In this work, we studied Pt-embedded CeO_2 catalysts prepared by a simple one-step synthesis based on sol-gel method, in comparison to Pt/CeO_2 catalyst prepared by traditional impregnation in the DRM reaction. The doping of CeO_2 with Zr was also evaluated in the embedded structure. The objective of this chapter is to evaluate the embedded effect only over oxygen mobility to understand the differences between the carbon removal mechanism in the two structures. The characterization of the samples was performed by N_2 physisorption, Transmission Electron Microscopy and X-ray Diffraction. The oxygen reducibility and mobility were analyzed by Temperature-Programmed reduction, Isotopic Oxygen Exchange and Oxygen Storage capacity (OSCC). The carbon formation was analyzed by Temperature-Programmed Oxidation and Raman Spectroscopy. The carbon removal mechanism with focus on oxygen mobility and adsorbed species during reaction conditions was investigated by using Oxygen Isotopic Exchange and *in-situ* Diffuse Reflectance for *Infrared* Fourier Transform Spectroscopy.

7.2 Results and discussion

7.2.1 Catalyst Characterization

The results of catalyst chemical composition reported in Table 7.1 indicate that experimental values for Pt loading and Ce/Zr molar ratio are similar to the nominal content (i.e., 1 wt% Pt and Ce/Zr = 4.0). All calcined catalysts exhibited approximately the same BET surface area calculated by N_2 physisorption, which is expected since the

synthesis procedure of the support was similar. The addition of Zr did not improve BET surface area when the catalyst was submitted to calcination at 400 °C. However, Pt/CeO_2 and $Pt@CeO_2$ showed remarkable decrease in the surface area after reduction at 800 ºC (< 10 m^2/g), which is associated with CeO_2 sintering at high temperature (AY; ÜNER, 2015; LI; VAN VEEN, 2018). On the other hand, $Pt@CeZrO_2$ catalyst underwent lower decrease in surface area than ceria supported catalysts, suggesting that Zr enhanced the thermal stability of ceria. This is likely due to the formation of a $CeZrO_2$ solid solution (HORI et al., 1998), which minimizes ceria sintering and reduces the loss of surface area at high temperature.

Table 7.1. Chemical composition and BET surface area of calcined and reduced samples.

Catalyst	Pt (%)	Ce/Zr molar ratio	BET Surface Area (m^2/g)	
			Calcined	Reduced
Pt/CeO_2	0.9	---	47	< 10
$Pt@CeO_2$	0.8	---	51	< 10
$Pt@CeZrO_2$	0.8	4.3	49	22

TEM images of Pt/CeO_2, $Pt@CeO_2$ and $Pt@CeZrO_2$ catalysts after reduction at 800 ºC are shown in Fig. 7.1. In spite of the very low surface area, all ceria supported catalysts have very small Pt particles in the range: 2-5 nm (Pt/CeO_2) and 2-6 nm ($Pt@CeO_2$ and $Pt@CeZrO_2$), regardless the synthesis procedure (impregnation and sol-gel method). Some authors (DAMYANOVA et al., 2009; PANTU; GAVALAS, 2002) observed strong Pt sintering when the catalyst is submitted to high temperature at different atmospheres and synthesis procedure. This result reveals that all catalysts presented a high resistance against Pt sintering. It is expected that the embedded structure creates a physic barrier avoiding the agglomeration of Pt nanoparticles at high temperature, as observed in our previous work with Ni as active phase (Chapter 4). However, the surprising result for Pt/CeO_2 catalyst prepared by impregnation can suggest that the position of Pt in the catalyst is not a classical formation of Pt nanoparticles over ceria surface but a different catalyst system could have been formed. More characterizations will carry out in this work in order to explain this high resistance to Pt sintering in the Pt/CeO_2 catalyst.

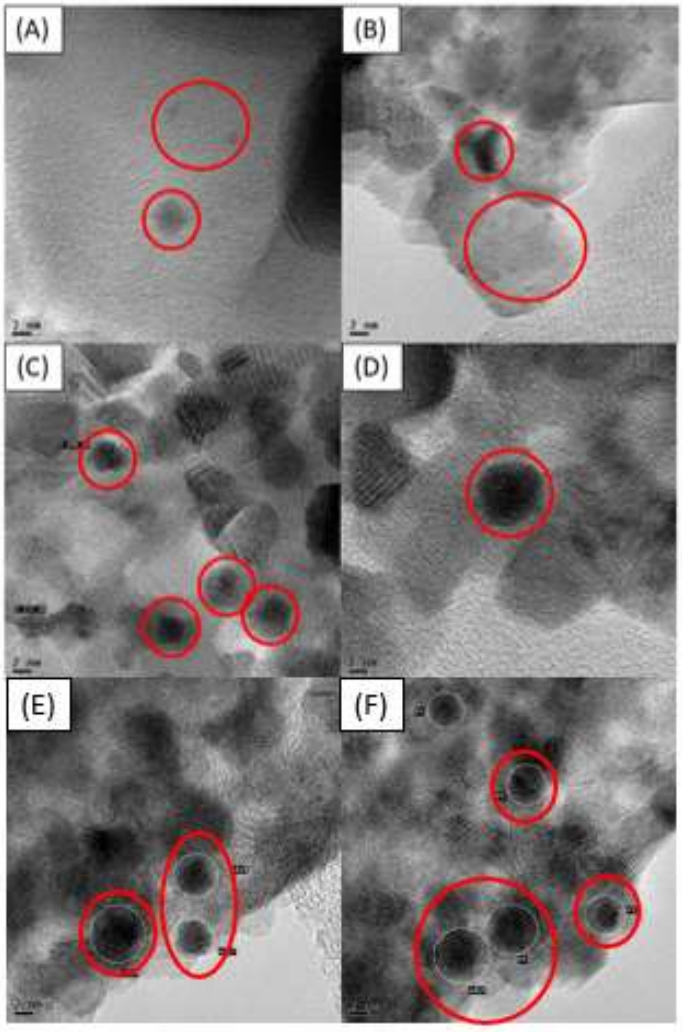

Figure 7.1. TEM images of (A, B) Pt/CeO_2, (C, D) $Pt@CeO_2$ and (E, F) $Pt@CeZrO_2$ catalysts after reduction at 800 °C.

The Raman spectra of the calcined samples are shown in Fig. 7.2. The spectrum of CeO_2 support is also presented for comparison. The support exhibits only one intense band at 462 cm^{-1} assigned to the symmetrical stretching mode between the eight oxygen atoms bound to the cerium atom in the triple degenerate F_{2g} mode. The addition of Pt over CeO_2 by impregnation or sol-gel procedures does not affect the spectrum of Pt/CeO_2 and $Pt@CeO_2$, respectively, in comparison to the support. The $Pt@CeZrO_2$ sample presents a shift in the frequency of the first-order F_{2g} peak to higher value (469 cm^{-1}), beyond the band at 224 cm^{-1} ascribed to second-order transverse acoustic mode (2TA) (NAKAJIMA; YOSHIHARA; ISHIGAME, 1994). Therefore, the absence of the shift in the F_{2g} band for the Pt/CeO_2 and $Pt@CeO_2$ catalysts show that the addition of Pt

does not affect the ceria structure. However, the addition of Zr occurs into ceria lattice, leading to the formation of $CeZrO_2$ solid solution.

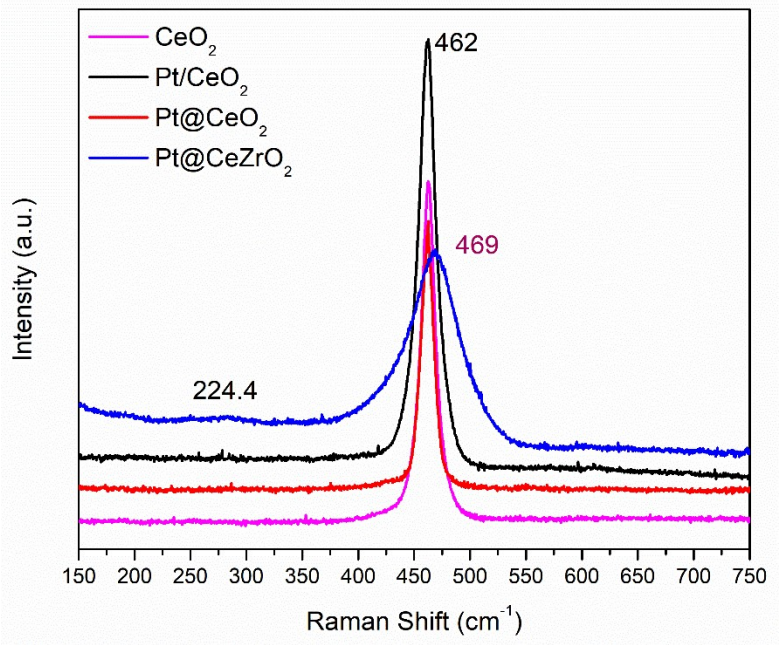

Figure 7.2. Raman shift of the fresh samples.

Fig.7.3 displays the XRD patterns of the CeO_2 support and the $Pt@CeO_2$ and $Pt@CeZrO_2$ calcined samples. All diffractograms exhibit only the characteristic lines of CeO_2 with fluorite structure (PDF 34-0394) at $2\theta = 28.7°$, 33.2° and 47.7°. The typical lines of Pt oxide were not observed that is likely due to the low metal loading and/or high Pt dispersion. The $Pt@CeO_2$ catalyst exhibited similar CeO_2 lattice parameter compared to CeO_2 support (Table 7.2), which indicates the formation of isolated Pt oxide nanoparticles embedded into ceria matrix. Doping CeO_2 with Zr shifted the diffraction lines to higher 2θ position (Fig. 7.3). According to the literature, this result is ascribed to the formation of a $CeZrO_2$ solid solution (FARIA et al., 2014; KOZLOV et al., 2002), with partial replacement of Ce^{4+} (0.97 Å) with Zr^{4+} (0.84 Å) resulting in a lattice contraction (BONK et al., 2015). The XRD data accords very well with the observation on the Raman spectra.

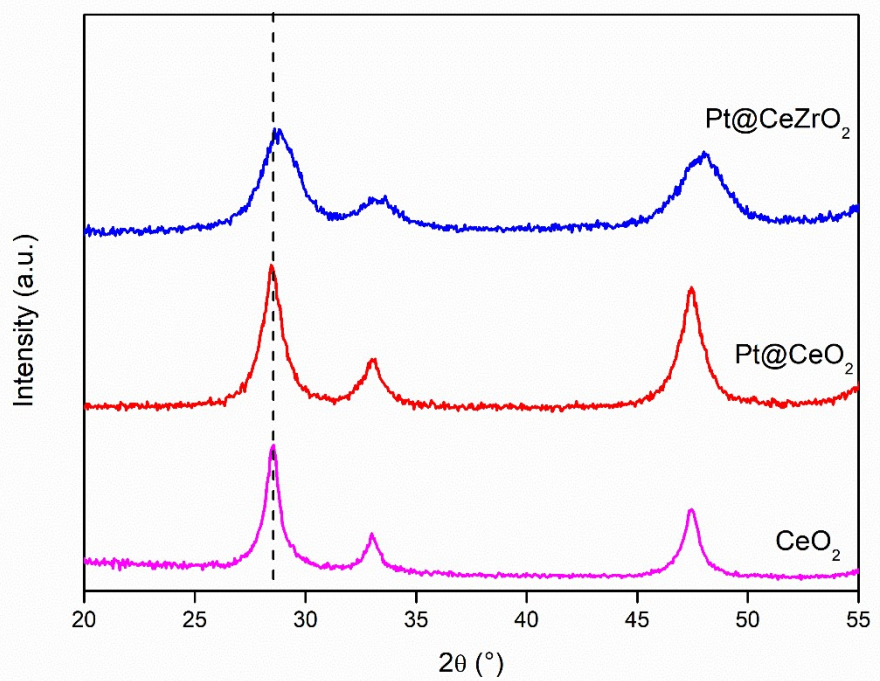

Figure 7.3. X-ray diffraction patterns of calcined samples.

Ceria support exhibited the largest CeO_2 crystallite size after calcination (11 nm), but the addition of Pt decreased the CeO_2 crystallite size. The presence of Pt interacting with Ce seems to avoid the sintering of ceria, and for that reason, Pt-containing catalysts had smaller crystallite size than pure CeO_2 after calcination. After reduction at 800 °C, the CeO_2 crystallite size strongly increased for Pt@CeO_2 catalysts, explaining the high loss of specific surface area observed by N_2 physisorption. The formation of $CeZrO_2$ solid solution leads to a higher thermal stability in the material, as observed before in the N_2 physisorption. The catalyst presented the smallest ceria crystallite size and the lowest growth (93%) after reduction at 800 ºC, reinforcing that the solid solution, enhanced the thermal stability of support.

Table 7.2. CeO_2 crystallite size and CeO_2 lattice parameter obtained from XRD for samples after calcination and after pretreatment of reduction.

Catalyst	CeO_2 Crystallite Size (nm)	CeO_2 Lattice Parameter (Å)
CeO_2	11.1	5.4230
Pt@CeO_2	7.4 (39.6)*	5.4243
Pt@$CeZrO_2$	4.2 (8.1)*	5.3630

* CeO_2 crystallite size after reduction at 800 °C.

TPR profiles are shown in Fig. 7.4 and 7.5. Firstly, the TCD signal was monitored at room temperature after admission of H_2/Ar mixture in the reactor for time enough to observe the return of signal to baseline in order to monitor the H_2 consumption at room temperature. For the Pt/CeO_2 catalyst only one intense peak is detected with area = 1085 a.u., which corresponds to the dead volume of the reactor. After heating, the reduction of Pt/CeO_2 catalyst is characterized by an intense peak at 256 °C followed by small peaks at 410 and 486 °C. The intense peak can be attributed to Pt oxide reduction interacting with CeO_2 surface (LEE et al., 2016; PINO et al., 2003; VITA et al., 2016). The H_2 uptake is 615 μmol/g_{cat} (Table 7.3), higher than the theoretical H_2 amount required to total Pt oxide reduction (i.e. PtO_2/Pt^0 = 103 μmol/g_{cat}), indicating that ceria was also reduced in this range of temperature due to the H_2 spillover effect (DAMYANOVA et al., 2009; JACOBS et al., 2004). H_2 reduces Pt oxides species but upon dissociating on the metal, hydrogen also spills onto ceria surface which promotes the release of active oxygen close to Pt-CeO_2 interface by reducing ceria as well (GOLUNSKI et al., 1995; ROCCHINI et al., 2002). The peaks observed at 410 and 486 °C for Pt/CeO_2 corresponds to the reduction of superficial ceria without interaction with Pt. Finally, a reduction peak appears at 800 °C corresponding to ceria bulk reduction, which means that the presence of Pt does not affect significantly the reduction at high temperature, as observed by Lee et al. (2016).

The embedded $Pt@CeO_2$ and $Pt@CeZrO_2$ catalysts presented the intense peak correspondent to the dead volume of the reactor at room temperature, however during the return of the signal to baseline there is a large second peak, indicating the consumption of H_2 from gas phase in these two catalysts. After deconvolution of these peaks, the H_2 uptake observed for both embedded catalysts ($Pt@CeO_2$ = 1092 μmol H_2/g_{cat} and $Pt@CeZrO_2$ = 983 μmol H_2/g_{cat}) was higher than the theoretical H_2 required to total Pt oxide reduction (i.e. PtO_2/Pt^0 = 103 μmol/g_{cat}). This indicates that the H_2 after Pt oxide reduction spillover on the metal surface, generating H* species chemisorbed on Pt metallic particles. Some authors reported the reduction of Pt-based catalyst at sub-ambient temperature (BOND; GELSTHORPE, 1987; LIOTTA et al., 2004; MCCABE; WONG; WOO, 1988; MUKRI; WAGHMARE; HEGDE, 2013; PARK; TZOU; SACHTLER, 1986; PINO et al., 2003; VITA et al., 2016). Peak temperature at sub-ambient temperature were obtained for $Ti_{1-x}Pt_xO$ (MUKRI; WAGHMARE; HEGDE, 2013), Pt/SiO_2 (MCCABE; WONG; WOO, 1988), Pt/Al_2O_3 (MCCABE; WONG; WOO, 1988) and Pt/CeO_2 (PINO et al., 2003; VITA et al., 2016) catalysts , where the

authors associated the peak around -30 °C to the reduction of Pt^{4+} to Pt^{0} isolated particles. Pino et al. (2003) observed a reduction peak at -30 °C for the Pt/CeO_2 catalyst prepared by combustion method. In their work, they associated the reduction kinetic to the interaction with ceria, where the high synergy between Pt and Ce promoted by the synthesis procedure facilities the Pt reduction at low temperature. Therefore, the reduction at room temperature observed for both embedded catalysts can be correlated to the reduction of isolated Pt oxides nanoparticles embedded into ceria structure.

The TPR profiles are close for embedded catalysts with the absence of peaks in the temperature range 30 – 800 °C. However, as observed before, a high consumption of H_2 is measured when introducing the hydrogen at room temperature. It is explained by a high amount of H* chemisorbed species over Pt metallic particles. The absence of desorption peak (negative TCD signal) indicates that the ceria reduction is promoted by spillover effect at some unknown temperature during the heating without modification in the TCD signal and H_2 consumption from gas phase in the range 100-500 °C.

$Pt@CeO_2$ catalyst also presented a reduction peak at high temperature (800 ºC) ascribed to ceria bulk reduction, whereas $Pt@CeZrO_2$ did not show any relevant reduction peak at the entire range of temperature. This result agrees with other works (FORNASIERO et al., 1995; HORI et al., 1998; MATTOS et al., 2002; SILVA et al., 2005) that reported that the doping of ceria with Zr promoted the mobility of oxygen from the bulk to surface during the process of oxygen release. The reduction of Ce^{4+} to Ce^{3+} is limited by the stress energy arising from the volume expansion, but the introduction of Zr^{4+}, which has a smaller ionic radius compared to Ce^{4+}, compensates this stress energy due to the formation of structure defects (LI et al., 2019; VLAIC et al., 1997).

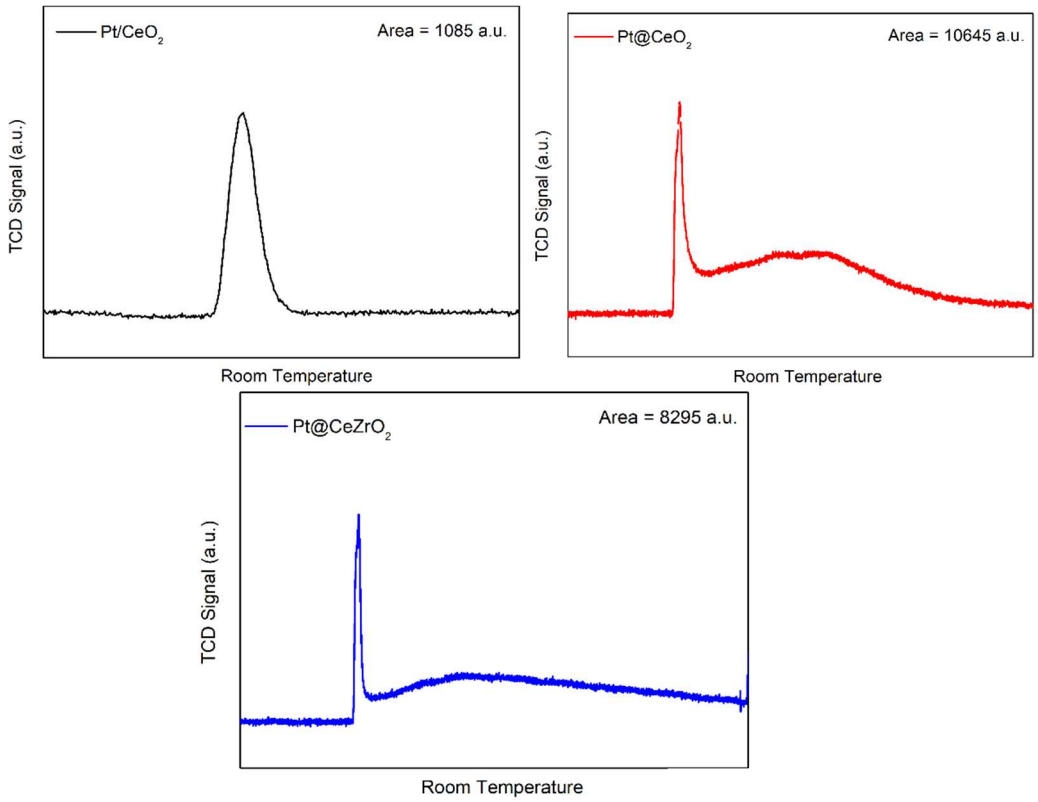

Figure 7.4. H_2 consumption from gas phase at room temperature monitored by TCD.

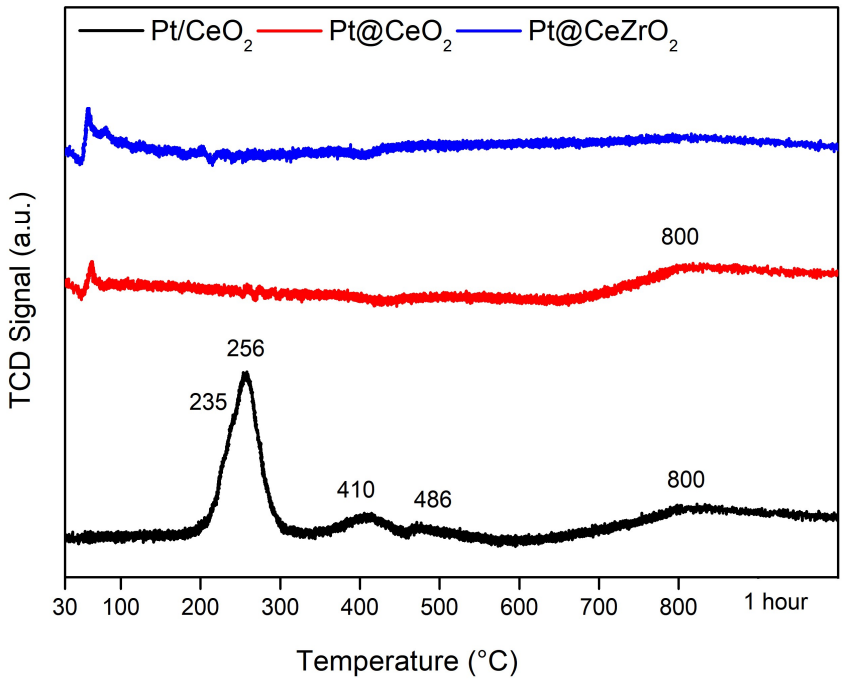

Figure 7.5. TPR curves of the fresh catalysts.

The H_2 uptake and Ce reduction degrees were estimated by considering three regions of temperatures: room temperature, below 500 °C and above 500 °C. The results are presented in Table 7.3. The Pt@CeO_2 and Pt@$CeZrO_2$ catalysts exhibited a higher H_2 uptake, mainly at room temperature. The Pt/CeO_2 catalyst is harder to reduce compared to embedded catalysts. The data shows the difficulty of the metal to activate the H_2 over its surface and it suggests that this metal can have some particularity in its boundary. More powerful techniques, such as EXAFS, are required to explain better the position of Pt in the Pt/CeO_2 catalyst prepared by impregnation. The formation of isolated nanoparticles of Pt oxides into embedded structure promotes a higher contact area between Pt and Ce that favors the process of release oxygen from ceria structure, increasing ceria reducibility. Therefore, the formation of embedded structure enhanced the extent of ceria reduction, promoting the creation of oxygen vacancies in the material during reduction of active phase.

Table 7.3. H_2 uptake during the TPR experiment.

Catalyst	H_2 uptake (µmol/g_{cat})			Theoretical H_2 consumption for Ce^{4+}/Ce^{3+} reduction (µmol/g_{cat})	Percentage of $Ce^{4+/}Ce^{3+}$ reduction (%)
	Room Temperature	Lower Temperature (< 500 °C)	Higher Temperature (> 500 °C)		
CeO_2	---	625	146	5810	13
Pt/CeO_2	---	615	108	5752	13
Pt@CeO_2	1092	---	159	5761	22
Pt@$CeZrO_2$	983	---	---	4849	20

OSCC was measured by introducing CO pulses for each pre-oxidized catalyst at 400 and 500 °C, and results are listed in Table 7.4. The values obtained are in accordance with other publications (LAFAYE; BARBIER; DUPREZ, 2015; MIKULOVÁ et al., 2007). Pt/CeO_2 catalyst presented higher OSCC compared to Pt@CeO_2, which can be a consequence of embedded structure where some Pt sites are inaccessible to CO molecule. The most part of oxygen vacancies are generated during CO pulses, however some oxygen vacancies are still presented in the fresh Pt@$CeZrO_2$

catalyst due the formation of solid solution, as observed by XRD and Raman, justifying the higher value. Doping ceria with Zr enhances OSCC, because of the formation of Ce-Zr solid solution and the participation of oxygen species through the Ce-Zr crystal lattice (in Pt@$CeZrO_2$) from bulk phase. The insertion of Zr into ceria has been reported to enhance OSCC. Trovarelli et al. (1997) observed the maximum O_2 uptake for Ce/Zr molar ratio between $0.6 < Ce/Zr < 0.8$. The same increase in OSCC value was observed by Madier et al. (1999). The higher OSCC observed for Pt@$CeZrO_2$ is in agreement with the results obtained by these authors.

Table 7.4. OSCC measurements for catalysts at 400 °C and 500 °C.

Catalyst	OSCC (µmol O/g)	
	400 °C	**500 °C**
Pt/CeO_2	356	444
Pt@CeO_2	175	248
Pt@$CeZrO_2$	684	795

The TPOIE curves (Fig. 7.6) reveal that the embedded structure has a great influence in the oxygen exchange process, decreasing the initial temperature to begin the exchange. Oxygen exchange activity for Pt/CeO_2 catalyst begins at 380 °C (N_e = 29 x 10^{20} at.g^{-1} at 500 °C). The embedded Pt@CeO_2 catalyst presents lower initial temperature of exchange (360 °C) and the N_e at 500 °C is higher than the calculated for Pt/CeO_2 (N_e = 33 x 10^{20} at.g^{-1}). Doping CeO_2 with Zr decreased the temperature to oxygen exchange (300 °C) and increased the value of N_e for all range of temperature (N_e = 38 x 10^{20} at.g^{-1}). All the catalysts showed similar isotopomer distribution during the experiment, indicating the occurrence of both simple and multiple heterolytic exchange mechanisms (MADIER et al., 1999).

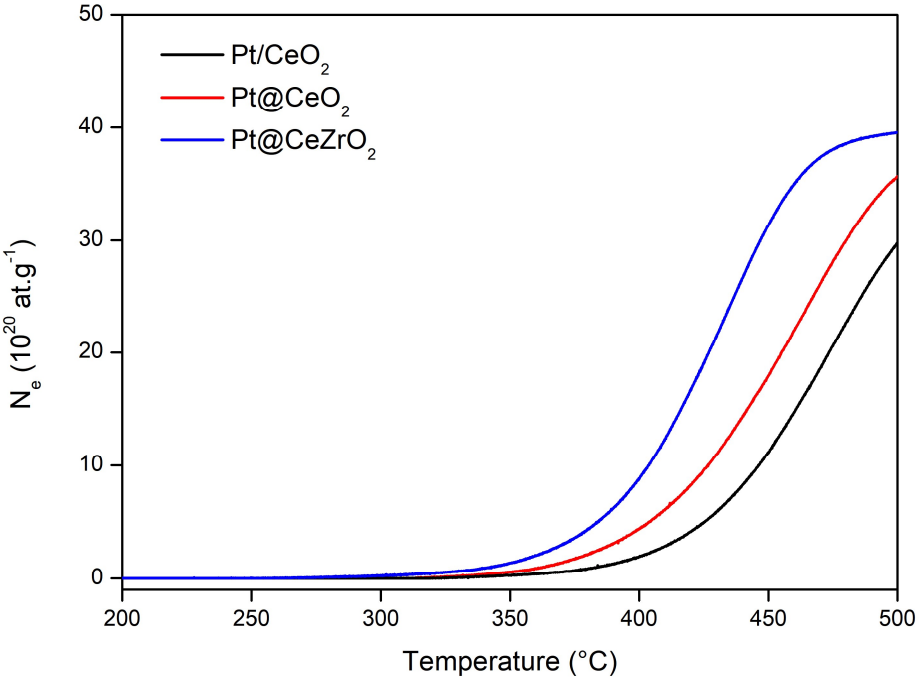

Figure 7.6. Evolution of the number of exchanged oxygen atoms during TPOIE over Pt/CeO_2, $Pt@CeO_2$ and $Pt@CeZrO_2$.

Results of isothermal experiments of oxygen isotopic exchange (IOIE) carried out at 400 °C are depicted in Fig. 7.7. The experiments at 450 and 500 °C are shown in Appendix C and indicate the same trend than the one observed at 400 °C. The kinetic of oxygen exchange for Pt/CeO_2 is lower than in $Pt@CeO_2$, in agreement with the results of TPOIE experiments. The formation of Ce-Zr solid solution favored the kinetic of oxygen exchange as also demonstrated in the TPOIE experiments. The IOIE results show the positive effect of embedded structure to promote the oxygen exchange in the support compared to impregnated sample, increasing the percentage of O atoms exchanged (Table 7.6). Moreover, the participation of oxygen species from bulk phase enhances the value of N_e in the $Pt@CeZrO_2$ catalyst.

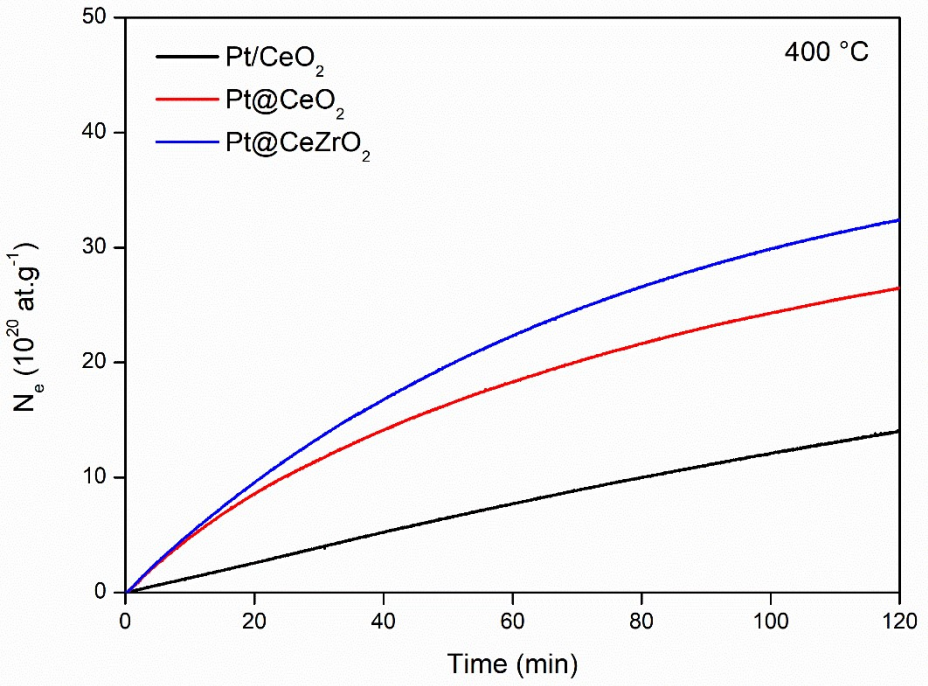

Figure 7.7. Evolution of the number of exchanged oxygen atoms during IOIE at 400 °C over Pt/CeO_2, $Pt@CeO_2$ and $Pt@CeZrO_2$.

Table 7.5. Number and percentage of O atoms exchanged at 400 °C.

Catalyst	Ne (10^{20} at.g^{-1})	O atoms exchanged (%)
Pt/CeO_2	12	17
$Pt@CeO_2$	26	37
$Pt@CeZrO_2$	33	45

Table 7.6 presents the initial rate of exchange (R_e) for each catalyst evaluated at different temperatures and activation energy for the exchange process. The embedded catalysts have lower activation energy with faster exchange compared to the impregnated Pt/CeO_2, resulting in an exchange process more efficient in these catalysts. The poor oxygen mobility observed for Pt/CeO_2 catalyst are in agreement with the TPR results, where it was observed a low H_2 activation. In the IOIE, the low O_2 activation can be explained by same reason and it suggests some particularity in the Pt boundary. Again, EXAFS can be a powerful technique to understand better the environmental of Pt in this catalyst.

There is a clear difference in the exchange process between the catalysts in terms of N_e and R_e. Embedded-Pt into ceria-zirconia structure presented the highest values of N_e and R_e with lower activation energy. Therefore, these results indicate that Pt location in the catalyst structure affects the oxygen mobility, in such a way that Pt embedded into the support structure enhances the oxygen exchange, demanding lower activation energy due to the higher metal-CeO_2 interaction.

Table 7.6. Initial rate of exchange at different temperatures and activation energy for the catalysts.

Catalyst	Initial Rate of Exchange (R_e) (10^{17}.at.g^{-1}.s^{-1})			Activation Energy (kJ.mol^{-1})
	400 °C	450 °C	500 °C	
Pt/CeO_2	0.5	2.9	27.5	170.5
Pt@CeO_2	7.1	47.1	176.0	138.8
Pt@$CeZrO_2$	13.3	48.4	265.0	128.8

7.2.2 DRM reaction

The stability tests were performed with CH_4/CO_2 molar ratio equal 1.0 and 1.5 simulating a real biogas during 24 hours at 800 °C. Fig. 7.8 shows the conversion of CH_4 and CO_2 during time on stream (TOS) for all catalysts. The results revealed that all catalysts were quite stable during the reaction, even under high CH_4/CO_2 molar of 1.5. The CO_2 conversion was higher than the CH_4 conversion for all tests, with a H_2/CO lower than 1.0, which indicates the occurrence of Reverse Water Gas-Shift Reaction (RWGS) (DA FONSECA et al., 2019; FARIA et al., 2014). The increase in CH_4/CO_2 molar ratio diminishes the CH_4 conversion because of the excess of methane in the feed in comparison to the stoichiometric value, increasing the CO_2 conversion. H_2/CO molar ratio also increased, suggesting that the CH_4 decomposition is favored in excess of CH_4. Serrano-Lotina and Daza (2014) also observed a decrease in CH_4 conversion with higher H_2 selectivity upon feeding the reactor with CH_4/CO_2 higher than one. At this condition, the RWGS is less favorable, decreasing the consumption of H_2 to produce CO.

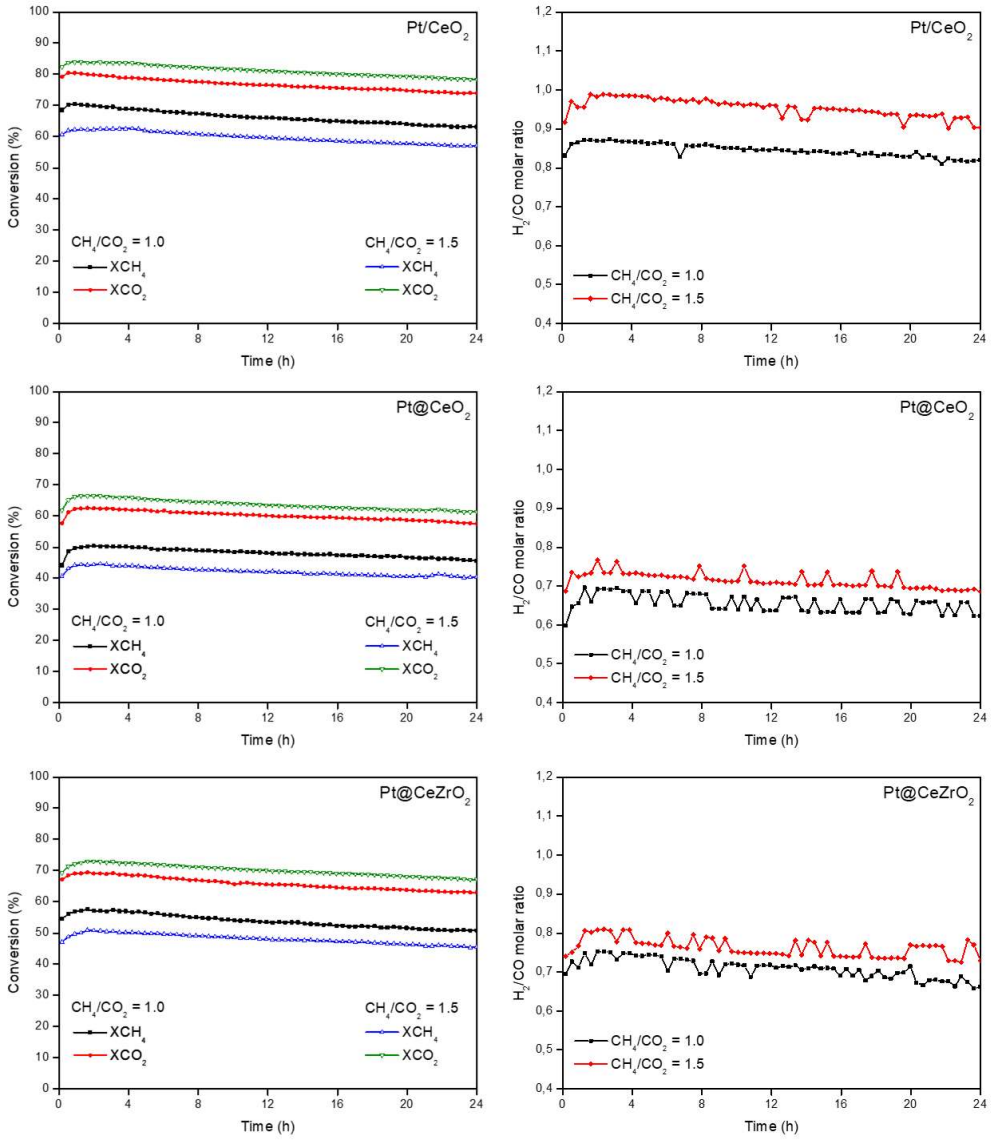

Figure 7.8. Catalytic stability tests at 800 °C using CH_4/CO_2 molar ratio of 1.0 and 1.5.

7.2.3 Characterization of post-reaction catalysts.

The deactivation by coke formation is one of the major problems to the design of catalysts for the DRM reaction. In order to investigate the amount of carbon and its morphology, the spent catalysts were analyzed by Raman, TEM and TPO. Raman spectra of the used catalysts after reaction under CH_4/CO_2 = 1.0 did not show evidences of carbon deposits. Increasing the CH_4/CO_2 ratio to 1.5 led to the appearance of the bands characteristic of carbon deposits (Fig. 7.9). The spectra exhibited three bands at 1334, 1582 and 1611 cm^{-1}. The G-band at 1582 cm^{-1} is ascribed to ordered carbon structures, whereas the D-band at 1334 cm^{-1} is correlated to disordered carbon structures (ALVAREZ et al., 2002). The D'-band at 1611 cm^{-1} is reported in the literature as

defects in the carbon structures (CUESTA et al., 1994). The presence of D-band suggests the formation of multi-walled carbon nanotubes (MWNCT) (BELIN; EPRON, 2005).

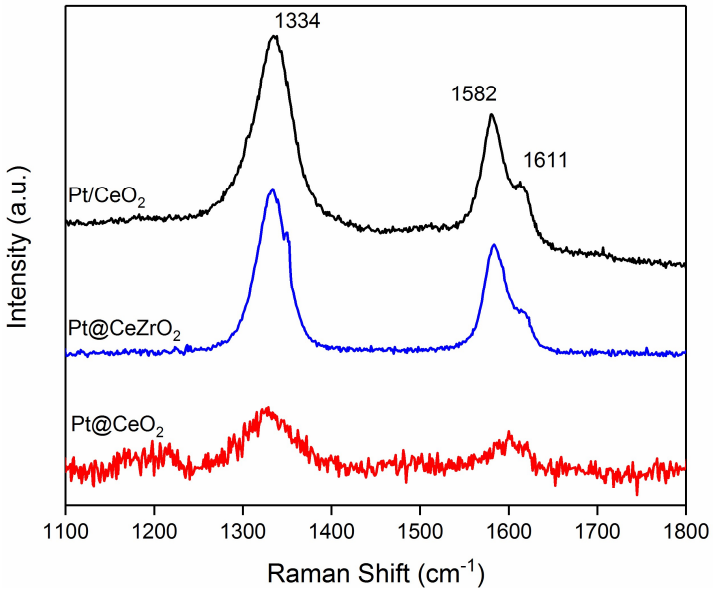

Figure 7.9. Raman spectra for the post-reaction samples (catalytic tests at T = 800 °C during 24 h and CH_4/CO_2 = 1.5).

The TPO experiments were performed to quantify the amount of carbon formed during the DRM using CH_4/CO_2 = 1.5 and the profiles are shown in Fig. 7.10. The TPO profiles presented two peaks at around 570 and 755 °C. However, the intensity of these peaks is clearly different depending on the catalysts. The intensity of the peak at low temperature region was higher in the TPO profile of Pt/CeO_2. $Pt@CeO_2$ and $Pt@CeZrO_2$ catalysts showed similar TPO profiles. According to the literature (DA FONSECA et al., 2019; DE LIMA et al., 2010; RABELO-NETO et al., 2018; SILVA et al., 2005), the peak located at 570 °C is ascribed to single-walled or multi-walled carbon filamentous and the peak at 755 °C is related to graphitic carbon species. Therefore, the TPO suggests the formation of carbon filaments which agrees with the Raman spectra. The formation of carbon filaments is preferential over Pt/CeO_2 catalyst prepared by impregnation. Table 7.7 lists the carbon formation rate for all catalysts. The rate of carbon formation for Pt/CeO_2 catalyst was two-fold higher than that for $Pt@CeO_2$ and $Pt@CeZrO_2$ catalysts. The higher resistance to carbon formation observed for the embedded catalysts is a consequence of the higher oxygen mobility in the materials. The capacity of the support to transfer oxygen from its structure to the coked metal

promotes the carbon removal mechanism (NORONHA et al., 2001). This carbon removal mechanism will be better discussed and described in single steps with *in-situ* DRIFTS in the next section.

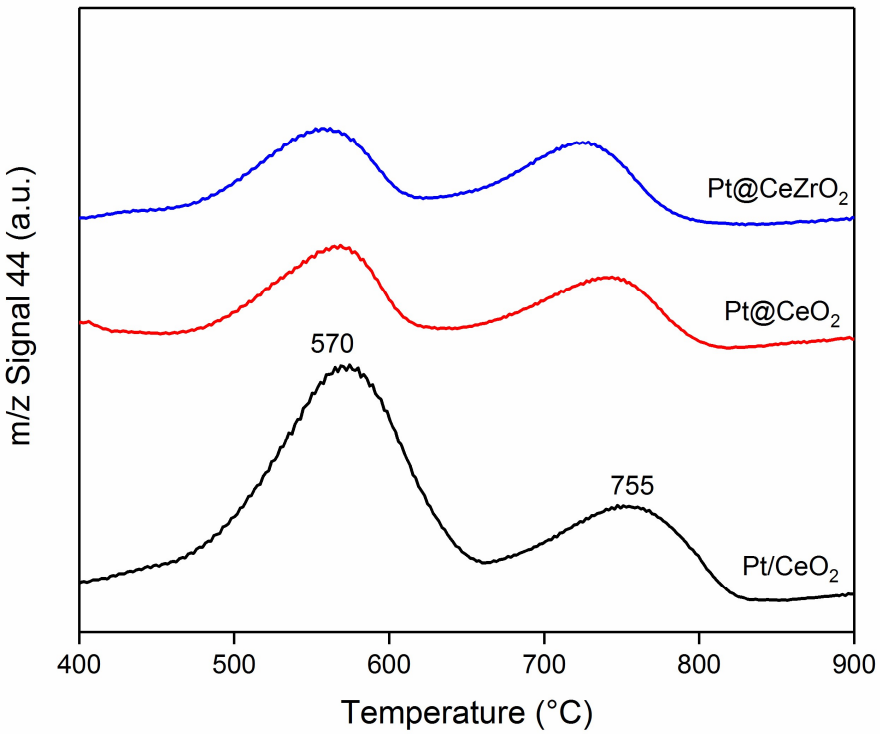

Figure 7.10. TPO analysis for the post-reaction samples (catalytic tests at T = 800 °C during 24 h and CH_4/CO_2 = 1.5).

Table 7.7. Rates of carbon formation during the DRM reaction (T = 800 °C during 24 h, CH_4/CO_2 = 1.5).

Catalyst	Rate of carbon formation ($mgC.g_{cat}^{-1}.h^{-1}$)
Pt/CeO_2	0.12
$Pt@CeO_2$	0.06
$Pt@CeZrO_2$	0.07

Fig. 7.11 shows the TEM images of the post-reaction Pt/CeO_2, $Pt@CeO_2$ and $Pt@CeZrO_2$ catalysts. The amount of carbon is very low and the images do not show carbon filaments on the TEM images of all samples, in agreement with TG analysis. However, it is possible to observe some particularity of Pt particles after reaction.

Pt/CeO_2 catalyst still maintained small Pt particles around 5 nm but its position more located in the boundary of the support, which can indicate a possible Pt sintering at long-time operation. The $Pt@CeO_2$ catalyst besides maintaining small Pt particles, the distribution over CeO_2 support is more homogeneous due the embedded structure. The $Pt@CeZrO_2$ catalyst presented a slightly increase in Pt size on the sample $Pt@CeZrO_2$ compared to reduced sample and it can explain the high intensity of peaks ascribed to carbon structures in Raman spectra for this catalyst. The Fig. 7.11 - E and F shows Pt particles around 20 nm.

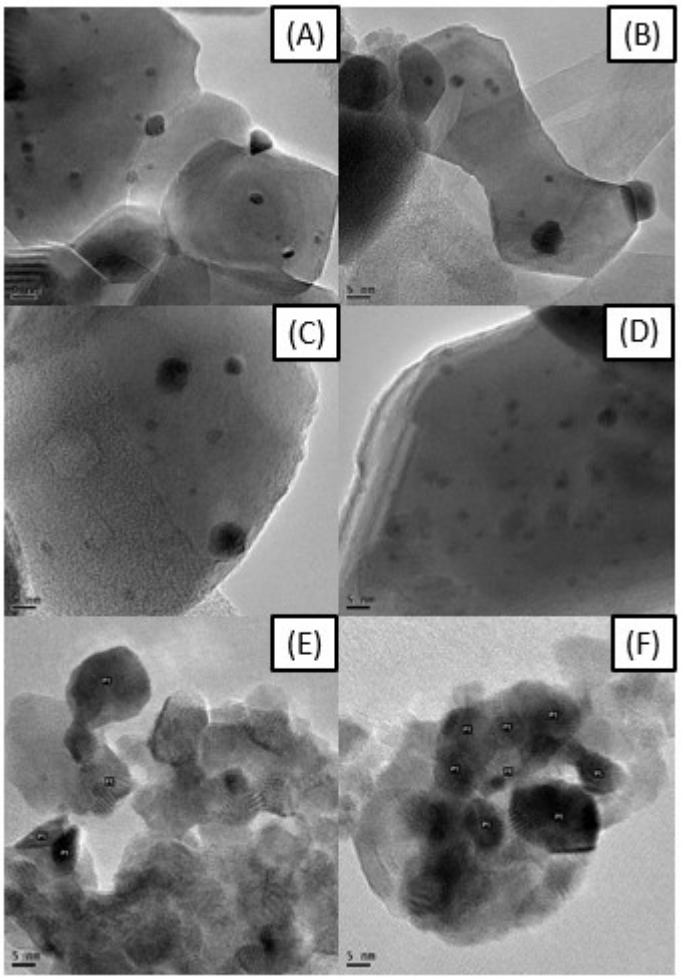

Figure 7.11. TEM images of (A, B) Pt/CeO_2, (C, D) $Pt@CeO_2$ and (E, F) $Pt@CeZrO_2$ catalysts after reaction at 800 °C and CH_4/CO_2 = 1.5.

7.2.4 Mechanism of carbon formation

To study the carbon removal mechanism, DRIFTS was performed switching the feed between CH_4/N_2 (Fig. 7.12), CO_2/N_2 (Fig. 7.13), CH_4/N_2 (Fig. 7.14) and CH_4/CO_2 (Fig. 7.15) flows (the last one as the reactional mixture CH_4:CO_2 = 1:1). The spectra were divided by region for better understanding due the difference in the scale. Under CH_4 atmosphere, Pt/CeO_2 catalyst presented a band centered at 1910 cm^{-1}, close to values obtained in the literature for bridged-CO adsorbed on Pt particles (POZDNYAKOVA et al., 2006). For $Pt@CeO_2$ and $Pt@CeZrO_2$ catalysts this band appears at 1890 and 1915 cm^{-1}, respectively. It is well accepted in the literature (O'CONNOR; MEUNIER; ROSS, 1998; ROSTRUP-NIELSEN, 1972; ROSTRUP-NIELSEN; HANSEN, 1993) that the CH_4 dehydrogenation occurs on the metal particle, generating reactive carbon structures, called as C_α. This carbon can polymerize towards inactive carbon species (C_β) or to be oxidized by oxygen from the support, generating CO (ROSTRUP-NIELSEN, 1974). The donation of oxygen changes the oxidation state of Ce^{4+} to Ce^{3+}, creating oxygen vacancies. The formation of Ce^{3+} species can be assumed to occur for Pt/CeO_2 catalyst due to the band observed at 2110 cm^{-1}, which are characteristic from the forbidden $^2F_{5/2} \rightarrow {}^2F_{7/2}$ electronic transition of Ce^{3+} (BINET; BADRI; LAVALLEY, 1994). The formation of Ce^{3+} species also occurs over $Pt@CeO_2$ and $Pt@CeZrO_2$ catalysts but it is more difficulty to observe its characteristic band due to the overlapping with other bands ascribed to CO linearly adsorbed in the range 2000-2200 cm^{-1}.

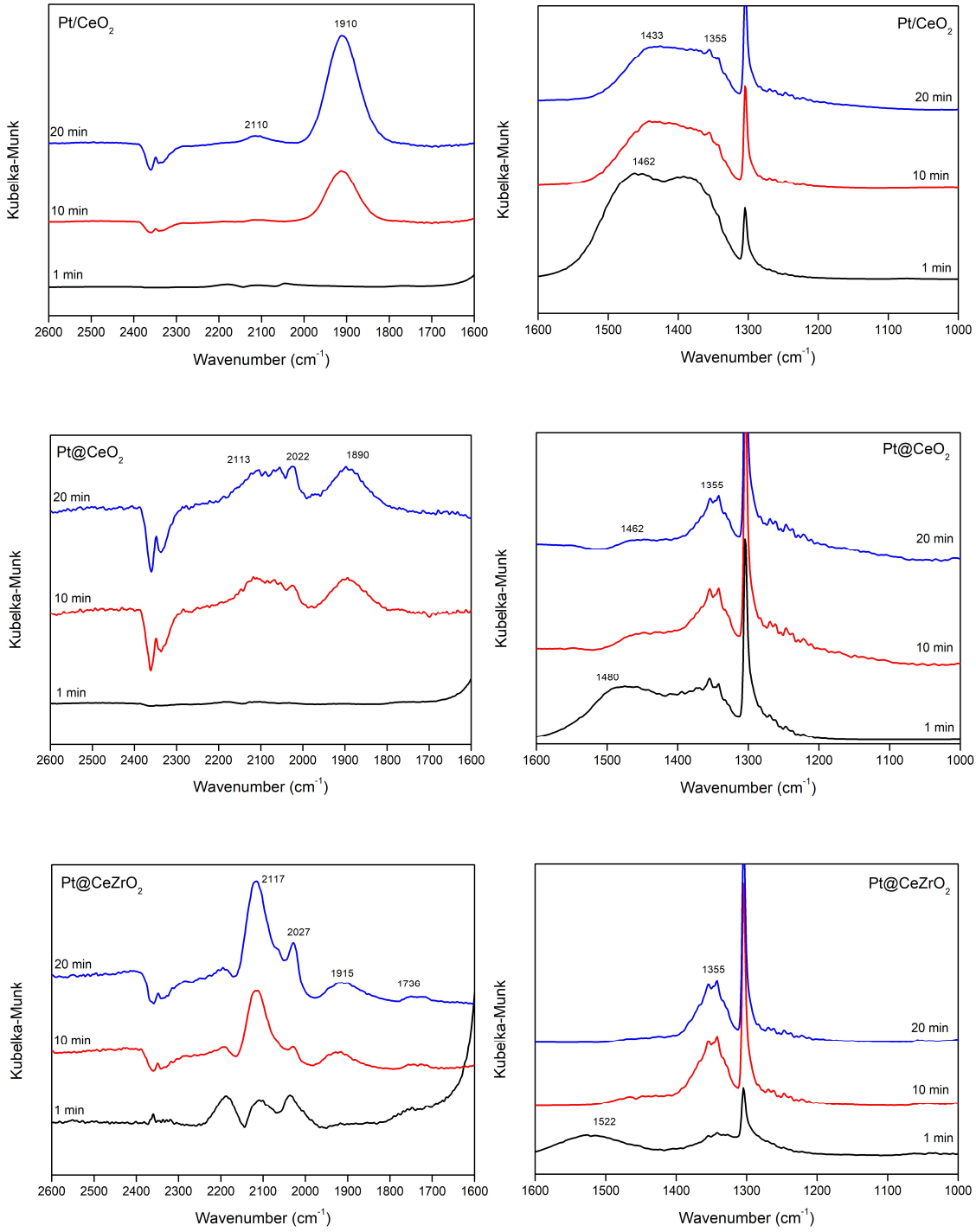

Figure 7.12. DRIFTS spectra obtained for different catalysts at 750 °C under flow of CH_4/N_2 after 1, 10 and 20 min (black, red and blue lines).

Bands assigned to C-H bond (VERMÖHLEN et al., 2000) were observed in the range of 1600 and 1000 cm^{-1}. The intense bands around 1300 and 1345 cm^{-1} are characteristic of CH_4 in gas phase. After 1 min under CH_4/N_2, the Pt/CeO_2 catalyst presented a band at 1462 cm^{-1} which shifted to 1433 cm^{-1} after 20 minutes. These bands are ascribed to $\delta(CH_2)_n$ vibration (VERMÖHLEN et al., 2000) and are attributed to coke precursors during the DRM. $Pt@CeO_2$ catalyst also presented band ascribed to $\delta(CH_2)_n$ vibration at 1480 cm^{-1}, which shifted to 1462 cm^{-1} after 20 minutes. On the other hand, $Pt@CeZrO_2$ presented a band at higher wavenumber (1522 cm^{-1}) and only CH_4 in gas phase was detected after 20 minutes. This finding indicates the efficiency of the embedded Ce-Zr catalyst to remove coke precursors, promoting a faster oxidation of these species to CO. Based on DRIFTS results, the first path in the carbon removal mechanism can be proposed as follows, in which * represents a metallic site, O_L is a lattice oxygen and V_O is an oxygen vacancy. Methane adsorbs on a metallic site (Eq.7.1) e follows dehydrogenation steps towards the formation of reactive carbon (Eq.7.2-7.5) which may abstract an oxygen from CeO_2 and $CeZrO_2$ lattice, creating an oxygen vacancy (Eq. 7.6).

$$CH_{4\,(g)} + * \rightleftharpoons CH_4* \quad (7.1)$$

$$CH_4* + * \rightleftharpoons CH_3* + H* \quad (7.2)$$

$$CH_3* + * \rightleftharpoons CH_2* + H* \quad (7.3)$$

$$CH_2* + * \rightleftharpoons CH* + H* \quad (7.4)$$

$$CH* + * \rightleftharpoons C* + H* \quad (7.5)$$

$$C* + O_L \rightleftharpoons CO* + V_O \quad (7.6)$$

Upon replacing CH_4/N_2 flow with CO_2/N_2, we observe an overlap of bands (1850 – 2250 cm^{-1}) assigned to different adsorbed CO species on the embedded $Pt@CeO_2$ and $Pt@CeZrO_2$ catalysts, indicating CO formation and desorption immediately and during the 20 min of experiment. That can be explained because the oxygen vacancies generated during the carbon oxidation step (Eq.7.6) are now occupied by CO_2, which supplies oxygen species and CO to the matrix surface (Eq.7.7). These (lattice) oxygen species react with C* (Eq.7.8), promoting the carbon removal from the metal particles by desorbing CO (Eq.7.9). On the other hand, CO formed from the CO_2

scission on oxygen vacancy (V_O) desorbs immediately from the CeO_2 or $CeZrO_2$ matrix (Eq.7.10). Besides adsorbing on oxygen vacancies, CO_2 acts as Lewis acid adsorbing on O_2^- surface ions (Eq.7.11) present on ceria forming different carbonate species (BINET; DATURI; LAVALLEY, 1999), as indicated by bands in the region of 1600 and 1000 cm^{-1}. The bands at 1490, 1385 and 1300 cm^{-1} are characteristic of monodentate carbonate, hydrogen carbonate and bidentate carbonate adsorbed on ceria, respectively (BINET; DATURI; LAVALLEY, 1999; POZDNYAKOVA et al., 2006). The results show that the bidentate carbonate is formed only in the embedded catalysts, preferably for Pt@$CeZrO_2$. The formation of bidentate carbonate species requires two lattice oxygen atoms bounded to Ce. This is an indicative that the embedded catalysts present more reactive oxygen on surface, as observed in the isotopic exchange measurements. The high amount of reactive oxygen and oxygen storage capacity observed for Pt@$CeZrO_2$ provides a catalyst with high oxygen mobility. Therefore, the second path of carbon removal mechanism can be proposed as follows, in which the subscribed Ce indicates an adsorption site in the CeO_2 or $CeZrO_2$ matrix:

$$CO_{2\,(g)} + V_O + Ce \rightleftharpoons CO_{Ce} + O_L \quad (7.7)$$

$$C^* + O_L \rightleftharpoons CO^* + V_O \quad (7.8)$$

$$CO^* \rightleftharpoons CO_{(g)} + * \quad (7.9)$$

$$CO_{Ce} \rightleftharpoons CO_{\,(g)} + Ce \quad (7.10)$$

$$CO_{2\,(g)} + O^{2-} \rightleftharpoons CO_3^{2-}{}_{Ce} \quad (7.11)$$

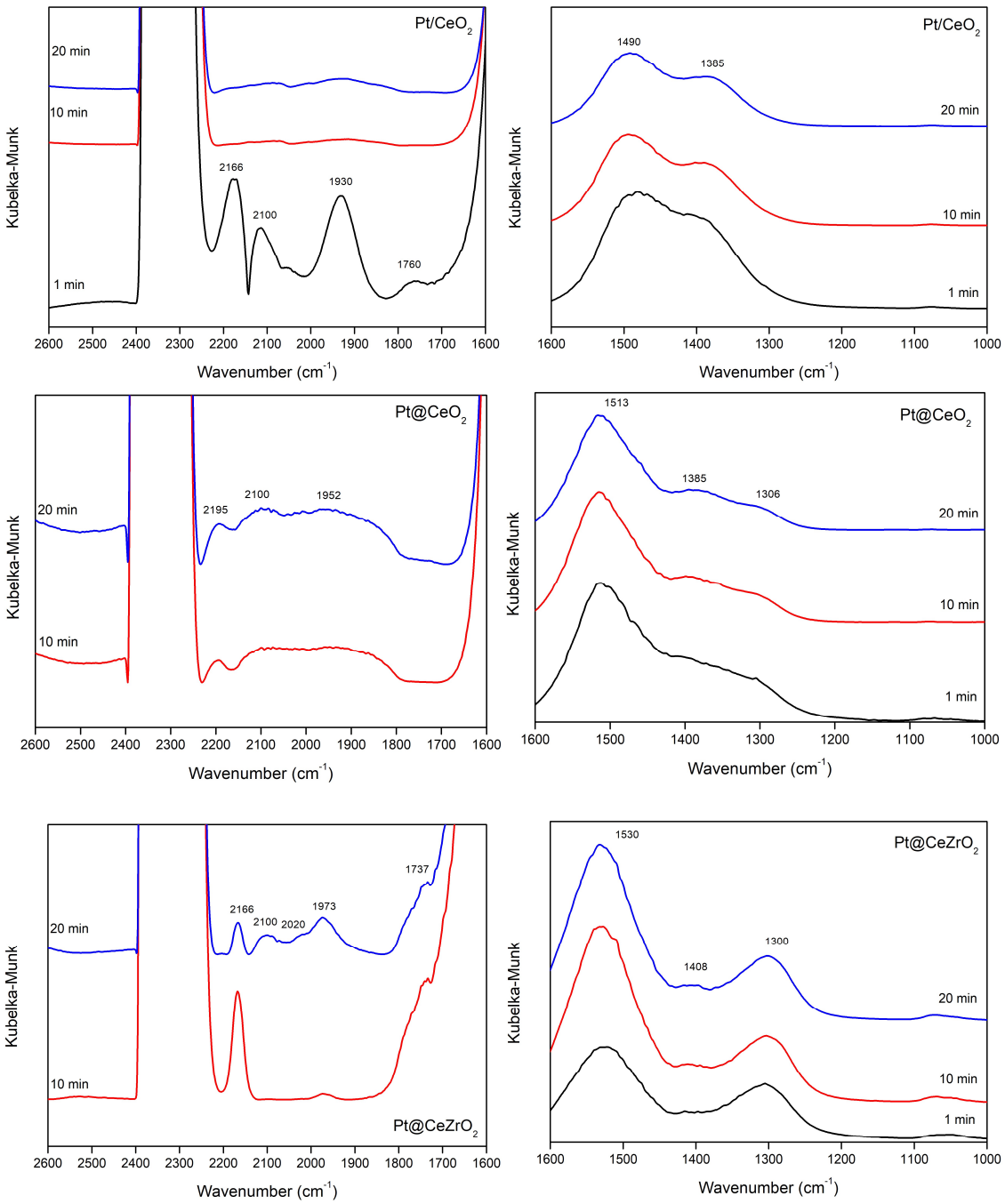

Figure 7.13. DRIFTS spectra obtained for different catalysts at 750 °C under flow of CO_2/N_2 after 1, 10 and 20 min (black, red and blue lines).

After 20 min, the flow was switched back to CH_4/N_2 and we observe different bands in the range 2600-1600 cm^{-1} (Fig. 7.14) which may be interpreted as carbon oxidation. All catalysts presented a band around 2150 cm^{-1} ascribed to CO in gas phase and a band at 1910 cm^{-1} assigned to CO adsorbed on Pt, as observed previously under CH_4/N_2 atmosphere. Furthermore, a consumption of carbonate species as suggested by the decrease of bands in the range 1600-1000 cm^{-1} is observed with increasing time.

Pt/CeO_2 and $Pt@CeO_2$ catalysts after 20 minutes under CH_4 atmosphere presented only a band at 1439 cm^{-1} ascribed to $\delta(CH_2)_n$ vibration, close to the value observed before the addition of CO_2. Therefore, the carbonates were consumed during the CH_4 decomposition. In this sense, the carbonates species are not spectators in the mechanism, but carbonates act supplying oxygen to the vacancies (Eq.7.12) which are generated during the carbon oxidation step (Eq.7.13). Similar mechanism was observed by O'Connor et al. (1998) during the DRM reaction using *in-situ* DRIFT spectroscopy. The $Pt@CeZrO_2$ catalyst even after 20 min still present the characteristic band of monodentate carbonate at 1500 cm^{-1}. The CH_4 decomposition is not favored on $Pt@CeZrO_2$ and the carbon oxidized was very low compared to other catalysts. The third part of carbon removal mechanism can be proposed:

$$C^* + O_L \rightleftharpoons CO^* + V_O \quad (7.12)$$

$$CO_3^{2-}{}_{Ce} + 2\ V_O + Ce \rightleftharpoons 2\ O_L + CO_{Ce} \quad (7.13)$$

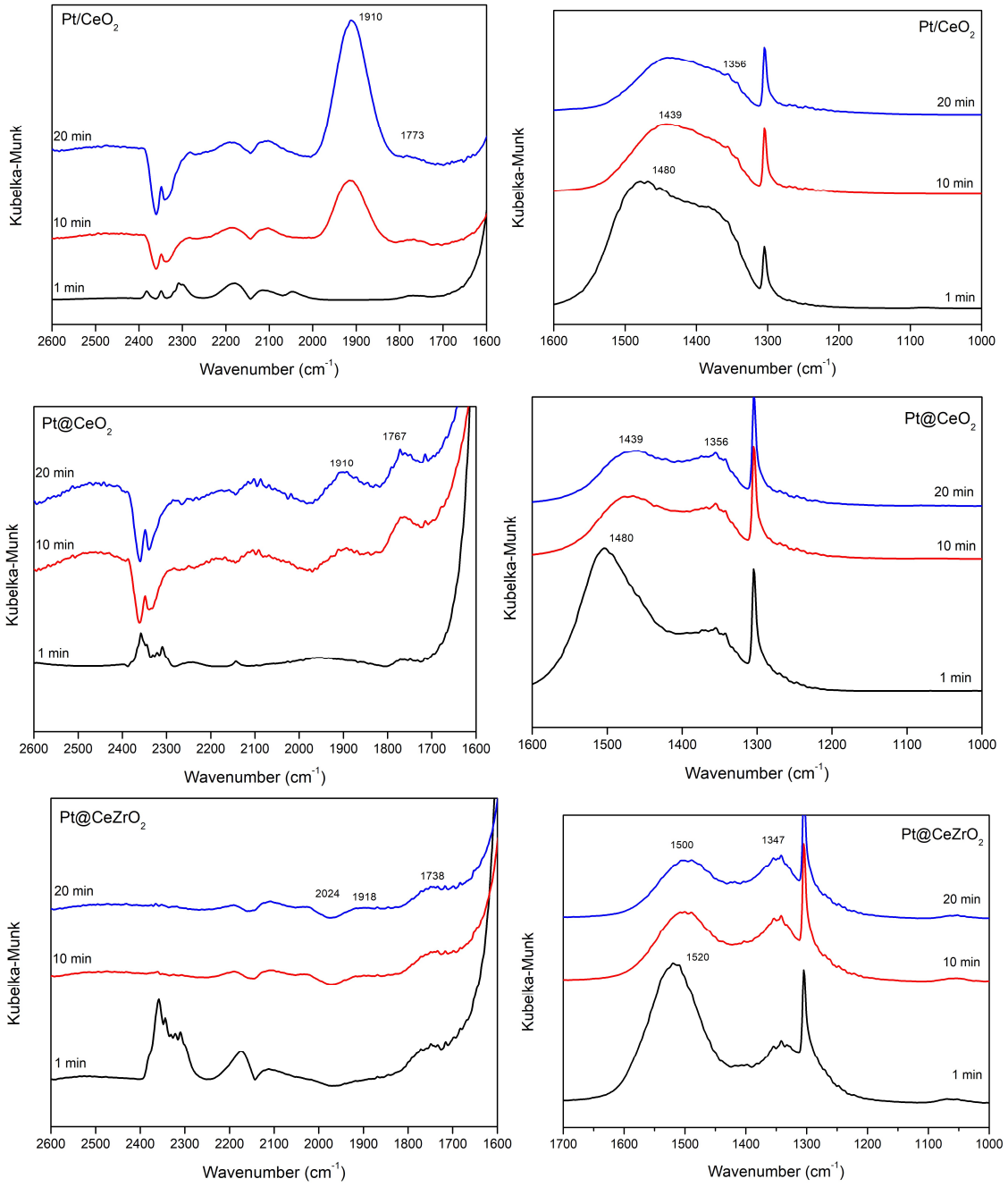

Figure 7.14. DRIFT spectra obtained for different catalysts at 750 °C under flow of CH_4/N_2 after 1, 10 and 20 min (black, red and blue lines).

Fig. 7.15 presents DRIFT spectra under dry reforming conditions for all catalysts by switching CH_4/N_2 flow to CH_4/CO_2. In the 2600 – 1600 cm^{-1} range (not shown), only CO and CO_2 in gas phase were observed. In the 1600 – 1000 cm^{-1} range, the catalysts presented the characteristic band of monodentate carbonate, which increases as a function of time, especially for $Pt@CeZrO_2$ catalyst.

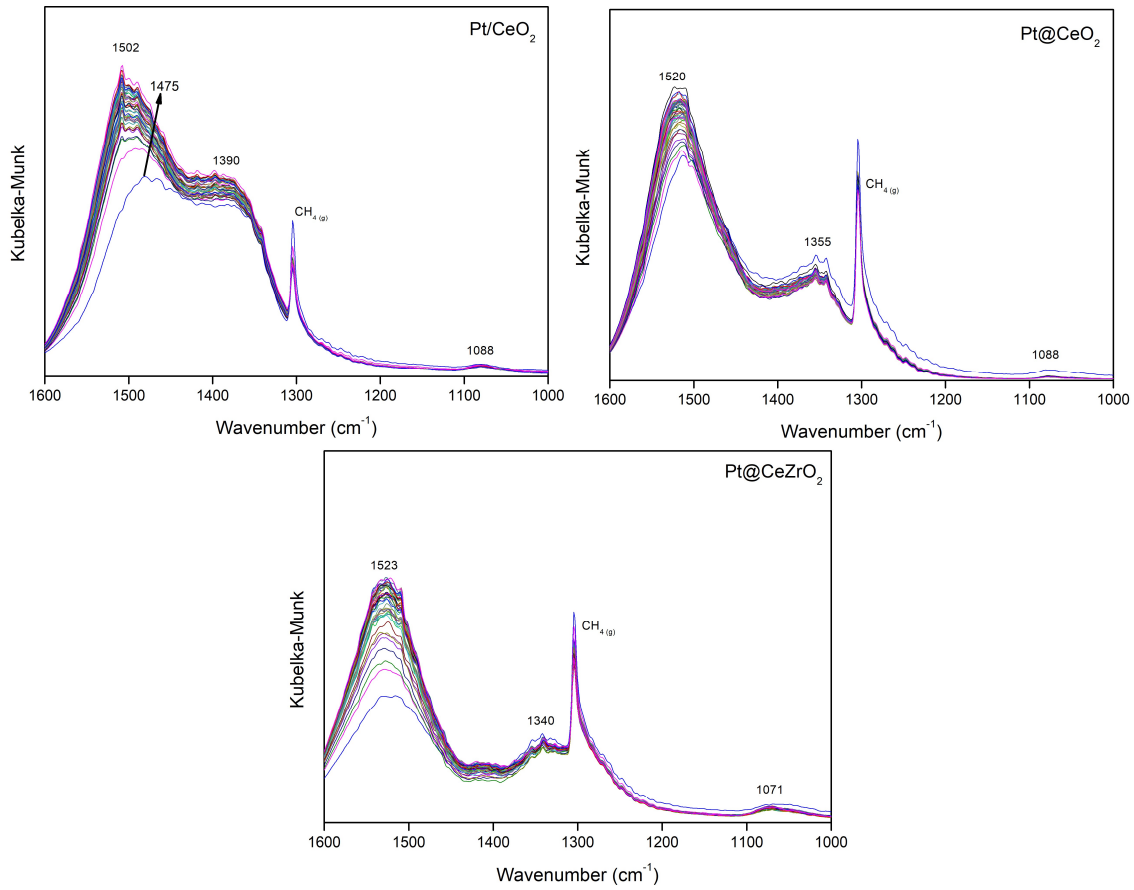

Figure 7.15. DRIFT spectra obtained for different catalysts at 750 °C under flow of CH_4/CO_2 up to 20 min.

7.2.5 The effect of Pt embedded into CeO_2 to increase the resistance to carbon formation during the DRM.

The mechanism of DRM is extensively studied in the literature (BRADFORD; VANNICE, 1999; WEI; IGLESIA, 2004a) and there is a consensus about the role of metal and support. The metal acts as site for CH_4 adsorption and subsequent dehydrogenation towards formation of carbon species which can be precursor of coke. The role of redox supports is to prevent the formation of coke by its oxidation using the lattice oxygen. Therefore, the reactivity of these lattice oxygen species and the interaction between the support and metal are important characteristics of the catalyst to promote the mechanism of carbon removal. Yan et al. (2019) have demonstrated the importance of reactive oxygen species in contact with Ni particles to prevent carbon formation on the Ni/CeO_2-SiO_2 catalyst. The interaction between Ni and lattice oxygen from CeO_2 allows the oxidation of C_α to CO before the formation of stable carbon structures, as observed in this present work by DRIFTS measurements.

The rate of CH_4 dehydrogenation is strongly affected by the metal particle size (ROSTRUP-NIELSEN, 1972). The presence of small particles inhibits the initiation step of coke formation (BITTER; SESHAN; LERCHER, 1999). In the Chapter 4 we performed a comparative study between embedded Ni@CeO_2 and Ni@$CeZrO_2$ catalysts and Ni/CeO_2 prepared by incipient wetness impregnation. Ni@$CeZrO_2$ catalytic system presented two remarkable features: (i) it avoided the embedded Ni particles to change in size; and (ii) enhanced the oxygen mobility, which both benefited the carbon removal mechanism. In the present work, we did not find evidences of metal sintering for the Pt/CeO_2 and Pt@CeO_2 catalysts here studied. Therefore, once these catalysts here presented Pt metal particles with similar small size, the mechanism of accumulation and removal of carbon species (coke) was influenced by the oxygen mobility rather than the metal particle size. The rates of carbon formation were relatively slow for all samples (Table 7.8) which can be specially ascribed to the small size of Pt nanoparticles, however the rates were slower to the embedded catalysts indicating that the highest oxygen mobility of these materials and ceria reducibility (which removes carbon more efficiently) leads to a more desirable balance between formation and removal of carbon. Raman spectra of post-reaction sample could show some points with high carbon formation for the Pt@$CeZrO_2$ catalyst even with the highest oxygen mobility in the catalyst series. It could be related to the Pt sintering observed after reaction by TEM images.

The oxygen mobility is strongly affected by the location of Pt in the catalyst. The embedded structure presented higher oxygen mobility due to the intimate contact between Pt and CeO_2 or $CeZrO_2$. The reactive oxygen species observed by TPR, ISOE and DRIFTS in our work promotes the carbon removal mechanism for Pt@CeO_2 and Pt@$CeZrO_2$ catalysts.

7.3 Conclusions

The preparation of Pt@CeO_2 and Pt@$CeZrO_2$ catalysts led to Pt nanoparticles embedded into ceria matrix, promoting the resistance to carbon formation during the dry reforming of biogas. The location of Pt in the embedded structure inhibited the sintering process at high temperature and enhanced the interaction with ceria. Furthermore, the reactivity of lattice oxygen species promotes the carbon removal mechanism, responsible for cleaning up the Pt nanoparticle surface. Therefore, the higher oxygen

mobility observed for the embedded catalysts resulted in an efficient mechanism of carbon removal during the dry reforming of biogas.

CHAPTER 8

Final Conclusions and Suggestions

8.1 General Conclusions

A detailed study about encapsulated metal catalysts in the Dry Reforming of Methane reaction was performed in this thesis. Firstly, was evaluated the embedded structure where metal nanoparticles are embedded into CeO_2 support. Ni@CeO_2 embedded catalyst was tested in the DRM in comparison with Ni/CeO_2 prepared by traditional impregnation. The results demonstrated that the encapsulated effect caused a decrease in the sintering process and increased the metal-support interaction, resulting in better oxygen mobility. The contribution of these two factors justified a low amount of coke observed on the Ni@CeO_2 catalysts, however, some coke formation was still detected.

Modifying the CeO_2 shell by doping with Gd, Sm, and Zr with Ce/dopant molar ratio = 4.0 led to different results as a function of the metal nature. The doping with Gd and Sm introduced oxygen vacancies by charge compensation due to the insertion of these cations into ceria lattice, but their presence reduced the ceria reducibility and the carbon removal mechanism was not favored resulting in higher carbon formation compared to undoped Ni@CeO_2 catalyst. The doping with Zr also introduced oxygen vacancies in the material through structural defects, and concomitantly the insertion of Zr into ceria lattice promoted the ceria bulk reduction, increasing the amount of reducible Ce. Furthermore, the addition of Zr increased thermal stability, avoiding Ni sintering during the reduction process. The Ni@$CeZrO_2$ catalyst presented high activity and no carbon formation was detected after 24 h on TOS. The increase of Zr in the Ce-Zr solid solution affected the catalytic activity, once the increase of Zr decreased the methane conversion. The low availability of oxygen vacancies on Ce/Zr = 1.0 and 0.25 decreased CO_2 adsorption rate over the support and more CO_2 was available to adsorb over Ni sites, promoting its re-oxidation and decreasing CH_4 adsorption sites.

The replacement of Ni by Pt leaded to a better understanding of the carbon removal mechanism over embedded catalysts since the effect of particle size was the same comparing both catalysts prepared by impregnation or sol-gel method.. Pt sintering was avoided on Pt/CeO_2; Pt@CeO_2 and Pt@$CeZrO_2$ and the differences on carbon formation are correlated only to oxygen mobility in the support. The *in-situ* DRIFTS analysis and Oxygen Isotopic Exchange showed that the embedded structures presented higher availability of surface oxygen species, which take place directly in the

carbon gasification process, decreasing the amount of carbon formed after 24 h on TOS with $CH_4/CO_2 = 1.5$.

In this work another encapsulated structure was analyzed, where Ni nanoparticles were dispersed into a redox mesoporous support. The addition of Ni by Evaporation Induced Self-Assembly (EISA) method increased Ni dispersion, resulting in smaller Ni nanoparticles in comparison to Ni addition by impregnation. The addition of Ce increased OSCC, responsible for increasing the density of surface oxygen species under DRM condition. The catalyst 10Ni-CeAl tested for 72 h with $CH_4/CO_2 = 1.0$ was stable without coke formation, which indicated that the EISA method was appropriate to produce Ni dispersed catalysts with high surface area and oxygen mobility for application in reforming reactions.

Therefore, this thesis allowed us to develop two different catalysts resistant to coke formation for application in the Dry Reforming of Methane. The methodology to encapsulate the metal by core@shell or mesoporosity implies obtaining important features for the catalysts: it avoids metal sintering and enhances the oxygen mobility over the catalyst. Ni@$CeZrO_2$ and 10Ni-CeAl arise as coke resistant catalysts for biogas upgrading for the production of syngas or hydrogen.

8.2 Suggestions

This work provided a detailed study about the characterization of resistant catalyst to coke formation. Therefore, some suggestions follow:

- Testing different reactions for which the deactivation by coke formation or sintering is a challenge in the process, such as the steam reforming, or the ones where the use of supports with high oxygen mobility are required.
- EXAFS study in Pt-based catalysts.
- Deposition of Ni@$CeZrO_2$ or 10Ni-CeAl over supports with high surface area, such as Al_2O_3.

CHAPTER 11

Bibliographic References

ABDULLAH, B.; ABD GHANI, N. A.; VO, D. V. N. Recent advances in dry reforming of methane over Ni-based catalysts. **Journal of Cleaner Production**, v. 162, p. 170–185, 2017.

ABDULRASHEED, A. et al. A review on catalyst development for dry reforming of methane to syngas: Recent advances. **Renewable and Sustainable Energy Reviews**, v. 108, p. 175–193, 2019.

AL-FATESH, A. S. Promotional effect of Gd over Ni/Y_2O_3 catalyst used in dry reforming of CH_4 for H_2 production. **International Journal of Hydrogen Energy**, v. 42, n. 30, p. 18805–18816, 2017.

ALVAREZ, W. E. et al. Characterization of Single-Walled Carbon Nanotubes (SWNTs) Produced by CO Disproportionation on Co−Mo Catalysts. **Chemistry of Materials**, v. 14, n. 4, p. 1853–1858, 2002.

AMENOMIYA, Y.; MORIKAWA, Y.; PLEIZIER, G. Infrared spectroscopy of $C^{18}O_2$ on alumina. **Journal of Catalysis**, v. 46, n. 3, p. 431–433, 1977.

AMIN, R. et al. Hydrogen production by corncob/CO_2 dry reforming over CeO_2 modified Ni-based MCM-22 catalysts. **International Journal of Hydrogen Energy**, v. 41, n. 30, p. 12869–12879, 2016.

ARAUJO, G. C. DE et al. Catalytic evaluation of perovskite-type oxide $LaNi_{1-x}Ru_xO_3$ in methane dry reforming. **Selected Contributions of the XX Ibero-American Symposium of Catalysis**, v. 133–135, p. 129–135, 2008.

ARIBI, K. et al. Structure, morphology and reducibility of ceria-doped zirconia. **Journal of Molecular Structure**, v. 1156, p. 369–376, 2018.

ARORA, S.; PRASAD, R. An overview on dry reforming of methane: strategies to reduce carbonaceous deactivation of catalysts. **RSC Advances**, v. 6, n. 110, p. 108668–108688, 2016.

AUGUSTO, B. L. et al. Nickel/gadolinium-doped ceria anode for direct ethanol solid oxide fuel cell. **International Journal of Hydrogen Energy**, v. 39, n. 21, p. 11196–11209, 2014.

AVETISOV, A. K. et al. Steady-state kinetics and mechanism of methane reforming with steam and carbon dioxide over Ni catalyst. **Journal of Molecular Catalysis A: Chemical**, v. 315, n. 2, p. 155–162, 2010.

AY, H.; ÜNER, D. Dry reforming of methane over CeO_2 supported Ni, Co and Ni–Co catalysts. **Applied Catalysis B: Environmental**, v. 179, p. 128–138, 2015.

BAKHMUTSKY, K. et al. A versatile route to core-shell catalysts: synthesis of dispersible M@oxide (M=Pd, Pt; oxide=TiO_2, ZrO_2) nanostructures by self-assembly. **ChemSusChem**, v. 5, n. 1, p. 140–8, 2012.

BAKTASH, E. et al. Alumina coated nickel nanoparticles as a highly active catalyst for dry reforming of methane. **Applied Catalysis B: Environmental**, v. 179, p. 122–127, 2015.

BALLARINI, A. D. et al. Reforming of CH_4 with CO_2 on Pt-supported catalysts: Effect of the support on the catalytic behavior. **Selected Contributions of the XIX Ibero American Catalysis Symposium**, v. 107–108, p. 481–486, 30 out. 2005.

BARRIO, L. et al. Unusual Physical and Chemical Properties of Ni in $Ce_{1-x}Ni_xO_{2-y}$ Oxides: Structural Characterization and Catalytic Activity for the Water Gas Shift Reaction. **The Journal of Physical Chemistry C**, v. 114, n. 29, p. 12689–12697, 2010.

BARTHOLOMEW, C. H. Carbon Deposition in Steam Reforming and Methanation. **Catalysis Reviews**, v. 24, n. 1, p. 67–112, 1982.

BECERRA, A. et al. Stable Ni/Al_2O_3 catalysts for methane dry reforming. **Granular Matter**, v. 3, n. 1, p. 79–81, 2001.

BEDRANE, S.; DESCORME, C.; DUPREZ, D. Investigation of the oxygen storage process on ceria- and ceria–zirconia-supported catalysts. **Catalysis Today**, v. 75, n. 1–4, p. 401–405, 2002.

BELIN, T.; EPRON, F. Characterization methods of carbon nanotubes: a review. **Materials Science and Engineering: B**, v. 119, n. 2, p. 105–118, 2005.

BIAN, Z.; KAWI, S. Sandwich-Like Silica@Ni@Silica Multicore-Shell Catalyst for the Low-Temperature Dry Reforming of Methane: Confinement Effect Against Carbon Formation. **ChemCatChem**, v. 10, n. 1, p. 320–328, 2018.

BINET, C.; BADRI, A.; LAVALLEY, J.-C. A Spectroscopic Characterization of the Reduction of Ceria from Electronic Transitions of Intrinsic Point Defects. **The Journal of Physical Chemistry**, v. 98, n. 25, p. 6392–6398, 1994.

BINET, C.; DATURI, M.; LAVALLEY, J.-C. IR study of polycrystalline ceria properties in oxidized and reduced states. **Catalysis Today**, v. 50, n. 2, p. 207–225, 1999.

BITTER, J. H. et al. The role of the oxidic support on the deactivation of Pt catalysts during the CO_2 reforming of methane. **Second Japan-EC Joint Workshop on the Frontiers of Catalytic Science and Technology for Energy, Environment and Risk Prevention**, v. 29, n. 1, p. 349–353, 1996.

BITTER, J. H.; SESHAN, K.; LERCHER, J. A. Mono and Bifunctional Pathways of CO_2/CH_4 Reforming over Pt and Rh Based Catalysts. **Journal of Catalysis**, v. 176, n. 1, p. 93–101, 1998.

BITTER, J. H.; SESHAN, K.; LERCHER, J. A. Deactivation and Coke Accumulation during CO_2/CH_4 Reforming over Pt Catalysts. **Journal of Catalysis**, v. 183, n. 2, p. 336–343, 1999.

BOND, G. C.; GELSTHORPE, M. R. A study of EUROPT-1 by temperature-programmed reduction. **Applied Catalysis**, v. 35, n. 1, p. 169–176, 1987.

BONIFACIO, C. S. et al. Thermal Stability of Core–Shell Nanoparticles: A Combined in Situ Study by XPS and TEM. **Chemistry of Materials**, v. 27, n. 20, p. 6960–6968, 2015.

BONK, A. et al. Low-Temperature Reducibility of $M_xCe_{1-x}O_2$ (M = Zr, Hf) under Hydrogen Atmosphere. **The Journal of Physical Chemistry C**, v. 120, n. 1, p. 118–125, 2015.

BONURA, G.; CANNILLA, C.; FRUSTERI, F. Ceria–gadolinia supported NiCu catalyst: A suitable system for dry reforming of biogas to feed a solid oxide fuel cell (SOFC). **Applied Catalysis B: Environmental**, v. 121–122, p. 135–147, 2012.

BORCHERT, H. et al. Nanostructured, Gd-Doped Ceria Promoted by Pt or Pd: Investigation of the Electronic and Surface Structures and Relations to Chemical Properties. **The Journal of Physical Chemistry B**, v. 109, n. 43, p. 20077–20086, 2005.

BOYANO, A. et al. Conventional and advanced exergoenvironmental analysis of a steam methane reforming reactor for hydrogen production. **Journal of Cleaner Production**, v. 20, n. 1, p. 152–160, 2012.

BRADFORD, M. C. J.; VANNICE, M. A. CO_2 Reforming of CH_4. **Catalysis Reviews**, v. 41, n. 1, p. 1–42, 1999.

CAMPBELL, C. T.; PEDEN, C. H. F. Oxygen Vacancies and Catalysis on Ceria Surfaces. **Science**, v. 309, n. 5735, p. 713, 2005.

CARGNELLO, M. et al. Synthesis of dispersible Pd@CeO_2 core-shell nanostructures by self-assembly. **Journal of the American Chemical Society**, v. 132, n. 4, p. 1402–1409, 2010.

CHEIN, R.-Y.; FUNG, W.-Y. Syngas production via dry reforming of methane over CeO_2 modified Ni/Al_2O_3 catalysts. **A Special Issue on Advanced Hydrogen Production Technologies**, v. 44, n. 28, p. 14303–14315, 2019.

CHEN, C. et al. High-temperature calcination improves the catalytic properties of alumina-supported Pd@ceria prepared by self assembly. **Journal of Catalysis**, v. 306, p. 109–115, 2013a.

CHEN, J. et al. Effect of preparation methods on structure and performance of Ni/$Ce_{0.75}Zr0_{.25}O_2$ catalysts for CH_4–CO_2 reforming. **Fuel**, v. 87, n. 13, p. 2901–2907, 2008.

CHEN, W. et al. High carbon-resistance Ni/$CeAlO_3$-Al_2O_3 catalyst for CH_4/CO_2 reforming. **Applied Catalysis B: Environmental**, v. 136–137, p. 260–268, 2013b.

CUESTA, A. et al. Raman microprobe studies on carbon materials. **Carbon**, v. 32, n. 8, p. 1523–1532, 1994.

DA FONSECA, R. O. et al. Study of the effect of Gd-doping ceria on the performance of $Pt/GdCeO_2/Al_2O_3$ catalysts for the dry reforming of methane. **Catalysis Today**, 2019.

DA SILVA, A. A. A. et al. Effect of the type of ceria dopant on the performance of Ni/CeO_2 SOFC anode for ethanol internal reforming. **Applied Catalysis B: Environmental**, v. 206, p. 626–641, 2017.

DAMYANOVA, S. et al. The effect of CeO2 on the surface and catalytic properties of $Pt/CeO_2–ZrO_2$ catalysts for methane dry reforming. **Applied Catalysis B: Environmental**, v. 89, n. 1, p. 149–159, 2009.

DAMYANOVA, S. et al. Ni-based catalysts for reforming of methane with CO_2. **International Journal of Hydrogen Energy**, v. 37, n. 21, p. 15966–15975, 2012.

DAN, M.; MIHET, M.; LAZAR, M. D. Hydrogen and/or syngas production by combined steam and dry reforming of methane on nickel catalysts. **International Journal of Hydrogen Energy**, v. 45, n. 49, p. 26254-26264,2020.

DAS, S. et al. Silica–Ceria sandwiched Ni core–shell catalyst for low temperature dry reforming of biogas: Coke resistance and mechanistic insights. **Applied Catalysis B: Environmental**, v. 230, n. February, p. 220–236, 2018.

DE LIMA, S. M. et al. Evaluation of the performance of Ni/La_2O_3 catalyst prepared from $LaNiO_3$ perovskite-type oxides for the production of hydrogen through steam reforming and oxidative steam reforming of ethanol. **Applied Catalysis A: General**, v. 377, n. 1, p. 181–190, 2010.

DEGUCHI, H. et al. EXAFS study of doped ceria using multiple data set fit. **Solid State Ionics**, v. 176, n. 23, p. 1817–1825, 2005.

DOU, J. et al. Sandwiched $SiO_2@Ni@ZrO_2$ as a coke resistant nanocatalyst for dry reforming of methane. **Applied Catalysis B: Environmental**, v. 254, p. 612–623, 2019.

DUARTE, R. B. et al. Study of Sm_2O_3-doped CeO_2–Al_2O_3-supported Pt catalysts for partial CH_4 oxidation. **Applied Catalysis A: General**, v. 399, n. 1–2, p. 134–145, 2011.

DUPREZ, D. et al. Oxygen storage and mobility on model three-way catalysts. **Topics in Catalysis**, v. 16/17, n. 1/4, p. 49–56, 2001.

DURGASRI, D. N.; VINODKUMAR, T.; REDDY, B. M. Facile synthesis of catalytically active CeO2–Gd2O3solid solutions for soot oxidation. **Journal of Chemical Sciences**, v. 126, n. 2, p. 429–435, 2014.

ELURI, R.; PAUL, B. Synthesis of nickel nanoparticles by hydrazine reduction: mechanistic study and continuous flow synthesis. **Journal of Nanoparticle Research**, v. 14, n. 4, p. 1–14, 2012.

FANG, X. et al. Methane Dry Reforming over Coke-Resistant Mesoporous Ni-Al_2O_3 Catalysts Prepared by Evaporation-Induced Self-Assembly Method. **ChemCatChem**, v. 7, n. 22, p. 3753–3762, 2015.

FARIA, E. C. et al. Hydrogen production through CO_2 reforming of methane over Ni/$CeZrO_2$/Al_2O_3 catalysts. **Natural Gas Conversion the Status and Potentials in the Light of NGCS-10**, v. 228, p. 138–144, 2014.

FERREIRA-APARICIO, P. et al. A Transient Kinetic Study of the Carbon Dioxide Reforming of Methane over Supported Ru Catalysts. **Journal of Catalysis**, v. 184, n. 1, p. 202–212, 1999.

FERREIRA-APARICIO, P. et al. Mechanistic aspects of the dry reforming of methane over ruthenium catalysts. **Applied Catalysis A: General**, v. 202, n. 2, p. 183–196, 2000.

FERREIRA-APARICIO, P.; GUERRERO-RUIZ, A.; RODRÍGUEZ-RAMOS, I. Comparative study at low and medium reaction temperatures of syngas production by methane reforming with carbon dioxide over silica and alumina supported catalysts. **Applied Catalysis A: General**, v. 170, n. 1, p. 177–187, 1998.

FIGUEROA, S. J. A.; PRESTIPINO, C. PrestoPronto: a code devoted to handling large data sets. **Journal of Physics: Conference Series**, v. 712, n. 1, p. 12–16, 2016.

FONSECA, J. et al. Unexpected redox behavior of large surface alumina containing highly dispersed ceria nanoclusters. **Nanoscale**, v. 11, n. 3, p. 1273–1285, 2019.

FONSECA, J. DA S. L. et al. Cooperative effect between copper and gold on ceria for CO-PROX reaction. **Recent developments in the characterization and application of nanostructured ceria based catalysts-Prof. Serafin Bernal Festschrift**, v. 180, n. 1, p. 34–41, 2012.

FORNASIERO, P. et al. Rh-Loaded CeO_2-ZrO_2 Solid-Solutions as Highly Efficient Oxygen Exchangers: Dependence of the Reduction Behavior and the Oxygen Storage Capacity on the Structural-Properties. **Journal of Catalysis**, v. 151, n. 1, p. 168–177, 1995.

FORZATTI, P.; LIETTI, L. Catalyst deactivation. **Catalysis Today**, v. 52, n. 2, p. 165–181, 1999.

FU, Y.-P.; CHEN, S.-H.; HUANG, J.-J. Preparation and characterization of $Ce_{0.8}M_{0.2}O_{2-\delta}$ (M=Y, Gd, Sm, Nd, La) solid electrolyte materials for solid oxide fuel cells. **International Journal of Hydrogen Energy**, v. 35, n. 2, p. 745–752, 2010.

GOLUNSKI, S. E. et al. Origins of low-temperature three-way activity in Pt/CeO_2. **Applied Catalysis B: Environmental**, v. 5, n. 4, p. 367–376, 1995.

GROSSO, D. et al. Fundamentals of Mesostructuring Through Evaporation-Induced Self-Assembly. **Advanced Functional Materials**, v. 14, n. 4, p. 309–322, 2004.

GUNDUZ MERIC, G.; ARBAG, H.; DEGIRMENCI, L. Coke minimization via SiC formation in dry reforming of methane conducted in the presence of Ni-based core–shell microsphere catalysts. **International Journal of Hydrogen Energy**, v. 42, n. 26, p. 16579–16588, 2017.

GURAV, H. R. et al. Influence of preparation method on activity and stability of Ni catalysts supported on Gd doped ceria in dry reforming of methane. **Journal of CO_2 Utilization**, v. 20, p. 357–367, 2017.

HAN, B. et al. Syngas production from methane steam reforming and dry reforming reactions over sintering-resistant Ni@SiO_2 catalyst. **Research on Chemical Intermediates**, v. 46, p. 1–14, 2019.

HARSHINI, D. et al. Catalytic Hydrogen Production via Dry Reforming of Methane Over Ni/$Ce_{0.65}Hf_{0.25}M_{0.1}O_{2-\delta}$ (M = Tb, Sm, Nd, Pr and La). **Catalysis Letters**, v. 144, n. 4, p. 656–662, 2014.

HELVEG, S.; SEHESTED, J.; ROSTRUP-NIELSEN, J. R. Whisker carbon in perspective. **Catalysis Today**, v. 178, p. 42–46, 2011.

HENNINGS, U.; REIMERT, R. Investigation of the structure and the redox behavior of gadolinium doped ceria to select a suitable composition for use as catalyst support in the steam reforming of natural gas. **Applied Catalysis A: General**, v. 325, n. 1, p. 41–49, 2007.

HORI, C. E. et al. Thermal stability of oxygen storage properties in a mixed CeO_2-ZrO_2 system. **Applied Catalysis B: Environmental**, v. 16, n. 2, p. 105–117, 1998.

HU, Y. H.; RUCKENSTEIN, E. Catalytic Conversion of Methane to Synthesis Gas by Partial Oxidation and CO_2 Reforming. **Advances in Catalysis**, v. 48, p. 297-345, 2004.

HUANG, Q. et al. Synthesis of a Highly Active and Stable Nickel-Embedded Alumina Catalyst for Methane Dry Reforming: On the Confinement Effects of Alumina Shells for Nickel Nanoparticles. **ChemCatChem**, v. 9, n. 18, p. 3563–3571, 2017.

International Energy Agency (IEA), Global Energy & CO_2 Status Report 2019, https://www.iea.org/reports/global-energy-co2-status-report-2019, Paris, 2019.

Intergovernmental Panel on Climate Change (IPCC)**,** Renewable energy sources and climate change mitigation: special Report of the Intergovernmental Panel on Climate Change. **Cambridge University Press,** New York, 2012.

Intergovernmental Panel on Climate Change (IPCC), Climate Change 2007: The Physical Science Basis EXIT. Contribution of Working Group I to the Fourth Assessment Report of the Intergovernmental Panel on Climate Change. **Cambridge University Press,** Cambridge, United Kingdom, 2007.

IZQUIERDO, U. et al. Tri-reforming: A new biogas process for synthesis gas and hydrogen production. **International Journal of Hydrogen Energy**, v. 38, n. 18, p. 7623–7631, 2013.

JACOBS, G. et al. Low Temperature Water–Gas Shift: Role of Pretreatment on Formation of Surface Carbonates and Formates. **Catalysis Letters**, v. 96, n. 1, p. 97–105, 2004.

JANG, W.-J. et al. A review on dry reforming of methane in aspect of catalytic properties. **Catalysis Today**, v. 324, p. 15–26, 2019.

JIANG, S. et al. Insight into the reaction mechanism of CO_2 activation for CH_4 reforming over NiO-MgO: A combination of DRIFTS and DFT study. **Applied Surface Science**, v. 416, p. 59–68, 2017.

KAMBOLIS, A. et al. Ni/CeO_2-ZrO_2 catalysts for the dry reforming of methane. **Applied Catalysis A: General**, v. 377, n. 1, p. 16–26, 2010.

KARACA, T.; ALTINÇEKIÇ, T. G.; FARUK ÖKSÜZÖMER, M. Synthesis of nanocrystalline samarium-doped CeO_2 (SDC) powders as a solid electrolyte by using a simple solvothermal route. **Ceramics International**, v. 36, n. 3, p. 1101–1107, 2010.

KARAM, L. et al. Nanostructured Nickel Aluminate as a Key Intermediate for the Production of Highly Dispersed and Stable Nickel Nanoparticles Supported within Mesoporous Alumina for Dry Reforming of Methane. **Molecules (Basel, Switzerland)**, v. 24, n. 22, p. 4107, 2019.

KAŠPAR, J.; FORNASIERO, P.; GRAZIANI, M. Use of CeO_2-based oxides in the three-way catalysis. **Catalysis Today**, v. 50, n. 2, p. 285–298, 1999.

KATHIRASER, Y. et al. Highly active and coke resistant Ni/SiO_2 catalysts for oxidative reforming of model biogas: Effect of low ceria loading. **Journal of CO_2 Utilization**, v. 19, p. 284–295, 2017.

KAYDOUH, M.-N. et al. Effect of the order of Ni and Ce addition in SBA-15 on the activity in dry reforming of methane. **GECat 2014 – Advances and prospects in heterogeneous catalysis**, v. 18, n. 3, p. 293–301, 2015.

KHAJENOORI, M.; REZAEI, M.; MESHKANI, F. Dry reforming over CeO_2-promoted Ni/MgO nano-catalyst: Effect of Ni loading and CH_4/CO_2 molar ratio. **Journal of Industrial and Engineering Chemistry**, v. 21, p. 717–722, 2015.

KIM, J.-H. et al. Effect of metal particle size on coking during CO_2 reforming of CH_4 over Ni–alumina aerogel catalysts. **Applied Catalysis A: General**, v. 197, n. 2, p. 191–200, 2000.

KITLA, A.; SAFONOVA, O. V.; FÖTTINGER, K. Infrared Studies on Bimetallic Copper/Nickel Catalysts Supported on Zirconia and Ceria/Zirconia. **Catalysis Letters**, v. 143, n. 6, p. 517–530, 2013.

KOZLOV, A. I. et al. Effect of Preparation Method and Redox Treatment on the Reducibility and Structure of Supported Ceria–Zirconia Mixed Oxide. **Journal of Catalysis**, v. 209, n. 2, p. 417–426, 2002.

KUEMMEL, M. et al. Thermally Stable Nanocrystalline γ-Alumina Layers with Highly Ordered 3D Mesoporosity. **Angewandte Chemie**, v. 117, n. 29, p. 4665–4668, 2005.

KUHN, M. et al. Structural characterization and oxygen nonstoichiometry of ceria-zirconia ($Ce_{1-x}Zr_xO_{2-\delta}$) solid solutions. **Acta Materialia**, v. 61, n. 11, p. 4277–4288, 2013.

LAFAYE, G.; BARBIER, J.; DUPREZ, D. Impact of cerium-based support oxides in catalytic wet air oxidation: Conflicting role of redox and acid–base properties. **Catalysis by ceria**, v. 253, p. 89–98, 2015.

LAOSIRIPOJANA, N.; ASSABUMRUNGRAT, S. Catalytic dry reforming of methane over high surface area ceria. **Applied Catalysis B: Environmental**, v. 60, n. 1, p. 107–116, 2005.

LAOSIRIPOJANA, N.; SUTTHISRIPOK, W.; ASSABUMRUNGRAT, S. Synthesis gas production from dry reforming of methane over CeO_2 doped Ni/Al_2O_3: Influence of the doping ceria on the resistance toward carbon formation. **Chemical Engineering Journal**, v. 112, n. 1, p. 13–22, 2005.

LE, T. A. et al. CO and CO_2 methanation over supported Ni catalysts. **Special issue of International Symposium on Catalytic Conversion of Energy and Resources**, v. 293–294, p. 89–96, 2017.

LEE, J. et al. How Pt Interacts with CeO_2 under the Reducing and Oxidizing Environments at Elevated Temperature: The Origin of Improved Thermal Stability of Pt/CeO_2 Compared to CeO_2. **The Journal of Physical Chemistry C**, v. 120, n. 45, p. 25870–25879, 2016.

LI, C.; CHEN, Y.-W. Temperature-programmed-reduction studies of nickel oxide/alumina catalysts: effects of the preparation method. **Thermochimica Acta**, v. 256, n. 2, p. 457–465, 1995.

LI, M.; VAN VEEN, A. C. Tuning the catalytic performance of Ni-catalyzed dry reforming of methane and carbon deposition via $Ni\text{-}CeO_{2-x}$ interaction. **Applied Catalysis B: Environmental**, v. 237, p. 641–648, 2018.

LI, P. et al. A review on oxygen storage capacity of CeO_2-based materials: Influence factors, measurement techniques, and applications in reactions related to catalytic automotive emissions control. **Catalysis Today**, v. 327, p. 90–115, 2019.

LI, S. et al. A $Ni@ZrO_2$ nanocomposite for ethanol steam reforming: enhanced stability via strong metal–oxide interaction. **Chemical Communications**, v. 49, n. 39, p. 4226–4228, 2013.

LI, S.; GONG, J. Strategies for improving the performance and stability of Ni-based catalysts for reforming reactions. **Chemical Society Reviews**, v. 43, n. 21, p. 7245–7256, 2014.

LI, Z. et al. Design of highly stable and selective core/yolk–shell nanocatalysts—A review. **Applied Catalysis B: Environmental**, v. 188, p. 324–341, 2016.

LI, Z.; WANG, Z.; KAWI, S. Sintering and Coke Resistant Core/Yolk Shell Catalyst for Hydrocarbon Reforming. **ChemCatChem**, v. 11, n. 1, p. 202–224, 2019.

LIANG, T.-Y.; CHEN, H.-H.; TSAI, D.-H. Nickel hybrid nanoparticle decorating on alumina nanoparticle cluster for synergistic catalysis of methane dry reforming. **Fuel Processing Technology**, v. 201, p. 106335, 2020.

LIM, Z.-Y. et al. Porosity effect on ZrO_2 hollow shells and hydrothermal stability for catalytic steam reforming of methane. **Journal of Materials Chemistry A**, v. 4, n. 1, p. 153–159, 2016.

LIOTTA, L. F. et al. Influence of the SMSI effect on the catalytic activity of a Pt(1%)/$Ce_{0.6}Zr_{0.4}O_2$ catalyst: SAXS, XRD, XPS and TPR investigations. **Applied Catalysis B: Environmental**, v. 48, n. 2, p. 133–149, 2004.

LIU, H. et al. La-promoted Ni-hydrotalcite-derived catalysts for dry reforming of methane at low temperatures. **Fuel**, v. 182, p. 8–16, 2016.

LIU, J. Catalysis by Supported Single Metal Atoms. **ACS Catalysis**, v. 7, n. 1, p. 34–59, 2016.

LUISETTO, I. et al. Ni/CeO2–Al2O3 catalysts for the dry reforming of methane: The effect of $CeAlO_3$ content and nickel crystallite size on catalytic activity and coke resistance. **Applied Catalysis A: General**, v. 500, p. 12–22, 2015.

LUISETTO, I. et al. Dry reforming of methane over Ni supported on doped CeO_2: New insight on the role of dopants for CO_2 activation. **Journal of CO_2 Utilization**, v. 30, p. 63–78, 2019.

LUNSFORD, J. H. Catalytic conversion of methane to more useful chemicals and fuels: A challenge for the 21st century. **Catalysis Today**, v. 63, n. 2–4, p. 165–174, 2000.

LUSTEMBERG, P. G. et al. Room-Temperature Activation of Methane and Dry Reforming with CO2 on Ni-CeO_2(111) Surfaces: Effect of Ce^{3+} Sites and Metal–Support Interactions on C–H Bond Cleavage. **ACS Catalysis**, v. 6, n. 12, p. 8184–8191, 2016.

MA, Q. et al. Combined methane dry reforming and methane partial oxidization for syngas production over high dispersion Ni based mesoporous catalyst. **Fuel Processing Technology**, v. 188, p. 98–104, 2019.

MADIER, Y. et al. Oxygen Mobility in CeO_2 and $Ce_xZr_{(1-x)}O_2$ Compounds: Study by CO Transient Oxidation and $^{18}O/^{16}O$ Isotopic Exchange. **The Journal of Physical Chemistry B**, v. 103, n. 50, p. 10999–11006, 1999.

MAJEWSKI, A. J.; WOOD, J. Tri-reforming of methane over $Ni@SiO_2$ catalyst. **International Journal of Hydrogen Energy**, v. 39, n. 24, p. 12578–12585, 2014.

MAKRI, M. M. et al. Effect of support composition on the origin and reactivity of carbon formed during dry reforming of methane over 5wt% $Ni/Ce_{1-x}M_xO_{2-\delta}$ ($M=Zr^{4+}$, Pr^{3+}) catalysts. **ICP, a meeting point for catalysis around the world. 40th Anniversary**, v. 259, p. 150–164, 2016.

MARINHO, A. L. A. et al. Steam reforming of ethanol over Ni-based catalysts obtained from $LaNiO_3$ and $LaNiO_3/CeSiO_2$ perovskite-type oxides for the production of hydrogen. **Applied Catalysis A: General**, v. 520, p. 53–64, 2016.

MARINHO, A. L. A. et al. Embedded Ni nanoparticles in CeZrO2 as stable catalyst for dry reforming of methane. **Applied Catalysis B: Environmental**, v. 268, p. 118387, 2020.

MARK, M. F.; MAIER, W. F. CO_2-Reforming of Methane on Supported Rh and Ir Catalysts. **Journal of Catalysis**, v. 164, n. 1, p. 122–130, 1996.

MARTIN, D.; DUPREZ, D. Mobility of Surface Species on Oxides. 1. Isotopic Exchange of $^{18}O2$ with ^{16}O of SiO_2, Al_2O_3, ZrO_2, MgO, CeO_2, and CeO_2-Al_2O_3. Activation by Noble Metals. Correlation with Oxide Basicity. **Journal of Physical Chemistry**, v. 100, n. 22, p. 9429–9438, 1996.

MATTOS, L. V. et al. Partial oxidation of methane on Pt/Ce–ZrO2 catalysts. **Catalysis Today**, v. 77, n. 3, p. 245–256, 2002.

MCCABE, R. W.; WONG, C.; WOO, H. S. The passivating oxidation of platinum. **Journal of Catalysis**, v. 114, n. 2, p. 354–367, 1988.

MELCHIONNA, M.; TROVARELLI, A.; FORNASIERO, P. 2 - Synthesis and properties of cerium oxide-based materials. In: SCIRÈ, S.; PALMISANO, L. (Eds.). .

Cerium Oxide (CeO_2): Synthesis, Properties and Applications. [s.l.] Elsevier, 2020. p. 13–43.

MIKULOVÁ, J. et al. Characterizations of platinum catalysts supported on Ce, Zr, Pr-oxides and formation of carbonate species in catalytic wet air oxidation of acetic acid. **Advanced Catalytic Oxidation Processes**, v. 124, n. 3, p. 185–190, 2007.

MIRONOVA-ULMANE, N. et al. Raman scattering in nanosized nickel oxide NiO. **Journal of Physics: Conference Series**, v. 93, 2007.

MO, L. et al. Highly dispersed supported metal catalysts prepared via in-situ self-assembled core-shell precursor route. **International Journal of Hydrogen Energy**, v. 40, n. 39, p. 13388–13398, 2015.

MOGENSEN, M.; SAMMES, N. M.; TOMPSETT, G. A. Physical, chemical and electrochemical properties of pure and doped ceria. **Solid State Ionics**, v. 129, n. 1, p. 63–94, 2000.

MOLINA, R.; PONCELET, G. α-Alumina-Supported Nickel Catalysts Prepared from Nickel Acetylacetonate: A TPR Study. **Journal of Catalysis**, v. 173, n. 2, p. 257–267, 1998.

MONTE, R. D.; KAŠPAR, J. On the Role of Oxygen Storage in Three-Way Catalysis. **Topics in Catalysis**, v. 28, n. 1, p. 47–57, 2004.

MONTINI, T. et al. Fundamentals and Catalytic Applications of CeO_2-Based Materials. **Chem Rev**, v. 116, n. 10, p. 5987–6041, 2016.

MORRIS, S. M.; FULVIO, P. F.; JARONIEC, M. Ordered Mesoporous Alumina-Supported Metal Oxides. **Journal of the American Chemical Society**, v. 130, n. 45, p. 15210–15216, 2008.

MUKRI, B. D.; WAGHMARE, U. V.; HEGDE, M. S. Platinum Ion-Doped TiO_2: High Catalytic Activity of Pt^{2+} with Oxide Ion Vacancy in $Ti^{4+}_{1-x}Pt^{2+}_xO_{2-x}$ Compared to Pt^{4+} without Oxide Ion Vacancy in $Ti^{4+}_{1-x}Pt^{4+}_xO_2$. **Chemistry of Materials**, v. 25, n. 19, p. 3822–3833, 2013.

NAKAJIMA, A.; YOSHIHARA, A.; ISHIGAME, M. Defect-induced Raman spectra in doped CeO_2. **Physical Review B**, v. 50, n. 18, p. 13297–13307, 1994.

NAKAMURA, J. et al. Role of support in reforming of CH_4 with CO_2 over Rh catalysts. **Catalysis Letters**, v. 25, n. 3, p. 265–270, 1994.

NATESAKHAWAT, S. et al. Deactivation characteristics of lanthanide-promoted sol–gel Ni/Al_2O_3 catalysts in propane steam reforming. **Journal of Catalysis**, v. 234, n. 2, p. 496–508, 2005.

NÉMETH, M. et al. Impregnated Ni/ZrO_2 and Pt/ZrO_2 catalysts in dry reforming of methane: Activity tests in excess methane and mechanistic studies with labeled $^{13}CO_2$. **Applied Catalysis A: General**, v. 504, p. 608–620, 2015.

NIK ROSELINA, N. R.; AZIZAN, A.; LOCKMAN, Z. Synthesis of nickel nanoparticles via non-aqueous polyol method: Effect of reaction time. **Sains Malaysiana**, v. 41, n. 8, p. 1037–1042, 2012.

NORONHA, F. B. et al. Correlation between catalytic activity and support reducibility in the CO_2 reforming of methane over $Pt/Ce_xZr_{1-x}O_2$ catalysts. **Chemical Engineering Journal**, v. 82, n. 1–3, p. 21–31, 2001.

OCHOA, A. et al. Coke formation and deactivation during catalytic reforming of biomass and waste pyrolysis products: A review. **Renewable and Sustainable Energy Reviews**, v. 119, p. 109600, 2020.

O'CONNOR, A. M.; MEUNIER, F. C.; ROSS, J. R. H. An In-situ DRIFTS Study of the Mechanism of the CO_2 Reforming of CH_4 over a Pt/ZrO_2 Catalyst. **Studies in Surface Science and Catalysis**, v. 119, p. 819–824, 1998.

OLIVEIRA, J. F. G. DE; TRINDADE, T. C. G. World Energy Matrix. In: OLIVEIRA, J. F. G. DE; TRINDADE, T. C. G. (Eds.). . **Sustainability Performance Evaluation of Renewable Energy Sources: The Case of Brazil**. Cham: Springer International Publishing, 2018. p. 1–17.

OMOREGBE, O. et al. Influence of Lanthanide Promoters on Ni/SBA-15 Catalysts for Syngas Production by Methane Dry Reforming. **Proceeding of 4th International**

Conference on Process Engineering and Advanced Materials (ICPEAM 2016), v. 148, p. 1388–1395, 2016.

PADI, S. P. et al. Coke-free methane dry reforming over nano-sized NiO-CeO_2 solid solution after exsolution. **Catalysis Communications**, v. 138, p. 105951, 2020.

PAKHARE, D.; SPIVEY, J. A review of dry (CO_2) reforming of methane over noble metal catalysts. **Chem. Soc. Rev.**, v. 43, n. 22, p. 7813–7837, 2014.

PALMA, V. et al. Experimental and numerical investigations on structured catalysts for methane steam reforming intensification. **Journal of Cleaner Production**, v. 111, p. 217–230, 2016.

PANTU, P.; GAVALAS, G. R. Methane partial oxidation on Pt/CeO_2 and Pt/Al_2O_3 catalysts. **Applied Catalysis A: General**, v. 223, n. 1, p. 253–260, 2002.

PAPADOPOULOU, C.; MATRALIS, H.; VERYKIOS, X. Utilization of Biogas as a Renewable Carbon Source: Dry Reforming of Methane. In: GUCZI, L.; ERDÔHELYI, A. (Eds.). **Catalysis for Alternative Energy Generation**. New York, NY: Springer New York, 2012. p. 57–127.

PARK, S. H.; TZOU, M. S.; SACHTLER, W. M. H. Temperature programmed reduction and re-oxidation of platinum in y-zeolites. **Applied Catalysis**, v. 24, n. 1, p. 85–98, 1986.

PÉREZ-CHÁVEZ, A. M.; MAYER, L.; ALBERTÓ, E. Mushroom cultivation and biogas production: A sustainable reuse of organic resources. **Energy for Sustainable Development**, v. 50, p. 50–60, 2019.

PÉREZ-COLL, D. et al. Reducibility of $Ce_{1-x}Gd_xO_{2-\delta}$ in prospective working conditions. **Journal of Power Sources**, v. 173, n. 1, p. 291–297, 2007.

PERRICHON, V. et al. Reduction of cerias with different textures by hydrogen and their reoxidation by oxygen. **Journal of the Chemical Society, Faraday Transactions**, v. 90, n. 5, p. 773–781, 1994.

PIJOLAT, M. et al. Thermal stability of doped ceria: experiment and modelling. **Journal of the Chemical Society, Faraday Transactions**, v. 91, n. 21, p. 3941–3948, 1995.

PINO, L. et al. A comparative study of Pt/CeO_2 catalysts for catalytic partial oxidation of methane to syngas for application in fuel cell electric vehicles. **Applied Catalysis A: General**, v. 243, n. 1, p. 135–146, 2003.

PIUMETTI, M. et al. Nanostructured ceria-zirconia catalysts for CO oxidation: Study on surface properties and reactivity. **Applied Catalysis B: Environmental**, v. 197, p. 35–46, 2016.

POMPEO, F. et al. Study of Ni and Pt catalysts supported on α-Al_2O_3 and ZrO_2 applied in methane reforming with CO_2. **Applied Catalysis A: General**, v. 316, n. 2, p. 175–183, 2007.

POZDNYAKOVA, O. et al. Preferential CO oxidation in hydrogen (PROX) on ceria-supported catalysts, part I: Oxidation state and surface species on Pt/CeO_2 under reaction conditions. **Journal of Catalysis**, v. 237, n. 1, p. 1–16, 2006.

PU, J. et al. Ceria-promoted $Ni@Al_2O_3$ core-shell catalyst for steam reforming of acetic acid with enhanced activity and coke resistance. **International Journal of Hydrogen Energy**, v. 43, n. 6, p. 3142–3153, 2018.

RABELO-NETO, R. C. et al. CO_2 reforming of methane over supported $LaNiO_3$ perovskite-type oxides. **Applied Catalysis B: Environmental**, v. 221, p. 349–361, 2018.

RADLIK, M. et al. Dry reforming of methane over $Ni/Ce_{0.62}Zr_{0.38}O_2$ catalysts: Effect of Ni loading on the catalytic activity and on H_2/CO production. **International Symposium on Air & Water Pollution Abatement Catalysis (AWPAC)Voume 2 – Catalytis for renewable energy**, v. 18, n. 11, p. 1242–1249, 2015.

RAO, B. G.; MUKHERJEE, D.; REDDY, B. M. Chapter 1 - Novel approaches for preparation of nanoparticles. In: FICAI, D.; GRUMEZESCU, A. M. (Eds.). **Nanostructures for Novel Therapy**. [s.l.] Elsevier, 2017. p. 1–36.

ROCCHINI, E. et al. Reduction and Oxygen Storage Behavior of Noble Metals Supported on Silica-Doped Ceria. **Journal of Catalysis**, v. 211, n. 2, p. 407–421, 2002.

RODRIGUEZ, J. A. et al. Properties of CeO_2 and $Ce_{1-x}Zr_xO_2$ Nanoparticles: X-ray Absorption Near-Edge Spectroscopy, Density Functional, and Time-Resolved X-ray Diffraction Studies. **The Journal of Physical Chemistry B**, v. 107, n. 15, p. 3535–3543, 2003.

ROH, H.-S. et al. Combined H_2O and CO_2 Reforming of Methane Over Ni–Ce–ZrO_2 Catalysts for Gas to Liquids (GTL). **Catalysis Letters**, v. 125, n. 3–4, p. 283–288, 2008.

ROSSIGNOL, S.; GÉRARD, F.; DUPREZ, D. Effect of the preparation method on the properties of zirconia-ceria materials. **Journal of Materials Chemistry**, v. 9, n. 7, p. 1615–1620, 1999.

ROSTRUP-NIELSEN, J. Equilibria of decomposition reactions of carbon monoxide and methane over nickel catalysts. **Journal of Catalysis**, v. 27, n. 3, p. 343–356, 1972.

ROSTRUP-NIELSEN, J. Coking on nickel catalysts for steam reforming of hydrocarbons. **Journal of Catalysis**, v. 33, n. 2, p. 184–201, 1974.

ROSTRUP-NIELSEN, J.; BAK HANSEN, J.-H. CO_2-Reforming of Methane over Transition Metals. **Journal of Catalysis**, v. 144, n. 1, p. 38–49, 1993.

ROSTRUP-NIELSEN, J. R.; PEDERSEN, K.; SEHESTED, J. High temperature methanation: Sintering and structure sensitivity. **Applied Catalysis A: General**, v. 330, p. 134–138, 2007.

ROSTRUP-NIELSEN, J.; TRIMM, D. L. Mechanisms of carbon formation on nickel-containing catalysts. **Journal of Catalysis**, v. 48, n. 1, p. 155–165, 1977.

RUCKENSTEIN, E.; HU, Y. H. The effect of precursor and preparation conditions of MgO on the CO_2 reforming of CH_4 over NiO/MgO catalysts. **Applied Catalysis A: General**, v. 154, 185-205, 1997

SADYKOV, V. et al. Oxygen mobility of Pt-promoted doped CeO_2–ZrO_2 solid solutions: Characterization and effect on catalytic performance in syngas generation by

fuels oxidation/reforming. **6th World Congress on Oxidation Catalysis Lille, France, 5-10 July 2009 Towards an integrated approach in innovation and development**, v. 157, n. 1, p. 55–60, 2010.

SADYKOV, V. A. et al. Mobility and reactivity of lattice oxygen in Gd-doped ceria promoted by Pt. **Reaction Kinetics and Catalysis Letters**, v. 85, n. 2, p. 367–374, 2005.

SAHLI, N. et al. Ni catalysts from $NiAl_2O_4$ spinel for CO_2 reforming of methane. **Catalysis, Nanomaterials and Environment**, v. 113, n. 3, p. 187–193, 2006.

SÁNCHEZ-SÁNCHEZ, M. C.; NAVARRO, R. M.; FIERRO, J. L. G. Ethanol steam reforming over $Ni/M_xO_y–Al_2O_3$ (M=Ce, La, Zr and Mg) catalysts: Influence of support on the hydrogen production. **EHEC2005**, v. 32, n. 10, p. 1462–1471, 2007.

SARKAR, B. et al. Reforming of methane with CO_2 over Ni nanoparticle supported on mesoporous ZSM-5. **Special Issue dedicated to Paul Ratnasamy on the occasion of his 70th birthday**, v. 198, n. 1, p. 209–214, 2012.

SATO, S. et al. Basic properties of rare earth oxides. **Applied Catalysis A: General**, v. 356, n. 1, p. 57–63, 2009.

SAW, E. T. et al. Highly Active and Stable Bimetallic Nickel-Copper Core-Ceria Shell Catalyst for High-Temperature Water-Gas Shift Reaction. **ChemCatChem**, v. 7, n. 20, p. 3358–3367, 2015.

SCHEFFER, B.; MOLHOEK, P.; MOULIJN, J. A. Temperature-programmed reduction of $NiOWO_3/Al_2O_3$ Hydrodesulphurization catalysts. **Applied Catalysis**, v. 46, n. 1, p. 11–30, 1989.

SERRANO-LOTINA, A.; DAZA, L. Influence of the operating parameters over dry reforming of methane to syngas. **International Journal of Hydrogen Energy**, v. 39, n. 8, p. 4089–4094, 2014.

SHAIKHUTDINOV, SH. K. et al. Size and Support Effects for CO Adsorption on Gold Model Catalysts. **Catalysis Letters**, v. 86, n. 4, p. 211–219, 2003.

SHE, Y. et al. Rare earth oxide modified CuO/CeO_2 catalysts for the water–gas shift reaction. **International Journal of Hydrogen Energy**, v. 34, n. 21, p. 8929–8936, 2009.

SHYU, J. Z.; WEBER, W. H.; GANDHI, H. S. Surface characterization of alumina-supported ceria. **The Journal of Physical Chemistry**, v. 92, n. 17, p. 4964–4970, 1988.

SILVA, P. P. et al. Effect of Ce/Zr ratio on the performance of $Pt/CeZrO_2/Al_2O_3$ catalysts for methane partial oxidation. **Selected Contributions of the XIX Ibero American Catalysis Symposium**, v. 107–108, p. 734–740, 2005.

SINGH, K.; ACHARYA, S. A.; BHOGA, S. S. Low temperature processing of dense samarium-doped CeO_2 ceramics: sintering and intermediate temperature ionic conductivity. **Ionics**, v. 13, n. 6, p. 429–434, 2007.

SOLYMOSI, F.; KUTSÁN, GY.; ERDÖHELYI, A. Catalytic reaction of CH_4 with CO_2 over alumina-supported Pt metals. **Catalysis Letters**, v. 11, n. 2, p. 149–156, 1991.

SORIA, M. A. et al. Thermodynamic and experimental study of combined dry and steam reforming of methane on Ru/ZrO_2-La_2O_3 catalyst at low temperature. **International Journal of Hydrogen Energy**, v. 36, n. 23, p. 15212–15220, 2011.

STAGG-WILLIAMS, S. M. et al. CO_2 Reforming of CH_4 over Pt/ZrO_2 Catalysts Promoted with La and Ce Oxides. **Journal of Catalysis**, v. 194, n. 2, p. 240–249, 2000.

STROUD, T. et al. Chemical CO_2 recycling via dry and bi reforming of methane using $Ni\text{-}Sn/Al_2O_3$ and $Ni\text{-}Sn/CeO_2$-Al_2O_3 catalysts. **Applied Catalysis B: Environmental**, v. 224, p. 125–135, 2018.

SUN, N. et al. Effect of pore structure on Ni catalyst for CO_2 reforming of CH_4. **Energy & Environmental Science**, v. 3, n. 3, p. 366–369, 2010.

TAKANABE, K. et al. Influence of reduction temperature on the catalytic behavior of Co/TiO_2 catalysts for CH_4/CO_2 reforming and its relation with titania bulk crystal structure. **Journal of Catalysis**, v. 230, n. 1, p. 75–85, 2005.

TANG, C. et al. High Carbon-Resistance $Ni@CeO_2$ Core–Shell Catalysts for Dry Reforming of Methane. **Kinetics and Catalysis**, v. 58, n. 6, p. 800–808, 2017.

TANIGUCHI, T. et al. Identifying defects in ceria-based nanocrystals by UV resonance Raman spectroscopy. **Journal of Physical Chemistry C**, v. 113, n. 46, pp. 19789-19793, 2009.

TELES, C. A. et al. The role of defect sites and oxophilicity of the support on the phenol hydrodeoxygenation reaction. **Applied Catalysis B: Environmental**, v. 249, p. 292–305, 2019.

TERRIBILE, D. et al. The preparation of high surface area CeO_2–ZrO_2 mixed oxides by a surfactant-assisted approach. **Catalysis Today**, v. 43, n. 1, p. 79–88, 1998.

THERDTHIANWONG, S.; SIANGCHIN, C.; THERDTHIANWONG, A. Improvement of coke resistance of Ni/Al_2O_3 catalyst in CH_4/CO_2 reforming by ZrO_2 addition. **Fuel Processing Technology**, v. 89, n. 2, p. 160–168, 2008.

TIAN, H. et al. Recent Advances on the Design of Group VIII Base-Metal Catalysts with Encapsulated Structures. **ACS Catalysis**, v. 5, n. 8, p. 4959–4977, 2015.

TROVARELLI, A. et al. Nanophase Fluorite-Structured CeO_2–ZrO_2 Catalysts Prepared by High-Energy Mechanical Milling. **Journal of Catalysis**, v. 169, n. 2, p. 490–502, 1997.

ULLAH KHAN, I. et al. Biogas as a renewable energy fuel – A review of biogas upgrading, utilization and storage. **Energy Conversion and Management**, v. 150, p. 277–294, 2017.

U.S. Energy Information Administration (EIA). International energy outlook 2019—with projections to 2050. Available at www.eia.gov. Accessed 18 Mar 2020.

USMAN, M.; WAN DAUD, W. M. A.; ABBAS, H. F. Dry reforming of methane: Influence of process parameters—A review. **Renewable and Sustainable Energy Reviews**, v. 45, p. 710–744, 2015.

VERMÖHLEN, K. et al. Adsorption of polyacrylic acid on aluminium oxide: DRIFT spectroscopy and ab initio calculations. **Colloids and Surfaces A: Physicochemical and Engineering Aspects**, v. 170, n. 2, p. 181–189, 2000.

VERYKIOS, X. E. Mechanistic aspects of the reaction of CO_2 reforming of methane over Rh/Al_2O_3 catalyst. **Catalytic Conversion of Carbon Dioxide**, v. 255, n. 1, p. 101–111, 2003.

VITA, A. et al. Hydrogen-rich gas production by steam reforming of n-dodecane: Part I: Catalytic activity of Pt/CeO_2 catalysts in optimized bed configuration. **Applied Catalysis B: Environmental**, v. 199, p. 350–360, 2016.

VLAIC, G. et al. Relationship between the Zirconia-Promoted Reduction in the Rh-Loaded $Ce_{0.5}Zr_{0.5}O_2$ Mixed Oxide and the Zr–O Local Structure. **Journal of Catalysis**, v. 168, n. 2, p. 386–392, 1997.

WANG, F.; XU, L.; SHI, W. Syngas production from CO_2 reforming with methane over core-shell $Ni@SiO_2$ catalysts. **Journal of CO2 Utilization**, v. 16, p. 318–327, 2016.

WANG, J. B. et al. Study of ceria-supported nickel catalyst and effect of yttria doping on carbon dioxide reforming of methane. **Applied Catalysis A: General**, v. 218, n. 1, p. 69–79, 2001.

WANG, N. et al. One-pot Synthesis of Ordered Mesoporous NiCeAl Oxide Catalysts and a Study of Their Performance in Methane Dry Reforming. **ChemCatChem**, v. 6, n. 5, p. 1470–1480, 2014.

WANG, S.; LU, G. Q. (MAX). Carbon dioxide reforming of methane to synthesis gas over Metal-Supported catalysts: State of the Art. **Energy & Fuels**, v. 10, n. 1, p. 896–904, 1996.

WANG, X. et al. Ceria-based Catalysts for the Production of H_2 Through the Water-gas-shift Reaction: Time-resolved XRD and XAFS Studies. **Topics in Catalysis**, v. 49, n. 1–2, p. 81–88, 2008.

WANG, X. et al. $Pt@CeO_2$ multicore@shell self-assembled nanospheres: clean synthesis, structure optimization, and catalytic applications. **J Am Chem Soc**, v. 135, n. 42, p. 15864–72, 2013.

WANG, X. et al. l-Arginine-Triggered Self-Assembly of CeO_2 Nanosheaths on Palladium Nanoparticles in Water. **Angewandte Chemie International Edition**, v. 55, n. 14, p. 4542–4546, 2016.

WANG, X.; ECONOMIDES, M. CHAPTER 7 - Gas-To-Liquids (GTL). In: WANG, X.; ECONOMIDES, M. (Eds.). **Advanced Natural Gas Engineering**. [s.l.] Gulf Publishing Company, 2009. p. 243–287.

WANG, Y. et al. Facile synthesis of Cu@CeO_2 and its catalytic behavior for hydrogenation of methyl acetate to ethanol. **ChemCatChem**, v. 9, n. 12, p. 2085–2090, 22 jun. 2017.

WEI, J.; IGLESIA, E. Isotopic and kinetic assessment of the mechanism of reactions of CH_4 with CO_2 or H_2O to form synthesis gas and carbon on nickel catalysts. **Journal of Catalysis**, v. 224, n. 2, p. 370–383, 2004a.

WEI, J.; IGLESIA, E. Isotopic and kinetic assessment of the mechanism of methane reforming and decomposition reactions on supported iridium catalysts. **Physical Chemistry Chemical Physics**, v. 6, n. 13, p. 3754–3759, 2004b.

WOLFBEISSER, A. et al. Methane dry reforming over ceria-zirconia supported Ni catalysts. **Catalysis Today**, v. 277, p. 234–245, 2016.

XIANG, X. et al. One-Pot Synthesis of Ordered Mesoporous NiSiAl Oxides for Catalyzing CO_2 Reforming of CH_4. **European Journal of Inorganic Chemistry**, v. 2016, n. 21, p. 3396–3404, 2016.

XIANG, X. et al. Promoting Effect of KIT-6 to Support Ni-$Ce_{0.8}Gd_{0.2}O_{2-\delta}$ as Efficient Coke-Resistant Catalysts for Carbon Dioxide Reforming of Methane. **European Journal of Inorganic Chemistry**, v. 2020, n. 7, p. 631–637, 2020.

XU, L. et al. Ordered mesoporous alumina supported nickel based catalysts for carbon dioxide reforming of methane. **7th Petite Workshop on the Defect Chemical Nature of Energy Materials, 14-17 March 2011, Storaas, Kongsberg, Norway**, v. 37, n. 9, p. 7497–7511, 2012.

XU, L. et al. CO_2 reforming of CH_4 over rare earth elements functionalized mesoporous Ni–Ln (Ln = Ce, La, Sm, Pr)–Al–O composite oxides. **International Journal of Hydrogen Energy**, v. 39, n. 7, p. 3253–3268, 2014.

XU, L.; SONG, H.; CHOU, L. Mesoporous nanocrystalline ceria–zirconia solid solutions supported nickel based catalysts for CO_2 reforming of CH_4. **International Journal of Hydrogen Energy**, v. 37, n. 23, p. 18001–18020, 2012.

XU, Z. et al. Bound-state Ni species — a superior form in Ni-based catalyst for CH_4/CO_2 reforming. **Applied Catalysis A: General**, v. 210, n. 1, p. 45–53, 2001.

YAN, X. et al. Highly efficient and stable Ni/CeO_2-SiO_2 catalyst for dry reforming of methane: Effect of interfacial structure of Ni/CeO_2 on SiO_2. **Applied Catalysis B: Environmental**, v. 246, p. 221–231, 2019.

YANG, E. et al. Combined steam and CO_2 reforming of methane over $La_{1-x}Sr_xNiO_3$ perovskite oxides. **Special Issue of Catalysis Today for NGCS 11 Tromsø.**, v. 299, p. 242–250, 2018.

YANG, L. et al. Progress and perspectives in converting biogas to transportation fuels. **Renewable and Sustainable Energy Reviews**, v. 40, p. 1133–1152, 2014.

YAO, H. Ceria in automotive exhaust catalysts I. Oxygen storage. **Journal of Catalysis**, v. 86, n. 2, p. 254–265, 1984.

YASYERLI, S. et al. Ru incorporated Ni–MCM-41 mesoporous catalysts for dry reforming of methane: Effects of Mg addition, feed composition and temperature. **International Journal of Hydrogen Energy**, v. 36, n. 8, p. 4863–4874, 2011.

YENTEKAKIS, I. V. et al. Effect of support oxygen storage capacity on the catalytic performance of Rh nanoparticles for CO_2 reforming of methane. **Applied Catalysis B: Environmental**, v. 243, p. 490–501, 2019.

YUAN, Q. et al. Facile Synthesis for Ordered Mesoporous γ-Aluminas with High Thermal Stability. **Journal of the American Chemical Society**, v. 130, n. 11, p. 3465–3472, 2008.

ZHANG, C. et al. Pt-based core-shell nanocatalysts with enhanced activity and stability for CO oxidation. **Chem Commun (Camb)**, v. 49, n. 90, p. 10647–9, 2013a.

ZHANG, F. et al. Effects of Zr Doping into Ceria for the Dry Reforming of Methane over Ni/$CeZrO_2$ Catalysts: In Situ Studies with XRD, XAFS, and AP-XPS. **ACS Catalysis**, v. 10, n. 5, p. 3274–3284, 2020.

ZHANG, J.; LI, F. Coke-resistant Ni@SiO_2 catalyst for dry reforming of methane. **Applied Catalysis B, Environmental**, v. 176–177, p. 513–521, 2015.

ZHANG, L. et al. CO_2 reforming with methane reaction over Ni@SiO_2 catalysts coupled by size effect and metal-support interaction. **Fuel**, v. 256, p. 115954, 2019.

ZHANG, M. et al. Structural Characterization of Highly Stable Ni/SBA-15 Catalyst and Its Catalytic Performance for Methane Reforming with CO2. **Chinese Journal of Catalysis**, v. 27, n. 9, p. 777–781, 2006.

ZHANG, S. et al. Ceria-Doped Ni/SBA-16 Catalysts for Dry Reforming of Methane. **ACS Catalysis**, v. 3, n. 8, p. 1855–1864, 2013b.

ZHANG, Z. L. et al. Reforming of Methane with Carbon Dioxide to Synthesis Gas over Supported Rhodium Catalysts: I. Effects of Support and Metal Crystallite Size on Reaction Activity and Deactivation Characteristics. **Journal of Catalysis**, v. 158, n. 1, p. 51–63, 1996.

ZHENG, W. et al. Effects of CeO_2 addition on Ni/Al_2O_3 catalysts for the reaction of ammonia decomposition to hydrogen. **Applied Catalysis B: Environmental**, v. 80, n. 1, p. 98–105, 2008.

ZHOU, H.-P. et al. Thermally Stable Pt/CeO_2 Hetero-Nanocomposites with High Catalytic Activity. **Journal of the American Chemical Society**, v. 132, n. 14, p. 4998–4999, 2010.

ZHOU, L. et al. Effect of $NiAl_2O_4$ Formation on Ni/Al_2O_3 Stability during Dry Reforming of Methane. **ChemCatChem**, v. 7, n. 16, p. 2508–2516, 2015.

ZIELIŃSKI, J. Morphology of nickel/alumina catalysts. **Journal of Catalysis**, v. 76, n. 1, p. 157–163, 1982.

Appendix A - Supporting Information Chapter 4

- Isothermal Oxygen Isotopic Exchange at 350 °C

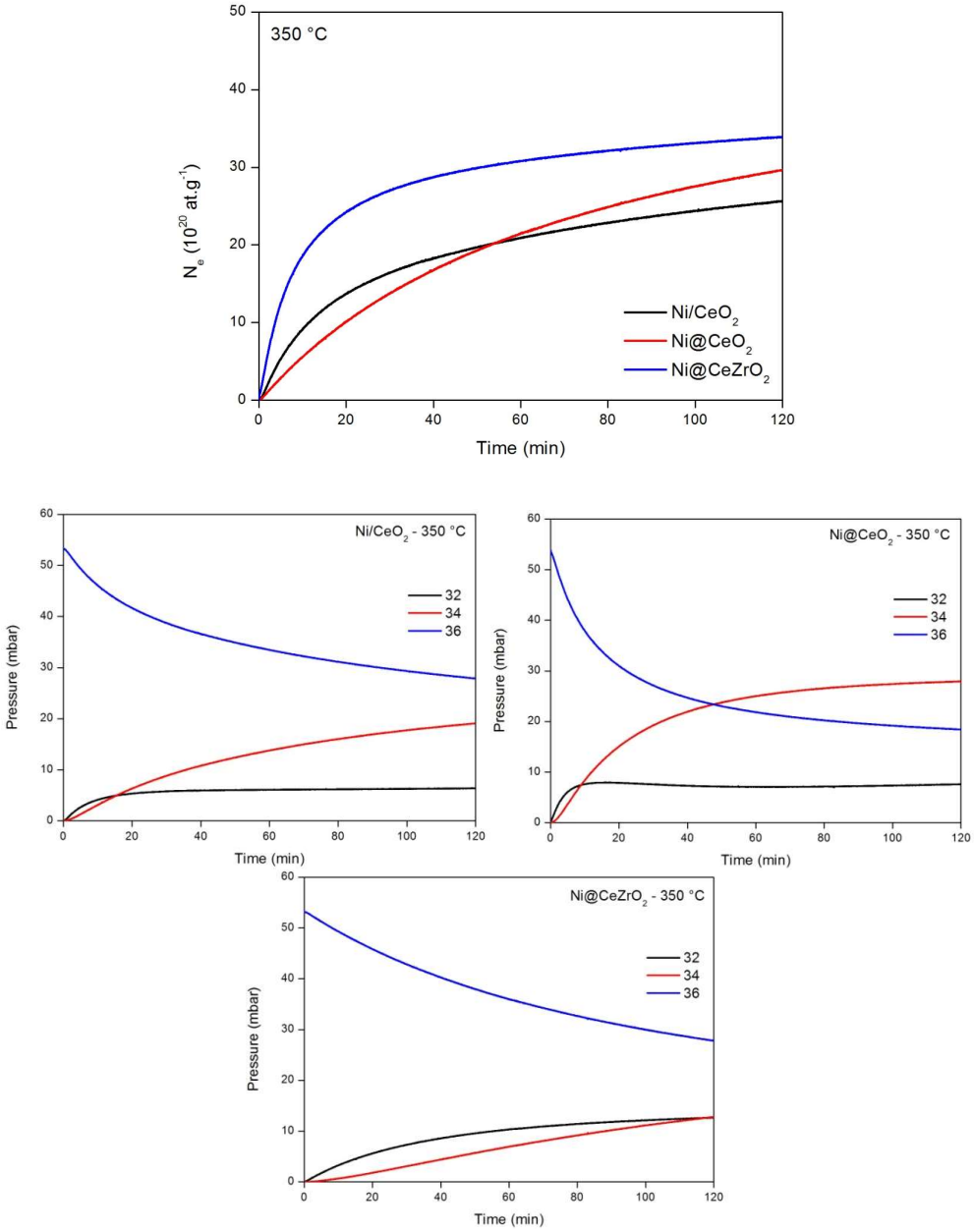

Figure S1 - Evolution of the number of exchanged oxygen atoms during IOIE at 350 °C and the isotopic distribution of each catalyst.

- Isothermal Oxygen Isotopic Exchange at 450 °C

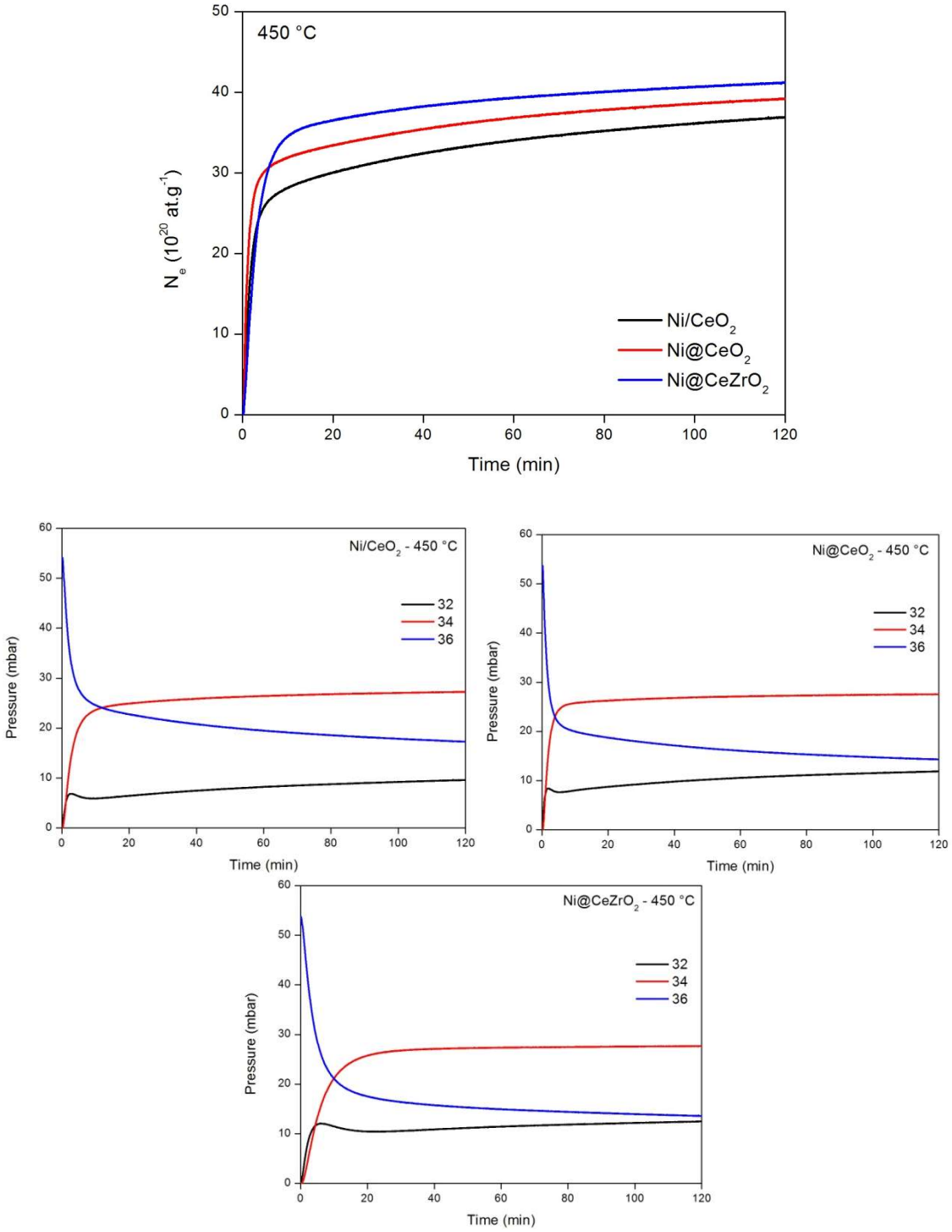

Figure S2 - Evolution of the number of exchanged oxygen atoms during IOIE at 450 °C and the isotopic distribution of each catalyst.

Appendix B – Supporting Information Chapter 6

- XRD at low angle

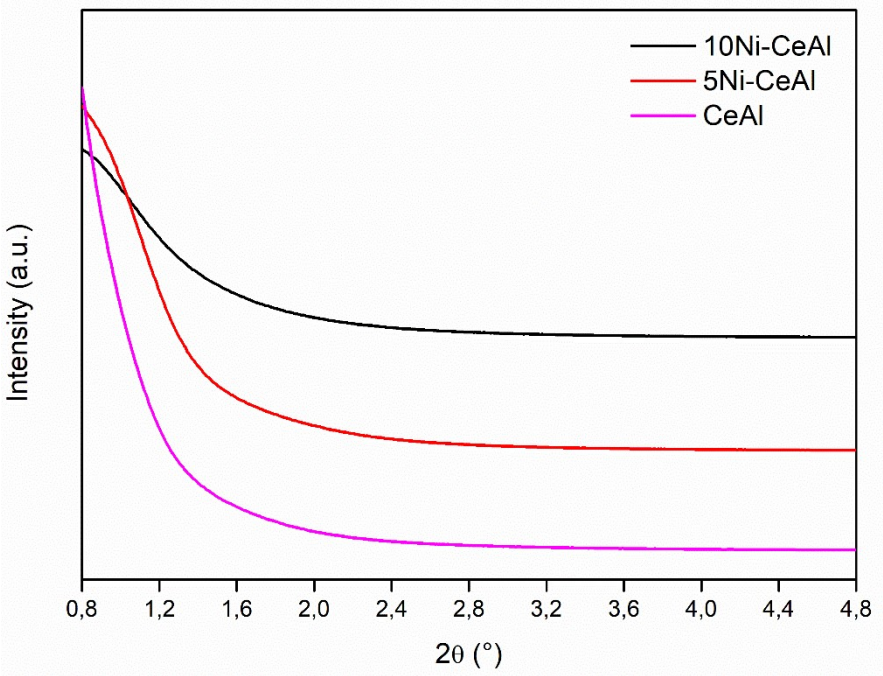

Figure S1 – XRD at low angle of the CeAl support, 5Ni-CeAl and 10Ni-CeAl.

- Raman of post-reaction sample

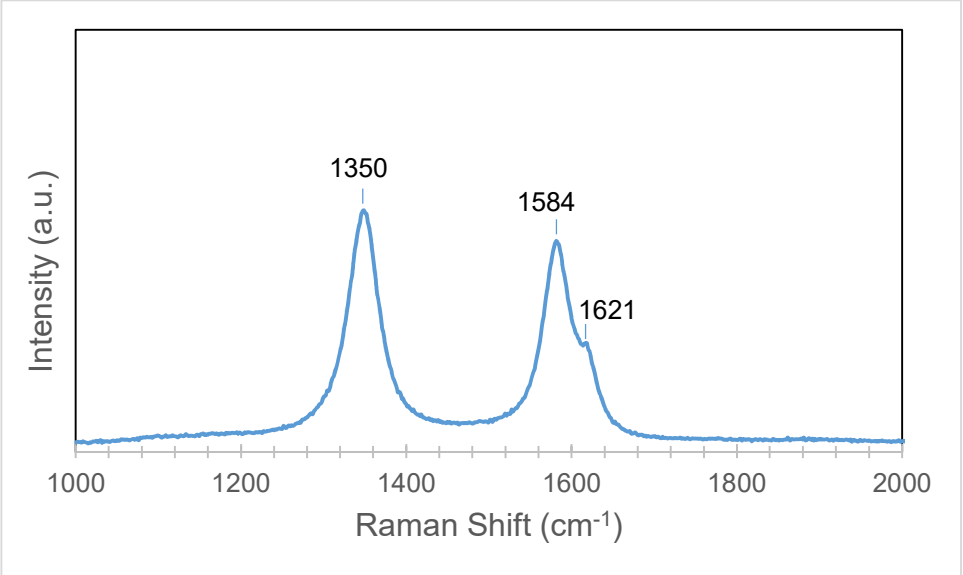

Figure S2 – Raman spectra of spent 10Ni/CeAl catalyst after DRM at 800°C

The position of the D band at 1350 cm^{-1} and G band at 1584 cm^{-1} are well consistent with the presence of MWCNT. The decomposition of the spectra enable the determination of a degree of graphitization which is related to the intensity ratio I_D(1350 cm^{-1})/I_G(1584 cm^{-1}). The lower is the I_D/I_G ratio, the higher is the degree of graphitization. For 10Ni/CeAl a ratio of 1.4 is calculated which corresponds to a low degree of graphitization.

- NH_3-TPD

The samples were reduced in the same conditions than the catalytic test and then 5%NH_3/He (30 mL/min) was flushed at 100°C during 45 min. After desorption of the physisorbed NH_3 at 100°C during 1h, the TCD signal was registered during the TPD under He flow (30mL/min) from 100 to 700°C. In the Figure S3, the TCD signal was converted in molar flow of NH_3 and normalized to 1g of sample for comparison.

A peak of desorption of very low intensity was observed between 150 and 350°C for all the samples which indicates that the concentration and strength of the acid sites are very weak on these catalysts. By integrating the 3 curves as a function of time, we obtained the following ranking of acidity:

10Ni-Al > 10Ni/CeAl > 10Ni-CeAl

Note that the uncertainties in the quantification is high because of the low intensity of the signal.

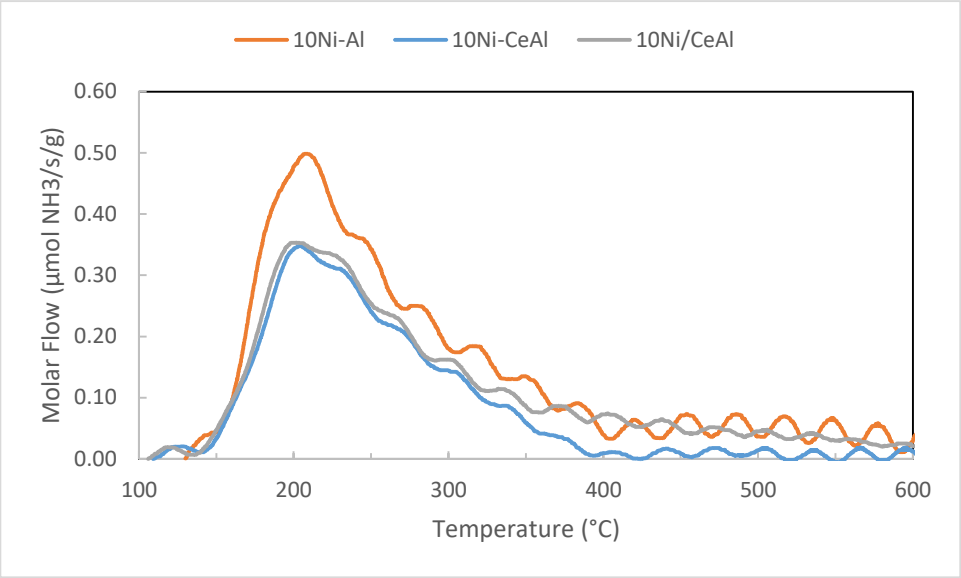

Figure S3 – NH_3-TPD of 10Ni-Al, 10Ni-CeAl and 10Ni/CeAl catalysts

Appendix C – Supporting Information Chapter 7

- Isothermal Oxygen Isotopic Exchange at 450 °C

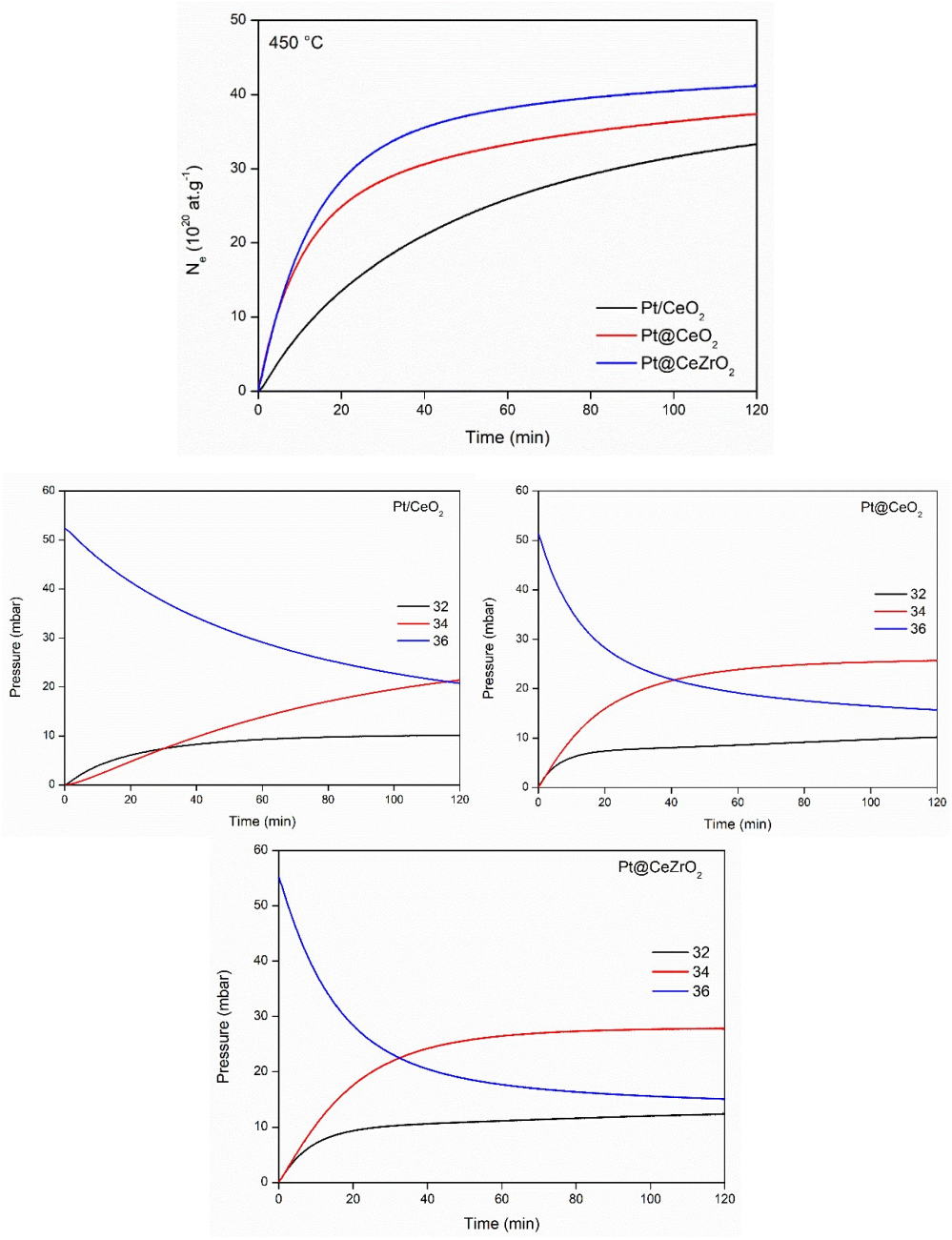

Figure S1 - Evolution of the number of exchanged oxygen atoms during IOIE at 450 °C and the isotopic distribution of each catalyst.

- Isothermal Oxygen Isotopic Exchange at 500 °C

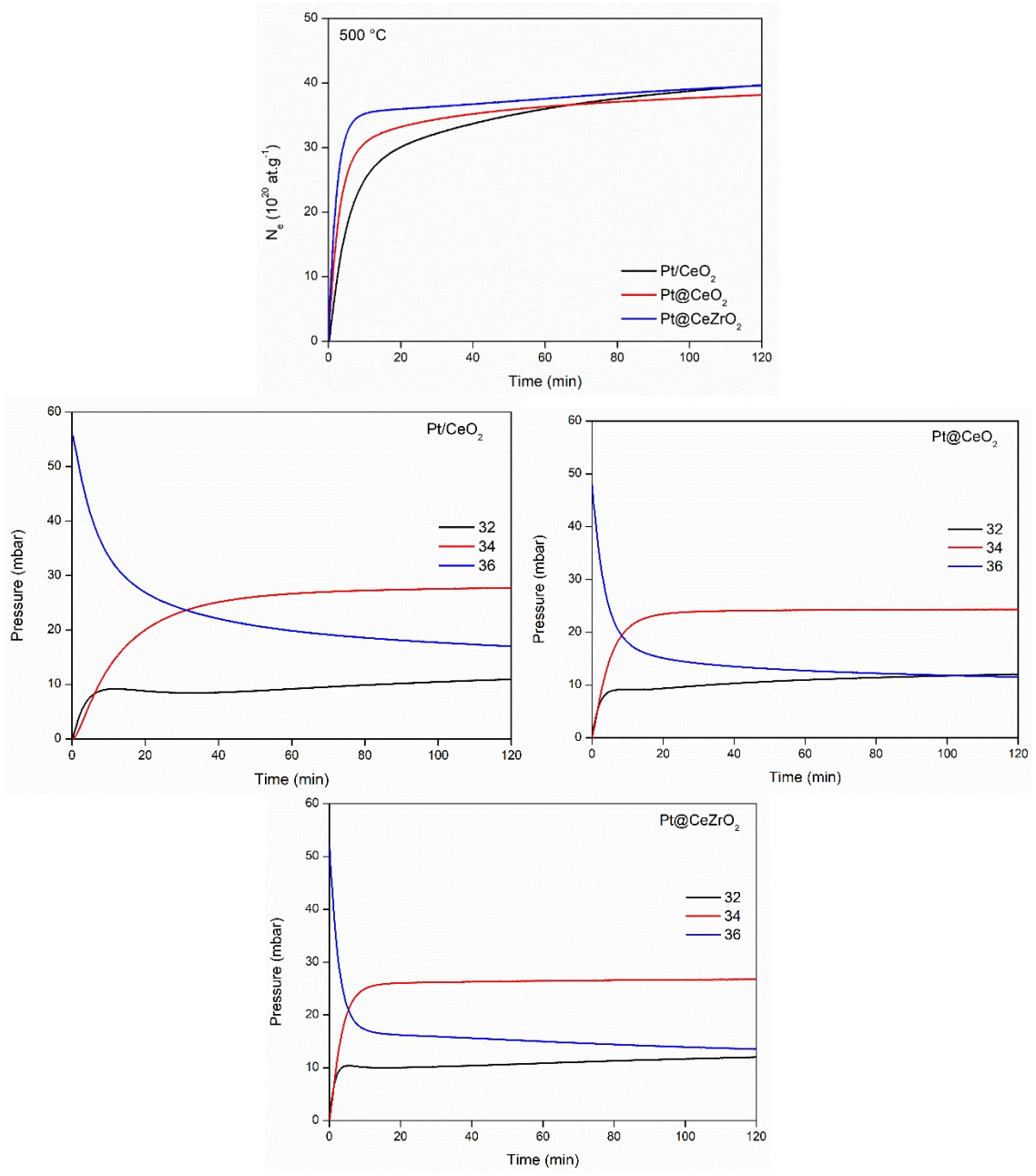

Figure S2 - Evolution of the number of exchanged oxygen atoms during IOIE at 500 °C and the isotopic distribution of each catalyst.

Appendix D – X-ray Patterns Reference

- **CeO_2**

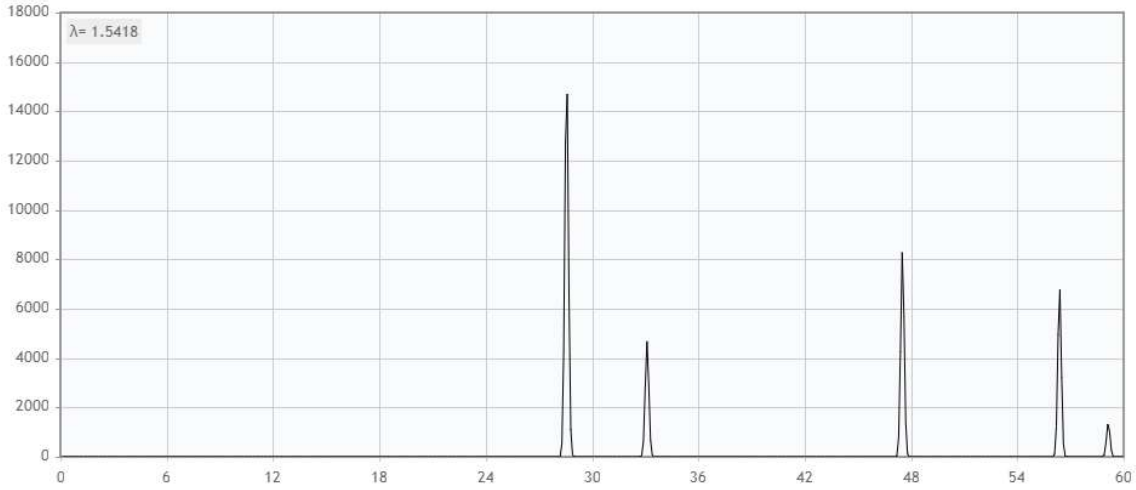

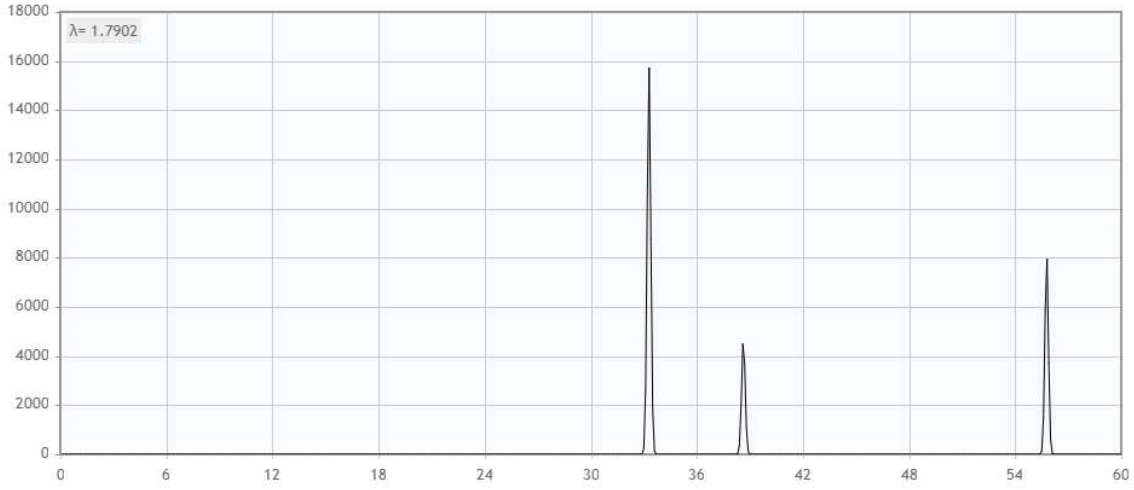

- **NiO**

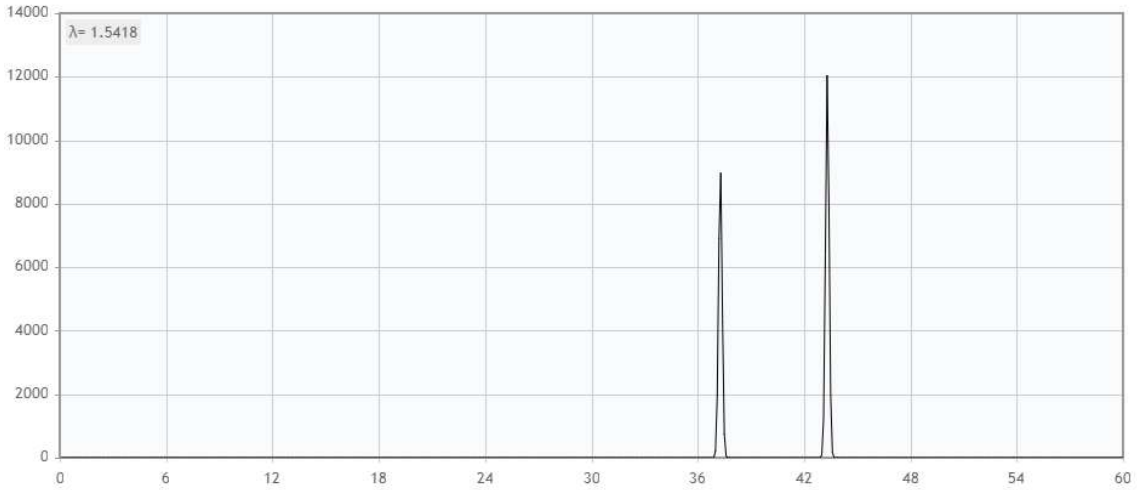
λ= 1.5418
14000
12000
10000
8000
6000
4000
2000
0
0
6
12
18
24
30
36
42
48
54
60

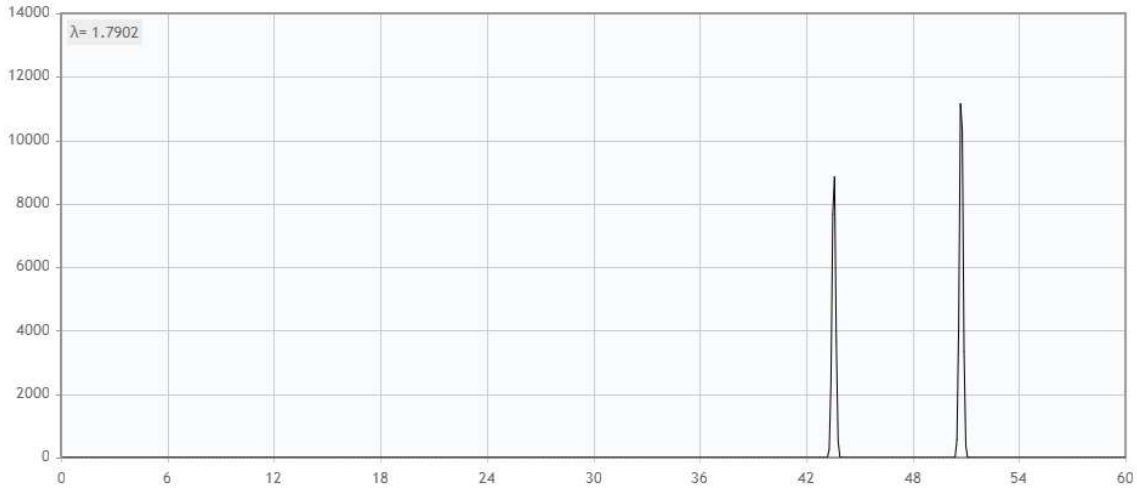
λ= 1.7902
14000
12000
10000
8000
6000
4000
2000
0
0
6
12
18
24
30
36
42
48
54
60

- **Ni**

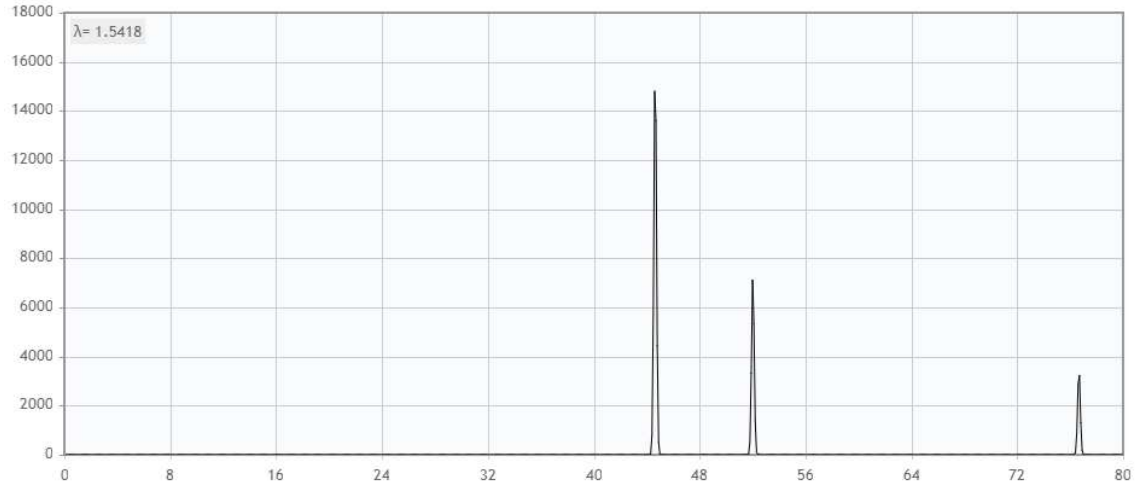
λ= 1.5418
18000
16000
14000
12000
10000
8000
6000
4000
2000
0
0
8
16
24
32
40
48
56
64
72
80

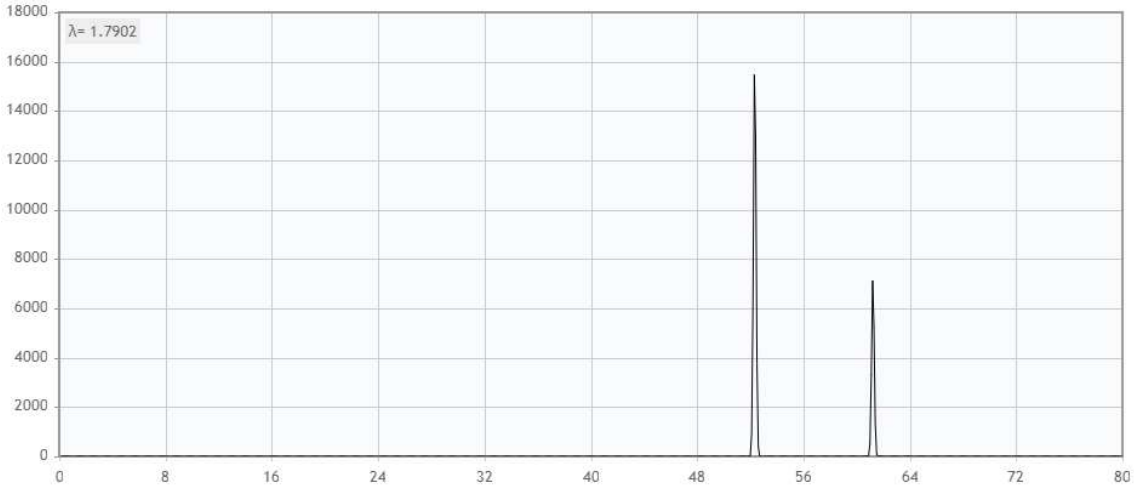
λ= 1.7902
18000
16000
14000
12000
10000
8000
6000
4000
2000
0
0
8
16
24
32
40
48
56
64
72
80

- **Al_2O_3**

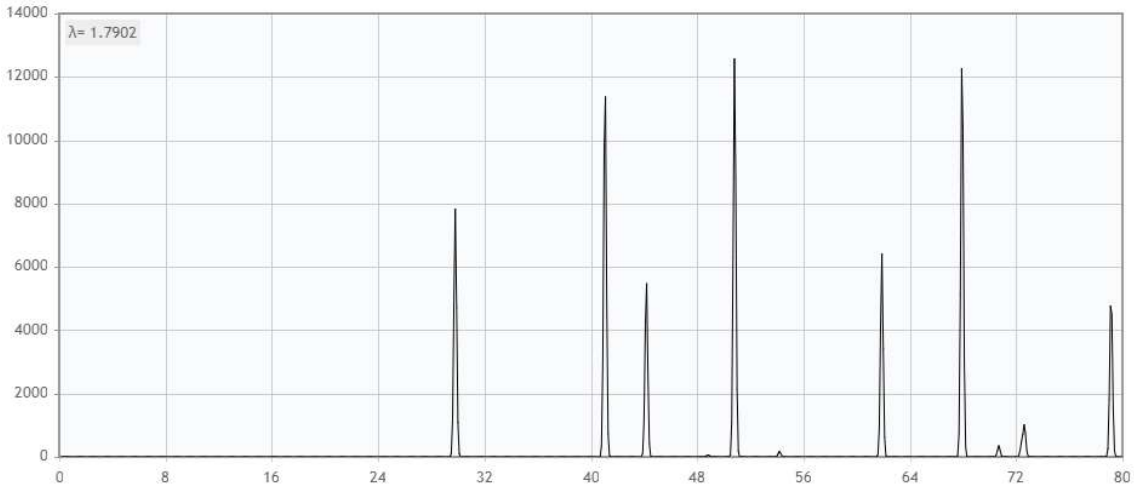
λ= 1.7902
14000
12000
10000
8000
6000
4000
2000
0
0
8
16
24
32
40
48
56
64
72
80

Appendix E – Conferences and Congress Published Works

- MARINHO, A. L. A.; TONIOLO, F. S.; NORONHA, FABIO B.; BION, N.; EPRON, F. Desenvolvimento de catalisadores à base de Ni embebido em CeO2 para a produção de gás de síntese via reação de reforma seca do metano. In: Congresso Brasileiro de Catálise, 2019, São Paulo. Congresso Brasileiro de Catálise, 2019.
- MARINHO, A. L. A.; TONIOLO, F. S.; NORONHA, FABIO B. Dry reforming of methane for hydrogen production over Ni@CeO2 with core-shell structure. In: 22nd World Hydrogen energy Conference, 2018, Rio de Janeiro.
- MARINHO, A. L. A.; TONIOLO, F. S.; NORONHA, FABIO B.; BION, N.; EPRON, F. Dry reforming of methane for hydrogen production over CeO2-Ni embedded catalyst. In: 14th European Congress on Catalysis, 2019, Aachen. 14th European Congress on Catalysis, 2019.

Appendix F – Licenses for Images Publication

Figure 2.1

This is a License Agreement between UFRJ ("You") and Royal Society of Chemistry ("Publisher") provided by Copyright Clearance Center ("CCC"). The license consists of your order details, the terms and conditions provided by Royal Society of Chemistry, and the CCC terms and conditions.

All payments must be made in full to CCC.

Order Date
03-Sep-2020
Order license ID
1060505-1
ISSN
1460-4744
Type of Use
Republish in a thesis/dissertation
Publisher
ROYAL SOCIETY OF CHEMISTRY
Portion
Image/photo/illustration

LICENSED CONTENT

Publication Title
Chemical Society reviews
Author/Editor
Royal Society of Chemistry (Great Britain)
Date
01/01/1972
Language
English
Country
United Kingdom of Great Britain and Northern Ireland
Rightsholder
Royal Society of Chemistry
Publication Type
e-Journal
URL
http://www.rsc.org/csr

REQUEST DETAILS

Portion Type
Image/photo/illustration
Number of images / photos / illustrations
1
Format (select all that apply)
Print, Electronic
Who will republish the content?
Academic institution
Duration of Use
Life of current edition
Lifetime Unit Quantity
More than 2,000,000
Rights Requested
Main product
Distribution
Worldwide
Translation
Original language of publication
Copies for the disabled?
No
Minor editing privileges?
Yes
Incidental promotional use?
No
Currency
USD

NEW WORK DETAILS

Title
Thesis
Instructor name
André Marinho
Institution name
UFRJ
Expected presentation date
2020-10-23

ADDITIONAL DETAILS

Order reference number
N/A

The requesting person / organization to appear on the license UFRJ	**Page or page range of portion** 4
REUSE CONTENT DETAILS	**Title of the article/chapter the portion is from** A review of dry (CO2) reforming of methane over noble metal catalysts
Title, description or numeric reference of the portion(s) Figure 2	**Author of portion(s)** Royal Society of Chemistry (Great Britain)
Editor of portion(s) N/A	**Issue, if republishing an article from a serial** N/A
Volume of serial or monograph N/A	**Publication date of portion** 2014-09-04

Figure 2.4

This Agreement between Federal University of Rio de Janeiro -- André Marinho ("You") and Elsevier ("Elsevier") consists of your license details and the terms and conditions provided by Elsevier and Copyright Clearance Center.

License Number	4901480471636
License date	Sep 03, 2020
Licensed Content Publisher	Elsevier
Licensed Content Publication	Renewable and Sustainable Energy Reviews
Licensed Content Title	Coke formation and deactivation during catalytic reforming of biomass and waste pyrolysis products: A review
Licensed Content Author	Aitor Ochoa,Javier Bilbao,Ana G. Gayubo,Pedro Castaño
Licensed Content Date	Mar 1, 2020
Licensed Content Volume	119
Licensed Content Issue	n/a
Licensed Content Pages	1
Start Page	109600
End Page	0
Type of Use	reuse in a thesis/dissertation
Portion	figures/tables/illustrations
Number of figures/tables/illustrations	1
Format	both print and electronic
Are you the author of this Elsevier article?	No
Will you be translating?	No
Title	DEVELOPMENT OF CATALYTIC PROCESS FOR BIOGAS UPGRADING: STUDY OF STRUCTURE AND OXYGEN MOBILITY OF Ni AND Pt NANOPARTICLES EMBEDDED CATALYSTS
Institution name	Federal University of Rio de Janeiro
Expected presentation date	Oct 2020
Portions	Figure 6
Requestor Location	Federal University of Rio de Janeiro Rua Henrique Ferreira

	Rio de Janeiro, 21550290 Brazil Attn: Federal University of Rio de Janeiro
Publisher Tax ID	GB 494 6272 12
Total	0.00 USD

Figure 2.5

This Agreement between Federal University of Rio de Janeiro -- André Marinho ("You") and Elsevier ("Elsevier") consists of your license details and the terms and conditions provided by Elsevier and Copyright Clearance Center.

License Number	4901481111714
License date	Sep 03, 2020
Licensed Content Publisher	Elsevier
Licensed Content Publication	Renewable and Sustainable Energy Reviews
Licensed Content Title	A review on catalyst development for dry reforming of methane to syngas: Recent advances
Licensed Content Author	Abdulrahman Abdulrasheed,Aishah Abdul Jalil,Yahya Gambo,Maryam Ibrahim,Hambali Umar Hambali,Muhamed Yusuf Shahul Hamid
Licensed Content Date	Jul 1, 2019
Licensed Content Volume	108
Licensed Content Issue	n/a
Licensed Content Pages	19
Start Page	175
End Page	193
Type of Use	reuse in a thesis/dissertation
Portion	figures/tables/illustrations
Number of figures/tables/illustrations	1
Format	both print and electronic
Are you the author of this Elsevier article?	No
Will you be translating?	No
Title	DEVELOPMENT OF CATALYTIC PROCESS FOR BIOGAS UPGRADING: STUDY OF STRUCTURE AND OXYGEN MOBILITY OF Ni AND Pt NANOPARTICLES EMBEDDED CATALYSTS
Institution name	Federal University of Rio de Janeiro
Expected presentation date	Oct 2020
Portions	Figure 1
Requestor Location	Federal University of Rio de Janeiro Rua Henrique Ferreira Rio de Janeiro, 21550290 Brazil Attn: Federal University of Rio de Janeiro
Publisher Tax ID	GB 494 6272 12
Total	0.00 USD

Figure 2.6

This is a License Agreement between UFRJ ("You") and Royal Society of Chemistry ("Publisher") provided by Copyright Clearance Center ("CCC"). The license consists of your order details, the terms and conditions provided by Royal Society of Chemistry, and the CCC terms and conditions.

All payments must be made in full to CCC.

Order Date
03-Sep-2020
Order license ID
1060512-1
ISSN
1460-4744
Type of Use
Republish in a thesis/dissertation
Publisher
ROYAL SOCIETY OF CHEMISTRY
Portion
Image/photo/illustration

LICENSED CONTENT

Publication Title
Chemical Society reviews
Author/Editor
Royal Society of Chemistry (Great Britain)
Date
01/01/1972
Language
English
Country
United Kingdom of Great Britain and Northern Ireland
Rightsholder
Royal Society of Chemistry
Publication Type
e-Journal
URL
http://www.rsc.org/csr

REQUEST DETAILS

Portion Type
Image/photo/illustration
Number of images / photos / illustrations
1
Format (select all that apply)
Print, Electronic
Who will republish the content?
Academic institution
Duration of Use
Life of current edition
Lifetime Unit Quantity
Up to 499
Rights Requested
Main product

Distribution
Worldwide
Translation
Original language of publication
Copies for the disabled?
No
Minor editing privileges?
No
Incidental promotional use?
No
Currency
USD

NEW WORK DETAILS

Title
DEVELOPMENT OF CATALYTIC PROCESS FOR BIOGAS UPGRADING: STUDY OF STRUCTURE AND OXYGEN MOBILITY ON Ni AND Pt NANOPARTICLES ENCAPSULATED CATALYSTS
Instructor name
André Marinho
Institution name
UFRJ
Expected presentation date
2020-10-23

ADDITIONAL DETAILS

Order reference number
N/A
The requesting person / organization to appear on the license
UFRJ

REUSE CONTENT DETAILS

Title, description or numeric reference of the portion(s)
Scheme 2
Editor of portion(s)
N/A
Volume of serial or monograph
N/A
Page or page range of portion
4

Title of the article/chapter the portion is from
Strategies for improving the performance and stability of Ni-based catalysts for reforming reactions
Author of portion(s)
Royal Society of Chemistry (Great Britain)
Issue, if republishing an article from a serial
N/A
Publication date of portion
2019-07-01

Figure 2.7

This is a License Agreement between UFRJ ("You") and Royal Society of Chemistry ("Publisher") provided by Copyright Clearance Center ("CCC"). The license consists of your order details, the terms and conditions provided by Royal Society of Chemistry, and the CCC terms and conditions.

All payments must be made in full to CCC.

Order Date
03-Sep-2020
Order license ID
1060516-1
ISSN
1364-548X
Type of Use
Republish in a thesis/dissertation
Publisher
ROYAL SOCIETY OF CHEMISTRY
Portion
Image/photo/illustration

LICENSED CONTENT

Publication Title
Chemical communications
Author/Editor
Royal Society of Chemistry (Great Britain)
Date
01/01/1996
Language
English
Country
United Kingdom of Great Britain and Northern Ireland
Rightsholder
Royal Society of Chemistry
Publication Type
e-Journal

REQUEST DETAILS

Portion Type
Image/photo/illustration
Number of images / photos / illustrations
1
Format (select all that apply)
Print, Electronic
Who will republish the content?
Academic institution
Duration of Use
Life of current edition
Lifetime Unit Quantity
Up to 499
Rights Requested
Main product
Distribution
Worldwide
Translation
Original language of publication
Copies for the disabled?
No
Minor editing privileges?
No
Incidental promotional use?
No
Currency
USD

NEW WORK DETAILS

Title
DEVELOPMENT OF CATALYTIC PROCESS FOR BIOGAS UPGRADING: STUDY OF STRUCTURE AND OXYGEN MOBILITY ON Ni AND Pt NANOPARTICLES ENCAPSULATED CATALYSTS
Instructor name
André Marinho
Institution name
UFRJ
Expected presentation date
2020-10-23

ADDITIONAL DETAILS

Order reference number
N/A
The requesting person / organization to appear on the license

UFRJ

REUSE CONTENT DETAILS

Title, description or numeric reference of the portion(s)
Figure 1
Editor of portion(s)
N/A
Volume of serial or monograph
N/A
Page or page range of portion
1

Title of the article/chapter the portion is from
A Ni@ZrO2 nanocomposite for ethanol steam reforming: enhanced stability via strong metal–oxide interaction
Author of portion(s)
Royal Society of Chemistry (Great Britain)
Issue, if republishing an article from a serial
N/A
Publication date of portion
2012-10-01

Figure 2.8

This Agreement between Federal University of Rio de Janeiro -- André Marinho ("You") and Elsevier ("Elsevier") consists of your license details and the terms and conditions provided by Elsevier and Copyright Clearance Center.

License Number	4901500931279
License date	Sep 03, 2020
Licensed Content Publisher	Elsevier
Licensed Content Publication	Renewable and Sustainable Energy Reviews
Licensed Content Title	A review on catalyst development for dry reforming of methane to syngas: Recent advances
Licensed Content Author	Abdulrahman Abdulrasheed,Aishah Abdul Jalil,Yahya Gambo,Maryam Ibrahim,Hambali Umar Hambali,Muhamed Yusuf Shahul Hamid
Licensed Content Date	Jul 1, 2019
Licensed Content Volume	108
Licensed Content Issue	n/a
Licensed Content Pages	19
Start Page	175
End Page	193
Type of Use	reuse in a thesis/dissertation
Portion	figures/tables/illustrations
Number of figures/tables/illustrations	1
Format	both print and electronic
Are you the author of this Elsevier article?	No
Will you be translating?	No
Title	DEVELOPMENT OF CATALYTIC PROCESS FOR BIOGAS UPGRADING: STUDY OF STRUCTURE AND OXYGEN MOBILITY OF Ni AND Pt NANOPARTICLES EMBEDDED CATALYSTS
Institution name	Federal University of Rio de Janeiro
Expected presentation date	Oct 2020
Portions	Figure 3
Requestor Location	Federal University of Rio de Janeiro Rua Henrique Ferreira Rio de Janeiro, 21550290

	Brazil Attn: Federal University of Rio de Janeiro
Publisher Tax ID	GB 494 6272 12
Total	0.00 USD

Figure 2.9

This Agreement between Federal University of Rio de Janeiro -- André Marinho ("You") and John Wiley and Sons ("John Wiley and Sons") consists of your license details and the terms and conditions provided by John Wiley and Sons and Copyright Clearance Center.

License Number	4901500131860
License date	Sep 03, 2020
Licensed Content Publisher	John Wiley and Sons
Licensed Content Publication	ChemCatChem
Licensed Content Title	One-pot Synthesis of Ordered Mesoporous NiCeAl Oxide Catalysts and a Study of Their Performance in Methane Dry Reforming
Licensed Content Author	Ning Wang, Zhenxin Xu, Jie Deng, et al
Licensed Content Date	Feb 24, 2014
Licensed Content Volume	6
Licensed Content Issue	5
Licensed Content Pages	11
Type of use	Dissertation/Thesis
Requestor type	University/Academic
Format	Print and electronic
Portion	Figure/table
Number of figures/tables	1
Will you be translating?	No
Title	DEVELOPMENT OF CATALYTIC PROCESS FOR BIOGAS UPGRADING: STUDY OF STRUCTURE AND OXYGEN MOBILITY OF Ni AND Pt NANOPARTICLES EMBEDDED CATALYSTS
Institution name	Federal University of Rio de Janeiro
Expected presentation date	Oct 2020
Portions	Figure 4
Requestor Location	Federal University of Rio de Janeiro Rua Henrique Ferreira Rio de Janeiro, 21550290 Brazil Attn: Federal University of Rio de Janeiro
Publisher Tax ID	EU826007151
Total	0.00 USD

Figure 2.10

Order Date
03-Sep-2020
Order license ID
1060517-1
ISSN
2040-3372
Type of Use
Republish in a thesis/dissertation
Publisher
RSC Pub
Portion
Image/photo/illustration

LICENSED CONTENT

Publication Title
Nanoscale
Author/Editor
National Center for Nanoscience and Technology., Royal Society of Chemistry (Great Britain)
Date
01/01/2009
Language
English
Country
United Kingdom of Great Britain and Northern Ireland
Rightsholder
Royal Society of Chemistry
Publication Type
e-Journal
URL
http://www.rsc.org/Publishing/Journals/NR/index.asp

REQUEST DETAILS

Portion Type
Image/photo/illustration
Number of images / photos / illustrations
1
Format (select all that apply)
Print, Electronic
Who will republish the content?
Academic institution
Duration of Use
Life of current edition
Lifetime Unit Quantity
Up to 499
Rights Requested
Main product
Distribution
Worldwide
Translation
Original language of publication
Copies for the disabled?
No
Minor editing privileges?
No
Incidental promotional use?
No
Currency
USD

NEW WORK DETAILS

Title
DEVELOPMENT OF CATALYTIC PROCESS FOR BIOGAS UPGRADING: STUDY OF STRUCTURE AND OXYGEN MOBILITY ON Ni AND Pt NANOPARTICLES ENCAPSULATED CATALYSTS
Instructor name
André Marinho
Institution name
UFRJ
Expected presentation date
2020-10-23

ADDITIONAL DETAILS

Order reference number
N/A
The requesting person / organization to appear on the license
UFRJ

REUSE CONTENT DETAILS

Title, description or numeric reference of the portion(s)
Figure 10
Editor of portion(s)
N/A
Volume of serial or monograph
N/A
Page or page range of portion
1282

Title of the article/chapter the portion is from
Unexpected redox behaviour of large surface alumina containing highly dispersed ceria nanoclusters
Author of portion(s)
National Center for Nanoscience and Technology.; Royal Society of Chemistry (Great Britain)
Issue, if republishing an article from a serial
N/A
Publication date of portion
2019-11-01